Probing the effect of conformational changes in protein complexes by vibrational spectroscopy : bioenergetics and allostery

Michelle Yegres

UNIVERSITÉ DE STRASBOURG

ÉCOLE DOCTORAL DES SCIENCE CHIMIQUES

Institut de Chimie UMR 7140

THÈSE

Présentée par

Michelle YEGRES

Pour obtenir le grade de

Docteur de l'Université de Strasbourg

Discipline / Spécialité : Chimie

Probing the effect of conformational changes in protein complexes by vibrational spectroscopy: bioenergetics and allostery

Sonder l'effet des changements conformationnels dans les complexes de protéines par spectroscopie vibrationnel: bioénergétique et allostery

Présenté le 24 Avril 2014

Thése dirigée par:

Prof. Petra Hellwig

Membres du jury:

Dr. Yves MELY	Université de Strasbourg
Dr. David MOSS	Karlsuhe Institute of Technology
Prof. Peter RICH	University College London

Argumentation cannot suffice for the discovery of a new work, since the subtlety of Nature is greater many times than the subtlety of argument.

-Francis Bacon

TABLE OF CONTENTS

ABSTRACT

The mechanism of enzyme regulation through conformational changes is a key pattern in governing cell behavior. In this thesis the focus is on three protein complexes that reflect how protein activity can be regulated by different effectors. Different spectroscopic techniques, like IR and Raman spectroscopy, were used is order to follow the secondary and tertiary conformational changes in protein structure to identify their roles. The first protein of interest was PDZ1 from MAGI-1, involved in cellular signaling. This scaffold domain is known to interact with the E6 protein from HPV16. It was demonstrated that the different conformational states and their affinities to the C-terminus of the viral protein is regulated by the dynamics of the hydrogen bonding network formed by the connection of specific amino acids in three regions of the protein. Study of mutations around the C-terminal area of the protein and the βC strand were performed; demonstrating that both regions are crucial for assembly of the hydrogen bonding network to stabilize the substrate binding. These results leads to conclude that the pathogenicity and prevalence of a particular virus like HPV16 is in its ability to build a stronger hydrogen bonding network in comparison to the natural binder. The allosteric model and the "shift population" model agree that, upon binding, conformational changes distant from a carboxylate binding group might be the key to understanding the binding dynamics between the PDZ domains and the viral proteins.

The second protein of interest was a model that constitutes a small scale prototype of the conformational changes observed in more complex proteins; it is a short Copper-binding peptide, the amyloid-beta peptide, known to be involved in Alzheimer's disease. The objective with this model was to describe the effect of histidine ligands in the metal centers upon Copper (Cu) reduction, a key electrochemical reaction in the development of Alzheimer's. FTIR difference spectroscopy showed two different spheres of coordination for Cu(II) and Cu(I). The major changes in the structure are dominated by the contribution of the imidazole ring of His residues (His6, His13 and His14), in addition to Asp1 and Tyr10 residues. Changes in the coordination geometry could be key to the pH-dependency of the aggregation observed in the presence of Cu(I). Accordingly, it can be suggested that the formation of the fibrils observed in Alzheimer's patients is not only triggered by the presence of Cu but it is strongly affected by its redox state.

The last system of interest was a metalloprotein, the NADH:ubiquinone oxidoreductase (complex I), which plays a key role in the cellular bioenergetics. This protein bears several Fe-S clusters and one flavin and its activity is regulated by the energy produced by a bound substrate and the electron transfer of its cofactors. The metal ligand-vibrations of the cofactors are described in their oxidized and reduced states. Using electrochemistry coupled to FTIR, Resonance Raman and Fluorescence spectroscopies, the investigation of complex I led to the conclusion that the properties of the metal centers are dictated, to a large extent, by their surrounding environment. In addition, changes in the conformation of the protein have a high impact on their redox properties and by the same token on the proper function of the protein. Furthermore, site-direct mutagenesis was used to probe the properties of N1a and N2. Besides the metal cofactors, this study proved the presence of a new quinone cofactor located close to the membrane domain.

Based on these studies, it is evident that the regulation of protein function through conformational changes is ruled by different factors where the effectors usually target specific amino acids that trigger a cascade reaction through other regions or domains of the protein. An interesting fact obtain from the result summary is that the far infrared region can become a new approach for the study of protein function. This work adds evidence that conformational transitions are more widespread than previously thought and that structural plasticity is essential for the biological activity of proteins.

RESUMÉ

Le mécanisme de régulation des enzymes à travers les changements conformationnels est un processus clé dans le contrôle du fonctionnement cellulaire. L'un des procédés, les plus fondamentaux, l'instant fascinant biologiques est le pliage d'une séquence linéaire d'acides aminés dans la structure tridimensionnelle d'une protéine fonctionnelle. La capacité des protéines à se replier en structures uniques et pour générer un large éventail de fonctions dépend directement de la séquence d'acides aminés et sur les interactions moléculaires entre chacun des acides aminés et de leur environnement.

Une protéine fonctionnelle doit être plié dans la "forme active" à droite. Néanmoins, il arrive que, sous certaines conditions, une protéine mal repliée devient une "forme inactive". Très souvent, ce repliement conduit à un dysfonctionnement cellulaire et la réaction biologique indésirable peut arriver. Dans les cas extrêmes, le mauvais repliement des protéines peut conduire à des modèles cellulaires qui sont traduits dans les maladies.

Il existe de nombreux mécanismes par lesquels les activités des protéines sont contrôlés. Les plus couramment décrit un est par la liaison de molécules effectrices, qui fonctionne souvent en induisant des changements conformationnels qui produisent des formes inactives ou actives de la protéine.

Cette thèse est focalisée sur l'étude de trois complexes protéiques qui reflètent comment l'activité de protéines peut être est régulée par différents effecteurs. Pour cela, différentes spectroscopies ont étaient utilisées pour suivre les changements conformationnels des structures secondaire et tertiaire d'une protéine.

Spectroscopie de vibration est le terme générique utilisé pour décrire des techniques d'analyse qui permettent d'analyser les vibrations des obligations. Les plus couramment utilisés sont l'infrarouge et la spectroscopie Raman. Les deux techniques sont complémentaires caractéristique fournissant des vibrations fondamentales qui sont largement utilisés pour la détermination et l'identification de la structure moléculaire et capable suivent interactions moléculaires.

Les vibrations IR et Raman sont généralement caractérisés par leur fréquence (énergie), l'intensité (caractère polaire ou polarisabilité respectivement), et de l'environnement des obligations; comme l'agencement géométrique, la présence de groupes fonctionnels et la

résistance de la liaison elle-même 10. Etant donné que les niveaux d'énergie de vibration sont uniques à chaque molécule, l'IR et le spectre Raman fournissent une "finger print" pour un type particulier de molécule.

Comme l'objectif de cette thèse est de caractériser les systèmes de protéines différentes où la fonction de la protéine est réglable via des interactions moléculaires avec une extrinsèque et / ou l'agent intrinsèque. Trois système différent a été choisi.

La première protéine d'intérêt est PDZ1 de MAGI-1, impliquées dans la signalisation cellulaire. Les domaines PDZ ont été initialement caractérisés comme un séquence de 90 acides aminés répétée de trois protéines différentes appartenant à la famille MAGUK: un humain PSD-95 située dans les densités postsynaptiques de neurones, une protéine cloisonnées de jonction Drosophila: disques grande DLG et ZO-1 et un protéine de jonction serrée présent sur la surface de la membrane cytoplasmique. Les protéines PDZ sont généralement ciblés lors de l'infection par différents virus avec des cycles de réplication bien distinctes. L'association de certains PMP virales avec les protéines PDZ entraîne une perte de la fonction de PDZ, soit par le biais de la dégradation par le protéasome ou des changements dans le contrôle de conformation des protéines clés dans les structures cellulaires.

Dans cette étude, les résultats de l'interaction entre PDZ1 et de petits peptides qui imitent la protéine virale suggéré, que les différences d'affinités sont directement corrélées aux liaisons hydrogène, ce qui mène à conclure que la pathogénicité et la prévalence d'un virus particulier comme le HPV16 sont liées à son habilitée à former un réseau de liaison hydrogène très solide comparé au substrat naturel. Le model allostérique et que le de "shift population" sont en accord que, lors de la coordination du substrat, des changements conformationnels loin d'un carboxylate, sont la clé pour la compréhension de la dynamique de liaison entre la PDZ et la protéine virale.

En particulier, cette étude de thèse de l'interaction de PDZ1 domaine de MAGI-1 et la protéine E6 du virus du papillome humain 16. Les PDZ motifs de reconnaissance de domaine encodés en haute risque papillome humain Virus (HPV) sont la cible de diverses protéines cellulaires via la protéine -les interactions protéiques. Il est important de noter que le «risque élevé» reste virus HPV qui agissent comme l'agent étiologique des cancers du col, il s'agit notamment de HPV16, HPV18, HPV31 et HPV45. Leur potentiel oncogène repose sur l'action coopérative de deux produits de gènes viraux précoces, les protéines E6 et E7; Ces

protéines sont connues pour se lier à de nombreuses protéines et de modifier l'activité du cycle cellulaire, ayant un rôle direct dans le développement et le maintien de l'état malin

Comme résultats, il a été démontré que les différents états conformationnels et leurs affinités vis-à-vis le C-terminal de la protéine virale sont régulées par la dynamique des liaisons hydrogène formées par un réseau qui connecte des acides aminés localisés dans les trois domaines de la protéine. L'étude de mutations aux alentours du C-terminal de la protéine et de la chaine βC était réalisée et elle a démontré que les deux domaines sont critiques pour l'assemblage du réseau des liaisons hydrogène afin de stabiliser la coordination du substrat.

En outre, le dernier modèle allostérique, le modèle de la «shift population», a proposé que lors de la liaison, des changements conformationnels distales au groupe carboxylate peut-être la clé pour comprendre la dynamique de liaison entre les domaines PDZ et les protéines virales. La dynamique du ligand-dépendante de ce comportement allostérique et la signalisation inter-moléculaire peuvent être directement liés à des chaînes latérales méthyle. La β-augmentation lors de la liaison déclenche les groupes d'acides aminés spécifiques CH rend le réseau d'hydrogène forte, comme cela a été observé dans nos résultats. Cependant, les détails moléculaires de cette allostery interdomain ne sont encore pas connus.

La deuxième protéine d'intérêt est une protéine modèle qui représente un petit prototype du changement conformationnel observé dans des protéines plus complexes. Il s'agit d'un peptide court capable de coordinner le cuivre. Ce n'est autre que le peptide β-amyloïde, connu d'être impliqué dans la maladie d'Alzheimer. Les ions métalliques jouent un rôle crucial dans les systèmes vivants. Environ un tiers des protéines besoin de lier les métaux pour leur stabilité et / ou de la fonction. Ils peuvent servir d'agents de reticulation, étant donné que les ions métalliques se lient généralement à travers plusieurs interactions avec des chaînes latérales d'acides aminés; ils peuvent également servir de centres redox pour la catalyse ou réactifs comme électrophiles en catalyse et ils peuvent jouer un rôle de régulation dans les protéines conformation. L'objectif ici est de décrire l'effet des ligands histidine lors de la réduction du cuivre, qui est une réaction électrochimique critique pour le développement d'Alzheimer.

Pour cette étude, nous avons utilisé le peptide tronqué Aβ16 contient les 16 premiers acides aminés (aa) de la partie hydrophile qui contient le site de liaison de haute affinité, a été

étudiée comme un modèle pour la coordination des métaux de transition, EPR, Raman et IR les études de la coordination de Cu (II) avec la courte (16 acides aminés) et le natif (39-42 acides aminés) peptide ont montré que la différence de monomère aussi bien que dans la forme agrégée, entre le peptide court et long, ce qui rend Aβ16 modéliser un très bon candidat pour des études spectroscopiques..

La spectroscopie FT-IR différentielle a montré deux sphères de coordination pour le Cu(I) et le Cu(II). Les majeurs changements spectraux sont dominés par les vibrations de l'imidazole des différentes histidines (His6, His13 et His14) ainsi que la contribution des résidus Asp1 et Tyr10. Les modifications de la géométrie de coordination peuvent être la cause de la dépendance-pH de l'agrégation du peptide observée en présence du Cu(I). Pour cela, il est possible de suggérer que la formation des fibrilles observées chez les patients d'Alzheimer n'est pas seulement stimulée par la présence du cuivre même mais elle est fortement affectée par ses réactions rédox.

Changements dans la structure ont été observés, où les groupes C = O, NH et CN du squelette sont perturbées en raison de la liaison Cu. Dans le réduit aussi bien que dans le complexe oxydé CuAβ la structure semble être formée principalement par β-feuille. Bien que la réduction en cuivre ne induire un réarrangement de la chaîne principale, telle que le réarrangement de la structure lors de la réduction se traduit par des déplacements des bandes d'amide pour réduire le nombre d'onde, en comparant les spectres de différence avec les spectres des complexes CuIIAβ16 de études[3] précédente. Ceci indique que la formation de fibrilles observées chez les patients AD n'est pas déclenché uniquement par la présence de Cu et de son processus d'oxydo-réduction. Il peut être proposé que l'effet des ions métalliques dans la maladie d'Alzheimer est un processus en deux étapes comme il a été décrit par Faller[145, 350] et par Hardy et Selkoe[351]. En premier lieu, la mise au point des fibrilles est dépendante du pH et de la contribution de la protonation des autres acides aminés est suggéré. La deuxième étape sera la production de ROS induite par Aß.

La dernière protéine d'intérêt est une métalloprotéine, la NADH:ubiquinone oxidoréductase (complexe I), La membrane lié NADH: ubiquinone oxydoréductase, le complexe respiratoire I, est le premier complexe d'enzyme dans les chaînes respiratoires des mitochondries et plusieurs bactéries. Il est le principal point d'entrée d'électrons de la chaîne respiratoire, cette protéine joue un rôle majeur dans la bioénergétique cellulaire. Cette

protéine contient plusieurs centres Fe-S et une flavine et son activité est régulée par l'énergie produite par la liaison avec un substrat ainsi que le transfert d'électrons de ces cofacteurs.

Il a été suggéré que les éléments centraux de la bioénergétique modernes, tels que le couplage de réactions d'oxydoréduction et la translocation des ions sont basés sur l'interaction des cofacteurs dans une variété de protéines. Comment transfert d'électrons est réversible converti en changements structurels ou vice versa est une question qui reste encore sans réponse. L'objectif de ce travail sera centres Fe-S, une classe importante de électrons cofacteurs de transfert.

Les vibrations métal-ligands de ces cofacteurs à l'état oxydé et à l'état réduit sont décrites ici. En utilisant l'électrochimie couplée aux spectroscopies FT-IR, Raman de résonance et de fluorescence, les investigations sur le complexe I ont conduit à conclure que les propriétés des centres métalliques sont largement influencées par l'environnement proche. De plus, les changements conformationnels de la protéine ont un effet considérable sur les propriétés rédox et par la même, sur le bon fonctionnement de la protéine. Par ailleurs, la mutagenèse dirigée était utilisée pour étudier les propriétés des centres N1a et N2.

A part des cofacteurs métalliques, cette étude a montré l'existence d'un nouveau cofacteur, une quinone localisée proche du domaine membranaire. Par les spectres d'émission de fluorescence obtenus avec une technique d'électrochimie couplé permis de suivre le titrage d'oxydoréduction d'un éventuel co-facteur de la quinone de complexe I qui n'est pas présente dans le fragment, en outre, le potentiel point milieu a été déterminée et les propriétés décrites.

Suite à ces études, il est évident que la régulation de la fonction de protéines à travers les changements conformationnels est imposée par leurs différents cofacteurs où les effecteurs ciblent en général des acides aminés spécifiques, qui déclenchent une cascade de réaction à travers d'autres domaines protéiques. Ce travail offre une nouvelle affirmation que les transitions conformationnels sont beaucoup plus répandues que l'on croyait. De même cette étude offre une évidence que la plasticité structurale est essentielle à l'activité des protéines.

I’m indebted to Prof. Petra Hellwig who gave me the opportunity to learn and gain experience and knowledge in the field of proteins spectroscopy. Her continuous supervision and helpful advices were a major push forward that brought me to this achievement. Furthermore I would like to thank the Centre International de Recherche aux Frontières de la Chimie (FRC) for their financial support and the University of Strasbourg.

I’m truly grateful for my colleagues and their support, especially in the hard times to adapt to a new environment and their help with all the administrative part. To Alicia, Batoul, Fred, Julien, Lea, Mireille, Sebastien, Thomas, Yashvin and specially to Maddy, who took the time to correct this thesis and teach me how to improve my English.

My greatest thanks to Prof. Thorsten Friedrich’s group, especially to Marius Schulte, Klaudia Morina and Martha Vranas for their collaboration and guidance in the preparation of several of the samples and furthermore for their time in teaching me. To the group of Dr. Gilles Travè, especially to Dr. Juan Ramirez, without our discussions about all the possibilities I think the PDZ project would not have taken the same right turn. Also, I’m grateful to Dr. Nominé for discussions and corrections, to bring me back to the good path when I was stuck with technical problems. For his recommendations and patience with all my questions and suggestions.

I’m grateful to all the friends that I have acquired along the way. For all those trips and new places that we visited together, for the good experiences that kept us together in times of adaptation and change and learning, with our clear hope that I will speak a better French one day. All of you had made this journey something special, where I have learned so much about so many cultures.

At last, to my pivots that have kept me in one piece no matter what happened in my surrounding. To Raquel, for believing in me and taking care of all that I did not want to deal in order to have the space and time to be someone better. To Youssef, without your effort and patience I would have been somewhere else, over the rainbow, you make my present and future, clear and happy. And for my sister and my mother, you are my strength to keep going no matter what, to be better every day and to smile even if the world will fall down.

ABREVIATIONS

Å	Angstrom
Aβ	Amyloid-β
AD	Alzheimer's disease
ATCUN	amino terminal Cu(II)- and Ni(II)-binding motif
ATR	Attenuated total reflection
ATS	antiporters
CCD	charge coupled device
CD	circular dichroism spectroscopy
Cu	Copper
Da	Dalton
dGTS	Deuterated triglycine sulfate
DTT	Dithiothreitol
Em	Midpoint potential
EPR	Electron Paramagnetic resonance
FADH2	Flavin adenine dinucleotide
Fe-S	Iron sulfur cluster
FMN	Flavin mononucleotide
FTIR	Fourier transform infrared
HPV	Human Papillomavirus
HSA	human serum albumin protein
IPTG	Isopropyl β-D-thiogalactopyranoside
IR	infrared
KNF	Koshland-Némethy-Filmer allostery model
LB	Luria-Bertani medium
MAGI-1	Membrane-Associated Guanylate kinase with an Inverted arrangement
MAGUK	Membrane-Associated Guanylate Kinases
MCT	Mercury Cadmium Telluride
MWC	Monod-Wyman-Changeux allostery model
mV	mili-Volts
NAD^+	Nicotinamide adenine dinucleotide (oxidized form)
NADH	Nicotinamide adenine dinucleotide (reduced form)
NADPH	Nicotinamide adenine dinucleotide phosphate (reduced form)
NMR	Nuclear magnetic resonance
NOEs	intermolecular nuclear Overhauser enhancements
Nuo	NADH:ubiquinone oxidoreductase subunit
PDB	Protein Data Bank
PMB	Protein Binding Motifs
Q	Quinone (oxidized)
RE	Reference electrode
ROS	Reactive Oxygen Species
RR	Resonance Raman
SHE	Standard hydrogen electrode
SHE'	Standard hydrogen electrode pH 7
UV	Ultraviolet
TDC	Transition dipole coupling
TM	transmemebrane
v/v	Volume to volume parentage
VDOS	vibrational density of states
vis	Visible
w/v	Weight to volume parentage
YPG	yeast extract, peptone and glycerol
YP	yeast extract, peptone

Vibrations

ν	stretching vibrations
δ	bending vibrations

LIST OF FIGURES

LIST OF TABLES

1 INTRODUCTION. Protein mechanics: conformation vs. function

All organisms require a tight regulation of their molecular machinery to be able to react dynamically and adapt to their environment. The first and primary units of this molecular machinery are proteins, the major working horses of the cell. One of the most basic, yet fascinating, biological processes is the folding of a linear sequence of amino acids into the three-dimensional structure of a functional protein[19, 20]. The ability of proteins to fold in unique structures and to generate a wide range of functions depends directly on the amino acid sequence and on the molecular interactions between each amino acid and their environment[21-23].

A functional protein needs to be folded in the right "active form". Nevertheless, it happens that, under certain condition, a misfolded protein becomes an "inactive form"[24, 25]. Very often, this misfolding leads to cell malfunction and undesired biological reaction can happen. In extreme cases, the misfolding of proteins can lead to cellular patterns that are translated into diseases[26-28].

As the conformation of the protein is important for its function, studying the causes that can change or perturb its conformation had been the objective of thousands of studies[29-32]. The mechanism of enzyme regulation through the changes of its conformation is a key pattern in governing cell behavior. Virtually all proteins known today have been suggested to be regulated in one way or another; as a consequence, the intriguing question of protein regulation has been studied intensively over the last decades. The need for a better understanding of how proteins are regulated is still a major field of endeavor in biology, chemistry and physics; even new multidisciplinary areas have emerged in the search for better and more precise answers.

There are many mechanisms by which the activities of proteins are controlled. The most commonly described one is by the binding of effector molecules, which often work by inducing conformational changes that produce inactive or active forms of the protein[25, 33-35]. Effectors may be as small as protons or metal ions, or as large as another macromolecule, or a protein. These effectors may bind non-covalently or may modify the covalent structure of the protein, reversibly or irreversibly[19, 21].

When the effector is a metal ion, the protein is denominated as metal binding protein. In these proteins their activity is regulated by the presence or absence of one or several metal ions, which compete for binding in a specific arrangement forming a sphere of metal coordination with specific amino acids that can act as donor or acceptor according to the metal ion valence[36]. In other cases, when the effector is added to the protein as part of the post-transductional process, the effector becomes a cofactor. Some cofactors are Iron-Sulfur (Fe-S) clusters and flavins[37-40]. When the protein bears this type of cofactor, they are called metalloproteins and flavoproteins, respectively. When an enzyme's catalytic activity is initiated by a covalent modification, such as the presence of a cofactor, it can process thousands of substrate molecules per second and if that substrate is another enzyme, the amplification is further magnified[33, 41, 42].

When the effector is another protein it is usually called a ligand. Ligands, including reaction products, may also bind to sites remote from the active site and in doing so either activate or inhibit the protein[19, 21]. Proteins regulated in this way tend to be oligomerically and allosterically regulated[43]. Although, non-covalent modification of a protein provides a simple mechanism, it can be a regulatory signal than can produce a very large output[25, 33]. Many proteins that regulate cell behavior are constructed in a modular pattern from a number of different small domains with distinct binding specificities and functions. Interaction domains can be divided into distinct families whose members are related by sequence, structure, and ligand-binding properties[33, 44, 45]. Different members of a family recognize somewhat different sequences or structures, providing specificity for the proteins into which they are inserted[43, 45].

The focus of this work is to study three systems that reflect how protein activity can be regulated by these effectors. The first protein of interest is involved in cellular signaling, PDZ1 from MAGI-1. It is a scaffold domain that is known to interact with viral proteins. Their different conformational states and their affinity to several ligands had been proposed to be regulated by the dynamics of the hydrogen bonding network. The second molecule of interest is the amyloid-beta 16 peptide (Aβ16) that is a model compound for the naturally occurring Aβ39-42. The latter peptide forms β-sheets rich fibrils in the brain which leads to Alzheimer's disease. The exact mechanism of action of Aβ39-42 is not clearly known. But nevertheless, it is strongly believed that the binding of transition metals, such as copper, to its hydrophilic part formed by the first 16 amino acids, leads to the production of Reactive

Oxygen Species (ROS). The objective of studying Aβ16 is to better understand the binding of Cu ions and how the redox reaction induces significant changes in the conformation of the peptide. More precisely, particular attention is given to the role of the histidine residues in the coordination, and by the same token, in the conformational changes.

The last system of interest is a metalloprotein, NADH: ubiquinone oxidoreductase (complex I), which plays a key role in the cell's bioenergetics. This protein bears several Fe-S clusters and one flavin and its activity is regulated by the energy produced by a bound substrate and the electron transfer between the cofactors. The aim is to describe the metal ligand vibration arising from the Fe-S cluster and how their changes between the reduced and oxidized state may control del conformational changes of the protein.

1.1 MAGI-1

Membrane-**A**ssociated **GU**anylate **K**inases (MAGUK) are a widely expressed and well-conserved group of proteins that play an essential role in the formation and regulation of scaffolding processes[46]. MAGUK consist of three modules: multiple N-termini PDZ domains, the Scr homology (SH3) domain and the guanylate kinase (GuK) domain[47].

All the MAGUKs studied to date are localized in cell-cell contact regions, such as tight epithelial junctions or synaptic junctions found in neurons[46]. Their main function is primarily based on their ability to form protein-protein interactions with cytoskeleton proteins microtubule/actin based machinery and molecules involved in signal transduction[48-51].

Recent studies have found a new kind of MAGUK proteins that have been designated as MAGI-1 for **M**embrane-**A**ssociated **G**uanylate kinase with an **I**nverted arrangement of protein-protein interaction domains. There are three main features that characterize this protein; the first, the GuK terminus is in the N-terminus instead of the C-terminus. This is where the category of "inverted" comes from; the second is the replacement of the **S**RC **H**omology **3** Domain (SH3) domains with two WW domains. They are so called due to two conserved tryptophan residues that bind to proline-rich peptide motifs. Finally, it contains five PDZ domains rather than the usual two or three[52]. Several *in vivo* and *in vitro* studies of this protein have shown the importance of the interactions between different ligands and their PDZ domains[53-55].

1.1.1 PDZ domains-Background

The PDZ domains were originally characterized as a repeated ~90 amino acid sequence from three different proteins belonging to the MAGUK family: a human **P**SD-95 located in neural postsynaptic densities, a *Drosophila* septate junction protein: discs large **D**LG and **Z**O-1 and a tight junction protein present on the surface of the cytoplasmic membrane[56-59].

Although all proteins from the MAGUK family contain PDZ domains as part of their structure, a variety of other proteins also have this scaffold domain as part of their structure[60-62]. These domains show considerable variation in their sequences, which is reflected in their functional roles and the diversity of binding specificities, that go from signaling in assembly pathways to ion channel signaling, cellular organization as well as protein trafficking and transport[63].

PDZ domains can be engaged in homotypical interactions (PDZ-PDZ dimers) or, more commonly, in heterotypic interactions in which the ligands are usually the C-terminus of a transmembrane or cytoplasmic protein[47]. These differences in interaction suggest that multiprotein complexes formed by different PDZ domains are able to perform different functions according to their target. The functionality is directly correlated to the specificity of the ligand[63, 64].

PDZ domains are predominantly found in multi-cellular organisms, more than 250 human PDZ domains are found in over 150 different proteins. The low abundance of PDZ domains in unicellular organisms could imply that PDZ domains may have co-evolved with multi-cellularity[60]. The functionality of PDZ domains can be modified by various means such as changes in physiological buffer conditions[65], electrostatic interactions[66], allosteric changes[67], auto-inhibition[15] and phosphorylation[68] which makes them a dynamic reference in the mechanism of regulation in cellular signaling.

1.1.2 Canonical structure of PDZ domains

Several crystal structures of PDZ domains have been solved by X-ray crystallography[69, 70], X-ray scattering or NMR[71-73]. The comparison of these studies has provided detailed information on the conserved architectures among PDZ domains. Their

structure (Figure 1.2-1) consists of six antiparallel β-sheets (βA ~ βF) and two α-helices, one short (αA) and one long (αB)[74]. The canonical PDZ family has a highly conserved fold, but secondary structures vary in length.

The N-terminal and the C-terminal domains are usually in close proximity to each other, on the opposite side from the peptide-binding site in a groove between the αB-helix and βB-strand structures, facilitating their integration into pre-existing protein scaffolds. The binding loop is located in a groove on the surface between the αB helix and the βB strand. The ligand peptide (colored yellow in Figure 1.1-1) is usually oriented antiparallel to the βB strand [63]. The C-terminal and the N-terminal do not have any specific secondary structure; in many PDZ domains these regions remains non-organized until the ligand binds[15].

The sequence identity between the PDZ domains is approximately 30% and even if they share the same core structure, PDZ domains often have variable loop regions and may contain additional secondary structural elements that affect the structure and function[75].

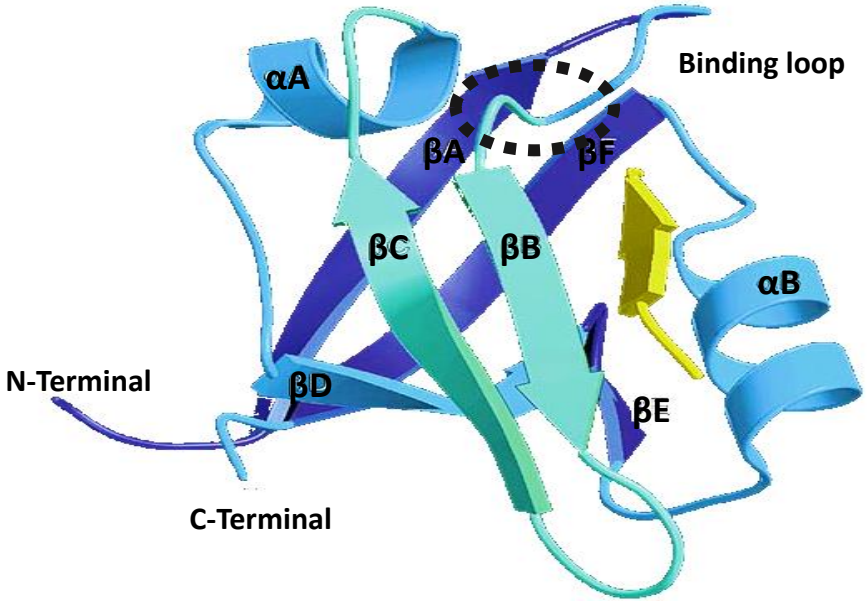

Figure 1.1-1. PDZ domain canonical structure. Ribbon diagram of PTP-BL PDZ2 (PDB: 1GM1) [15]

1.1.3 The carboxylate binding site

Ligand binding occurs via a β-strand addition mechanism[76] so-called since the ligand binds as an anti-parallel extension of the βB-strand. The PDZ domains recognize specific C-

terminal sequence motifs that are usually four residues in length, although in some special cases the specificity in the recognition can be extended to 8-10 residues[77].

The main chain of the βB strand interacts with the peptide ligand via the carboxylate binding loop, this single binding site is positioned in a groove between the αB and βB strand, is a highly conserved sequence, R/K-XXX-G-Φ-G-Φ, where X is any amino acid and Φ is a hydrophobic residue, such as Val, Ile, Leu, or Phe (Figure 1.1-2)[78]. The first Gly residue can vary among the canonical core and be replace by Ser, Thr or Phe[15]. The side chains of these residues forms a hydrophobic binding pocket that is part of the main properties of PDZ domains and is usually named as the GLGF motif. This carboxylate binding loop is critical for binding the free carboxylate of the C-terminal residue, also hydrophobic, of the peptide ligand.

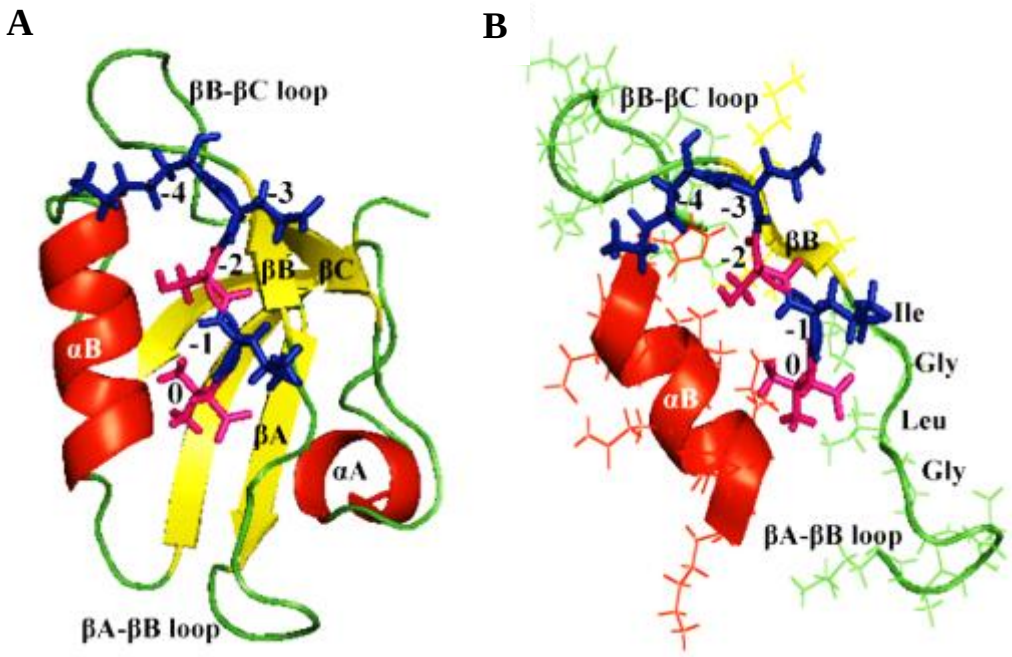

Figure 1.1-2. Representative structure of a PDZ domain with its ligand. A. PDZ domain (α-1 syntropin with a peptide (sticks form). B. The interaction of the peptide with the αB helix and the conserved ILGF segment. (PDB: 2PDZ)

It is important to note that is the second residue in the motif loop region adopts an α-helical conformation, while the third Gly residue in the loop region is fully conserved and adopts a left-handed α-helical conformation in structures available to date. The fourth residue adopts a β-sheet conformation. These specific conformations for each residue in the carboxylate-binding loop region allow amide groups to serve as the H-bonding donors with the terminal carboxylate of the ligand peptide. In addition to this motif, a guanidium group

from Arg in the βB strand interacts with the carboxylate of the first peptide residue via a water molecule [76].

For the peptide the first residue is named P_0, as the C-terminal is the ligand binding region the subsequent residues towards the N-terminus are named P_{-1}, P_{-2}, etc; usually the last four amino acids in the PDZ-binding motif are the most important for recognition.

When the ligand binds, the positions P_{-1} and P_{-3} (Figure 1.1-2.A blue sticks) point towards the solvent, whereas the P_0 and P_{-2} side chains (Figure 1.1-2.A pink sticks) point towards the binding pocket. This adjustment between the two proteins suggests that the ligand positions P_0 and P_{-2} are very important for the PDZ domain to recognize its ligand[75, 79]. The amino acids of PDZ lining in the binding pocket will therefore determine the nature of the selected C-terminal residue.

Even if each PDZ domain is only able to bind to one single peptide at a time, the interactions tend to be promiscuous; one PDZ domain can recognize various peptide ligands and the same ligand can be recognized by different PDZ domains[60].

1.1.4 Conformational properties – Specificity of the C-terminal binding site

In general, residues lining the binding pocket of the PDZ domains are hydrophobic; this property might account for the generalization that almost all PDZ domains select peptides with hydrophobic residues in the C-terminal. However, this selectivity is not highly restrictive, and can account for the variations in the C-terminal residues specified by each PDZ domain. Then it can be considered that the hydrophobicity is actually related to affinity more than being a pattern for selectivity.

As explained above, the P_0 and the P_{-2} position are the main pivots for peptide binding. Generally PDZ domains show greater specificity with amino acids upstream of the "0" position in peptide ligands. Extensive peptide library screens[80] revealed that the specificity of PDZ domain recognition can be divided into three classes according to the nature of the residues in the P_0 and the P_{-2} positions, Table 1.1-1 shows a summary of the specifications of each class. There are a few other PDZ domains that do not fall into any of categories, of which most of them are related to bacterial strains[60].

Table 1.1-1. Classification of PDZ according to specificity of the C-terminal peptides [81]

Class	C-terminal Peptide (sequence)	Interacting protein	PDZ domain
Class I X-S/T-X-V	E-S-D-V E-T-D-V	NMDAR2A[82] Shaker channel[83]	PSD-95 (PDZ2) MAGI-1(PDZ1)
X-S/T-X-L	Q-T-R-L D-S-T-L	GKAP[84] Voltage-gated Na Channel	Syntropin (PDZ1/2/3)
Class II X- Φ-X- Φ	E-Y-Y-V E-F-Y-A	Neurexin[29] Syndecan	CASK Synthenin
Class III X-D-X-V	V-S-D-V G-D-H-V	Melatonin receptors[85]	nNOs (PDZ1/2)
Others	G-D-X-V S-T-W-V	MeIR[46, 64]	MAGI-1 (PDZ2)

Despite this classification, a more recent comprehensive study that scanned a very large random peptide library showed that PDZ proteins can recognize up to the last seven residues at the carboxyl termini of proteins and that 16 distinct specificity classes can be identified[86, 87], although this classification has not been accepted by the scientific community because it has more exceptions than generalizations.

1.1.5 PDZ domains and the interaction with viral proteins

The initial discoveries of Protein Binding Motifs (PMB) in viral proteins emerged a decade ago from studies of three important viral oncoproteins, human adenovirus (Ad) E4-ORF1[88], human T-lymphotropic virus type-1 (HTLV-1) Tax[89], and **H**uman **P**apilloma**v**irus (HPV) E6 and E7[90]. In recent studies, however, many non-transforming viruses, such as influenza A virus and tick-borne encephalitis virus (TBEV), have been found to have proteins with PBMs that target many of the same PDZ proteins as do the PBMs from viral oncoproteins.

All this has led to the realization that a selected set of PDZ proteins are commonly targeted during infection by different viruses with quite distinct replication cycles. The association of some viral PBMs with PDZ proteins results in loss of PDZ function, either through proteasome-mediated degradation or changes in the conformational control of key proteins in cellular structures[91]. In other cases, however, the association of viral PBMs with their PDZ protein targets results in an apparent gain of function of the cellular protein. In both cases, the targeting of PDZ proteins and hence the modulation of cellular processes, are likely

to enhance viral replication, dissemination in the host, or transmission of the virus to new hosts[92].

1.1.5.1 PDZ domains and HPV

PDZ domain recognition motifs encoded in high-risk **H**uman **P**apilloma **V**iruses (HPVs) are the target of various cellular proteins via protein-protein interactions[93]. It is important to note that "high risk" remains for HPV viruses that act as the etiological agent of cervical cancers, these include HPV16, HPV18, HPV31 and HPV45[94]. Their oncogenic potential relies on the cooperative action of two early viral gene products, the proteins E6 and E7; these proteins are known to bind to many proteins and alter the activity of the cell cycle, having a direct role in the development and maintenance of the malignant state[95].

The HPV-PDZ interactions are in part associated with virally-induced cancer progression. The ligand induced conformational changes appear to be an important feature of some receptors that have regulatory functions [96].

Discs **l**arge protein (Dlg), **Mu**lti-domain **P**DZ **p**rotein 1 (MUPP-1), **H**uman **Scrib**ble protein (hScrib) and MAGI-1 are targets of HPV to induce proteasome-mediated degradation[97-99]. The E6 and E7 proteins are known to target PDZ domains[93], they have been the best characterized oncoproteins by many *in vivo* and *in vitro* studies[95]. Their function, at least in part, is the inactivation of the p53 tumor suppressor protein, through ubiquitin-mediated degradation[100, 101]. However little is known about the role of these interactions for the E6 and E7 function on viral life cycle of HPV.

Studies have shown those HPV viruses that are able to induce malignancy (high risk HPV) present a high level of E6 and E7 expression. An example of these viruses is HPV-16 and HPV-18. These proteins are known to be encoded by early genes of HPVs.

At the molecular level, few studies have explained the relevance of how the protein-protein interaction mediates different responses through the same binding process with the PDZ domains. Structural studies have indicated that the key remains in the conformational changes in the secondary and tertiary structure upon binding of the HPV proteins[47, 102, 103].

Each PDZ containing protein has a similar interaction with HPVs, regardless of the location in the cellular process or their structure[93]. For example, hDlg1 and hScrib are found

in the core components of polarity control at adherent junctions, and MAGI-1 is an essential scaffold protein for tight junction integrity. Not all the high-risk HPV E6 proteins recognize their different PDZ domain containing substrates with equal affinity, for example, hScrib and MAGI-1 are preferentially targeted by HPV-16 E6, while hDlg is targeted by HPV-18 E6 [104].

In parallel, comparison of different but very closely related PDZ domains in multiprotein complexes (the Dlg PDZ2 and PDZ3 and the PDZ1 domain of MAGI-1 and MAGI-3) has shown that the ligand selection is also determined and modulated by the sequences of the PDZ domains themselves[71, 104, 105]. It is important to note that, although many of the PDZ-containing targets of HPV E6 proteins contain multiple PDZ domains, so far only one PDZ domain per protein has been identified as the E6 target [96].

1.1.6 PDZ domains and their allosteric process

Allosteric regulation coordinates functional behaviors in biological networks through appropriate switches. From a biochemical perspective, allostery can be described as a perturbation at one place in a protein structure, such as the binding of a ligand that alters the binding affinity of a distant site or enzymatic activity[106].

Several models have been proposed to explain the allosteric mechanism. The Monod-Wyman-Changeux (MWC) model explains the conformational transition between two different co-existing states as a form of cooperativity[107]. The 'induced fit' Koshland-Némethy-Filmer (KNF) model described allostery as a binding event that causes conformational changes via a single propagation pathway[108]. Recently a new view of allosteric transitions supported by NMR studies and referred to as "the population shift model", has replaced the MWC and KNF models[44, 45, 109]. This model is based on PDZ domain binding mechanism[67, 110].

The model proposes that a protein in free form exhibits an ensemble of conformational states and ligand binding leads to a redistribution of the population of these states. From this point of view it becomes important to explore how protein dynamics may contribute to allostery and make communication possible within a protein. Contrasting with the classical allostery models, the population shift models also propose that allostery can be mediated without any significant conformational change and instead changes in dynamics may induce allostery[44, 111].

Recent experimental and theoretical evidence shows that allostery is not limited to multi-domain proteins or complexes but it may be even a fundamental property of all proteins and even of single domain proteins. In single domain proteins, residues that are energetically connected through structural rearrangements, can lead to different dynamics and can be defined by allosteric regulation[45, 112].

The selectivity of conformational changes in the PDZ domains upon binding may be modulated by an intradomain allosteric processes and a remote residue that is energetically connected to the functional binding site via an amino acid side chain, backbone interactions or a different arrangement of the intramolecular hydrogen bonding[110, 111].

Several energetic pathways could mediate this intradomain allostery. In the case of the PDZ domains and their interaction with HPV proteins, it has been predicted by computational studies in different modular PDZ multidomain proteins[66, 113, 114], but so far there are not many experimental studies that support the prediction data.

PDZ1 MAGI-1 is known to interact with HPV16 E6 protein. The NMR structure of the free and the bound forms are already available[71], making them good candidates for spectroscopic studies. This will allow conformational changes in the secondary structure and the possible changes to be followed by vibrational spectroscopy in modes related to the allosteric process, for example alterations in the hydrogen bonding network upon binding.

The association between the alterations in the electrostatic interactions as well as the conformational changes as part of the binding process can be described as allosterically regulated. The degree of perturbation by the effector can provide a parameter to determine how small motions give rise to a ligand-induced cooperativity. This mechanism might involve changes in the relative stability of the protein conformation, where the open (free protein) and closed states (bound) are driven by a shift of the population triggered by effector binding.

Through the description of the changes upon HPV16 E6 binding in PDZ1 MAGI-1, the aim of this study is to show if the viral binding can be described as this kind of allosteric process.

1.2 The binding of metal ions

Metal ions play a critical role in living systems. About one third of proteins need to bind metals for their stability and/or function. They can serve as cross-linking agents, since metal ions usually binds through several interactions with amino acid side chains; they also can serve as redox centers for catalysis or as electrophilic reactants in catalysis and they can play a regulatory role in proteins conformation[36, 115-117].

Metal binding sites in proteins are versatile due to their various coordination sites, their geometries and their ligating partners preferences which include backbone carbonyl oxygen; side-chain groups of Asp, Asn, Cys, Glu, Gln, His, Met, Ser, Thr, Tyr residues; and water molecules[36, 115, 118, 119]. Despite this variety, it has been proposed that many metal sites in proteins share a common feature: they are centered in a shell of hydrophilic ligands, surrounded by a shell of carbon-containing groups[118, 119]. The electron distributions in metal ions are highly symmetric, attracting electron-pair donors (Lewis bases) around the ion in a shell. In proteins, these electron pair donors are oxygen, nitrogen, and sulfur atoms[36].

1.2.1 Amyloid beta peptide

Aβ is produced from a precursor membrane protein by proteolytic processing and it is released into extracellular fluids as a soluble peptide[120-122]. This naturally occurring Aβ is a 39 to 42 amino acids length peptide. It has a hydrophilic N-terminus and a hydrophobic C-terminus (Figure 1.2-1)[123].

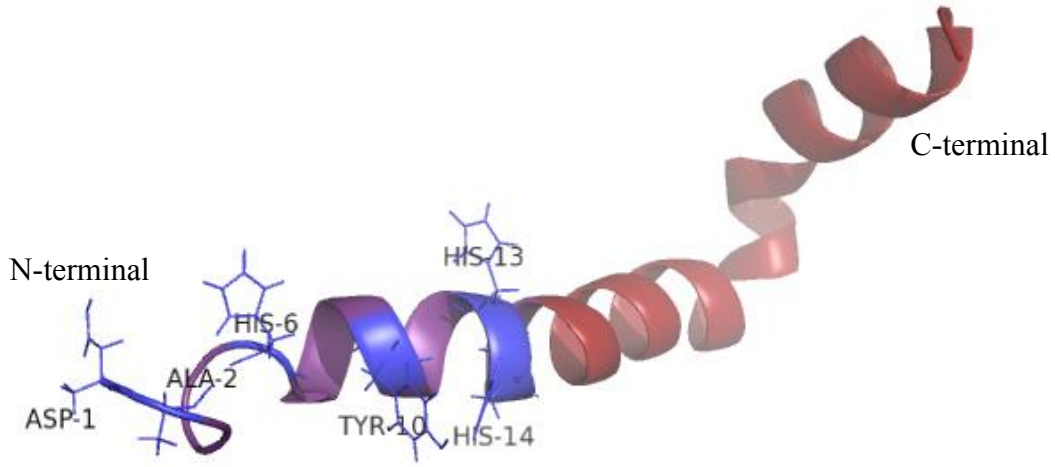

Figure 1.2-1. Schematic representation of the full length Aβ42 peptide. Highlighted in purple the 16 amino acid of the short peptide model A*β16* and in blue the amino acids that may coordinate the Cu ions. (PDB: 1IYT)

Under certain conditions, not clear though, Aβ aggregates and accumulates to form amyloid fibrils, which are insoluble and structurally dominated by β-sheet structures. The extensive deposition of these fibrils forms plaques resistant to degradation. These plaques are one of the main causes associated with neurodegenerative diseases as the Alzheimer's disease (AD)[122, 124, 125].

According to the latest studies, an emerging picture is that the Aβ peptides in aqueous solution undergo a hydrophobic collapse together with identical partners followed by a relatively slow process leading to more ordered secondary and tertiary (quaternary) structures in the growing aggregates (Figure 1.2-2)[124, 126, 127].

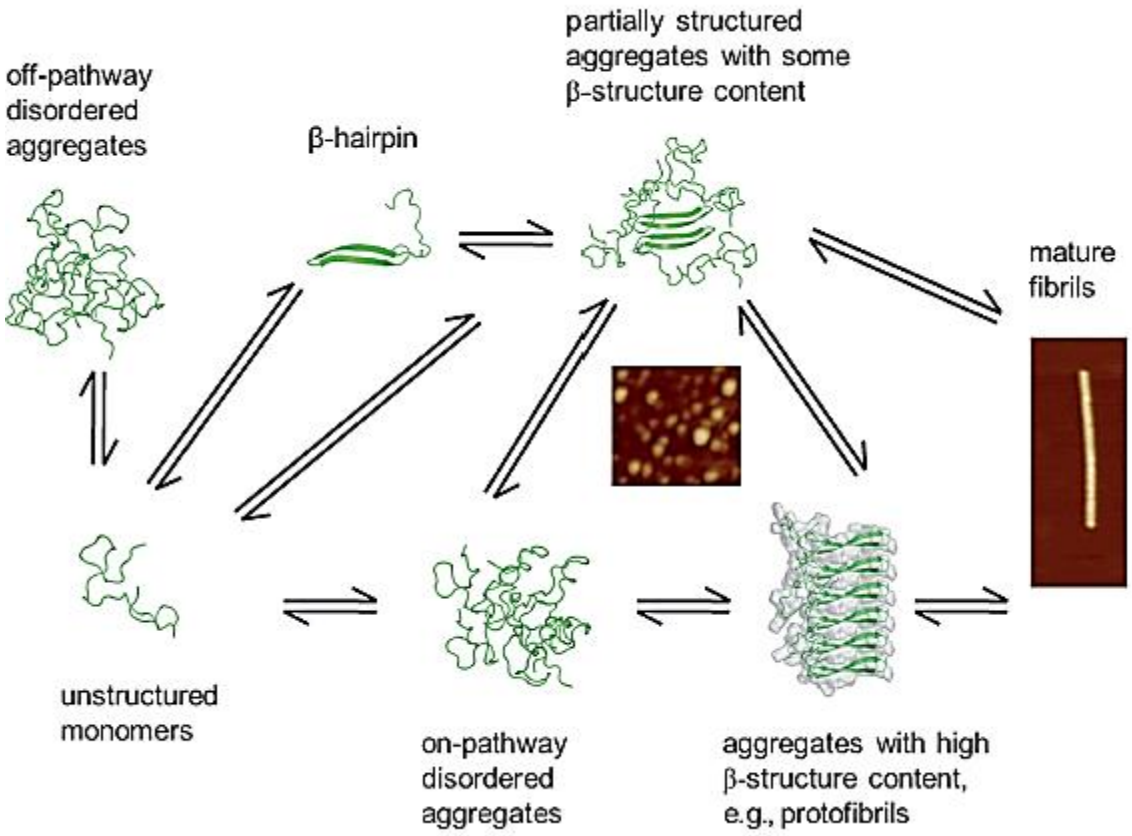

Figure 1.2-2. Schematic model for possible Aβ aggregation pathways—the mature fibrils can be formed from aggregated states of Aβ and monomers in combination. Adapted from Wärmländer *et al*[122]

High concentrations (in the millimolar range) of several transition-metal ions, mainly Cu(II), Zn(II), and Fe(III), had been found in these plaques[128], with Cu(II) and Zn(II) being bound to the Aβ peptide[129, 130]. On this basis, it has been suggested that the Aβ peptide is

involved in the development of Alzheimer's disease via the coordination of transition metals (i.e. Cu, Fe, Al) causing the production of ROS which leads to the formation of A*β* plaques[131, 132].

The binding site for Cu(II) to the human Aβ was extensively studied with several techniques, including EPR[133, 134], NMR[123], CD[124], Raman[135] and cyclic voltammetry[136, 137]; yet the precise coordination remains under debate. According to the structural studies, this peptide has one high affinity binding site for Cu located in the N-terminus and lower affinity binding sites located in the C-terminus[123].

The truncated peptide A*β*16 contains the first 16 amino acids (a.a.) from the hydrophilic part which contains the high affinity binding site, had been extensively studied as a model for the coordination of transition metals[133, 138]EPR[134], Raman[135] and IR[3] studies of the Cu(II) coordination with the short (16 amino acids) and the native (39-42 amino acids) peptide showed that difference in the monomeric as well as in the aggregated form, between the short and long peptide, making A*β*16 model a very good candidate for further spectroscopic studies.

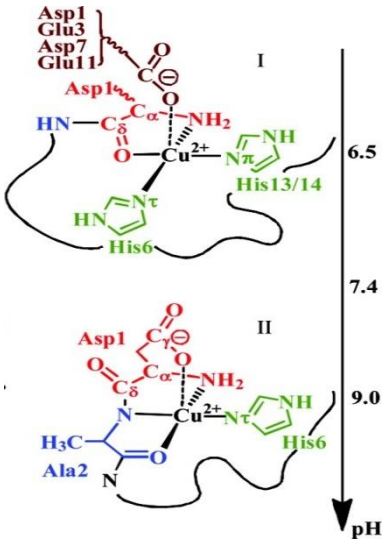

Figure 1.2-3. Schematic representation of the Cu(II) Aβ16 coordination at pH 6.5 and pH 8.9. Adapted from El Khoury *et al*[2-4]

Recent reviews agrees that at physiological pH (~7.4) the binding of the Cu(II) is pH dependent and two A*β* complexes are known to coexist; the predominant form at pH 6.5 and a minor form at pH 8.9, often denominated as component I and II respectively[133, 139, 140]. Furthermore, it was described that the peptide is coordinated by four ligands, 3N and 1O[121,

[141]. His6, His13 and His14 are involved, along with a possible contribution from Tyr10, the carboxylate group of Asp1, the amide C=O of Ala2 and the N-amine terminus[142-144].

The copper coordination at the different pH values had reflected the Cu(II) sphere of coordination have particular specifications. At pH 6.5 Cu(II) is coordinated by the Nτ of His6, the Nπ of His13 and His14, by the carboxylate group of Asp1 and the amide bond between several amino acids (Figure 1.2-3). On the other hand at pH 8.9 the coordination of Nτ of His6 remains as well as the carboxylate of Asp1, but know Ala2 and other amide bonds replace the previously described geometry[3, 145].

The next step in the study of the Cu coordination with the A*β* peptide is the describing of the Cu(I) coordination sphere, as the generation of harmful ROS occurs due to reduction of Cu(II) to Cu (I) by biological reducing agents like ascorbate, which is follow up by O_2 or H_2O_2 activation[146, 147]. Therefore shedding a light on the coordination of Cu(I) by A*β* peptides in order to better understand the redox transition and to elucidate the naturally occurring process that trigger the fibrils formation in the brain of Alzheimer's patients.

1.2.2 Model peptides

The Gly-His-Lys (GHK) and Asp-Ala-His-Lys (DAHK) peptides are naturally occurring high-affinity Cu(II) chelators found in blood plasma[148, 149]. The first is a Cu binding growth factor[150] and the second, is part of the N-terminal binding sequence of human serum albumin (HSA), which is the major protein involved in Cu transport[151, 152].

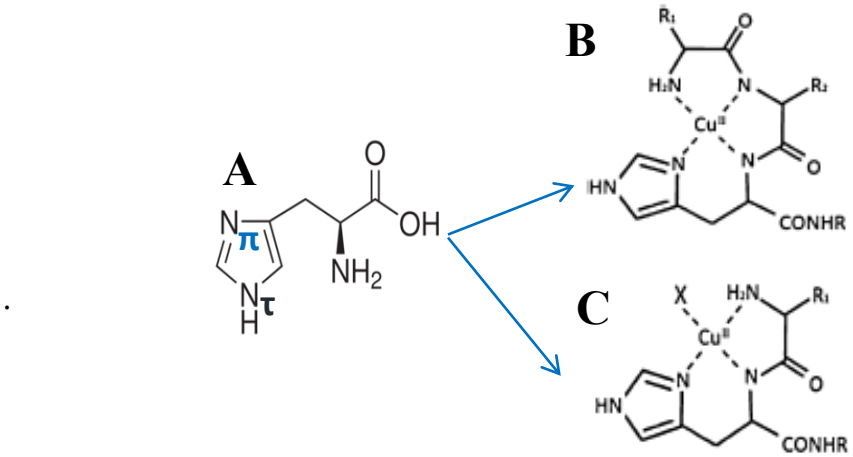

Figure 1.2-4. Scheme of A. His signaling Nπ and Nτ, B. Cu(II) coordination of an ATCUN motif like DAHK and C. Tripeptide like GHK Cu(II) complex with and equatorial labile coordination position (X). R denotes the side chains of the corresponding amino acids. Adapted from Trapaidze *et al*[5].

For DAHK, Cu(II) is bound via the amino terminal Cu(II)- and Ni(II)-binding (ATCUN) motif. The ATCUN motif is formed from a histidine in the third position, its preceding residue and the free N-terminus[152]. Four nitrogen atoms from these three residues act as metal ligands (Figure 1.2-4.B). The DAHK peptide as well as HSA was shown to be able to remove copper rapidly and stoichiometrically from Aβ[149]. In addition, *in vivo* studies demonstrated that DAHK is able to restrict Aβ aggregation, to suppress the catalytic ROS production, and to reduce neurotoxicity[153].

In comparison, GHK does not have an ATCUN motif. In solution it is known to coordinates Cu(II) acting as a tridentate chelator involving the N-terminal amino group of glycine, the amidyl nitrogen atom from the Gly-His peptide bond, and Nπ of the histidine imidazole ring (Figure 1.2-4.C)[154]. There is evidence that the fourth equatorial position is occupied preferably by an oxygen donor provided by an external ligand.

.

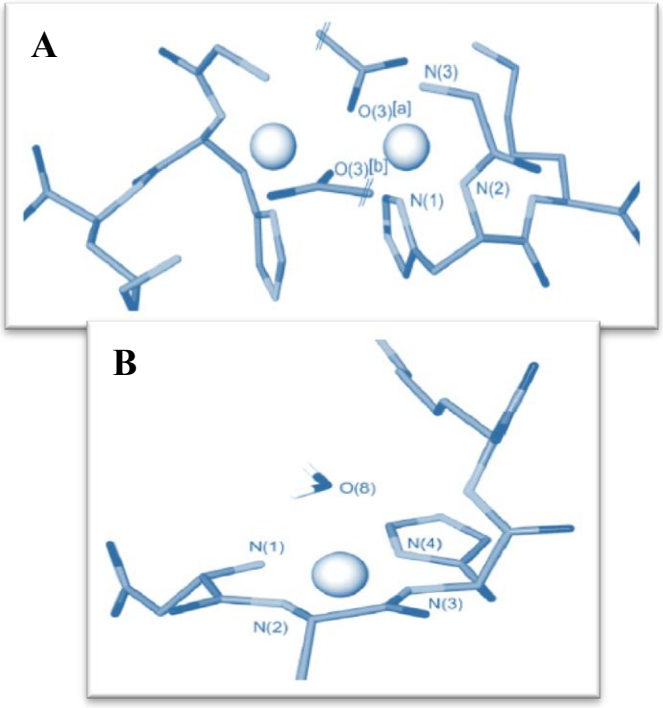

Figure 1.2-5. X-ray structure of the A. [Cu(II)(GHK)^2] complex and B. [Cu(II)DAHK] complex. Adapted from Hureau *et al*[4]

Recently studies with GHK demonstrated that its presence stimulates the growth and improve viability of several types of cultured cells and organisms, including neuronal cells. In addition, is also known to participate in the processes of wound healing and tissue repair[150].

Furthermore, it was also reported to compete successfully with Aβ for Cu(II) coordination, thus being able to act as a potential protector from Cu-Aβ toxicity[154, 155].

In the oxidized state, DAHK and GHK are known to bind Cu(II) by Nπ (Figure 1.2-4.A) of the His at physiological pH[4]. According to the X-ray structure[4] the principal Cu(II) anchor site is the His residue. In the case of GHK (Figure 1.2-5.A) the coordination sphere is formed by the glycine amino nitrogen (N(3)), deprotonated amide nitrogen of the Gly–His peptide bond (N(2)), the Nπ nitrogen of the imidazole of the histidine (N(1)) and the lysine carboxylate of a neighboring peptide (O(3)), leading to the formation of an equatorial binding plane around 3N and 1O residues.

For DAHK (Figure 1.2-5.B), Cu(II) is pentacoordinated with 4N ligands in equatorial positions: the Asp amino group (N(2)), two deprotonated amide functions from the first two peptide bonds (N(1)/N(2)) and the Nπ nitrogen of the imidazole side chain of the His residue (N(4)), as well as one water molecule from the environment[4, 156].

In general, both peptides structure, function and thermodynamics properties had been widely characterized alone and in presence of Cu(II); making them an excellent tool for the assignments of the bands obtained by FT-IR. Furthermore, their sphere of coordination can be a template in order to understand the behavior of the CuAβ complex.

1.3 The role of cofactors in protein function - Bioenergetics

All organisms rely on a chemiosmotic membrane system for energy transduction. It was suggested that the central features of modern bioenergetics, such as the coupling of redox reactions and ion translocation are based on the interaction of the cofactors in a variety of proteins. How electron transfer is reversibly converted into structural changes or vice versa is a question that still remains unanswered. The focus of this work will be Fe-S clusters, a major class of electron transfer cofactors.

Fe-S clusters. Fe-S cluster are cofactors that are linked by covalent bonds and hydrogen bonding interactions into protein scaffolds. They are redox-active centers in a variety of electron-transfer proteins and metalloenzymes[157, 158]. The catalytic activity of these metal centers may involve single or multiple electron transfers. Their functional range goes from simple electron transfer, redox sensing, regulation of gene expression to structure support[159-162].

There are different kinds of Fe-S cluster that are distinguished according to the number of Fe and S atoms that compose them. In this work the focus is on the binuclear and tetranuclear clusters (Figure 1.3-1). The name derives from the geometry of the Fe-S coordination. In these structures the metal ions are bound to the protein by amino acid side chains that have an additional coordination site, usually Cys or His residues[163, 164].

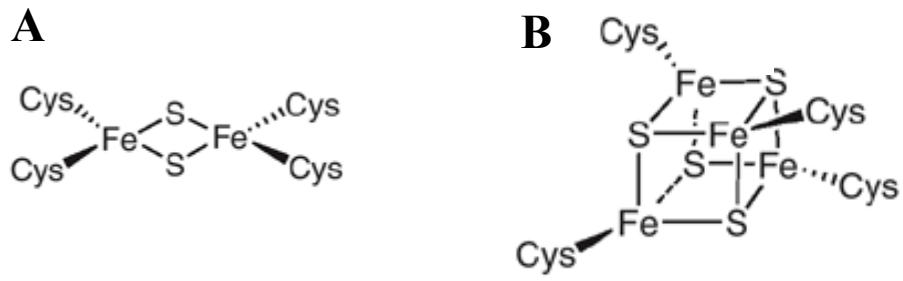

Figure 1.3-1. Iron sulfur cluster structure of A. Ferredoxin from spinach and B. Ferredoxin from *Clostridium pasteurianum*

It was suggested that proteins control their specific reactivity by the modification of the conformation in surrounding residues. Alternatively, the reactivity of the cluster itself triggers conformational changes that make protein function possible. In general, there is an agreement that the differences in midpoint potential (E_m) in the Fe-S cluster must be due to the nature of the interaction surrounding the cluster. But as many of these clusters have a regulatory function directly correlated to their redox properties, the correspondence between the conformational changes of the protein, their functionality and the geometry and the geometry of the cluster is not clear[159, 161, 164, 165].

Multiple Fe-S clusters are found in a variety of metalloproteins such as ferredoxins, hydrogenases and nitrogenases or complex I and complex II (succinate:ubiquinone oxidoreductase) of the mitochondrial electron transport chain.

Beratan *et al* [166], summarized that the main factors which have an influence in the reduction potential are the solvent exposure of the redox center, the hydrogen bonding network, the strength of the N-H…S bonds, the proximity and orientation of the backbone and side chains and also the electrostatic interactions of charged residues near the cluster motif.

1.4 Complex I and its cofactors

The membrane bound NADH:ubiquinone oxidoreductase, the respiratory complex I, is the first enzyme complex in the respiratory chains of mitochondria and several bacteria[167]. It is the main entrance point of electrons of the respiratory chain [168](Figure 1.4-1).

This enzyme is able to catalyze the transport of two electrons from NADH to quinone (Q) with the translocation of four protons from the negative inside to the positive outside of the cytoplasmic membrane in the case of bacterial systems and across the inner mitochondrial membrane in eukaryotes[18, 169, 170].

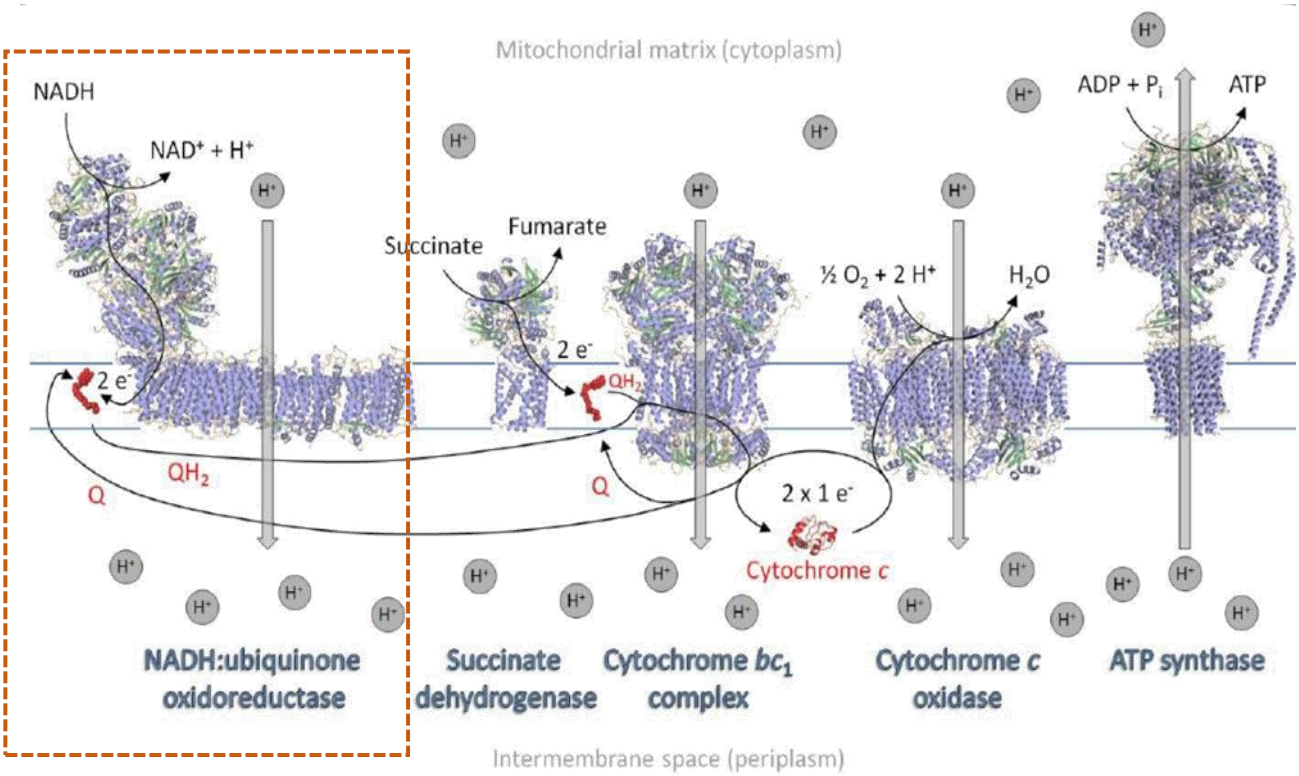

Figure 1.4-1. Scheme of the inner mitochondrial membrane (blue parallel lines) respiratory chain. The mobile electron carriers UQ and cytochrome *c* are highlighted in red. The proteins structure: NADH:ubiquinone oxidoreductase from *Thermus thermophilus* (PDB:4HEA), Succinate dehydrogenase (quinone) from *Sus scrofa* (PDB:3AEF) ; Cytochrome bc_1 complex from *Bos taurus* (PDB:2A06) ; Cytochrome *c* oxidase from *Bos taurus* (PDB: 2DYR) ; ATP synthase - Central stalk from *Saccharomyces cerev isiae* (2WPD) and stator from *Bos taurus* (PDB: 2CLY) ; Cytochrome *c* from *Bos taurus* (PDB: 2B4Z). Adapted from Kriegel[2]

The reaction has a maximum rate of about 200 cycles per second[171] and can be described by the following equation:

$$NADH + Q + 4\ H^+_{in} \rightarrow NAD^+ + QH_2 + 4\ H^+_{out}$$

(in = mitochondrial matrix/ cytoplasm ; out = intermembrane space / periplasm)

Beyond the main function of complex I, aberrant reactions such as ROS production have been shown to take place and in fact complex I has been shown to be one of the main sources of ROS in mitochondria[172-174]. There is evidence that ROS are considered to be a major cause of cellular oxidative stress. The free radical theory of aging proposes that it is a major determinant of life span[167, 175] through the accumulation of damage to mitochondrial proteins, lipids and DNA[176, 177]. Although there are numerous complex cellular mechanisms in place to help minimize the harmful effects of ROS, intracellular ROS production is implicated in many mitochondrial pathologies[178, 179] having an emphasis in neuromuscular diseases, like Leigh's disease and Parkinson Disease[172, 180-182].

1.4.1 Structure

Complex I is one of the largest membrane protein complexes known so far, its size vary between species from 0.5 MDa in prokaryotes to 1 MDa in eukaryotes (mitochondria). The general structure consists on a L-shaped assembly that can be seen as two parts, a hydrophilic arm connected to a membrane part (Figure 1.4-2)[183]. The *E. coli* complex I contains 14 different subunit and the mitochondrial complex I consists of 45 subunits. The nomenclature among the species differs as can be seen in Table 1.4-1.

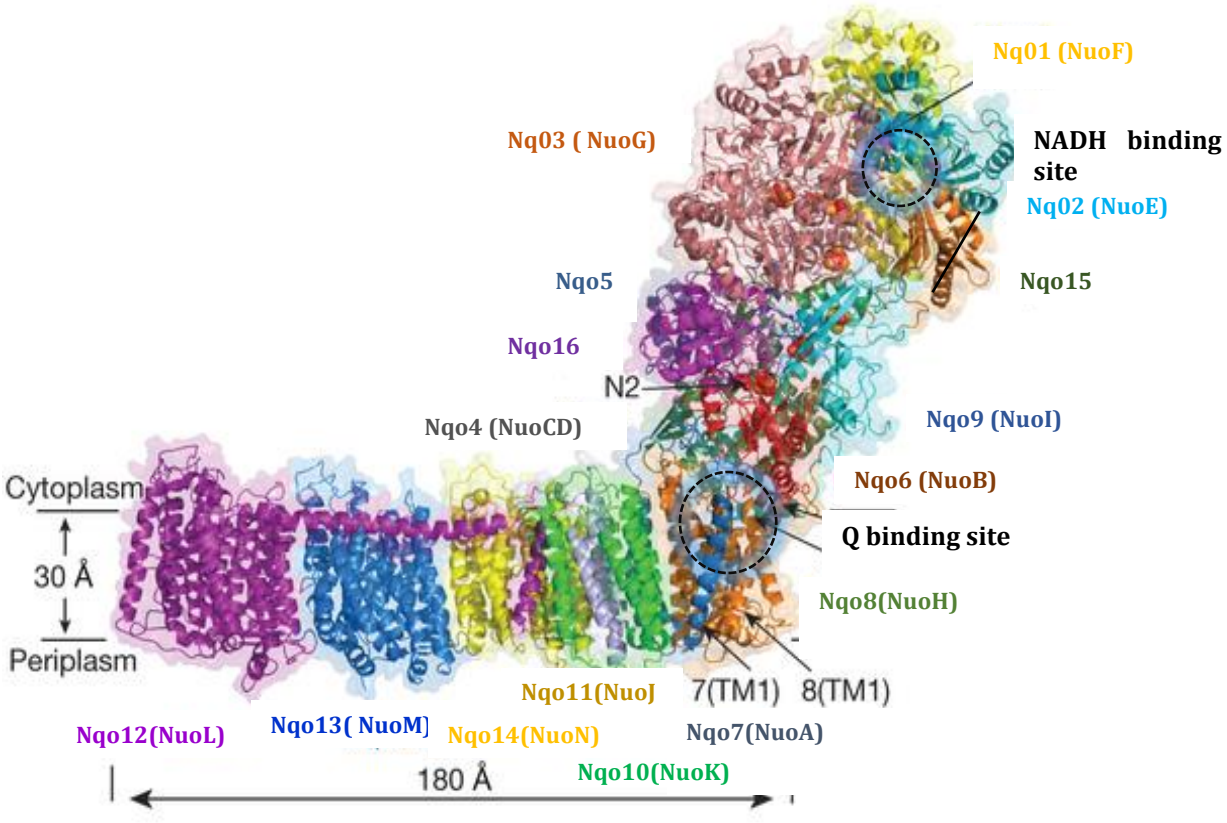

Figure 1.4-2. Schematic representation of complex I from *T. thermophilus*. The nomenclature is according to the *T. thermophilus* subunit and in parenthesis the nomenclature of subunits present in *E. coli*. Adapted from Baradan *et al* [167] (PDB: 4HEA)

The analysis of the electron density map from eukaryotic complex I crystals showed that the fold of a 14 subunit core is highly conserved among bacterial and eukaryotic systems. Seven of these subunits constitute the peripheral arm and another seven the membrane arm. None of these core subunits can be removed without compromising the enzyme's efficiency[16, 184]. This suggests that throughout the species, all complex I enzymes share a common mechanism[185, 186].

Recently, Baradan *et al*. have resolved the structure of the entire bacterial complex I from *T. thermophilus* at 3.3 Å resolution (PDB: 4HEA)[183] (Figure 1.4-2). The crystal structure of complex I of *Escherichia coli* [175], *Yarrowia lipolytica* and *Bos taurus*[187] have been partially solved.

Table 1.4-1. Nomenclature of the 14 core subunits of complex I with their bound cofactors and the predicted TM for each membrane subunit according to different species [18].

Enzyme domain	*Homo sapiens*	*Bos taurus*	*Y. lipolitica*	*T. Thermophilus*	*E. coli*	Proposed function
Hydrophilic arm	NDUFS1	75kDa	NUAM	Nqo3	NuoG	N1b, N4,N5,N7
	NDUFV1	51 kDa	NUBM	Nqo1	NuoF	FMN, N3 NADH binding
	NDUFS2	49 kDa	NUCM	Nqo4	NuoD	Q binding
	NDUFS3	30 kDa	NUGM	Nqo5	NuoC	Q binding
	NDUFV2	24 kDa	NUHN	Nqo2	NuoE	N1a
	NDUFS7	PSST	NUIM	Nqo6	NuoB	N2
	NDUFS8	TYKY	NUKM	Nqo9	NuoI	N6a, N6b
Membrane arm	ND1	ND1	NU1M	Nqo8	NuoH	Q binding
	ND2	ND2	NU2M	Nqo14	NuoN	H^+ translocation
	ND3	ND3	NU3M	Nqo7	NuoA	--
	ND4	ND4	NU4M	Nqo13	NuoM	H^+ translocation
	ND5	ND5	NU5M	Nqo12	NuoL	
	ND6	ND6	NU6M	Nqo10	NuoK	Structural support
	ND4L	ND4L	NULM	Nqo11	NuoJ	

The membrane domain contains a total of 63 transmembrane (TM) helices. The membrane arm is about 180 Å long and the peripheral arm has an extension of about 130 Å over the lipid bilayer. The peripheral arm is positioned on the top of the membrane subunit NuoH (Nq08) and it is the major interaction surface between the hydrophilic and the membrane part.

It is important to note that the peripheral arm provides a rigid scaffold bearing all the cofactors. Within the structure, in the hydrophilic arm there is a non-covalently bound **F**lavin **M**ononucleotide (FMN), coordinated in the NuoF subunit, it lies at the deep end of the solvent exposed cavity that contains a NADH binding site.

In *E. coli and T. thermophilus*, the rest of the cofactors are nine Fe-S clusters, two binuclear Fe–S clusters [2Fe-2S], named N1a and N1b, and seven tetranuclear clusters [4Fe-4S], named N2, N3, N4, N5, N6a, N6b and N7 (nomenclature according to Ohnishi)[188]. Their position in the structure is depicted in Figure 1.4-3. Depending on the organism, the peripheral arm can contain between eight to ten iron-sulfur (Fe-S) clusters, seven of which constitute the conserved electron transfer pathway among all the studied species[189].

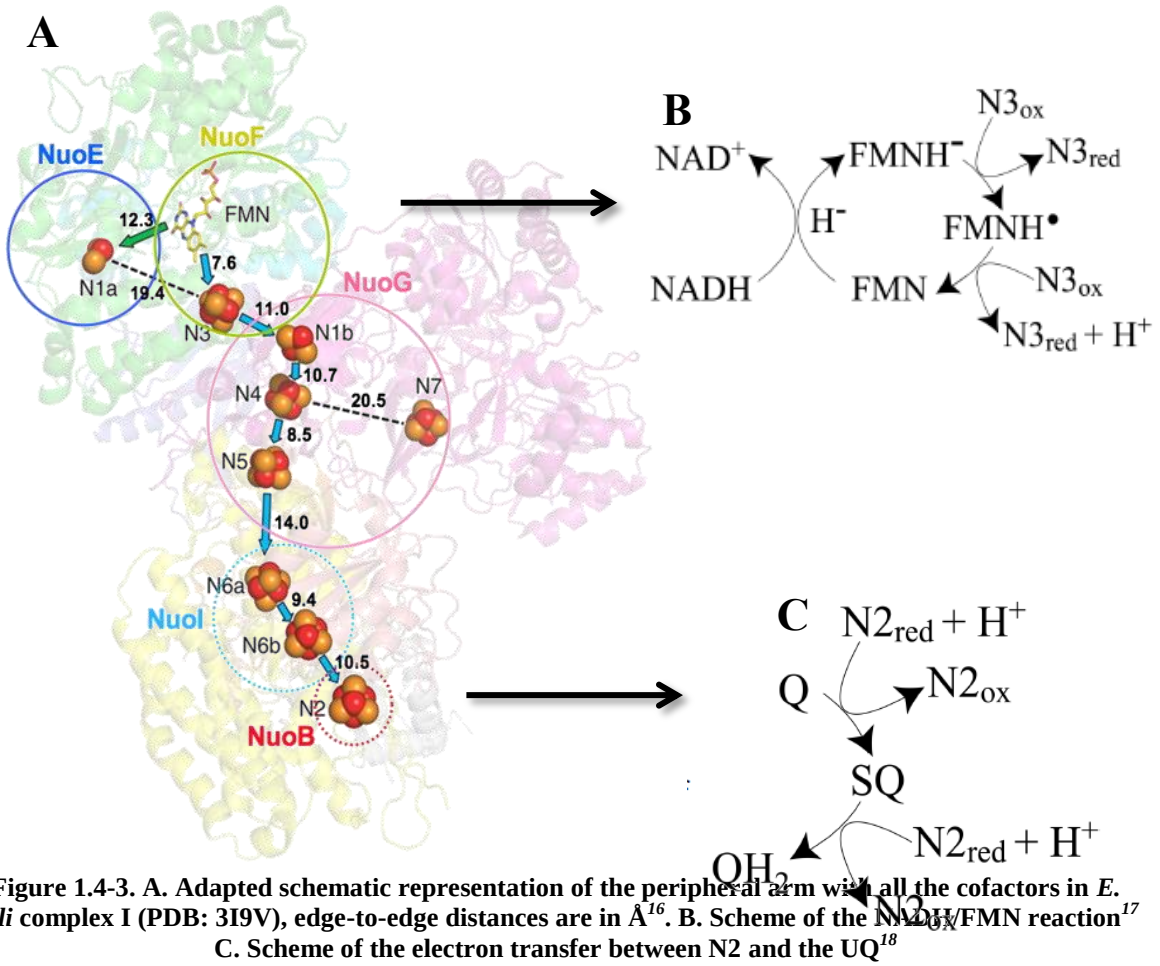

Figure 1.4-3. A. Adapted schematic representation of the peripheral arm with all the cofactors in *E. coli* complex I (PDB: 3I9V), edge-to-edge distances are in Å[16]. B. Scheme of the NADH/FMN reaction[17] C. Scheme of the electron transfer between N2 and the UQ[18]

The conserved electron transfer pathway connects the NADH binding site, located in the NuoF subunit, (Figure 1.4-2) with the tip of the domain (distant from the membrane) to the ubiquinone binding site located 20-25 Å above the membrane surface [190, 191]; It is

important to notice that these two sites are separated by a distance of nearly 100 Å. In contrast to the well-known FMN binding site, the description of the quinone binding remains approximate. Nevertheless, it is assumed that NuoH (Nqo8) together with NuoD (Nqo4) and NuoB (Nqo6) form a part of the quinone binding pocket[192, 193]. It was proposed that a large cavity at the interface between NuoB and NuoD binds the hydrophilic quinone head group [183, 189, 194]. This position is supported by the change in inhibitor sensitivity for mutations in this part of complex I from *Rhodobacter capsulatus* and *Y. lipolytica* [195, 196]

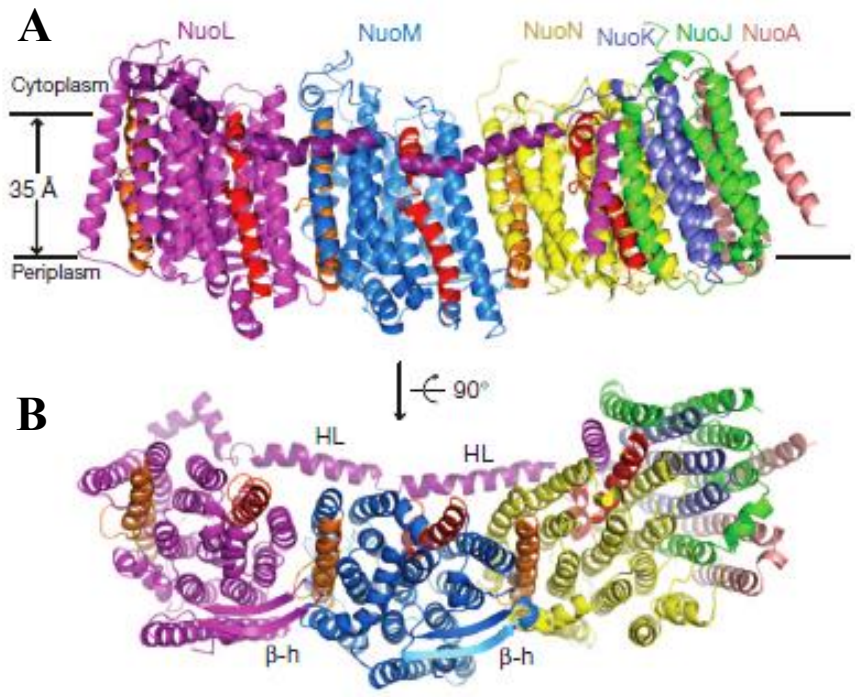

Figure 1.4-4. Scheme of the architecture of the membrane arm of *E. coli* complex I. A. Side view in the membrane plane. B. View from the periplasm into the membrane. Discontinuous helices are shown in red (TM7) and orange (TM12) Connecting elements as β-hairpins (β-h) are signalized[175].

Furthermore, spin labeling studies using different labelled complex I residues and a decyl-ubiquinone derivative with the spin label covalently attached to the alkyl chain confirm this position as the location of the quinone binding site [197]. The eukaryotic enzyme is known to use ubiquinone-10 while prokaryotic enzymes use other derivatives as menaquinone-8 (*T. thermophilus*), and ubiquinone-8 and menaquinone-8 (*E. coli)*[171, 198, 199].

In addition to the electron transferring cofactors, the enzyme subunits involved in the proton translocation have been described. In fact, an 11-helix bundle formed by the NuoA/J/K

subunits separates the peripheral arm from the subunits NuoN/M/L, which are monovalent cation/H^+ antiporters (ATS)[175]. They are located in the most distal position of the membrane arm. Each one of these subunits consists on 14 TM helices and includes two discontinuous TM helices connected by a peptide loop in the membrane. Such helices have been found also in other transporters and channels known to play roles in ion translocation[200].

In addition to the cofactors and the proton translocating subunits, several other subunits have structural roles. For example, NuoL has a supplementary C-terminal domain, which is not present in the other ATSs. This domain is formed by 15 TM helices holding a 110 Å long amphipathic helix (HL) aligned parallel to the membrane arm (see Figure 1.4-4). In mitochondrial complex I this helix has a length of 60 Å.

In contrast, the smaller subunits NuoA/J/K interact with large surface areas buried at the interfaces, as they present more hydrogen bonds and salt bridges than the other subunits. Their main function from the structural point of view seems to "glue" the end of the membrane domain stabilizing the complex. Conserved homologues of the core subunits are found in many organisms, they are smaller proteins which assembly and function had helped to untangle the mechanism of complex I [187, 201]. The NuoE/F/G subunits are also called as the N-module as they harbor NADH oxidase activity; this group is homologous to the group-3 of bidirectional NiFe hydrogenases. Furthermore, NuoB/C/D/I, also called to Q-module, has as homologous membrane-bound NiFe-hydrogenase. The subunits NuoA/H/K/L/M/N, named as the P-module for their proton transfer activity, is related to a class of membrane Na^+/H^+ Mrp antiporters[187, 196].

As described above, the bacterial and mitochondrial complex I possess the same cofactors for the electron transport and their activities are suppressed by the same inhibitors, such as rotenone and piericidin A[202-204]. As the handling and purification of the mitochondrial enzyme is complicated and delicate due to the number of post-translational modifications and the compositional heterogeneity, the bacterial complex I is a good model candidate to study the relation between the Fe-S clusters and the conformational changes that controls the protein function.

1.4.2 Mechanism

1.4.2.1 Overview

As it can be seen in Figure 1.4-3 with each NADH oxidation one quinone is reduced. The suggested coupling between electron transfer and proton translocation involves a long-range conformational changes that, so far, have not been fully understood. Several publications suggested that the mechanism is redox driven (direct) or conformational driven (indirect)[167, 169, 170, 205]. To date, the mixture of those two mechanisms seems to be the best proposal.

The L-shaped structure of complex I suggests that, as the peripheral arm bears all the known redox cofactors, most of the redox reactions do not contribute to the proton translocation, only the quinone reaction assisted by the N2 redox reaction might drive the proton translocation due to coupling of a direct and indirect mechanism. In general, the catalytic activity of Complex I is reversible and its rate and direction are controlled by Δp and by the redox states of the NADH and Q pools[169, 206].

1.4.2.2 Electron transfer

The electron transfer pathway in complex I (see Figure 1.4-3 blue arrows) had been deduced from the position and the midpoint potentials of the cofactors. The primary electron acceptor, FMN accepts two electrons from NADH as hybrid ions, becoming $FMNH_2$. Furthermore, the electrons are transferred one by one to the quinone along the Fe-S clusters chain[18]. FMN has thus to release one electron after another. The midpoint potential of $FMN/FMNH_2$ is -300 mV[205, 207]. The transfer of the first electron probably takes place to the N3 cluster (-270 mV) and then a chain of one [2Fe-2S] and six [4Fe-4S] clusters transfer the electrons through electron tunneling to the last cluster, N2, which has the most positive midpoint potential of the chain (-220 mV) [188, 208-210]. In general, the edge-to-edge distances between the clusters vary from 8.5 to 14 Å, where all clusters are found to be within efficient electron tunneling distance (< 14 Å) to the next cluster in the chain [211]. Nevertheless, it is important to stress that the distance between N5 and N6a is in the limit (14 Å). To explain the electron transfer between these two clusters the involvement of aromatic amino acids has been discussed[205, 212]. This is based on the theory that electrons are not only located on Fe-S clusters of complex I but also on the π-electron system of aromatic amino acids. This process

is called the "hopping" mechanism[213]. The geometrical arrangement of the cofactors combined with the favorable values of the redox potentials of neighboring centers, allows the electron to tunnel between FMN and N2 in a microsecond timescale, this was demonstrated experimentally by Verkhovskaya *et al.*[205] and it is consistent with the theoretical studies reported by Hayashi and Stuchebrukhov[214].

In Figure 1.4-5 the cascade of the electron transfer according to the midpoint potential (E_m) of the Fe-S clusters is described. N3, N1b, N4 N5 and N6a are called the "isopotential" clusters, as their midpoint potentials are very similar (-300 to -250 mV vs. SHE)[188, 215, 216]. Previous studies showed that changes in the conformation around the cluster during the electron transfer can shift the potential facilitating the electron transfer[217].

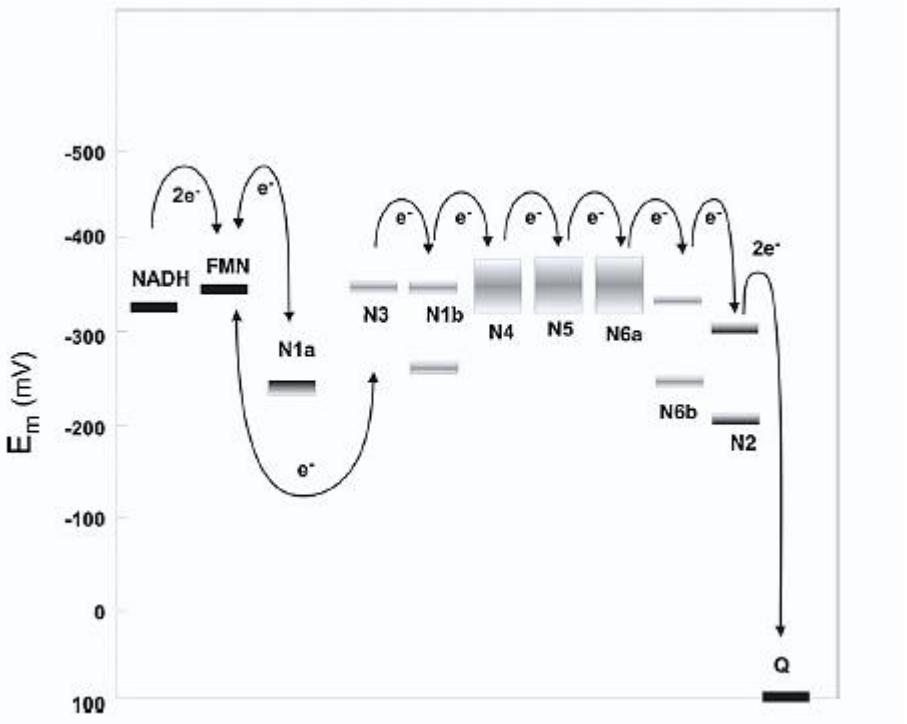

Figure 1.4-5. Midpoint potential energy profile of the substrates and cofactors from *E. coli* complex I. The potentials are indicated by bars, double bars means a splitted redox potential for clusters thermodynamically interacting with their neighbors: - high Em's represent intrinsic values, low Em's include interaction [194, 215].

N6b and N2 have the most positive *Em*, creating a potential gradient which attracts the electrons down the chain to N2[205, 215]. It had been reported in several studies that some of these values vary according to the species[196, 198]. It has to be taken in consideration that, according to the sequence, different residues might surround the cofactors changing in some degree the electrostatic interactions and the redox properties of the cluster.

Two additional Fe-S clusters, N1a and N7, were reported not to be part of the electron transfer chain. N7 is found only in the complex I from bacterial organisms and it does not participate in the electron transfer but recent studies have shown that it is essential for the stability of the structure[215, 218]. The function of N1a is still under debate, a more explicit description of the properties of this clusters will be given in section 1.4.3.

Besides, Ohnishi *et al* [212] and Verkhovskaya *et al*[205, 219] have proposed that there are two semiquinones that mediated and regulated the electron transfer between N2 and the quinone as the redox-driven coupling between the N2 cluster with semiquinone species had only been detected under steady conditions. Part of this work is to identify and to characterize the redox properties of these semiquinone cofactors by fluorescence spectroscopy.

The rates of electron transfer and properties of each of the Fe-S clusters in complex I have been largely studies by UV/vis, Mössbauer and EPR spectroscopies[194, 207, 215, 217, 220]. Furthermore, the recently resolved structure seems to provide a deeper understanding of the mechanism of complex I. Nevertheless, the puzzle is still far from being complete, especially when it comes to the understanding of how the properties of each Fe-S cluster can regulate the rate of electron transfer. Therefore, and in order to decipher the mechanism of complex I, a new approach must be taken. In this work a molecular approach of the metal-ligand vibrations of the Fe-S clusters via a full description of the vibrations of the oxidized and reduced states will be performed by RR and FT-IR spectroscopy. The intrinsic characteristic of each cluster will be depicted separately.

1.4.2.3 Proton transfer

The membrane arm is composed of seven subunits. As described above (see section 1.4.1) there are three major subunits NuoL, NuoM and NuoN, which are homologues of monovalent cation/H^+ antiporters (ATS)[167]. It has been proposed that the quinone redox chemistry leads to conformational changes that are then "transmitted" to the long horizontal helix from the NuoL subunit. This helix acts as a kind of piston to transmit the redox energy harvested and to release it in the peripheral arm to induce the proton translocation[183].

Due to these conformational changes, the monovalent cation/H^+ antiporters have two possible conformations: open in the reduced state and closed in the oxidized state (Figure 1.4-6.A). According to Baradaran *et al.*[183] and based on the structure, three putative proton

channels are proposed. They are located in the ATS NuoL, M and N and one goes through subunits NuoA/H/JK (Figure 1.4-6.B). They are all articulated around a structural particularity of Complex I: a chain of hydrophilic residues situated in the middle of the hydrophobic domain and running from the Q binding site through the distal α-helix of NuoL[167, 194, 204].

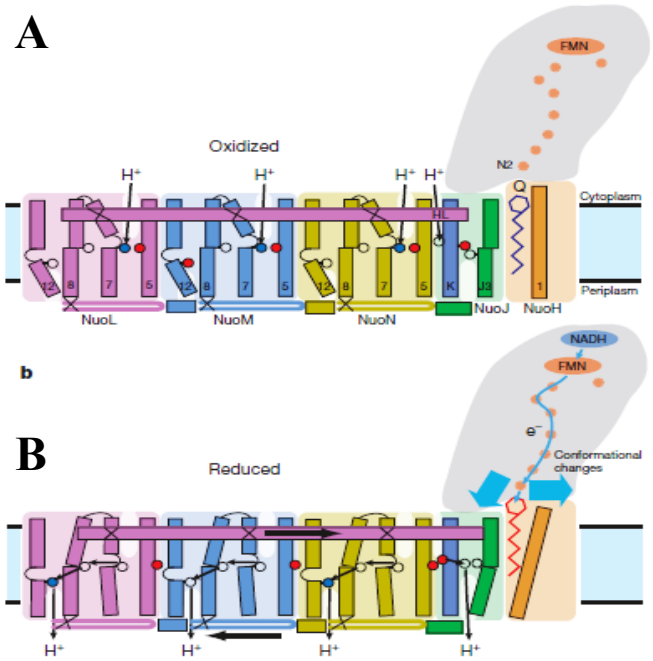

Figure 1.4-6. Schematic of the coupling between the electron transfer and proton transfer of *T. thermophilus* complex I. Adapted from Baradaran *et al*[183]

Besides the conformation-driven changes caused by helix HL on the subunits ATS, Efremov and Sazanov[175] discussed the involvement of a network of conserved polar residues as part of the proton translocation pathway. They suggested that preferentially Lys residues rather than carboxylate residues (i.e. Asp, Glu) act as main elements of the proton pump in subunits NuoL,NuoM and NuoN.

To enforce directional proton transfer, the proton channels should include such a gating mechanism and it should be controlled by the redox reaction[168]. Nevertheless, this mechanism only explains the translocation of 3 protons[168] whereas the fourth proton had been proposed to be translocated at the quinone binding site[221, 222].

1.4.3 Properties of the Fe-S clusters N1a and N2

N1a and N2 clusters have been for the last 20 years an important part of the puzzle in understanding the mechanism of complex I. These two clusters, have presented special

characteristics that made them a question mark. Both have a pH-dependent redox midpoint potential; furthermore, the value of the potential shifts across the different known species. Their Cys cluster motifs present particularities in the ligation of the cysteinyl residues that make them an interesting case of study by vibrational spectroscopy.

The binuclear Fe-S cluster N1a of NuoE in *E. coli* is not part of the main electron chain, as described in section 1.4.2.2. Its role had been a matter of investigation since Verkhovskaya *et al.*[205] showed that the cluster is EPR-silent except in the *E. coli* complex I. The cluster is coordinated by four Cys residues having a thioredoxin like-fold, the binding motif had been described as CysXXXXCysX_{35}CysXXXCys (X being any amino acid)[223]. The cluster is close to the interface of the NADH binding subunit (NuoF) and it is surrounded by more hydrophobic amino acid residues than the other clusters[183].

The crystal structure of the peripheral arm of complex I published in 2011 by Efremov *et al* (PDB: 3M9S)[224] showed that the distance from N1a to N3 is 19.4 Å and to the FMN is 12.3 Å. Accordingly, it is most probable that N1a accepts electrons from the reduced FMN but it is not able to directly transfer it to N3. It has been proposed that the second electron is transferred to N1a, given the midpoint potential of FMN/FMNH (-390 mV vs. SHE)[215]. Then the second electron is probably transferred from N1a back to the FMN, subsequently to the re-oxidized N3 and further to N2, as described above. The direct transfer to N1a is unlikely because of its low midpoint potential of -330 mV[217]. Nevertheless, the measurement of the intrinsic midpoint potential of N1a from different species by EPR and protein voltammetry showed that its values vary significantly, from -330 to -250 mV in bacteria and from -370 to -410 in mitochondria[6]. This may indicate that N1a has different roles among different species.

According to Hirst *et al*[18] the time-limited transfer of the second electron to N1a could prevent the formation of radicals at the FMN, also called flavo-semiquinone ($FMN^{\bullet -}$ or $FMNH^{\bullet}$). It is already known that complex I is responsible for the production of ROS and the solvent exposed FMN is discussed to be at the origin[225] and the role of N1a may be to prevent the production ROS[6, 226].

Similarly to N1a, the terminal N2 cluster in the NuoB subunit (see Figure 1.4-3) also exhibits different redox midpoint potential in different organisms; in *T. thermophilus* membranes the value is -300 mV[227], in *Rhodothermus marinus* it is below -450 mV[228] and for

most organism like *B. Taurus*, *Neurospora crassa*, *Paracoccus denitrificans* and *E. coli* it is ~-150 mV[6]. The high redox potential in comparison to the other Fe-S cluster in the electron chain makes this cluster susceptible to receive the electrons. After the electrons from NADH are transferred to the chain, the reduction of N2 was observed within 90 μs[215].

It is important to note that in all the organisms the decrease of the pH leads to a more positive midpoint potential. The cluster binding motif is conserved among all the species, the unique characteristic of this motif is that there are two adjacent Cys residues, Cys63 and Cys64 in *E. coli*, coordinating the metal center[197, 229]. In *E. coli* individual mutations of all four conserved Cys residues in NuoB resulted in a loss of complex I activity and of the EPR signal of N2 in the cytoplasmic membrane as well as in the isolated complex[209, 210]. Previous studies have proposed that this feature is the cause of the pH dependency of the E_m, as it may allow direct protonation of the cluster upon reduction[215, 230].

Despite the sheer efforts to elucidate the role of N2, it is still unclear why this cluster has a different potential and its potential is pH-dependent, in comparison to the others in the chain and furthermore how these differences might give them the function of not only being units for electron transfer but maybe, in some way, work as regulation barriers of the enzymatic activity.

In this work, RR, FT-IR, and UV/vis spectroscopies, isotopic labeling as well as site-direct mutagenesis are used to study the properties of these clusters. The aim is to characterize their coordination, and shed a light over the question so long asked about their function and what makes them so special in complex I.

1.5 Aim of the work

This research project has as a principal goal the application of different spectroscopic techniques to study how protein structure can be modified by different effectors modulating their functionality. The role of three effectors will be explored: viral proteins, metal ions as ligands and metal centers as the core of the protein function.

PDZ1 from MAGI-1 and its interaction with HPV16 E6:

1. Describe the role of PDZ1 in the ligand recognition of residues that bind outside the hydrophobic binding pocket.
2. Understand the role of the hydrogen bonding in the process of protein-protein interaction.
3. Depict catalytically-important side chains and deduce their environmental and structural changes in order to understand molecular reaction mechanism of PDZ1 in presence of HPV16 E6 protein.
4. Analyze if there are conformational changes in PDZ1 beyond the binding site. For this site direct-mutagenesis in the C-terminal and in the βB region were studied.
5. Correlate how the conformational changes in specific areas beyond the binding site can modulate the affinity of the viral protein, furthermore to specify how these changes can be defined as an allosteric process.

The coordination of Cu(I) by Aβ peptides:

1. Describe the sphere of coordination of Cu(I) with the Aβ16 peptide and how the redox reaction can trigger the formation of the Aβ fibrils.
2. Understand the reorganization of the Aβ16Cu-peptide upon redox reaction by means of electrochemically-induced FTIR difference spectroscopy.
3. Describe the redox differences spectra of DAHK and GHK at different pH values and to corroborate the behavior of the Aβ16 peptide in presence of Cu(I).

Mechanism of the Fe-S cluster from NADH: ubiquinone oxidoreductase (Complex I):

1. Describe the metal-ligand vibrations of the Fe-S clusters and their redox properties found in the low frequency region in infrared and resonance Raman.
2. Compare the reduced state of the cofactors obtained by electrochemistry to the chemically-reduced state obtained in presence of different nucleotides.

3. Define the conformational changes in the protein. Define the cofactor properties, or if changes in the geometry of the cofactors trigger conformational changes in the protein.
4. Analyze by site-direct mutagenesis conserved residues in the NuoE and NuoB subunit with the objective to understand the features of N1 and N2 pH-dependent clusters and how the environment can modulate their redox properties.
5. Substantiate the presence of quinoid cofactors in the membrane arm of complex I and calculate their midpoint potential by redox titration coupling fluorescence spectroscopy with electrochemistry.

2 TECHNICAL APPROACH. Spectroscopy.

Spectroscopy is a term used to describe the study of the interaction between a molecule and electromagnetic radiation. Different regions of the electromagnetic spectrum (Figure 2-1) can provide different kinds of information as a result of these interactions. The electromagnetic spectrum is a wide and continuous spectrum where light can be classified according to its energy.

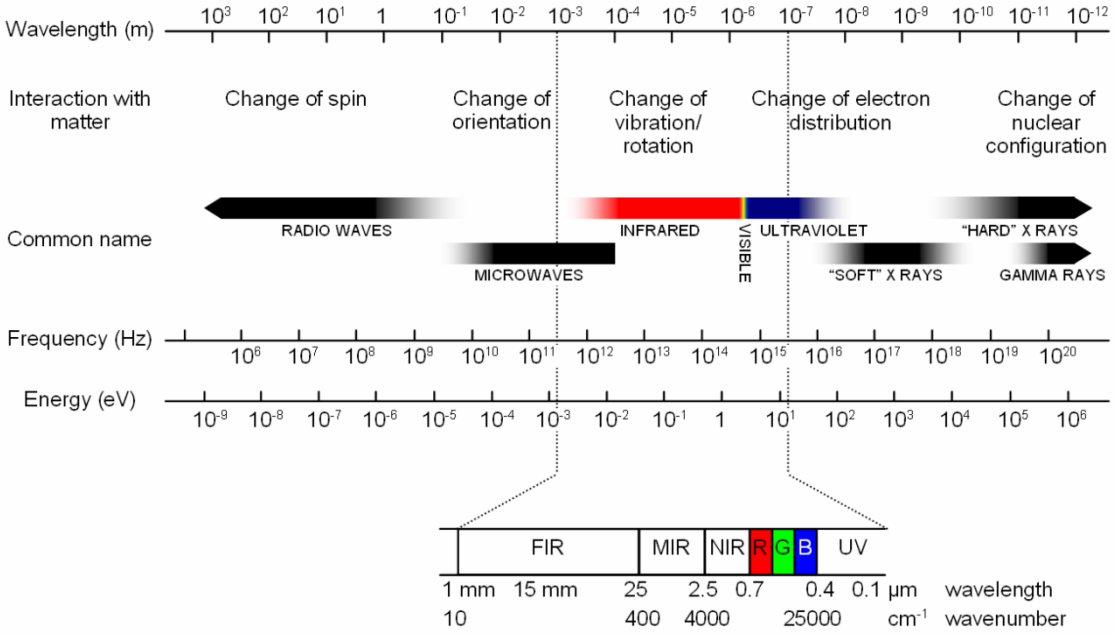

Figure 2-1. Electromagnetic spectrum characterized according to the wavelength (meters) and the frequency (Hertz) [232]

Parameters that can be described from the electric field amplitude of light as a function of time are the wavelength (λ), the frequency (υ) and the wavenumbers ($\tilde{\nu}$), which are related to each other via equation 2-1; where *c* corresponds to the velocity of light in vacuum (2.997 x 10^8 m s^{-1}) and *n* the refractive index of the medium [10].

$$\tilde{\nu} = \nu/(c/n) = 1/\lambda \qquad \text{Equation 2-1}$$

In this work, UV/vis, IR, Raman, and fluorescence spectroscopies were used in order to study biological molecules. The obtained data provides information about the electronic transition in the molecules upon the absorption (or emission) of photons (vis or fluorescence spectroscopies, respectively). These techniques were often combined with electrochemistry in order to determine the midpoint potentials of proteins cofactors.

2.1 Vibrational spectroscopy

Vibrational spectroscopy is the collective term used to describe analytical techniques that probe bond vibrations. The most commonly used are infrared and Raman spectroscopy. Both techniques are complementary providing characteristic of the fundamental vibrations that are extensively used for the determination and identification of molecular structure and able follow molecular interactions.

The IR and Raman vibrations are usually characterized by their frequency (energy), intensity (polar character or polarizability respectively), and the environment of bonds; like the geometric arrangement, the presence of functional groups and the strength of the bond itself [10]. Since the vibrational energy levels are unique to each molecule, the IR and Raman spectrum provide a "fingerprint" for a particular kind of molecule.

The fingerprint spectra provide information on molecular structure, conformation, and environment. Even though some vibrations may be active in both Raman and IR, these two forms of spectroscopy arise from different processes and different conditions. Both techniques involve the study of the interaction of radiation with molecular vibrations but differ in the way in which photon energy is transferred to the molecule by changing its vibrational state.

2.1.1 Molecular vibrations

In general the vibration of a molecule can be represented by the means of a harmonic oscillator. This classical model is built by two atom joined by a bond, according to the Hooke's Law this can be equivalent to two masses joined by a spring (as the bond is not rigid) of a force constant K. (Figure 2.1-1).

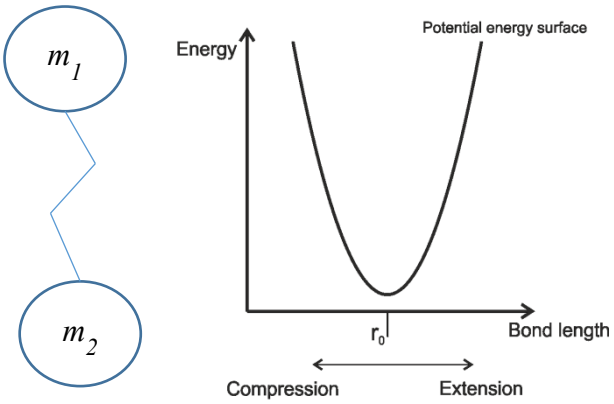

Figure 2.1-1. The simple harmonic oscillator.[10]

When the molecule vibrates, the atoms can move towards (compression) or away (extension) from each other with certain energy (frequency). The potential energy of the system is related to how much the spring is stretched or compressed. The vibrational frequency (ν) or normal mode described by Hooke's Law (Equation 2-2) will correspond to the properties of the chemical bond (*k*: the bond's force constant) and the mass of the atom (m_1 and m_2).

$$v = \frac{1}{2\pi}\sqrt{k\left(\frac{1}{m1}+\frac{1}{m2}\right)} \qquad \text{Equation 2-2}$$

The lighter the masses on the spring, or the tighter (stronger) the spring, the higher the vibrational frequency will be. Changes is the mass can give rise to an observable shift in the frequencies, which is the case of the labeled proteins or amino acids with ^{15}N and/or ^{13}C in comparison to the natural ^{14}N or ^{12}C [233] . The shifts in the wavenumber due to the difference in mass allow the detection of subtle conformational changes and contributions of specific amino acids or their side chains.

Similarly, according to the quantum chemistry model, vibrational frequencies are related to the strength of chemical bonds which in turn is related to bond length. Unlike the model of springs and spheres, molecules will vibrate only when a certain photon of a certain energy can be absorbed, leading the molecule to be excited from its ground state to the first excited state.

The possible vibrational states for a molecule are given by the vibration quantum number (*v*), which can have only integer values, and in addition can only change according to the rule $\Delta v = \pm 1$. The energy of each vibrational level (E_v) according to the quantum mechanics in a harmonic oscillator can be described as:

$$E_v = \left(v + \frac{1}{2}\right) h v_0 \quad (v=0,1,2,3\ldots.) \qquad \text{Equation 2-3}$$

v correspond to the fundamental frequency, *h* is Planck's constant (6.626×10^{-34} J.s) and v_0 is the frequencies of the molecule in the ground state. The harmonic oscillator is a valid model at equilibrium where the bond is in the ground state, but when a molecule is excited many other factors need to be taken into account; that is why the anharmonic oscillator

(Figure 2.1-2) becomes a better model to explain the molecular vibrations in this case [234]. The energy levels (E_v) of an anharmonic oscillator model are described by Equation 2-4.

$$E_v = hv_0\left[\left(n+\frac{1}{2}\right) - Xa\left(n+\frac{1}{2}\right)^2\right] \quad \text{Equation 2-4}$$

Xa define the magnitude of anharmonicity and *n* is the atomic energy level (n=1,2,3,…). Usually the vibrations of a large molecule like peptides or proteins are considered as a system of coupled anharmonic oscillators.

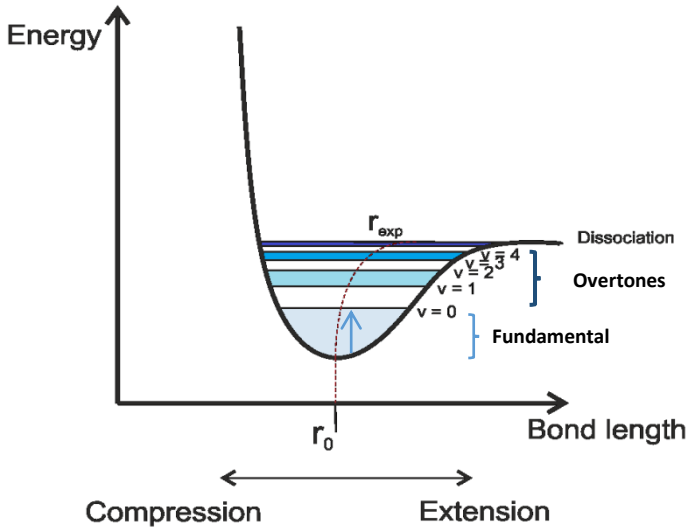

Figure 2.1-2. Energy levels of an anharmonic oscillator[9].

In vibrational spectroscopy, typically wavenumbers are used as main unit (w) (waves per unit length: cm^{-1}). According to this the model can be described as:

$$w = \frac{1}{2\pi c}\sqrt{K\left(\frac{1}{m_1}+\frac{1}{m_2}\right)} \quad \text{Equation 2-5}$$

Where *c* is the speed of light and *K* the force constant, which is a function of the bond energy between two atoms.

Each molecule of *n* atoms has three degrees of freedom, rotation, translation and vibration, for non-linear molecules 3*n*-6 vibrational modes are probable and for linear molecules the rule will be 3*n*-5, because of only two possible rotational degrees[10, 235].

Vibrational modes can be classified as a stretching vibration (ν) (change of bond length) and deformational vibration (δ) (change of bond angle). The stretching vibration can be further classified according to the symmetry of the vibrations as symmetrical and asymmetrical, as seen in Figure 2.1-3[9].

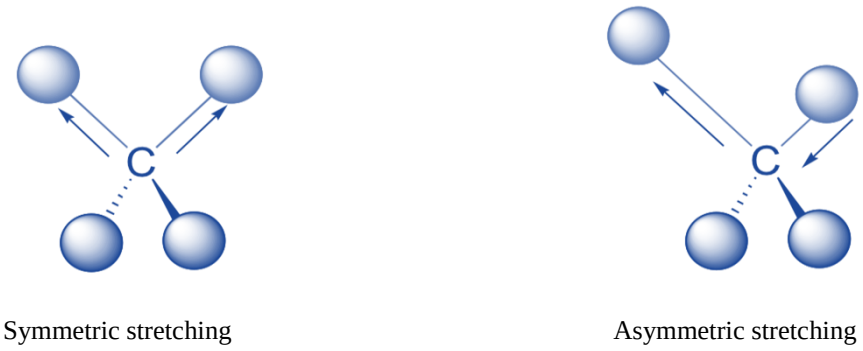

Figure 2.1-3. Stretching modes of a tetrahedral carbon.

The deformation vibrations are bending modes subdivided into in-plane and out-of-plane. Each one includes two types; the in-plane deformations are scissoring and rocking vibrations and the two out-of-plane deformations are wagging and twisting vibrations (Figure 2.1-4).

.

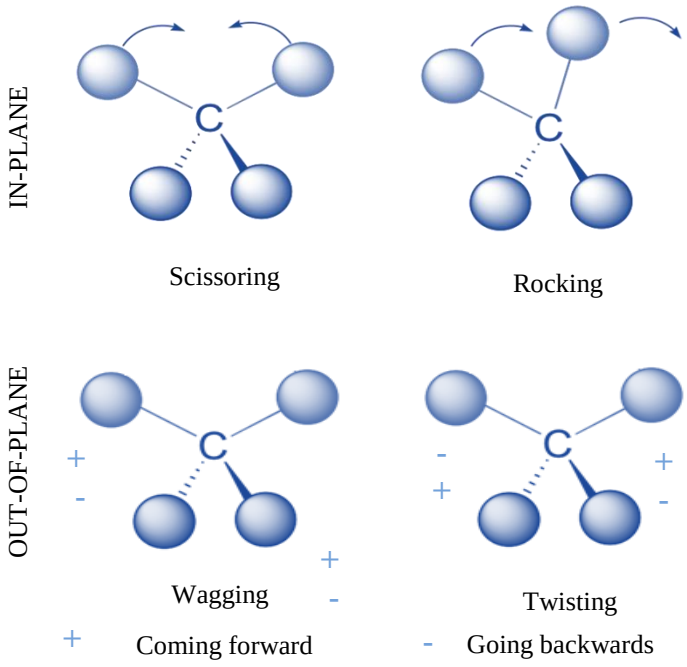

Figure 2.1-4. Bending modes of the tetrahedral carbon.

As the number of atoms in a molecule increase, so does the number of modes, as well as the associated complexity of the vibrational spectrum. Assigning normal modes to observed peaks in the experimental spectra can become a difficult task. Help is available from the characteristic modes of small molecules, which serve as excellent references for the interpretation of more complex molecules such as proteins. The symmetries of the normal modes can be classified by group theory[9].

In general the strong band in an IR spectrum of a compound corresponds to weak bands in Raman and vice versa, in the case that the vibration is Raman and IR active. In the case of IR, the intensity of the bands corresponds to the probability of changes in the electric dipole moment whereas in the case of Raman it depends on the polarizability itself [9, 234]. A more detailed explanation of the basic principles of Infrared and Raman active vibrations will be given in next section where each technique will be described (Sections 2.1.2 and 2.1.3).

2.1.2 Infrared spectroscopy (IR)

In infrared spectroscopy the sample is irradiated with a polychromatic infrared light. A photon is absorbed when the energy (frequency) of the light matches the energy required for a particular bond to vibrate within the sample, as described by Equation 2-6 where the transition from the initial state (*i*) to the final state (*f*) of higher energy requires the absorption of one photon of energy that is equal to ΔE, which gives rise to the signal under one condition that the dipole moment of the molecule changes during the vibration.

$$\Delta E = hc\left(\frac{1}{\lambda i} - \frac{1}{\lambda f}\right) \quad \text{Equation 2-6}$$

According to the Lambert-Beer's law (Equation 2-6), the absorption of light by a molecule is related to the concentration of the sample (*c*), the absorption coefficient (ε) and the pathlength (*d*). The intensity of a vibration is directly correlated to the amount of change of the dipole moment.

$$A = log\frac{Io}{I}\,\mathcal{E}.c.d \qquad \text{Equation 2-7}$$

The absorption of infrared light that induces transitions between the different vibrational energy levels is described by the model of an anharmonic oscillator (Figure 2.1-2), where the energy levels are not equidistant.

The infrared spectrum can be classified in three main regions, the near infrared (13000 – 4000 cm^{-1}), the mid infrared (MIR) (4000 – 400 cm^{-1}) and the far infrared (FIR) (400-10 cm^{-1}). In this work the molecular vibrations of proteins and peptides are studied in the MIR and the FIR regions.

2.1.2.1 IR spectrometer

Most common IR spectrometers are Fourier transform instruments. The main parts of these instruments are the IR light source, the interferometer and the detector. According to the region of the IR spectrum different sources and detectors are needed (see section 3.2.2).

The interferometer follows the Michelson diagram, described in Figure 2.1-5. The main components are a beamsplitter, a fixed and a moving mirror (for back and forward movement); these two mirrors are perpendicular to each other. The infrared light is split by the beamsplitter,50% of the light are transmitted to the moving mirror and 50% are reflected to the fixed mirror. Both mirrors return the beam back to the beamsplitter which reflects the half of both beams to the detector where they interfere according to their phase difference introduced by the path difference caused by the moving mirror.

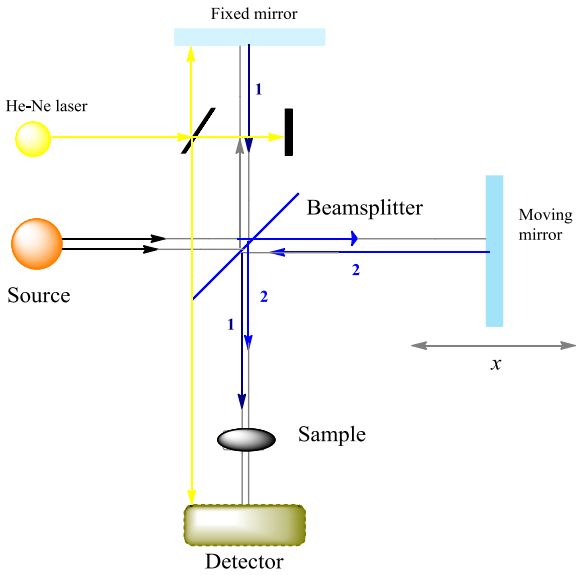

Figure 2.1-5. Schematic representation of the Michelson interferometer

This phase difference can be constructive (when the intensity is maximal) or destructive (the intensity is minimal), in this the paths are equivalent[9].

The intensity of these two beams is then measured as function of the difference in path, or the displacement of the movable mirror (Figure 2.1-6). Since the movable mirror displacement is uniform the interferogram can be plotted as a function of mirror position. The Fourier transform is applied on the interferogram and transforms into a spectrum

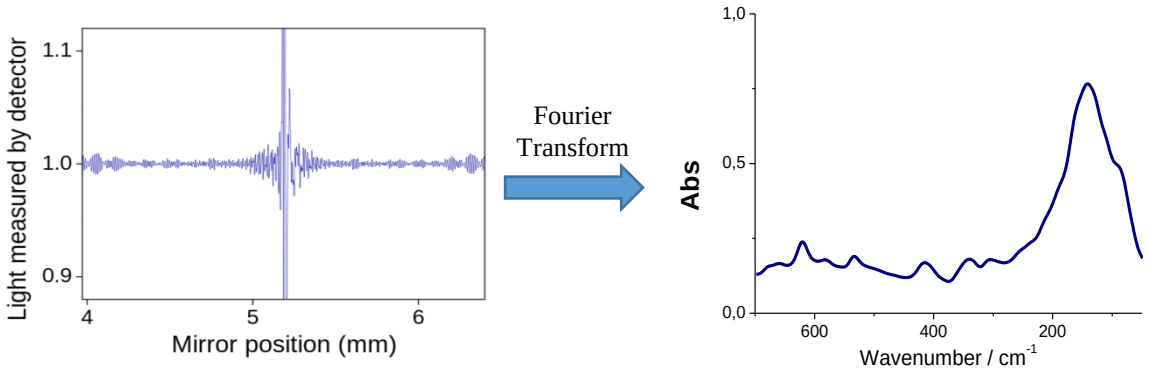

Figure 2.1-6. Interferogram of a monochromatic light and the resultant spectrum[10].

The Fourier Transformation can be described as a function of the source intensity (S):

$$S(\tilde{\nu}) = \int_0^{\infty} I(\delta)\cos(2\pi\delta\tilde{\nu})\, d\tilde{\nu} \qquad \text{Equation 2-8}$$

$\tilde{\nu}$ is the wavenumber (cm^{-1}), I is the intensity of the interferogram and δ is the optical path difference between the two beams [236]. To obtain a spectrum of a sample in the MIR or the FIR, the optics need to be suitable for the studied range, which is why in each spectral range, a different IR source, beamsplitter and detector are used (see section 3.2.2).

The IR spectrum is obtained by plotting the intensity (absorbance or transmittance) versus the wavenumber, where the intensity will be proportional to the energy difference between the ground and the excited state. For this reason the spectral band parameters to take into consideration are the position of the band maximum, the intensity of the band (height or area above the baseline), and the band shape.

2.1.3 Raman Spectroscopy

Raman spectroscopy is light-scattering event where a sample is irradiated with monochromatic light and the photons are either inelastically or elastically scattered (Figure

2.1-7). In this process the incident photon (hv_o) excites the molecule to a virtual level. Once in this virtual level the molecule will decay to an excited state emitting a scattered photon (hv). The incident photon has a higher energy than the vibrational quantum energy level and loses part of its energy to the molecular vibration with the remaining energy scattered as a photon with reduced frequency. This is inelastic scattering[10].

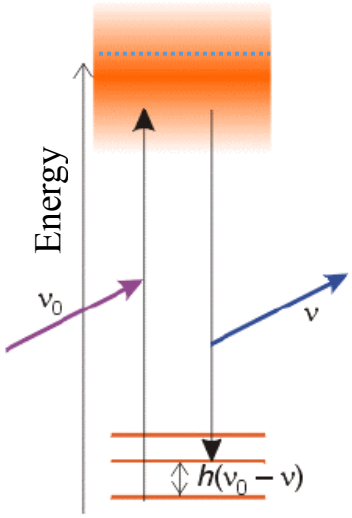

Figure 2.1-7. Scattering of the incident light giving the vibrational levels[10].

The intensity of the Raman scattering (I) is defined by the expression:

$$I = \frac{8\pi^4 \propto^2}{\lambda^4 r^2} (1 + cos^2\theta) I_0 \qquad \text{Equation 2-9}$$

Where α is the polarizability of the molecule, λ the wavelength of the incident radiation, r is the distance, between the center of scattering and the detector, θ the angle between the incident and the scattered light and *Io* the incident intensity [237].

Polarizability (α) can be defined by the measure of an electron cloud's ability to deform in contrast to the atomic nuclei. When a molecule is placed into an electric (or oscillating) field (E) the electrons are pulled towards the positive charge and the atomic nuclei towards the negative charge, which induces a dipole moment (μ) and results in scattering, as shown is equation 2-10.

$$\mu = \alpha E \qquad \text{Equation 2-10}$$

As the electric field due to an electromagnetic wave with an initial frequency ν_o is described as:

$$E = E_0 \cos 2\pi \nu_0 t \qquad \text{Equation 2-11}$$

The equation 2.-9 becomes:

$$\mu = \alpha E_0 \cos 2\pi v_0 t \qquad \text{Equation 2-12}$$

As described before the principal requirement for a vibration to be Raman active is when the molecule vibrates there must be a change in polarizability, this change depends on the geometry of the molecule. This can be caused by a change in the shape, size or orientation of the electron cloud that surrounds the molecule (Figure 2.1-8). The polarizability of a molecule ($\alpha_{p\sigma}$) can be fully described according to the Kramer Heisenberg Dirac (KHD) expression:

$$\alpha_{p\sigma} = = k \sum_I \left(\frac{\langle F|r_\rho|I\rangle\langle I|r_\sigma|G\rangle}{\omega_{GI-}\ \omega_{L-i\Gamma_I}} + \frac{\langle I|r_\rho|G\rangle\langle F|r_\sigma\rangle}{\omega_{IF+}\ \omega_{L-i\Gamma_I}}\right) \qquad \text{Equation 2-13}$$

α is the molecular polarizability, ρ and σ are the incident and scattered polarization directions, respectively. Σ corresponds to the sum over all vibronic states of the molecule as might be expected from the non-specific nature of scattering. Outside this the remaining terms are constants. *G* is the ground vibronic state, *I* is the vibronic state of an excited electronic state and *F* is the final vibronic state of the ground state.

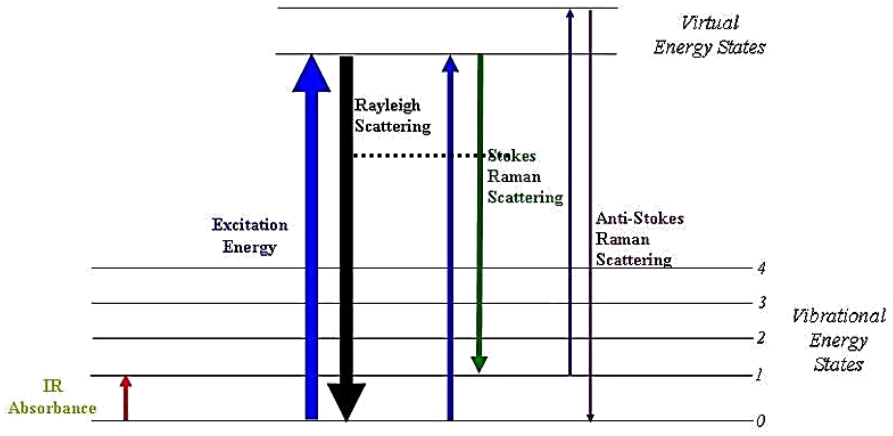

Figure 2.1-8. Diagram of the different possibilities of light scattering: Rayleigh, Raman (stokes and anti-stokes) [10]

Unlike in absorption spectroscopy, Raman scattering does not require matching of the incident radiation to the energy difference between the ground and excited states of the

molecule. The inelastically-scattered light (I_R), may lose (Stokes) or gain (Anti–Stokes) energy during this interaction. The emitted photon contains information about the molecular structure of the sample. When the scattered light has the same energy as the incident light the scattering it is elastic and termed Rayleigh scattering (Figure 2.1-8).

The Stokes radiation occurs at lower energy (longer wavelength) than elastic Rayleigh radiation, whereas anti-Stokes radiation has higher energy. The increase or decrease of the energy is related to the vibrational energy levels in the ground electronic state of the molecule, and as such, the observed Raman shift of the Stokes and anti-Stokes features are a direct measurement of the vibrational energies of the molecule.

Usually the spectrum is recorded only on the low-energy side to give Stokes scattering. Raman scattering should be expressed as a shift in energy from that of the exciting radiation and referred to as Δcm^{-1}, which in this work it will be simplified to cm^{-1} (Raman shift).

2.1.3.1 Resonance Raman

Resonance Raman (RR) exploits the effect of resonance enhancement of Raman scattering. If the wavelength of the exciting laser beam is within or close to the absorption band of an electronic transition of a molecule, the Raman scattered light is enhanced by several orders of magnitude (10^2 -10^4), providing a high degree of selectivity (Figure 2.1-9) Therefore, instead of exciting the molecule to a virtual energy state, it is excited to near one of its excited electronic transitions[237].

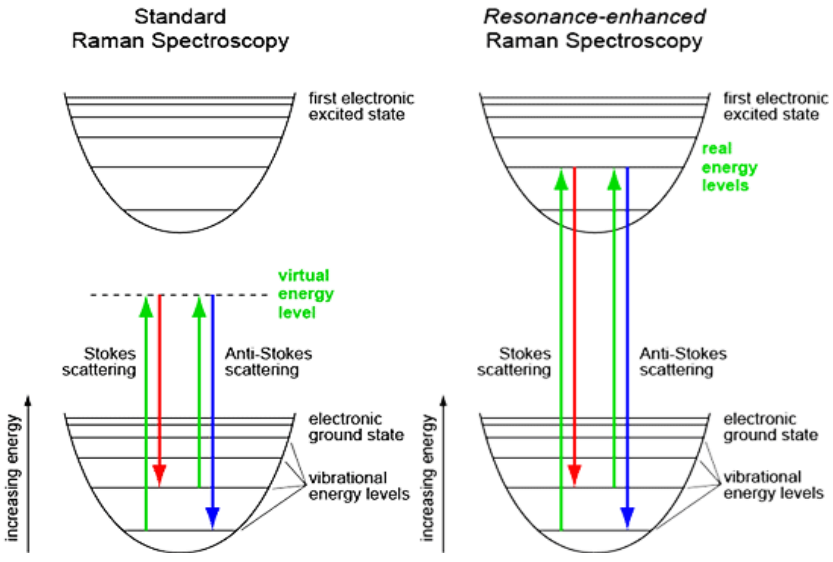

Figure 2.1-9. . Diagram of the Raman and resonance Raman scattering[7].

To obtain resonance Raman scattering, a laser beam is chosen which has an excitation frequency close to that of an electronic transition. Ideally, a tunable laser would be used for excitation and the frequency would be chosen to correspond exactly (or near) to the energy difference between the vibrational ground state and the first or second vibronic state of the excited state (Figure 2.1-9. left).

According to the first term of the denominator in equation 2-13:

$$\omega_{GI-}\ \omega_{L-i\Gamma_I}$$

The resonance condition is met when the energy difference between the lowest vibrational state of the ground electronic state *G* and the resonant vibronic state *I* (ω_{GI}) is of the same energy as the exciting light ω_L. In the resonance condition, almost all the interactions take place with one state. In this case the Σ sign in the KHD equation can be deleted, meaning that the resonance will depend only on the properties of this state [9, 10].

When absorption occurs, the energy may be lost either by transfer to the lattice and dissipation as heat or as fluorescence. The ratio of scattering to absorption is a property of the molecule and is difficult to predict. From a practical point of view, fluorescence interference limits the number of molecules which can be suitably studied by resonance Raman scattering. That is why it is important to choose and use the right setup to achieve the study of the molecule of interest.

Metalloproteins, carotenoids, chromophores in general and several other classes of biologically-important molecules have strong and allowed electronic transitions in the visible spectral range. The spectrum of chromophore moieties and their close environment is resonance enhanced in comparison to the surrounding structure. This allows the studies of a chromophoric site (often the active site) without spectral interference from the surrounding protein.

2.1.3.2 Resonance Raman spectrometer

RR spectrometers are dispersive instruments, based on grating units coupled to multi-channel detectors. Contemporary dispersive Raman spectrometers are equipped with silicon-based charge coupled device (CCD) multichannel detectors with a laser source operating in the ultraviolet, visible or near-infrared regions. A notch filter is used to block elastically-scattered light that would otherwise overwhelm the weak signal from the Raman or

inelastically-scattered photons (~ 1/106 scattered photons). The Raman scattered light may be dispersed according to the chosen wavelength.

Besides this, a typical micro-Raman system consists of a microscope, filters, slits, diffraction grating, necessary optics, detector and post-processing software (Figure 2.1-10). The laser light follows a path composed by neutral density (ND) filters and rejection filters. In the first stage of the system after passing through the spatial filter, which removes the higher order spatial modes so that the beam achieves a better focus, the light is directed to the microscope to focus on the sample. Scattered light from the sample is then collected by the objective and directed to the spectrometer.

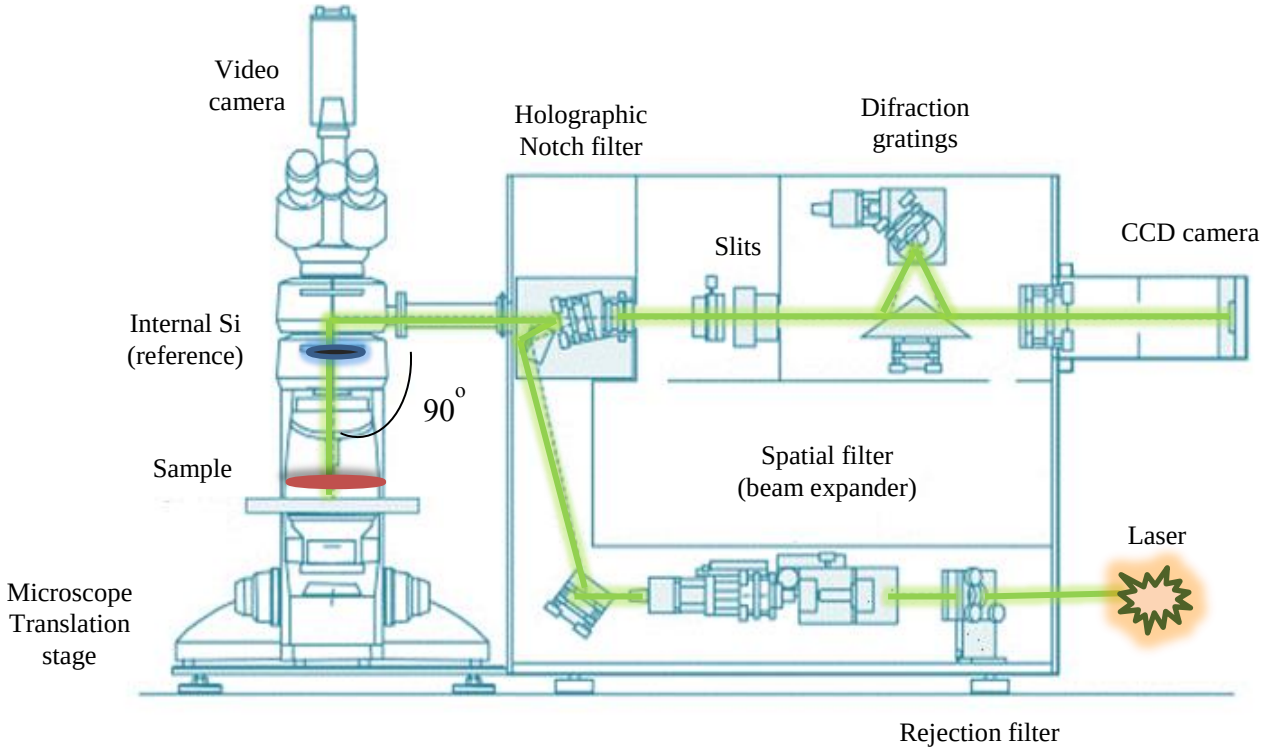

Figure 2.1-10. Scheme of a resonance Raman spectrometer (dispersive instrument)[9]

There are two basic geometries used for the collection of the Raman scattering: at 90° and 180°. For scattering spectra the 90° system is more suitable as the light can be scattered as a sphere forming a cone of light between the sample and the objective.

On the return path the elastically-scattered light is filtered by the holographic filter; these notch filters are designed to absorb all light of the frequency of the incident laser light.

Raman light is then separated by the diffraction grating into discrete wavelengths, where each of the scattered frequencies is measured simultaneously. When they arrive to the CDD, assuming a static scan is made, only a finite range of wavelength reaches the CCD via the diffraction grating. Photoelectrons are created in the CCD upon exposure to the scattered beam. The dispersed beam is spread vertically across horizontal lines of pixels, which are added, to integrate each signal. This electric signal is then processed by the integrated system software giving as a result the spectrum [10, 237].

2.2 Fluorescence Spectroscopy

Luminescence is described as the spontaneous emission of light from a substance. This phenomenon can be further divided in fluorescence and phosphorescence. Fluorescence is related to the excitation in a singlet state: an electron in an excited orbital become paired to a second electron in the ground vibrational state. As a consequence in returning to the ground state a photon is emitted. The average lifetime (τ) of a fluorophore can be defined as the time between the excited state and the return to the ground state (typically 10 x 10^{-9} s).

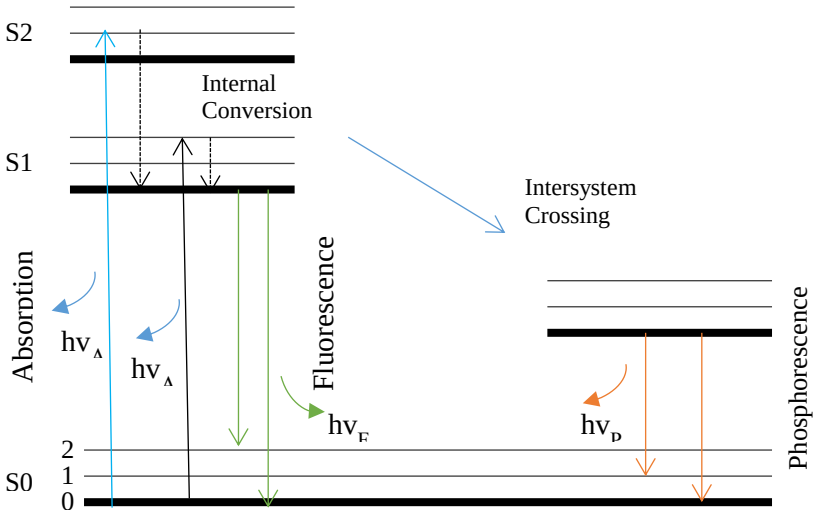

Figure 2.2-1. Scheme of a Jablonski diagram [11]

The process that occurs between the absorption and emission of light is usually illustrated by Jablonski's diagram. In Figure 2.2-1 it can be seen that in the ground state, the first and second electronic states are named as S0, S1, and S2, respectively. At each of these electronic energy levels the fluorophore can exist in a number of vibrational energy levels, named as 0, 1, 2, etc [11].

Following light absorption, several processes occur: a fluorophore is excited to some higher electronic level (S1 or S2). Molecules in a condensed phase rapidly relax to the lowest vibrational level of S1. This process is called internal conversion and generally occurs within 10^{-12} s or less and defines the fluorescence lifetime. The internal conversion is generally complete prior to emission; therefore, fluorescence emission results from a thermally equilibrated excited state, that is, the lowest energy vibrational state of S1.

The intensity, the position of the emission wavelength, and the lifetime are some of the properties that characterize a fluorophore. Fluorophore can be part of a molecule (intrinsic fluorophore) or added to it (extrinsic fluorophore). In the case of the proteins intrinsic fluorophores can be aromatic amino acids or cofactors [11].

Each fluorophore can have its own fluorescence properties. These properties are intrinsic to the fluorophore and can be modified according to the environment.

Aromatic amino acids as Trp, Tyr and Phe are responsible for the absorption and fluorescence of proteins in the UV range. Tryptophan is very sensitive to the local environment. The fluorescence of this amino acid in an environment with low polarity occurs at a maximum of 320 nm. Trp emission (intensity, polarization, and lifetime) can be a marker of changes in protein structure (folding or unfolding) and its environment (described by exciting the protein near the maximum approx. at 295 nm)[11]. Protein cofactors like flavin and quinone have been also shown to have fluorescence properties and several spectroscopic studies have been reported[40, 238-240]. Quinones show shifts in the UV-Vis and fluorescence spectra upon changes in redox state[238]. Flavins and flavoproteins have been shown to exhibit blue to green fluorescence under several different conditions[40], making this technique appropriate for spectroelectrochemical analysis of flavin-containing proteins, for instance, complex I.

In this work a setup described by Voicescu *et al.* [241] was adapted to perform spectroelectrochemistry studies. Figure 2.2-2 shows the optical pathway for the coupling of a steady state front-face fluorescence spectrometer with an electrochemical cell.

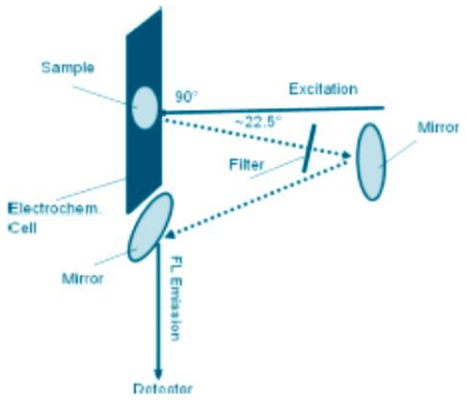

Figure 2.2-2. Optical pathway for electrochemically induced fluorescence analysis [241]

Fluorescence data are generally presented as emission spectra. A fluorescence emission spectrum is a plot of the fluorescence intensity versus wavelength (nanometers) or wavenumber (cm^{-1}). The emission spectra vary widely and are dependent upon the chemical structure of the fluorophore and the solvent in which it is dissolved, and the excitation wavelength to which it was exposed.

2.3 UV/Visible spectroscopy

While interaction with infrared light causes molecules to undergo vibrational transitions, the shorter wavelength, higher energy radiation in the UV (200-400 nm) and visible (vis) (400-700 nm) range of the electromagnetic spectrum causes many molecules to undergo electronic transitions. Electronic transitions occur when the energy from UV or visible light is absorbed by a molecule, where an electron jumps from a low energy to a high energy molecular orbital [8, 240]

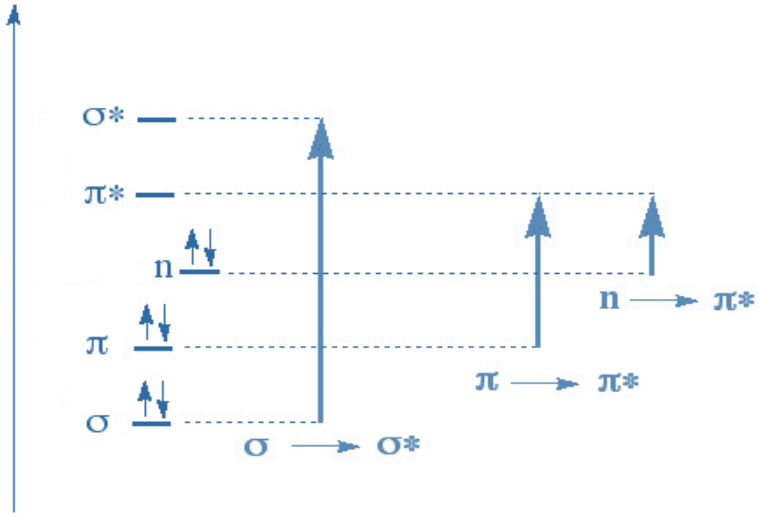

Figure 2.3-1. Scheme of the most common electronic transitions [8].

The differences in energy between orbitals depend on the atoms present and the nature of the bonding system. Most UV/vis transitions from bonding orbitals are based on n →π* or π→π* transitions, which occur across the UV/vis range related to unsaturated carbon functional groups. Distinctive absorption coefficients of n →π* transitions are below 100 $L.cm^{-1}.mol^{-1}$, while absorption coefficients of π→π* transitions exceed 1000 $L.cm^{-1}.mol^{-1}$ (Figure 2.3-1)[240].

One of the most basic applications of this technique is the use of the Beer-Lambert law to determine the concentration of a chromophore. This technique is also used easy to follow changes upon ligand binding. In addition, UV/vis can be used to do spectro-electrochemical studies

Through the spectra of redox proteins, the electrochemical properties of the cofactors present can be characterized. According to the absorption coefficient the peaks observed in the spectra can be assigned to specific structures, like flavin and Fe-S clusters; which have a distinctive absorption around 450 and 525 nm. Redox titrations monitored by UV/vis spectroscopy have proven to be a powerful technique to characterize redox properties of different kinds of cofactors inside proteins[215, 238, 242]. Spectroelectrochemical results are generally evaluated by fitting the resulting difference spectra from the titration with an equation that is a combination of the Lambert-Beer Law and the Nernst Law as described in previous studies (see section 3.2.5.1) [215, 242, 243].

2.4 Spectroscopy of small complexes, peptides and proteins

Information about structure, environment of amino acid side-chains, ligand, cofactors, and the changes in the protein backbone can be deduced from spectral parameters like band position, bandwidth and the absorption coefficient of the peaks present in a spectrum. The main signals that have been described in association with secondary structure of proteins and peptides are the amide bands. These bands are directly correlated to the polypeptide backbone vibrations. The principal amide contributions and their correlated vibrations can be seen in Figure 2.4-1.

Amide I, II and III bands can be found in Raman as well as IR spectra, but the out-of-plane motions in amide V, VI and VIII are only described for IR spectroscopy (Table 2.4-1).

In the case of IR spectroscopy the amide I region is the most commonly used to probe secondary structure of proteins, whereas in Raman spectroscopy it is amide III.

According to the frequency, the shape and the bandwidth of a peak, a deconvolution of this band can give the relative percentage of the secondary structure possible for peptides and proteins (Table 2.4-2). Many model compounds have been used to correlate between the position and the classification of secondary structure elements and their quantitative estimation, some of them are described by the studies of Kong and Yu[244], Goldberg and Chaffote[245] and Mikhonin *et al*[246] .

Table 2.4-1. Amide vibrations, frequencies and description of the peptide backbone (assignments are according to Kong[244] and Barth[247])

Amide	Wavenumber (cm-1)	Vibrations
A	3500-3200	ν(N-H), ν(O-H)
B	3200-3030	ν(C-H)
I	1700-1600	80% ν(C=O), ν(C-N), δ(N-H) and δ(CCN)
II	1590-1480	Coupled 60% δ(N-H) with ν(C-N), Coupled δ(C=O) and ν(C-C)
III	1400-1200	δ(N-H), ν(C-N), δ(C=O) and ν(C-C)
IV	780-650	δ(C=O) in- plane, ν(C-C)
V	600-540	δ(C-N) torsion
VI	540-500	δ(C=O) in-plane and out-of- plane (C-C-N) deformations
VII	290-250	δ (N-H) out-of-plane

Amide I. The amide I vibration arises mainly from the ν(C=O) vibration of the protein backbone. The fundamental mechanism that controls amide I sensitivity to secondary structure characterization is transition dipole coupling (TDC). The resonance of the interaction between the oscillating dipoles of neighboring amide groups and the coupling depends directly on their relative orientation and the distance between the groups. This coupling is stronger when the oscillators vibrate at the same frequency which consequently splits the resulting band in a wider shape and different frequency[245].

The advantage of using Amide I as marker for the characterization of secondary structure is based on the observation of the absorption coefficient of the backbone is so high that the band is barely affected by the nature of the amino acid side chain. On the other hand the principal disadvantage of following this band is that in the case of aqueous samples, the strong absorbance of water in the MIR spectral region (~1645 cm^{-1}) can overlap or modify the characteristics of the band, which is why samples dissolved in $^{2}H_2O$ can help in the confirmation of the assignments [244, 248]. Furthermore, the complementarity of IR and Raman spectroscopy can be a useful tool in the study of biological systems.

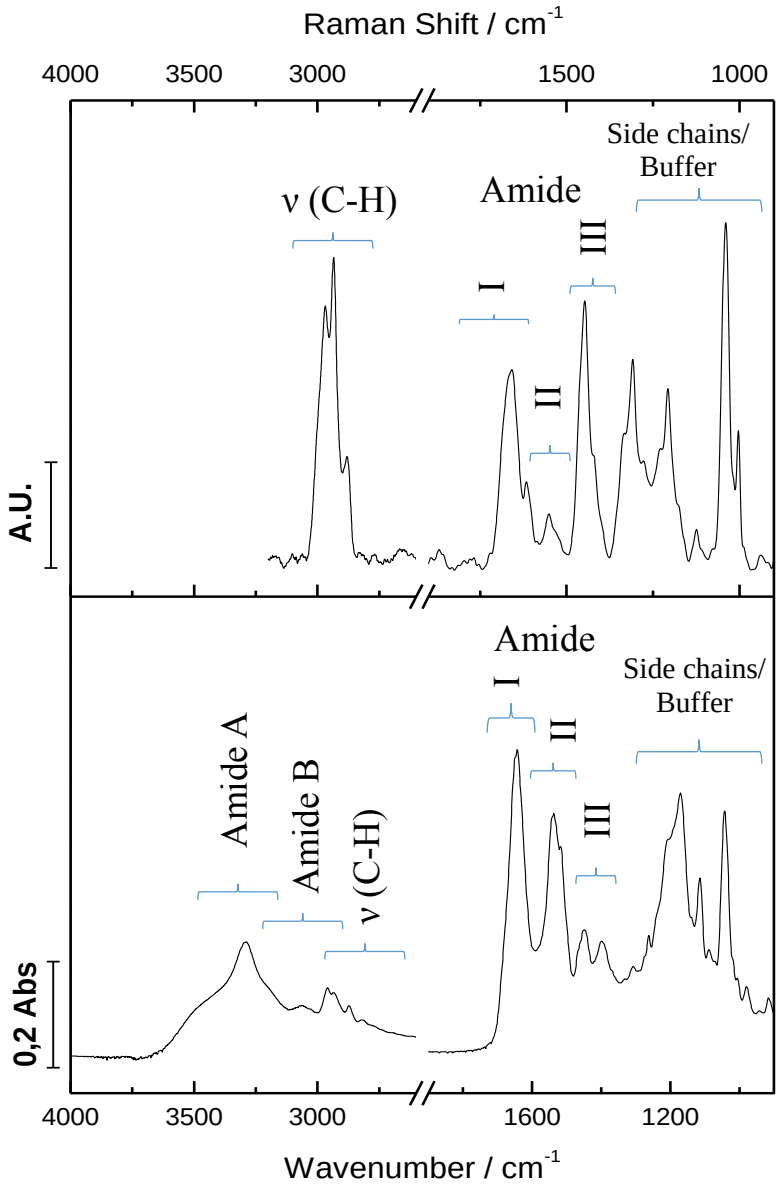

Figure 2.4-1. Vibrational modes in the mid frequency region of a metalloprotein (Complex I).

Table 2.4-2 Assignments of secondary protein structure motifs from the deconvolution of amide I (infrared) and amide III (Raman) [244, 246]

Amide I (Wavenumber/ cm^{-1})	Amide III (Raman shift / cm^{-1})	Assignment
1624-1642	1200-1240	β-sheet
1691-1696		
1648	1250-1270	Random coil
1655-1660	1280-1300	α-helix
1666	--	3_{10}-helix
1667-1685	1270-1280	β-turns

Amide II. This amide vibration is composed by the coupling of in-plane δ(N-H) and ν(C-N) with a small contribution from δ(C=O) and ν(C-C) modes. Some of the properties of this amide vibration is that it is hardly affected by amino acid side-chain contributions[247]; additionally it is sensitive to hydrogen deuterium exchange where the decoupling of in-plane δ(N-H) and ν(C-N) is excepted giving rise to the amide II' band. This amide II' is predominantly ν(C-N) and it arise around 1450 cm^{-1}, it might overlap with the H-O-D bending vibrations which is the reason why it is difficult to extract structural information from it[244]. On the other hand, amide II band may provide information on the accessibility of solvent to the peptide backbone.

Amide III. This is a complex band resulting from a mixture of several coupled modes (Table 2.4-1) The main advantage is that there is no water interference in this region in contrast to the amide I band. For IR it is possible to use the amide III region to determine protein secondary structure, but since the band has a lower absorption and is quite broad, it is hard to define specific characteristics from it. However, the amide III band in Raman spectroscopy is a better candidate for secondary structure studies due to its high scattering[249].

Shape, bandwidth and frequency of the amide III in a Raman spectrum depend on the Ramachandran dihedral angle (ψ)[13] (Figure 2.4-2). Raman spectra of model peptides have demonstrated that vibrations of individual peptide bonds are in general uncoupled [13, 246]; thus it may be possible to approximate protein Raman spectra as the linear sum of the spectra of individual peptide bonds. Due to this characteristics it is possible to correlate individual peptide bond Raman spectra to local secondary structure, an specific description of this assignment can be seen in Table 2.4-2[246].

.

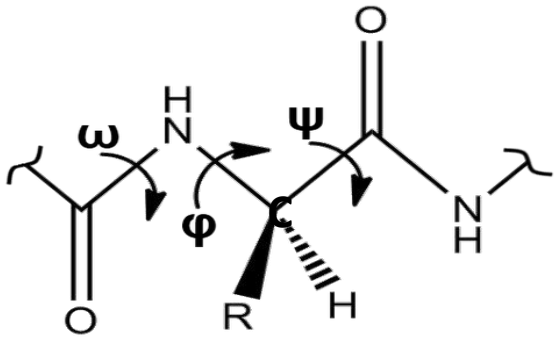

Figure 2.4-2. Ramachandran diagram of the ψ (psi), φ (phi), ω (omega) angles in a peptide bond[13].

In addition to the amide backbone vibrations, amino acid side chains can give rise to a considerable number of vibrations providing valuable information about protonation state, coordination and hydrogen bonding.

As an example, carbonyl group of Asp gives rise to an IR vibration around 1790-1710 cm^{-1}, when this group is hydrogen bonded this signal shift to lower frequencies[250]. Residues with aromatic ring as side chain can give rise to several vibrations; the protonation state of the His N atoms of its imidazole ring had been a subject of several studies[251], especially the correlation of these atoms with metal ions coordination or as binding partners with metal centers[135].

The environment provided by a protein can modulate the electron density and the polarity of bonds, thus changing the vibrational frequency and the absorption coefficient of the amino acid involved in the structure. A very well case of study is Tyr side chain where the deprotonation give rise to a signal with lower wavenumbers[250]. In Raman, this amino acid giving a Fermi doublet combination mode, which reported the ratio of the exposure to the solvent of this residue in the structure[252].

Furthermore, amino acid side chains vibrations are a helpful tool for the study of the mechanism of protein reactions as they are often involved in molecular reaction mechanisms, like allosteric mechanisms [253], enzymatic activity [254] and antibody recognition [255]. Due to the overlapping of many vibrations in the same frequency; site-direct mutagenesis [229, 248] and isotopically-labeled samples [233, 248, 256] can help to differentiate specific vibrations of interest. An example of this is a specific amino acid that forms a part of the metal coordination sphere within the protein structure. By site-direct mutagenesis the coordination of the metal can be perturbed and the function of specific amino acids function around the cluster can be determined. Furthermore, when working with synthetic peptides it can be a good choice to

add a labeled amino acid in the chain and in this way the attribution of the signals will be corroborated with the labeled amino acid.

2.4.1 The low frequency region.

For proteins, the low frequency region (below 1000 cm^{-1}) is characterized by in or out-of-plane amide vibrations (Table 2.4-1), bending vibrations of amino acids, metal-ligand vibrations (500-200 cm^{-1}) and the hydrogen bonding collective modes (Figure 2.4-3) (below 300 cm^{-1}). In the search for new methods for studying protein structure, conformational changes and the interaction between proteins and water this region represents an innovative challenge to characterize a variety of biological processes, ranging from photoisomerization events [166] to catalysis[113, 257].

Amide bands. The amide VI band was first described in the N-methylacetamide (NMA) model by Miyazawa *et al.*[258]. Recently it gained much more attention since it appears to be particularly sensitive to conformational changes and local environment. Amide VI (600-500 cm^{-1}) is mainly composed of out-of-plane C=O bending motions of the amide functional group and it is also composed of the contribution of in-plane and out-of-plane motions of the peptide backbone CONH groups[259]. Normal mode calculations described that the C=O in-plane bending mode (amide IV) is significantly mixed with the modes that give rise to the amide VI band.

Several studies of model compounds and proteins have shown the relation between secondary structure and the amide VI band[258, 259]. In polyamide-containing polymers the amide VI band appears at 580–590 cm^{-1}. Studies also indicated that the band position depends whether the molecule is in solution or in the crystalline form [260]. Latest studies have used this band as a marker in conformational changes upon metal binding [261, 262] and to describe protein-ligand interactions [263].

Metal-ligand vibrations. Detailed analysis of metal-ligand bond properties by means of vibrational spectroscopy is very useful; many proteins have metal centers, which act as cofactors or metal binding sites. The FIR absorbance spectra of several iron-sulfur proteins have been recorded (Figure 2.4-3)[264], with recent reports on proteins and related models showing that vibrational spectroscopy in the FIR domain is a promising technique [262, 265, 266].

The study of these sites and their redox states can provide information on metal-ligand bond properties and even characterize metal sphere coordination in proteins[267, 268].

Furthermore, RR spectroscopy selectively enhances the metal-ligand vibrations which lead to better resolve the resulting bands[269-271]. The complementarity of both, FIR and RR techniques gives an extended field to study metalloproteins.

Hydrogen bonding. The region below 300 cm^{-1} (Figure 2.4-3) includes information about the tertiary structure of proteins. Most of it is the collective mode of hydrogen bonding. The dynamics of the collective modes have been described to arise as a consequence of anharmonic interactions with other molecular normal modes[272] . Collective vibrational modes are distinct from the familiar MIR vibrational modes, which in general involve the motion of only pairs or small groups of molecules, these modes involve the collective motion of entire subunits of the protein with 50–100 atoms moving in an integrated set [260].

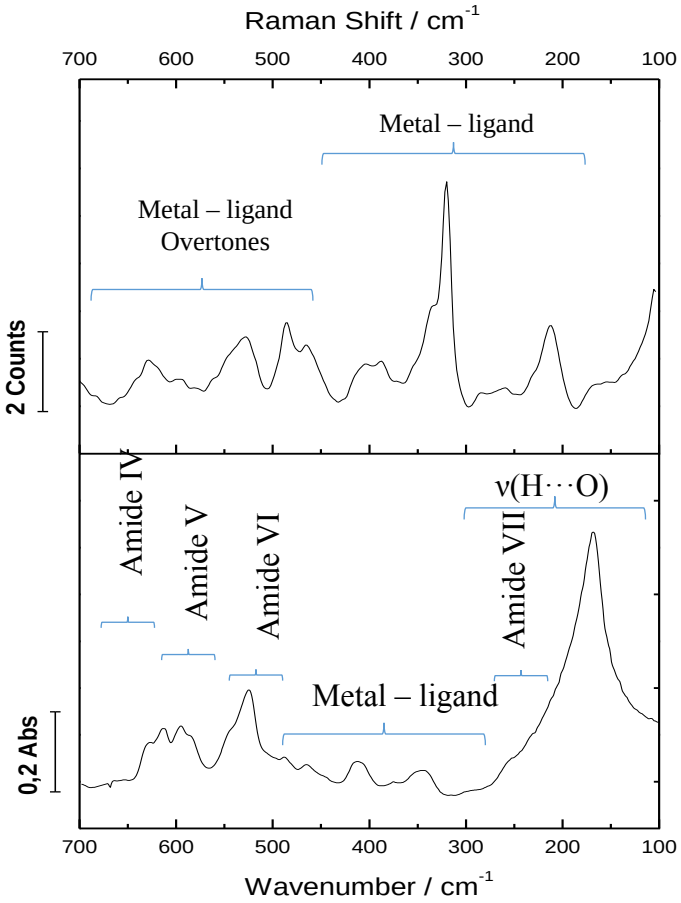

Figure 2.4-3. Vibrational modes in the low frequency region of a metalloprotein (Complex I)

So far, only a few studies, mainly computational studies[273], have described the relation of these collective modes to protein interactions. These vibrations are especially sensitive to the spatial structure of molecules and to intermolecular interactions. Structural elements like α-helices and β-sheet-folds are defined and stabilized by their unique pattern of hydrogen bonds.

The frequency and broadness of the signals depend on the polarizability of the hydrogen bonding features. This includes the contribution of the inter– and intra–molecular hydrogen bonding H…O and H…N stretching vibrations within a protein or with water molecules present in the environment[272]. Besides the contribution from the intra and intermolecular hydrogen bonding of proteins, the collective motions include also contributions from water chains within proteins and the hydration shells[272].

3 MATERIALS AND METHODS

3.1 Sample Preparation

Complex I and the NADH dehydrogenase fragment from *E. coli*, and the NuoEF subcomplex from *A. aeolicus* were prepared in the laboratory of Prof. Dr. Thorsten Friedrich, at the Institute for Biology, Albert-Ludwigs-Universität, Freiburg, Germany.

The sample preparations of PDZ1-MAGI-1, the wild-type (WT) and all the mutations were carried out in the laboratory of Prof. Dr. Gilles Travé, Oncoproteins team, in the Institut de Recherche de l'Ecole Supérieure de Biotechnologie, Unit "Biotechnology and Cellular Signaling, University de Strasbourg, Illkirch; in collaboration with Dr. Juan Ramirez and Dr. Yves Nominé.

The Aβ16, DAHK and GHK samples were obtained from the collaboration with laboratory of Prof. Dr. Peter Faller, Laboratoire de Chimie de Coordination, Université de Toulouse; and Prof. Dr. Pierre Dorlet, Laboratoire du Stress Oxydant et Détoxication, Gif-sur-Yvette, France.

3.1.1 Complex I Preparation

All the steps were made according to the protocol of Pohl *et al.* [274], where cell growth was followed by the preparation of the cytoplasmic membranes and then a two-step purification process to obtain the complete Complex I.

Cell culture. Competent cells from the *E.coli* strain ANN0221 (derivative of strain AN387) [275], were transformed with pBAD*nuo*/His-*nuoF* in a pre-culture of 50 mL of YP medium, which 16-20 hours of growth were transfer to a cell culture and grown anaerobically in a 200L fermenter or a 250mL culture in 1L conical flasks with YP medium at 37^{o}C. They were grown until the cell culture arrived out the stationary growth phase; the expression of the *nuo*-operon was induced with 0.2% (w/v) of L-arabinose after 1h. The cells were harvested by continuous flow centrifugation at 16000 g, at 4^{o}C and stored at -80 ^{o}C until further use.

Preparation of the Cytoplasmic Membranes. 30-40 g of cells (wet mass) were re-suspended in 4-fold volume of lysis buffer, composed of 50 mM MES/NaOH, 0.1 mM

phenylmethylsulfonyl fluoride (PMSF), 10 μg/mL DNAseI and 50 μg/mL lysozyme at pH 6.0. This solution was passed through a French pressure cell (SLM Aminco) at 110 MPa to disrupt the cells. All the steps were performed at 4°C. To remove the cell debris a centrifugation at 36000 g for 20 min was carried out, and the latest the cytoplasmic membranes were obtained by centrifugation at 250000 g for one hour. Membranes are collected are re-suspended in buffer (50 mM MES/NaOH , 50 mM NaCl, 5 mM $MgCl_2$ and 100 μM PMSF at pH 6.0), 1 mL was used for each g of membrane.

Detergent extraction. The re-suspended membranes were gently homogenized using a glass-Teflon homogenizer through several (3-4) cycles, incubating 15 min on ice in between each cycle; n-docecyl-β-D-maltoside (DDM) from 20% stock in water was added to the membrane suspension to a final concentration of 3%. After the last 15 min of incubation, the insolubilized material was removed by centrifugation at 250000 g for 20 min at 4°C.

Isolation of Complex I. All the steps were performed at 4°C. The supernatant obtained after the detergent extraction was applied to a 60 mL anion exchange chromatography column (Fractogel, EMD, Merck), that was previously equilibrated with 50 mM MES/NaOH, 50 mM NaCl, 0.1% DDM and 30 μM PMSF at pH 6.3.

The column was then washed with 35 mL buffer containing 50 mM MES 50 mM MES/NaOH, 150 mM NaCl, 0.1% DDM and 30 μM PMSF pH 6.0. The protein was eluted by applying 75 mL in a linear gradient of 150-350 mM NaCl with 50 mM MES/NaOH, 0.1% DDM and 30 μM PMSF at pH 6.0. This was performed at a flow rate of 6 mL/min. To select the fractions containing the protein of interest (Figure 7.1-A Appendix), NADH/ferricyanide oxidoreductase activity was measured (see section 3.1.5) and the fractions presenting activity were pooled for a later adjustment to a 20 mM imidazole concentration, by adding elution buffer composed of 50 mM MES/NaOH, 0.1% DDM and 500 mM imidazole, at pH 6.0.

The fractions pooled were loaded on to a 15 mL ProBond Ni^{+2}–IDA column (Invitrogen) that was previously equilibrated with 50 mM MES/NaOH, 200 mM NaCl, 20 mM imidazole, 0.1% DDM at pH 6.3, with a flow rate of 1.1 mL/min.

The column was then washed with the same buffer until the Abs_{280nm} decreased to the initial value. The protein elution was done at a flow the same flow rate with a step gradient from 20-500 mM imidazole with the elution buffer.

As for the previous steps, the collected fractions (Figure 7.1-B. Appendix) exhibiting NADH/ferricyanide oxidoreductase activity were pooled; washed with 50 mM MES/NaOH, 50 mM NaCl, and 0.1% DDM at pH 6.0 and concentrated by ultracentrifugation (100 kDa MWCO, Amicon Millipore). All the samples obtained were stored at -80^{o}C until further use. A resume of the yield in each step can be seen in Table 3.1-1.

Table 3.1-1. Isolation of *E. coli* Complex I from strain ANN0221 starting with 32 gr of cells (wet weight)

			NADH/ ferricyanide oxidoreductase activity		
Preparation	Volume [mL]	Protein [mg]	Total [μmol min^{-1}]	Specific [μmol min^{-1} mg-1]	Yield [%]
Membranes	12.5	545	2524	4.8	100
Extract	35	395	1796	4.5	79
Fractogel EMD	45.2	81	1301	16.3	53
ProBond Ni^{+2}-IDA	26.3	11	1196	113	42

3.1.1.1 Production and purification of Complex I variants

For the study of the variants, several mutations were studied in the NuoB subunit. All of them were prepared by the group of Prof. Dr. Thorsten Friedrich. Mutants of the three conserved Tyr on NuoB (Y139C, Y154H, Y114H and Y114H|Y139C) were generated by complementation of a chromosomal *nuoB* deletion strain with expression of nuoB from a plasmid as described by Flemming *et al.*[229] and carried out using the techniques in the studies of Flemming *et al.* [1] Mutations of the Glu (E67Q and E67D), were introduced together with the mutations of the Asp esidues D94N and D77N. The cells were grown and purified according to the protocol described above for the WT and stored at -80^{o}C for further use, with the same buffer conditions and concentration.

3.1.2 NADH dehydrogenase Fragment (NDF) preparation.

NDF was prepared according to the steps described by Bungert *et al.* [276]. Cell transformation, growth and induction were followed by a two-steps purification process.

Cell culture. Competent cells of the *E. coli* strain BL21 (DE3) (AGS, Heidelberg) [277] were transformed with pET-11a/*nuoB*-*G*/$NuoF_c$. This construct contained *nuo*B-G with a *Strep*-tag II coding sequence on the C-terminal of NuoF. All the cells were grown at 37^{o}C. A pre-culture was grown aerobically in a 1000 mL flask containing 250 mL of LB medium

until the optical density (OD) at λ=600 nm was 2 (10-12 hours). The resultant transformed cells of this pre-culture were grown in a 10 L LB culture in a fermenter of also LB medium under anaerobic conditions with 100 μg/mL of ferric ammonium citrate, 100 mg/L ammonium sulfate, 50 mg/L riboflavin and 0.5 mM of L-cysteine [207]. After the cell culture reached an absorbance between 0.6-0.8 (λ=600 nm), the exponential growth phase, the *nuo*B-G operon was induced by Isopropyl β-D-thiogalactopyranoside (IPTG) at a final concentration of 0.4 mM. The cells were harvested after they entered the stationary growth phase (OD_{600}=2-3) by centrifugation for 10 min at 4000 *g*. Cell pellets were washed with 50 mM MES/NaOH at pH 6.0 and stored at -80°C until further use.

^{54}Fe isotopically-labeled cell culture. For the preparation of the isotopically-labeled sample of NDF the M9 minimum media was used [278] adding 40 mg/mL of tryptophan and casein 10% (w/v) to enhance up the growth [279]. To prepare the iron solution 9.5 mg of ^{54}Fe (Trace, Science International Inc.) was dissolved in 25% HCl with continuous agitation. The ^{54}Fe solution was sterilized and added to the culture followed by a pH adjustment to 6.5. The rest of the protocol was as previously described for the non-labeled sample.

Isolation of NDF. 20-40 g of cells (wet mass) were re-suspended in 80 mL buffer (~120 mL) containing 50 mM MES/NaOH, 50 mM NaCl, 30 μM PMSF and 5 mM dithiothreitol (DTT) at pH 6.0, traces of DNAseI and lysozyme were added to prevent degradation of the protein of interest. The cells were disrupted by passing them through a French pressure cell at 110 MPa. From this step the cell debris and the cytoplasmic membranes were removed by centrifugation at 250000*g* for 1 hour.

The supernatant obtained was loaded into a 250 mL anion exchange chromatography column (Fractogel, EMD, Merck); which was previously equilibrated with 50 mM MES/NaOH, 50 mM NaCl, 30 μM PMSF and 5 mM (DTT) at pH 6.0. After loading the column was washed with this same buffer until the absorbance at 280 nm decreased to the initial value. The elution was made with a 30 mL linear salt gradient from 50-300 mM NaCl. All the steps were carried at a flow rate of 5 mL/min. The fractions that presented NADH/ferricyanide reductase activity were pooled (Figure 7.2. Appendix) and concentrated by ultrafiltration (100 kDa MWCO, Amicon Millipore) until half of the volume was reached. After this the pH was adjusted to 6.6 with 0.2 M NaOH solution.

Table 3.1-2. Isolation of *E. coli* NDF strain BL21 (DE3) pET-11a/*nuoB-G*/NuoF$_c$ starting with 37 gr of cells (wet weight)

			NADH/ ferricyanide oxidoreductase activity		
Preparation	Volume [mL]	Protein [mg]	Total [μmol min^{-1}]	Specific [μmol min^{-1} mg-1]	Yield [%]
Cytoplasm	75	1250	2983	3.5	100
Fractogel EMD	46	315.5	1672	53	62
StrepTactin-Sepharose	13	21	1196	121	46

The sample was applied to a 10 mL affinity chromatography column (*Strep*-Tactin Sepharose. 0.4x1.6 cm IBA) that was previously equilibrated with 50 mM MES/NaOH, 50mM NaCl, 30μM PMSF and 5mM (DTT) at pH 6.6 at a flow rate of 0.8 mL/min. The protein was aluted at the same flow rate with 2.5 mM D-Desthiobiotine in 50 mM MES/NaOH, 50 mM NaCl at pH 6.0. The fractions with NADH/ferricyanide (Fe-CN) reductase activity (Figure 7.2. Appendix) were pooled and concentrated by ultrafiltration (100 kDa MWCO, Amicon Milipore) and frozen with liquid nitrogen and preserved at -80^{o}C for further use. A resume of the yield in each step can be seen in Table 3.1-2.

The unlabeled and the ^{54}Fe NDF were purified with the same protocol.

3.1.3 NuoEF preparations

NuoEF was prepared according to the steps described by Kohlstädt *et al.*[280]. The cell transformation, growth and induction were followed by a three-step purification process.

Cell culture. Competent cells of the *E. coli* strain Rosetta(DE3)pLacI (Merck Biosciences, Nottingham) were transformed with the construct pETBlue-1/*nuoEF*His*G* and the cell growth for protein production was performed as described for NDF. After the harvest, the cell pellet was washed with 50 mM MOPS/ NaOH, 50 mM NaCl, pH 7.0, and stored at -80°C for further use.

Isolation of NuoEF. Between 10-15 g of cells (wet mass) were re-suspended in 30 mL 50 mM MOPS/NaOH, 200 mM NaCl, 20 mM imidazole and 30 μM PMSF at pH 7.0, traces of DNAseI were added to prevent degradation of the protein of interest. The cells were disrupted by passing through a French pressure cell twice at 110 MPa. The obtained suspension was centrifuged at 184000 g for 1h10 min.

The recovered cytoplasmic fraction (supernatant) was loaded into a 10mL affinity chromatography column (Probond Ni^{+2}-IDA 16mm x 50mm) equilibrated with 50 mM MOPS/NaOH, 200 mM NaCl, 20 mM imidazole, 30 μM PMSF,pH 7.0, at a flow rate of 1.5 mL/min. The column was then washed with the same buffer containing 100 mM imidazole until the absorbance at 280 nm decreased to the initial value. The protein was eluted using a 40 mL linear gradient from 100-500 mM imidazole at the same flow rate. The fractions that presented NADH/ferricyanide oxidoreductase activity were pooled (Figure 7.3-A appendix) and concentrated by ultrafiltration (30 kDa MWCO, Amicon Milipore) with a final volume of 500 μL.

Table 3.1-3. Isolation of NuoEF from *A. aeolicus* with the strain Rosetta (DE3)pLacl/pETBlue1NuoEFhis from 25 g of cells (wet weight)

			NADH/ ferricyanide oxidoreductase activity		
Preparation	Volume [mL]	Protein [mg]	Total [μmol min^{-1}]	Specific [μmol min^{-1} mg-1]	Yield [%]
Cytoplasm	59	701	2860	4	100
Probond Ni^{2+} – IDA	19	93	231	2.1	8
Superdex 200	8	19	98	5.1	4
Source 15Q	4	13	40.7	3.8	2

This sample was washed with 50 mM MOPS/NaOH and 150 mM NaCl at pH 7.0 and applied to a size exclusion chromatography (GeFi Superdex 200 16/60), that was previously equilibrated with the same buffer at a flow rate of 1 mL/min; the protein eluted approx. at 73 mL. At approx. 82 mL (Figure 7.3-B Appendix) a second peak was detected; this was attributed to an inactive form of the protein. To ensure the purity grade of the protein, fractions with NADH/ferricyanide oxidoreductase activity were pooled and a second size exclusion chromatography was performed (Figure 7.3-C Appendix) that showed a homogeneous peak at 73 mL approx. for the protein. The sample was concentrated by ultrafiltration (30 kDa MWCO, Amicon Millipore), and preserved at -80^{o}C for further use. A resume of the yield in each step can be seen in Table 3.1-3.

3.1.3.1 Production and purification of NuoEF variants

The plasmids pETBlue-nuoE_his_6F and pETBlue1-nuoEFhis were used as templates for site-direct mutagenesis to generate three new expression plasmids; three new plasmids

were produced containing mutations on NuoE: two single mutants (V90P and V136M), and a double mutant (V90P/V136M).

The cell growth and the isolation process were carried out as described before for the wild type. NuoEF variants V90P^{E}, V136M^{E} and V90P/V136M^{E} behaved equally throughout purification and no significant differences were seen in the chromatograms. Protein activity was always tracked by the NADH/Ferricyanide oxidoreductase assay and SDS-PAGE of purified samples indicated the presence of the two subunits forming the heterodimer, NuoE and NuoF.

The yield of the preparation was calculated for each variant by determining the amount of produced protein and its activity, described in Table 3.1-4 for V90P/V136M^{E}.

Table 3.1-4. Isolation of V90 P/V136M^{E} NuoEF variant strain Rosetta (DE3)pLacI/pETBlue1NuoEFhisV90P/V136M^{E} from 26 g of cells (wet weight)

			NADH/ ferricyanide oxidoreductase activity		
Preparation	Volume [mL]	Protein [mg]	Total [µmol min^{-1}]	Specific [µmol min^{-1} mg-1]	Yield [%]
Cytoplasm	160	1536.0	2860	3.1	100
Probond Ni^{+2} – IDA	12	49.2	489.6	9.9	10
Superdex 200	8	26.4	342.4	12.9	7
Source 15Q	6	16.2	279.6	17.5	6
Superdex 200	8	12.6	256.8	20.7	7

3.1.4 Quinone reductase fragment (QRF) preparation

The QRF fragment was prepared by the group of Prof. Dr. Thorsten Friedrich. This protein, consisting of all complex I subunits but NuoE, F and G, was obtained by alkaline treatment of the complex as previously reported[171]. The samples were washed by ultracentrifugation (50 kDa MWCO, Amicon Milipore) with 50 mM MES/NaOH, 50 mM NaCl and 0.5% DDM and stored at -80^{o}C in aliquots for further use.

3.1.5 Determination of NADH/ferricyanide oxidoreductase activity

To determine the enzymatic activity of the samples the reduction of ferricyanide by NADH was followed at λ=410 nm at room temperature, according to the assay described by Friedrich *et al.* [184]. The assay was performed in a 1cm x 1cm cuvette with a final volume of 1

mL containing 50 mM MES/NaOH, 50 mM NaCl, 1 mM $K_3[Fe(CN_6)]$, 0.2 mM NADH, pH 6.0 with 5 µL of the sample . The molar absorption coefficient of $K_3[Fe(CN_6)]$ (ε_{410} = 1 mM^{-1} cm^{-1}) was used along with the equation of Lambert-Beer law to determine the NADH/ferricyanide oxidoreductase activity in units of µmol min^{-1} mL^{-1} (U/mL).

3.1.6 CuA*β*16, DAHK and GHK

For the A*β*16 peptide, labeled and unlabeled samples will be studied for data analysis. The labeled samples included the ^{15}N labeling of His6, His13 and His14, and ^{13}C ^{15}N labeling for the Asp1 residue. Unlabeled A*β*16 peptides were purchased from Genecust (Dudelange, Belgium). The labeled amino acids were purchased from Eurisotop (St-Aubin, France) and sent to GENEPEP (Prades-le-Lez, France) for synthesis of the labeled peptides. Asp1 and His6 labeled are 97% pure and the His13 and His14-labeled to 95%.

GHK (Gly-His-Lys) peptide was bought from Bachem (Bubendorf, Switzerland). DAHK (Asp-Ala-His-Lys) peptide was bought from Bachem (Switzerland) or GeneCust (Dudelange, Luxembourg).

All the peptides were dissolved in pure water or in ^2H_2O to a final concentration of 5 mM. For spectroelectrochemistry experiments 10 µL of the peptide was mixed with $CuCl_2$ in 100 mM of phosphate buffer (pH 6.8/ pH 8.9) with 150 mM KCl. $CuCl_2$ was added in equimolar concentration (1:1) from a stock of 100mM $CuCl_2.2H_2O$ (Riedel−de Haën) dissolved in distilled water or ^2H_2O. Following the addition of $CuCl_2$ the pH (pD) was adjusted using HCl (DCl) or NaOH (NaOD). The samples were studied at pH 6.8 and 8.9.

3.1.7 PDZ1-MAGI-1 preparations

The preparation of the PDZ1 domain of MAGI-1 was done according to the steps described by Charbonnier *et al* [55] and Fournane *et al* [281] . The cell culture for overproduction of the protein was followed by a three steps purification process.

Cell culture. PDZ1 from MAGI-1 was overexpressed with *E. coli* strain BL21(DE3), transformed (heat shock) with the construct pETM41/His-6-MBP-SeqTEV-PDZ1. All cells were grown at 37°C. A 25 mL pre-culture was grown aerobically in a 200 mL flask containing

LB medium under continuous stirring at 230 rpm, until the optical density (OD) at λ=600 nm was 2 (overnight).

The pre-culture was added to 500 mL LB medium and kanamicina (30 mg/mL) in a 2 L flask. The culture was incubated and shaken (230-340 rpm) at 37^{o}C until the culture reached the exponential growth phase with an optical density between 0.6-0.8 (λ=600 nm). For the induction IPTG was added with a final concentration of 0.5 mM is added, and the culture was incubated at 15^{o}C (16 hours). The cells were harvested by centrifugation, and the pellets flash frozen in liquid nitrogen and stored at -80^{o}C until further use.

Isotopically labeled ^{15}N and ^{13}C cell culture. For the preparation of the isotopically labeled sample of PDZ1, M9 minimum media was used [278]. In the case of ^{15}N labeled cell culture $^{15}NH_4Cl$ was added as a nitrogen source, and in the case of ^{13}C labeled cell culture 1g/L of $^{13}C_6$ glucose (Isotec Inc.) was added as a carbon source.

Isolation of PDZ1. The cells obtained were re-suspended into a 40 mL of a "lysis" buffer containing 100 µL DTT (0.5 M), 12.5 µL DNAse (10 mg/mL), 12.5 µL RNAse (10 mg/mL), dissolved in buffer A: 50 mM Tris, 1 mM DTT, anti-protease cocktail (EDTA free) (Roche) and 200 mM NaCl pH 6.8. All steps were carried out at 4^{o}C. The cells were disrupted by sonication of a 1min pulse, followed by centrifugation at 16000*g* for 1h.

The supernatant was then filtered (Micropore 30 kDa MWCO) and loaded onto a 40 mL amylose agarose resin (New England Biolabs) that was previously equilibrated with buffer A at a flow rate of 1.5 mL/min. The column was then washed with the same buffer until the absorbance at 280 nm decreased to the initial value followed by the elution with buffer A containing 10 mM maltose. The fractions composed of the peak eluting at the same flow rate as before were pooled. This fraction corresponds to MBP-PDZ1. The MBP tag was removed by proteolitic cleavage with recombinant TEV protease at 8^{o}C, during 16 hours.

To remove the His6-MBP and the His-6 TEV, the digestion mix was loaded three times on a 2 mL Ni-NTA resin (Qiagen) that was pre-equilibrated with buffer A. The flow-through obtained was concentrated by ultrafiltration (5 KDa MWCO, Amicon Milipore) to a final volume of 2 mL.

The 2 mL obtained were applied to a size exclusion chromatography column (gel filtration, Hiload 16/60 Superdex 75, Amersham Bioscience) equilibrated with 20 mM Sodium Phosphate buffer, 1 mM DTT and 200 mM NaCl at pH 6.8. The protein eluted with the same buffer at approx. 65 mL. To verify the quality of the purification a SDS-PAGE (Figure 7.1-4) containing each one of the steps and the last pool fractions was carried out. The protein obtained was washed with 20mM phosphate buffer, 1 mM DTT and 50 mM NaCl, separated in 50 µL aliquots and kept at -80^{o}C.

3.1.7.1 Production and purification of PDZ1 domain variants

The following mutants of PDZ1-MAGI-1were cloned into the pETM-41 vector named above, PDZ1 K44/A, PDZ1 K44/E and PDZ1S113G| L114G|V115G hereafter named PDZ1 GGG.

The cell growth and the isolation process were carried out as described before for the WT (Section 3.1.7). PDZ1 variants SLV/GGG, K44E and K44A behaved equally throughout purification and no significant differences were seen in the chromatograms; the results of each purification step is seen in the SDS-PAGE, Figure 7.1-4 Appendix.

3.1.7.2 Synthetic peptides

Five synthetic peptides (Table 3.1-5) corresponding to C-terminal (ct) residues of HPV16 E6, were synthesized by P. Eberling (Chemical Peptide Synthesis Service, IGBMC, Strasbourg). Trifluoroacetic acid (TFA) was removed by lyophilization and HCl treatment as previously reported [282, 283]. Peptides were re-suspended in 20 mM Sodium phosphate buffer with 1 mM DTT and 50 mM NaCl, at a final concentration between 15-20 mM.

Table 3.1-5 Peptides originated from the viral oncoprotein sequence HPV16E6. (Mutated residues of 16E6$_{ct}$ are underscored in bold)

Name	No of residues	Sequence
16E6	11	RSSRTRRETQL
16E6 L_0/V	11	RSSRTRRETQ**V**
16E6 R_5/A	11	RSSRT**A**RETQ**V**
16E6$_{ct}$6 L_0/V	6	RRETQ**V**
16E6$_{ct}$5 L_0/V	5	RETQ**V**

3.1.7.3 The MAGI-1 PDZ1/16E6 complex

To follow the formation of the complex by spectroscopic techniques (RR and IR) a titration at different concentration ratios (1:1; 1:2; 1:3 and 1:6) of the PDZ1 domain with the 16E6 peptide was made. To make sure the frequencies observed were due to complex formation, the spectrum of PDZ1 and the 16E6 peptide, they were first measured alone. The ratio of 1:2 (PDZ1: peptide) was chosen to do the rest of the experiments.

3.2 Spectroscopy

UV/Visible and fluorescence spectroscopy were used for titrations of the cofactors of interest, whereas infrared and RR were used for more detailed protein analysis. Absorption with an attenuated total reflectance unit (ATR) and scattering spectra was used in frozen samples and samples in solution. For spectroelectrochemistry measurements a thin layer electrochemical cell was adapted to each one of the spectroscopic techniques with some variations according to the equipment and the frequencies studied as described below.

3.2.1 Spectroelectrochemistry

For the electrochemistry experiments an ultrathin layer cell was used to follow the spectroelectrochemical changes upon reduction and oxidation. This cell was designed by Moss *et al.* [14] and consists of a three-electrode system (Figure 3.2-1). In the PVC cell body with four inlets, the first one (a) is to provide contact with a gold grid (30 x30 μm mesh width, optical transparency of 55%, from Goodfellow, SARL, France), used as a working electrode. The second inlet (b) it was used to screw a contact with a platinum film used as counter electrode. The third inlet (c) was used to insert a Ag/AgCl 3M KCl reference electrode (+208 mV for SHE') (Figure 3.2-1). The fourth inlet (d) was used to add the same buffer were the sample is dissolved with the objective to provide connectivity between the electrodes after the cell is closed.

All the electrodes were connected to a potentiostat which regulates the potential applied to the working electrode. The gold grid, as the working electrode was chemically-modified with a solution containing 1 mM cysteamine and 1 mM 3-mercaptopropionic acid (3-MPA). The grid was immersed in the solution containing the modifiers for at least one hour before use at room temperature. These thiol-based compounds form a self-assembled monolayer of $–COO^-$ and $–NH_3^+$ groups that electrostatically interact with the protein [14] (Figure 3.2-2). Before adding the sample, the grid was washed with distilled water to remove

the non-covalently bound thiols and placed on the window. For each sample a new gold grid was used.

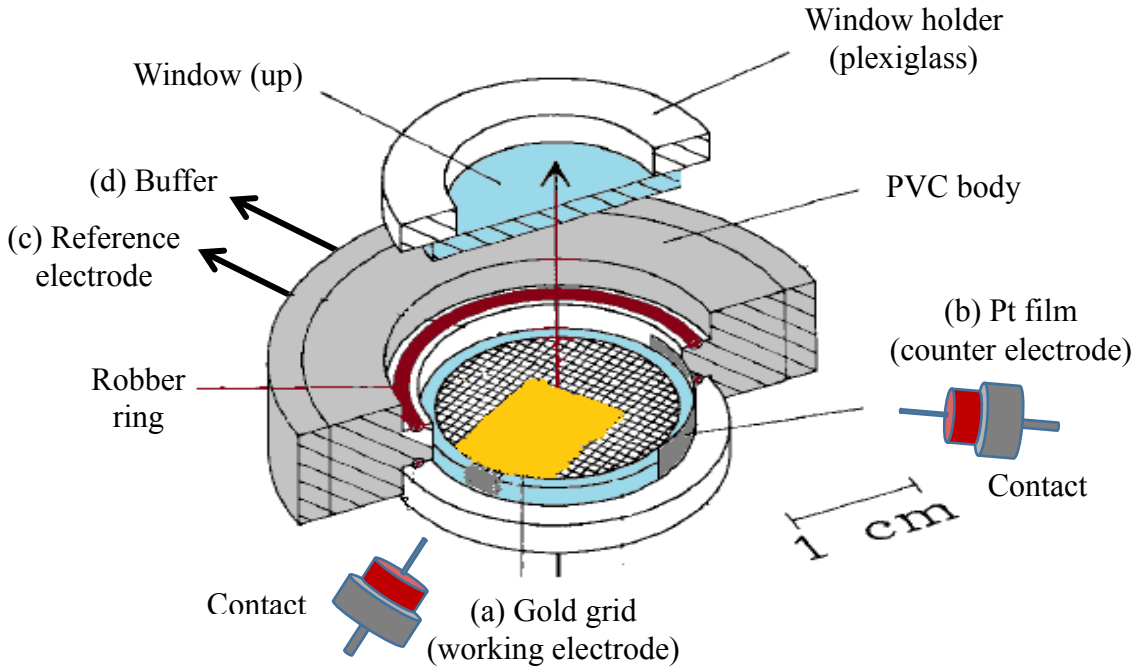

Figure 3.2-1. Diagram of the spectroelectrochemical cell and the different components. Adapted from Moss *et al* [14]

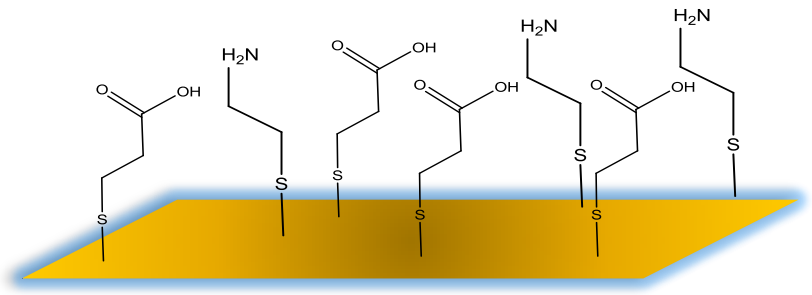

Figure 3.2-2 Schematic representation of the gold grip modification with cysteamine and 3-MPA

For studies in different spectral ranges a different set of window was used, for which the specifications are described in Table 3.2-1. For all electrochemical cells, the same thickness was used for both windows with the exception of RR where the working electrode was positioned on the polyethylene window (down) and was covered with a CaF_2 window (up).

Table 3.2-1. Windows characteristics according to each spectroscopic technique

Technique		Material	Thickness
Infrared	Mid (4000-800 cm^{-1})	CaF_2	4 mm
	Far (700-50 cm^{-1})	Si	2 mm 1 mm
Resonance Raman		CaF_2 Polyethylene	2 mm 1 mm
Uv/Visible		CaF_2	4 mm
Fluorescence		Quartz	4 mm

Table 3.2-2. List of the 19 mediators used for electrochemistry

Mediator	E_m(mV) vs. Ag/AgCl (3M KCl)	Source	Solvent
Ferrocenylmethyltrimethylammoniumiodide	607	Stern chemicals	Ethanol
1-1-ferrocenedicarboxylic acid	436	Fluka	Ethanol
Potassiumhexacyanoferrate (II) trihydrate	212	Riedel-de-Haën	Water
1-1-dimethlyferrocene	133	Sigma Aldrich	Ethanol
Quinhydrone	70	Fluka	Ethanol
Tetrachloro-1.4-benzoquinone (*p*-Chloranil)	72	Sigma Aldrich	Acetone
N,N,N,N-Tetramethyl-p-phenylenediamine dihydrochloride	62	Fluka	Water
2,6-dichlorophenolindophenol sodium salt hydrate	9	Biochemika	Ethanol
Hexaammirythenium (III) chloride	-8	Sigma Aldrich	Water
Anthraquinone-2-sulfonic acid sodium salt	-23	Sigma Aldrich	Water
1.4 naphthoquinone hydrate	-63	Sigma Aldrich	Water
Trimethylhydroquinone	-108	Sigma Aldrich	Ethanol
Anthraquinone	-108	Sigma Aldrich	Ethanol
5-Hydroxy-1,4-naphthiquinone	-158	Sigma Aldrich	Ethanol
Duroquinone	-198	Sigma Aldrich	Ethanol
Menadione	-220	Sigma Aldrich	Acetone
2-Hydroxyl-1,4-napthoquinone	-333	Sigma Aldrich	Ethanol
9,10-Anthraquinone-2,6-disulfonic acid disodium salt	-433	Sigma Aldrich	Ethanol
Neutral red	-515	Sigma Aldrich	Ethanol
1,1-Dimethyl-4,4-bypyridium dichloride hydrate	-628	Sigma Aldrich	Water

Cofactors in proteins are usually embedded in the protein structure. To make sure that electron transfer between the protein and the electrode is ensured, a mixture of 19 mediators (Table 3.2-2) with a final concentration of 25 µM were added to the sample prior to the

electrochemical measurements. At this concentration, with a path length below 10 μm, no spectra contribution from the mediators could be detected as seen previously[241, 284, 285]. The mediators mixture covers a wide range of redox potential as described in the work of Baymann *et al.* [286]. To assure a complete mixture between the mediators and the sample, the mixture was incubated at 4°C during at least 30 min prior to the measurements.

For the electrochemistry experiments 10 μL of the mediators/sample mixture was deposited on the working electrode. The cell was closed and filled with buffer, achieving a pathlength between 6-8 μm. The potential applied to the protein studied for the oxidized (Ox) and the reduced (Red) state, as well as the equilibration time are shown in Table 3.2-3. The potentials are applied to the working electrode vs. a Ag/AgCl 3KCl reference electrode.

Table 3.2-3. Potentials applied for the electrochemistry of the different samples studied (Potential is expressed in mV vs. SHE)

Sample	Potential (mV)		Equilibration time (sec)	
	Ox	Red	Ox	Red
Complex I from *E. coli*	+200	-450/ -500	180	300
NDF from *E. coli*	+200	-450	180	300
NuoEF from *A. aeolicus*	+200	-200	180	240
CuA*β*16 CuDAHK CuGHK	+700	-300	180	180

For the samples in organic solvents, the body of the cell was made of Teflon, and the holders of the windows were made of aluminum. The reference electrode was replaced by a pseudo reference electrode which was filled with the solution of the quinone as relative reference and a platinum wire as a counter electrode, as described by Bauscher *et al* [287].

3.2.2 Infrared measurements

All infrared spectra were recorded on a FT-IR spectrometer (Vertex 70, Bruker optics). The infrared measurements were carried out in two different spectral ranges mid (4000-800 cm^{-1}) and far (700-50 cm^{-1}) infrared, according to the frequencies used different equipment were adapted to the spectrometer. The specifications are described in Table 3.2-4. Two different types of measurement were made; the absorption spectra were recorded in an ATR unit and spectroelectrochemistry in transmission mode.

Table 3.2-4. . Equipment used in the infrared measurement according to the different spectral range

Source	MIR		FIR	
	ATR	Electrochemistry	ATR	Electrochemistry
Spectral range (cm^{-1})	4000-800	2000-800	800-50	600-50
Source	Globar		Hg vapor / synchrotron	
Beamsplitter	KBr		Si / Mylar	
Detector	MCT		Bolometer	
Mirror velocity (KHz)	20KHz		2.5KHz	5KHz
Resolution (cm^{-1})	2	4	2	4
Scans	256	256	256	128

Attenuated total reflection (ATR). The principle of an ATR unit is shown in Figure 3.2-3. The ATR technique is used as a total internal reflection that generates an evanescent wave. A beam of infrared light passed through the ATR crystal, in this case diamond, reflecting several times on the internal surface in contact with the sample. These reflections form the evanescent wave which extends into the sample[288].

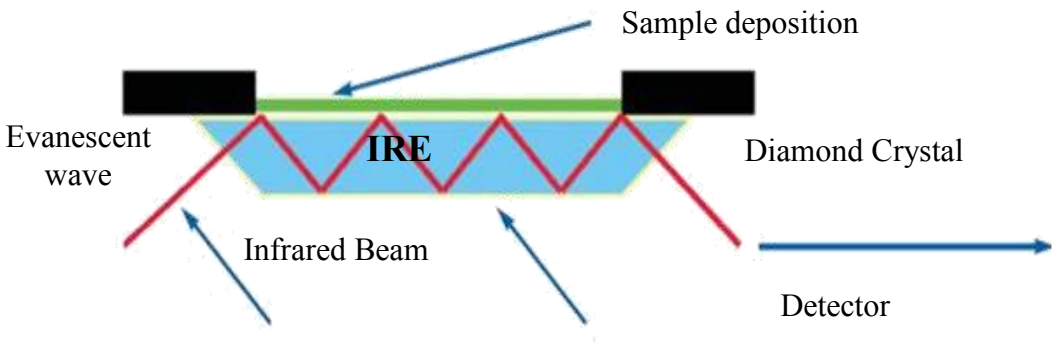

Figure 3.2-3 Scheme of an Attenuated Total reflectance unit.

The signal-to-noise ratio obtained depends on the number of reflections and on the total length of the optical path. Furthermore, it is important to consider that the evanescent effect is effective only when the crystal is made of an optical material with a higher refractive index than the studied sample[113].

The penetration depth of the evanescent wave is characterized by the distance (d_p) at which the intensity decays, this principle is described by the equation 3.1:

$$d_p = \frac{\lambda/n_1}{\sqrt{2\pi\left(sin^2\theta - \left(n_2/n1\right)^2\right)}}$$ Equation 3.1

Where λ: wavelength, n_1: refractive index of the IRE, n_2: refractive index of the sample and θ: angle of incidence[289].

The ATR unit used in this work is equipped with a diamond crystal (n_1), with an incidence of 45^o and samples dissolved in water (n_2) a penetration depth of 1.6 μm can be calculated with equation 3.1 (λ = 10^{-5} m), this value is typically between 0.5 and 2 micrometers. Normally between six and eight internal reflections are used, resulting in a total pathlength of about 10 μm.

This method had been applied to a wide range of proteins[248]. as proteins adsorb onto a surface, at saturating concentration forming a protein monolayer is a widely accepted notion[245]. Estimation of secondary structure following amide I and amide II had been widely studied and conformational changes due to different effectors proven[290]. Thus, this technique is an excellent tool to follow protein-protein and protein-metal interactions.

In this work for each experiment 3-4 μL of the sample was deposited on the diamond crystal and dried with argon at room temperature. The spectra obtained are the average of 20-30 spectra. Each measurement was repeated at least three times to assure reproducibility.

Synchrotron experiments. ATR-FIR spectra in the 600 − 0 cm^{-1} range were measured at 2 cm^{-1} resolution using a vacuum evacuated (10−5 mbar) Bruker IFS125 spectrometer of the FIR terahertz beamline AILES connected to the synchrotron source SOLEIL (L'Orme des Merisiers, Paris). The spectrometer was outfitted with a 6 μm Mylar beamsplitter and two different Si bolometer detectors (Infrared Laboratories, U.S.A.). The first bolometer, here named Bolometer1 allows recording the spectra in the range of 600-50 cm^{-1}, and the second one, Bolometer2, in the range of 80-0 cm^{-1}.

With Bolometer1 each final spectrum is the average of 5-10 spectra recorded with 128 scans at a mirror velocity of 80 KHz, while with Bolometer2 each spectrum is the average of 5-10 spectra recorded with 128 scans at 20 KHz. These measurements were performed with the aim of having an improved quality of the hydrogen bonding signature.

Spectroelectrochemistry. For each experiment approx. 30-40 cycles of oxidation and reduction (Ox ↔ Red) were performed. The final spectra were obtained by subtracting the reduced spectrum from the oxidized spectrum and at least 30 cycles were averaged. This was done in order to get a better insight of the protein function and to monitor structural changes upon reduction and oxidation. As can be seen in the Figure 3.2-4, the spectra of the oxidized and the reduced state are very similar, so in order to isolate the changes and follow the perturbations of the protein during the redox reaction more easily, the differential is calculated allowing in this way to have information of the process undertaken by the protein during both oxidation and reduction.

By this technique, specific vibrational modes that can be correlated to certain amino acid contributions, metal–ligand vibrations, changes in the secondary structure and even changes in the hydrogen bonding. In an oxidized - reduced (Ox-Red) spectrum, the positive signal will be correlated with the changes of the oxidized form and the negative signals with the reduced form. [14, 266, 272, 284]

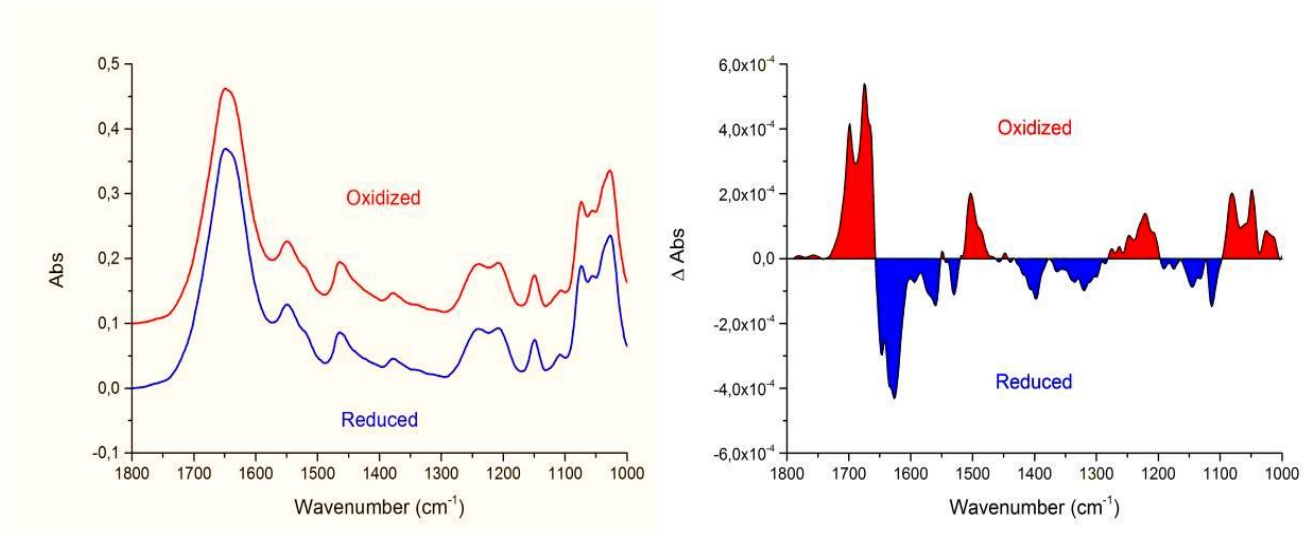

Figure 3.2-4. The absorption spectra in the oxidized and the reduced state follow by the differential. The positive signals correspond to the contribution in the oxidized state and the negative signals the contribution in the reduced state.

3.2.2.1 Study of the hydrogen bonding and secondary structure

In the study of the HPV16 E6 and its interaction with PDZ1 from MAGI-1, ATR measurements in the MIR and FIR were performed for each of the samples (see section

1.1.1.1) in H_2O and ^2H_2O. The samples were prepared according to what was explained in section 1.1.1.1.

In order to have a better understanding of the conformational changes in the secondary structure a deconvolution of Amide I was performed (1700-1600 cm^{-1}), the data was analyzed according to the method described by Venyaminov and Kalnin [291, 292]. After a baseline correction in the 1700-1590 cm^{-1} range, the second derivative of this curve was calculated, leading to negative peaks. The input from this calculations was taken as the parameters to perform a Gaussian fitting with a least-squares iterative correction[293].

Each resulting band was related to a given defined secondary structure element [294], and the calculation under the curve gave the approx. value (%) of each of these components inside the protein structure. The areas of all bands assigned to a given secondary structure were added and finally divided by the total area in order to obtain the contribution of each element. This was based on the assumption that the absorption coefficients in the amide I were equal for all the secondary structures [244].

3.2.2.2 Study of the metal-ligand vibrations

Fe-S Clusters. In the FIR spectral range, spectroelectrochemistry of NuoEF, NDF, ^{54}Fe NDF and Complex I was done at 5^{o}C to ensure the stability of the sample. The potential applied for the redox cycling was according to what was described in Table 3.2-3

Cu complexes. In the MIR spectral range, the electrochemistry of DAHK, GHK and Aβ16 in the presence of copper at pH 8.9 was performed. The electrochemical cell was kept at 15^{o}C to ensure the stability of the complex during the measurement.

3.2.3 Resonance Raman measurements

For all Raman measurements a Renishaw InVia Reflex Raman microprobe with a multi-wavelength facility and an excitation of 514.5 nm was used. A 100 mW argon ion laser is orientated normal to the sample. The detector is a charge-coupled device (CCD) device attached to a single spectrograph. Different holographic notch filters were used to reduce the interference of Rayleigh scattering with dual gratings on a kinematic mount (1800 and 2400 l/mm).

For the gratings scattered scan a 50x objective lens was used to focus the laser onto a 2 μm spot to collect the backscattered radiation. Approx. 150 points (20 μm^2 each) were mapped in order to ensure homogeneity of the sample. For all measurements the laser power was approx. 1 - 10 mW. The spectra were recorded in a range between 100 and 3200 cm^{-1}.

3.2.3.1 Study of the hydrogen bonding and secondary structure

The PDZ1-MAGI-1 interaction with the synthetics peptides that mimic HPV16E6 was performed recording the spectra range between 550 and 3200 cm^{-1}. A frozen sample was placed on a zinc selenide (ZnSe) window to give a better reflection which resulted in higher intensity of the signals. The different proteins spectra were recorded alone and in presence of the synthetic peptides. The synthetic peptides were also measured alone under the same conditions.

3.2.3.2 Study of metal-ligand vibrations

Fe-S Clusters. To study the Fe-S clusters and their environment, complex I, NDF, QRF, NuoEF, the complex I mutations and the NuoEF variants, were measured with an excitation wavelength of 514.5 nm. This wavelength was chosen with the aim to improve scattering to Fe-S clusters in relation to the flavin (FMN), as previous studies show that at 457.5 nm mainly FMN signals are detected [295]. For the grating scan of the protein alone all the samples were concentrated to approx. 250 μM and frozen with liquid nitrogen.

To follow the changes due to oxidation and reduction, the samples were studied in the presence of reduced nicotinamide adenine dinucleotide (NADH), its oxidized form (NAD^+) and the reduced phosphorylated form nicotinamide adenine dinucleotide phosphate (NADPH). A 10 mM solution of each nucleotide was dissolved in the same buffer as the sample. The nucleotides were added to the protein to a final concentration of 500 μM and 1 mM in different essays. After adding the nucleotides, the samples were incubated for 15 min at 4°C before recording the spectra. UV/Visible scans were done to monitor the reduction of the enzyme before recording the RR spectra.

For the study of the NuoEF variants (V90P, V136M and V90PV136M) in their reduced state, 20-fold excess of sodium dithionite was added it. For the reduced state with NADH, the same procedure explained in the previous paragraph was performed.

For the rest of the proteins cycling was perform using the electrochemical cell previously described coupled to a macro sampling set to the microscope with a long focal length lens (at 90^{o}). This enabled the cell to be located in a holder and illuminated from the side. All the measurements were performed at 10^{o}C to stabilize of the protein during the experiments. The samples were concentrated between 1-1.5 mM. The final spectra were an average of at least 10 cycles.

3.2.4 Fluorescence measurements

The fluorescence excitation spectra were recorded with a Fluorolog FL3-22 equipped with a 450 W Xenon Lamp and a TBX 04 detector (Horiba Jobin Yvon), using a bandpass for the excitation of 10 nm.

Titrations with the electrochemical cell were adapted to the fluorescence spectrometer as previously described[241]. The samples used were Complex I, NDF and quinone. All the measurements were performed at 5^{o}C to preserve the stability of the samples. The spectra were recorded at three different excitation wavelengths; 295 nm (Trp contribution), 365 nm (FMN contribution) and 420 nm (other chromophores).

In order to follow the redox-dependent shift, the intensity of the signal at 448 nm and 475 nm, observed in the emission spectra obtained with λ_{ex}=420 nm, was plotted vs. the potential in mV (SHE). To calculate the midpoint potential the curves fitted on the basis of the Nernst equation (Equation 3.1), taking into consideration a redox transition in the presence of three cofactors.

To compare the results to a model compound, Ubiquinone-10 was analyzed under the same conditions. Ubiquinone-10 was purchased from Sigma Aldrich. 1 mM solution was dissolved in CH_3CN (electrochemical grade). For electrochemistry, recrystallized tetra-butylammonium hexafluorophosphate ($TBAPF_6$) (Sigma Aldrich) at 10 mM concentration was added as a supporting electrolyte.

3.2.5 UV/visible measurements

To determine the midpoint potential of different cofactors present in a protein, titration with an electrochemical cell coupled (as described above) to an UV/vis spectrometer has been shown to be a powerful tool [242, 285].

For the study of the N1a in the NuoEF variants, UV/vis titrations were performed to calculate the changes in midpoint potential of the cluster due to the mutated residues. A Varian Cary 300 was used. The redox-dependent signals were followed between 350-800 nm. The data were recorded by applying a potential between 0 and -500mV (vs. Ag/AgCl). Steps (increase or decrease) of 20-30mV were used between 200-800 nm, with an equilibration time of 10-30 min at each step. All measurements were performed at 10^{o}C to preserve the stability of the protein.

The electrochemical titrations were found to be reversible as controlled by comparing fully oxidized minus fully reduced visible difference spectra at different points in the experiments. All the titrations were performed at least twice to ensure the reproducibility of the spectra obtained.

3.2.5.1 Determination of the redox midpoint potential (E*m*)

To calculate the midpoint potential (E_m) the protocol described by Euro *et al.* [215] was followed. The difference in intensity at 450 nm was plotted vs. the potential applied; this curve was fitted with the Nernst equation (Equation 3.1), modified to described the redox transition in the presence of three cofactors.

$$A(p) = \Sigma \frac{A\,max}{1+e^{(p-Em)\frac{nF}{RT}}} \quad \text{Equation 3.2}$$

A_{max} corresponds to the maximal change in absorbance, p for respective potential, E_m is the mid-point potential of the redox active group, n correspond to the number of electrons transferred, F is the Faraday constant (96485.3 C/mol), R is the universal gas constant (8.3144 J/K.mol) and T corresponds to the temperature in Kelvin.

4 RESULTS

4.1 The fingerprint print of the HPV16 E6 in a PDZ domain

4.1.1 Introduction

MAGI-1 is a protein localized predominantly in the tight junctions of epithelial cells. It is described as a scaffolding protein, bringing various intracellular proteins in proximity to the cell junction[64]. This protein bears six PDZ domains, named PDZ0 to PDZ5.

The PDZ1 of MAGI-1 is a target of those motifs, matching these sequences with a "class I" type (binding motif: X-S/T-X-V) (Table 3.1-5) PDZ domain. The solution structure of the C-terminal zinc-binding site of HPV16 E6 [296, 297] shows that the last 11 residues, including the canonical PDZ binding-motif, adopt a random conformation when not bound to their target[55].

Hold up-assays[55] and Surface Plasmon Resonance analysis (SPR) [298] of the E6-PDZ interaction revealed that a synthetic peptide corresponding to the 11 residues in the the C-terminus of the zinc-binding domain of HPV16 E6 can mimic the effect of the entire C-terminal domain, having the same interaction pattern with PDZ1 MAGI-1. The structures of the free (Figure 4.1-1A) and the bound forms (Figure 4.1-1.B) of PDZ1 in the presence of the synthetic peptide, named 16E6 L_0/V, have recently been solved by NMR[71].

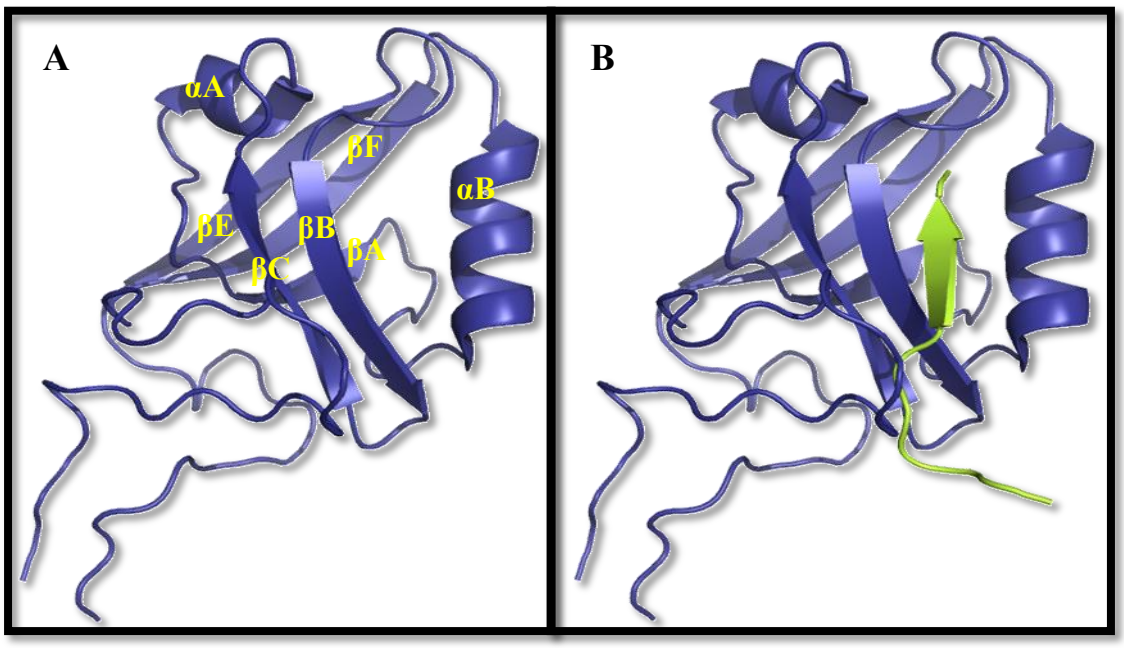

Figure 4.1-1. Schematic representation of A. PDZ1 MAGI-1 free form (PDB:2KPK) and B. bound form with HPV16 E6 L_0/V(PDB:2PKL)

These studies revealed that peptide residues outside the canonical PDZ binding motif are in direct contact with canonical regions of the PDZ domain, like the C-terminal. It has been reported that peptide binding induces important changes in backbone and the hydrogen bonding dynamics, but so far the NMR data have not present a full description of these changes, it had been focused only on backbone motions. Vibrational spectroscopic techniques, however allow recording complementary information on the hydrogen bonding dynamics of the canonical core and the extensions upon binding.

In this work we focus on the spectral characterization of the PDZ1 domain from MAGI-1 in presence of the HPV16 E6 synthetic peptides. Each protein was characterized alone in order to follow the conformational changes from the free form to the bound form. Mutations of important residues of the HPV16 E6 peptide related to the affinity were studied besides mutations in residues from the C-terminal region and in the βB-strand.

4.1.2 Overview of PDZ1 MAGI-1 spectroscopic studies

4.1.2.1 Infrared spectra

First, a complete description of the free PDZ protein and the free peptide was completed. The ATR absorbance spectra in the MIR region of WT (WT) PDZ1 MAGI-1 in buffer dissolved in H_2O and ^2H_2O buffer are shown in Figure 4.1-2.

The spectral range between 4000-800 cm^{-1} includes the main backbone vibrations as well as the contributions of amino acids side-chain vibrations. Amide A arises at 3285 cm^{-1}, amide B at 3063 cm^{-1} (Table 2.4-1) and the ν(C-H) vibrations including the asymmetric ν(CH_3) at 2962 cm^{-1}, the symmetric ν(CH_3) at 2874 cm^{-1} and the asymmetric ν(CH_2) at 2929 cm^{-1}.

Amide I arises at 1636 cm^{-1} and shifts to 1631 cm^{-1} upon deuteration. This band mainly involves the ν(C=O), but it has minor contributions from the out-of-phase ν(CN) vibration, the CCN deformation and the δ(NH) in-plane. The δ(NH) in-plane mode is known to be responsible for the sensitivity of the amide I band to N-deuteration of the backbone [247].

The deconvolution of amide I band shows the relative contribution of each secondary structure element. This analysis also gives an estimation of percentage and the kind of secondary structure in the protein. The main component of the secondary structure found here

are β-strand (60%) and β-turns (11%) which correspond to the five β-strands, 19% of α-helices and unorganized structure, corresponding to the two α-helix in PDZ1 and to 10% random coils. This is confirmed according to the structure resolved by NMR[71].

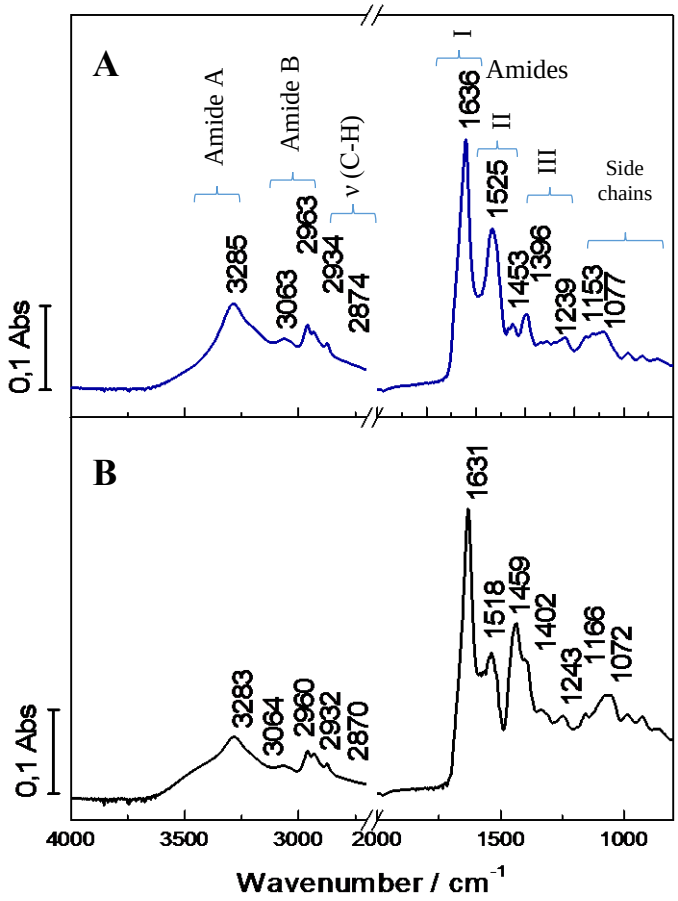

Figure 4.1-2. ATR MIR spectra of PDZ1 MAGI-1 WT. A. H_20 and B. ^2H_2O

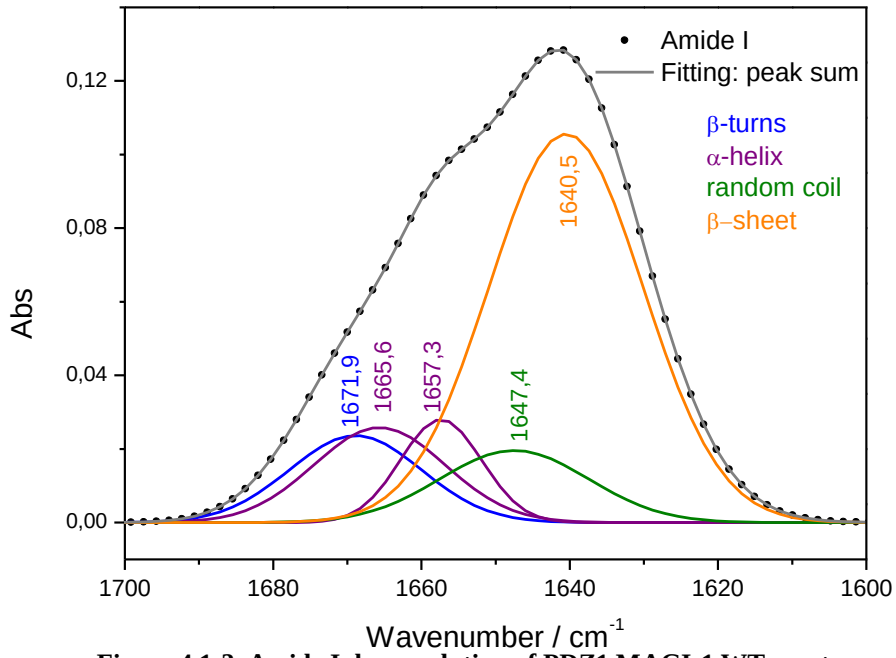

Figure 4.1-3. Amide I deconvolution of PDZ1 MAGI-1 WT spectrum.

(R^2: 0.99971)

Amide II, found at 1525 cm^{-1}, shifts to 1518 cm^{-1} in a ^2H_2O environment. The H/^{2}H exchange decouples the ν(C-N) from the δ(N-H) vibrations, giving rise to the Amide II' band at 1459 cm^{-1}. Amide II and amide II' will be affected in a different manner by the conformation and the environment of the amide group. For example, changes in the intramolecular hydrogen bonding have a direct effect on δ(N-H), which contributes to the amide II but not to the amide II' mode, this can be used as a marker to follow the solvent accessibility of the protein core[247].

The amide III band is observed at 1239 cm^{-1}. According to model studies[246] the frequency corresponds to a high percentage of β-sheet in the secondary structure, confirming the deconvolution of amide I.

Beside the amide bands, the contribution of the side chains of specific amino acids can be investigated (Figure 4.1-2). The band at 1153 cm^{-1} can be assigned to ν(C-O) vibration from Thr, Ser and Tyr. It had been shown that vibrations with large contributions of the stretching vibration of the polar C–O bond have relatively strong infrared intensities[250], also this band is sensitive to changes in the hydrogen bond of these residues[299-301]. A second signal at 1077 cm^{-1} corresponds to the CH_2 twist and the ν(C-O) from Glu residues, mostly[302]; nevertheless, in this region the contribution of many amino acids, are expected to be coupled, so not much conclusion can be obtained from this signal. Below 1000 cm^{-1} the signals included mainly contributions from the buffer (Figure 7.2-1 appendix).

In the FIR region the most significant signals in the spectra (Figure 4.1-4) are the Amide VI vibration, between 540-500 cm^{-1}, and the collective modes of hydrogen bonding, found below 300 cm^{-1}.

The broad signal seen at 513 cm^{-1}, amide VI, arises from several coupled vibrations, including the δ(C=O) out-of-plane and in-plane vibration of the COHN group as well as a minor contribution of C–C–N deformation[259]. In the ^2H_2O spectrum this band splits into two components, at 527 and 408 cm^{-1}. This indicates a possible decoupling of the modes that compose the band as in the case of Amide II[272].

For the signal at 408 cm^{-1}, it can be attributed the contribution of the δ(N-Cα-Cβ) modes of Ala and δ(Cβ-Cγ-C) modes of Leu, nevertheless, in this region the bending deformation modes of carboxylate groups as well as the torsional vibration of the ammonium

group of other side chains can be also expected, but there is no literature supporting this assignment for other than the aliphatic amino acids[303]. The band at 256 cm^{-1} corresponds mostly to the Amide VII modes (Table 2.4-1) [260], additionally, this region is characteristic of torsional vibrations as well as lattice modes. To date however, not much information about it is available[304].

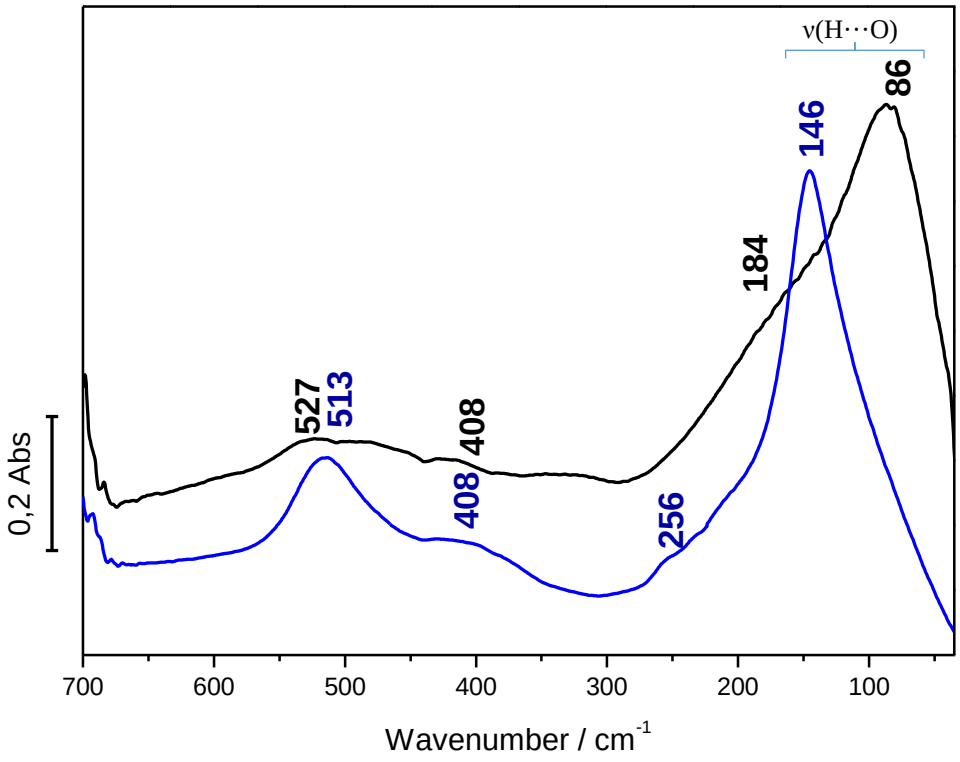

Figure 4.1-4. Far infrared spectra of PDZ1 WT in H_2O (blue line) and in ^2H_2O (black line).

The hydrogen bonding vibrations are sensitive to the structure of molecules and to intermolecular interactions. The band shape and position indicated the presence of water chains within the protein. Previous studies named this area the connectivity band[305].

Simulations of the vibrational density of states (VDOS) in polypeptides suggested that this vibrational mode is associated with the hydrogen bond populations present in α-helices and β-sheet, and that each form of secondary structure can account for the difference in shape and frequency of this band, also contributions of the out-of-plane δ(N-H) can be expected [306].

The difference in the band shape, in H_2O and ^2H_2O, could be correlated to the number of hydrogen bonds per molecule. According to the percolation model described by Brubach *et*

al. [305], the frequency of the band refers to the intermolecular motions that might involve non-covalent bonds, while the broadness is more related to the cohesion between the inter and intramolecular assembly. If there is a change of energy of one or two orders of magnitudes, their signature should arise at lower wavenumbers and increase the broadness.

Molecular dynamics simulations of the linear and nonlinear IR spectra of liquid water[307] described that in the low frequency region the contribution from water mainly originates from delocalized ν(O-H) vibrations given as linear combinations of symmetric and asymmetric stretching modes between two neighboring water molecules, where the closer they are the lower the frequency will be. An example of the complexity of this band is the difference in the frequency and shape upon deuteration. In H_2O a band at 146 cm^{-1} is seen. Upon deuteration it becomes a broad band with two components, 184 and 86 cm^{-1}.

4.1.2.2 Raman spectra

In the Raman spectrum (Figure 4.1-5), the amide I band is observed at 1667 cm^{-1}, amide II at 1585 cm^{-1} and amide III have two components, that arise at 1240 cm^{-1} and at 1270 cm^{-1}. The first one corresponds to the contribution of β-strands and the second the β-turn. In addition to these amide bands the in plane δ(Cα-H) is observed. Previous studies with ^{13}C substitution indicate that this band is primarily due to a vibration mode localized in the H-Cα–(C=O) network of the backbone. It generates two analog components that are seen at 1341 cm^{-1} and 1318 cm^{-1} [308]. However, for this last signal, the contribution of the amide III modes from the α-helical secondary structures is also expected[246].

The other relevant vibrations that have a high intensity arise at 1464 and 1449 cm^{-1}. These bands can both be assigned to the CH_2 scissoring mode of amino acids that have a methylene group in their side chain (Leu, Ile,Val and Pro). Below 1000 cm^{-1}, the signals mainly include contributions from the buffer (Figure 7.2-1 appendix).

A detailed description of the bands corresponding to the contribution of other amino acids side chains and their assignment is presented in Table 4.1-1.

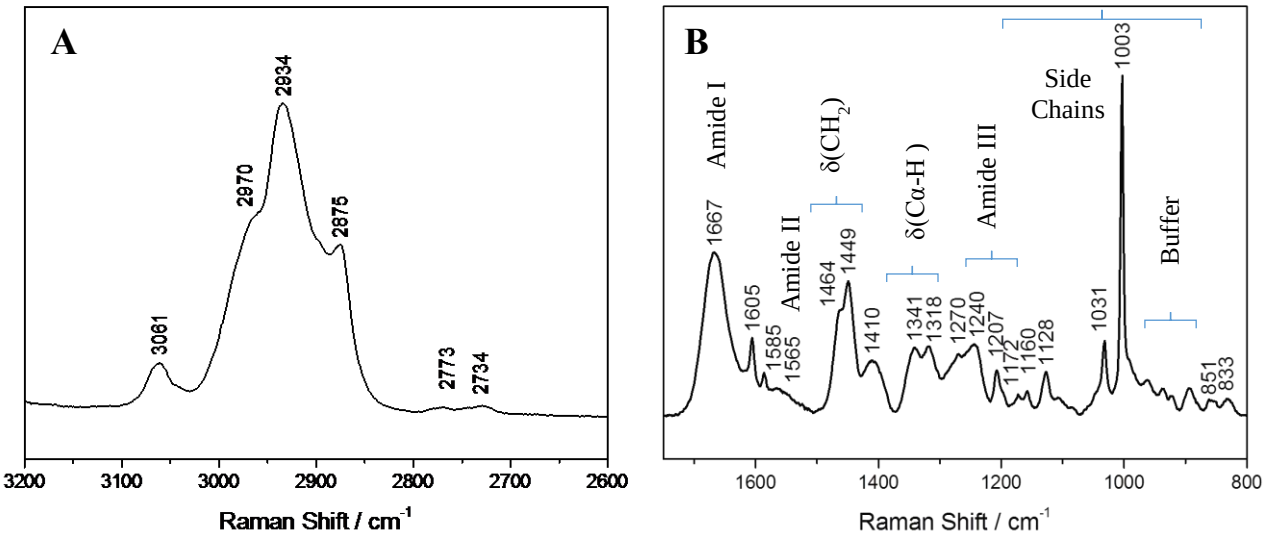

Figure 4.1-5. Raman spectrum of PDZ1-MAGI-1 WT. A. ν(C-H) region and B. Mid frequency region.

Table 4.1-1. Amino acid side chain contribution in the Raman spectrum of PDZ1 WT. Laser excitation: 514.5 nm (assignment were done based on the studies of Jenkins *et al.*[309] and Zhu *et al.*[310])

Frequency (cm^{-1})	Amino acid	Vibrations
1606	Tyr	Ring breathing
1585	His	ν(C-C)
1464/ 1449	Methlylene group (side chain)	$\delta(CH_2)$
1410	Thr	$\delta(CH_3)$
1207	Phe Tyr	symmetric ν(Ring –O)
1172	Met	rocking (C-O(H))
1160	Ile Leu	rocking N-H δ(Cγ1–Cβ–Cγ2)
1128	Arg Ser, Val	wagging N-H rocking N-H
1030	Thr Phe	OH deformation motion In plane δ(C-H) deformation
1003	Phe	Ring breathing
851 833	Tyr	Fermi doublet (ν_{16a}/ν_1)

Another related region that represents possible hydrogen bonding in proteins is the ν(C-H) region found between 2700- 3100 cm^{-1}. For PDZ1, six bands can be seen. A description of the different amino acids contribution to each signal as well as the vibration that gives rise to the band is given in Table 4.1-2. The scattering in this spectral region has also been considered to be related to hydrophobic groups like CH_2 and CH_3 [311].

Table 4.1-2. . ν (C-H) vibrational modes of PDZ1 WT by Raman spectroscopy. (Assignments are according to Howell et al[311])

Frequency (cm^{-1})	Amino Acid	Vibration
2734	Met	symmetric ν(C-H)
2773	His	symmetric ν(C-H)
2875	Ala, Val Ile Leu	symmetric ν($-CH_3$)
2934	Met	asymmetric ν(C-H)
2970	Ser,Thr	asymmetric ν(C-H)
3061	Tyr	ν(α-CH)

In summary, the spectral properties by IR and RR obtained agree with what is already published of the canonical structure of the PDZ domains along with the recently published NMR structure (Figure 4.1-1)[312]. Amide bands can be taken as markers to follow the conformational changes upon substrate binding. The Amide A and B in the ν(C-H) region in the infrared and the ν(Cα-H) in Raman can be compared to the hydrogen bonding collective modes observed in the FIR. These groups of vibrations can be used to describe the changes in the intra and intermolecular hydrogen bonding pattern. Finally, signals from specific amino acids as the Thr, Tyr, Phe and His can work as parameters to follow the configuration of the side chains and thus determine how these amino acids are involved, or not, in the binding mechanism.

4.1.3 Spectral properties of the HPV16 E6 peptide

The synthetic peptide 16E6 (RSSRTRRETQL) corresponding to the last 11 C-terminal residues of HPV16 E6, was analyzed. The first residue, Leu (P_0) was mutated for Val in order to mimic the homolog E6 viral protein from "high risk" HPV18 [99]. Shorter peptides (5th and 6th residue), were analyzed in order to understand the contribution of the first residues. Finally, a mutation of the Arg residue in the P_{-5} position was studied, since this residue may be the junction point between the PDZ domain and the viral protein[298]. The complete sequence of each peptide was presented in Table 3.1-5.

It is expected that the peptide in its free form does not have any specific secondary structure and that it adopts a rather flexible and extended structure (Figure 4.1-6)[296]. Changes in only one residue can have a high impact on the secondary structure and the interaction of

the residues with the solvent. Figure 4.1-7 shows the MIR and FIR spectra of the WT 16E6 peptide in comparison with the mutant peptides.

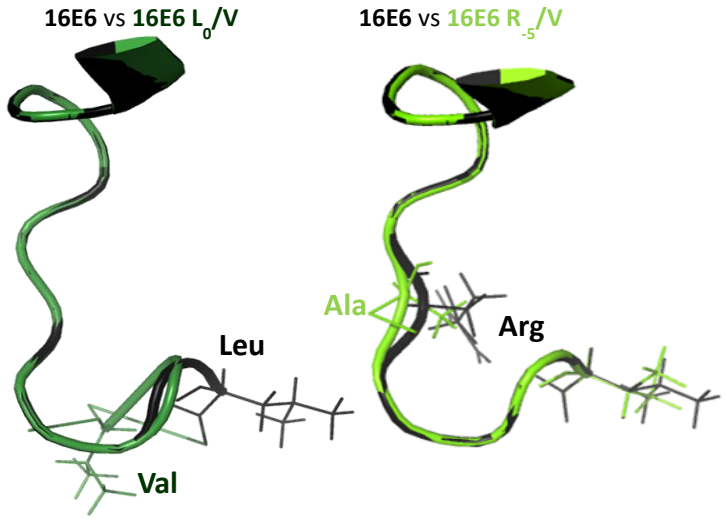

Figure 4.1-6. Schematic representation of the C-terminal wild type (11R) HVP16 E6 superimposed with the variants. (PDB: 2LJZ).

4.1.3.1 Infrared spectra

The mutations exhibit an amide A band at lower wavenumber, this peak shifts from 3282 cm^{-1} in 16E6 to 3277 cm^{-1} for the shorter peptides and in the case of 16E6 L_0/V and 16E6 R-$_5$/A to 3261 cm^{-1}, reflecting a stronger hydrogen bonding, alternating the level of flexibility is higher in the peptide, allowing more interaction with the environment. Amide B is observed around the same frequency for all the peptides.

The frequency and the sharpness of the amide I band at 1644 cm^{-1} in the WT 16E6 spectrum, indicates that this peptide is organized in a random coil. In the 16E6 L_0/V and 16E6 R_5/A peptides, the amide I band shifts to 1651 and 1657 cm^{-1}, respectively, indicating that these specific variations, have a large effect on the secondary structure. As it can be seen in Figure 4.1-7 the orientation of the backbone may change in the presence of the Val instead of Leu and in the case of 16E6 R-$_5$/A there is a shift in dihedral angle of the loop.

Furthermore, shifts in the amide II mode from 1543 cm^{-1} in the WT to 1536 cm^{-1} in the 11 residue variants spectra, confirm the conformational changes described previously.

In the FIR spectrum of the WT of 16E6, the amide VI band is found at 512 cm^{-1} and it shifts slightly to 517 cm^{-1} in the mutant 16E6 L_0/V, the shift is more clear than in the

spectrum of 16E6 R-$_5$/A, where this band is seen at 514 cm^{-1}, indicating that mutations in this position have a higher impact than the variation in the P-$_5$ position of the backbone modes (Figure 4.1-6).

Changes in the C=O stretching (Amide I) and not the bending backbone modes (Amide VI), may indicate that the backbone modifications are related with the differences hydrogen bonding as is the case for 16E6 R-$_5$/A. Confirming this, in the infrared spectra of the shorter peptides, the amide VI band shift from 512 cm^{-1} (16E6) to 525 cm^{-1} (16E6$_{ct}$ 6 L$_0$/V) and 529 cm^{-1} (16E6$_{ct}$ 5 L$_0$/V).

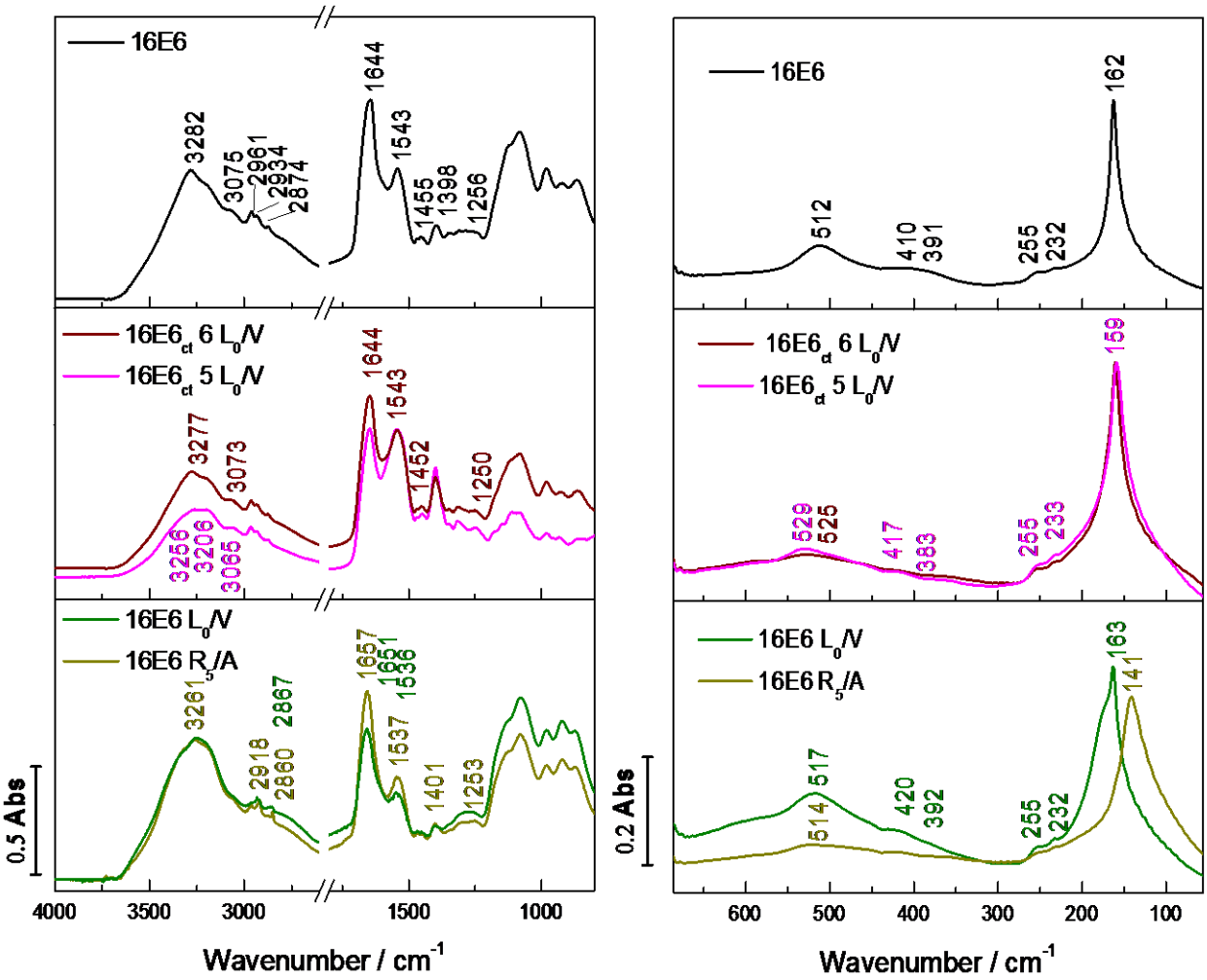

Figure 4.1-7. Mid (right) and far (left) infrared spectra of different peptides originated from the viral oncoprotein sequence HPV16E6. (The shifts of signals in comparison to 16E6 are in color)

The hydrogen bonding collective modes are found at 163 cm^{-1} in both spectra. The WT 16E6 and 16E6 L$_0$/V peptide, but there is a variation in the broadness of the signal, indicating that the modes have the same energy but there is a different rearrangement of the

hydrogen bonds. It is also important to consider that several modes are overlapping in this region, which makes the interpretation difficult.

For the 16E6 R_{-5}/A the signal shifts to 141 cm^{-1} and the band becomes broader, also pointing to a different organization of the hydrogen bonds. In the shorter peptides the bands have a similar broadness as the WT spectrum, although the main difference is a frequency shift to 159 cm^{-1}, indicating weaker hydrogen bonding, as the band is at higher frequencies.

4.1.3.2 Raman spectra

In the Raman spectra (Figure 4.1-8) the amide I band of the three 11-residue peptides have the same frequency, seen at 1675 cm^{-1}. For the shorter peptides, it arises at 1669 cm^{-1}. A similar pattern is observed for the amide II band, for the 11-residue peptides it arise at 1574 cm^{-1}, although a difference is seen between the $16E6_{ct}$ 5 L_0/V, where the band is seen at 1566 cm^{-1} and for $16E6_{ct}$ 5 L_0/V at 1551 cm^{-1}.

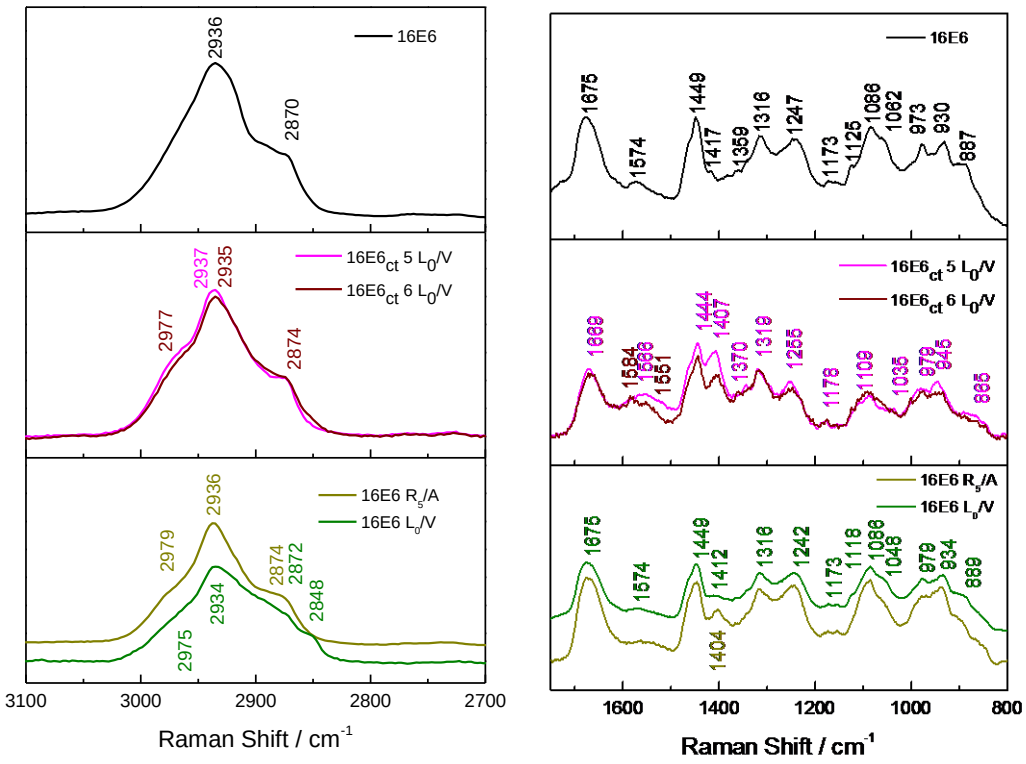

Figure 4.1-8. Raman spectra of the peptides from the viral oncoprotein sequence HPV16E6.

Amide III in the 16E6 spectrum includes two components at 1316 and 1247 cm^{-1}. The first component is related to the α-helix structure whereas the second corresponds to random coil contribution[246]. For 16E6 L_0/V and 16E6 R_{-5}/A the second component presents a

displacement to 1242 cm^{-1}, whereas for the shorter peptides both peaks are shifted to higher wavenumbers, to 1319 and 1255 cm^{-1}, respectively. In summary, it is evident that the shorter peptides have a very different conformation in comparison with the 11-residue peptides.

The rest of the observed bands below 1500 cm^{-1} are listed in Table 4.1-3, together with the corresponding assignments. Most of the signals are vibrational modes of the side chain of the amino acid sequence.

Table 4.1-3. Amino acid side chain contribution in the Raman spectrum of 16E6 and its variants. (The assignment were done based on the studies of Jenkins *et al.*[309], Zhu *et al.*[310] and Culka *et al.*[313])

Modes	Amino acids	16E6	$16E6_{ct}$ 5 L_0/V	$16E6_{ct}$ 5 L_0/V	16E6 L_0/V	16E6 R_{-5}/A
$\delta(CH_2)$	Glu,Gln, Arg	1449	1449	1449	1444	1444
Cβ rocking	Arg	1417	1412	1404	1407	--
CH def	Thr	--	--	--	1370	1370
Sym $\delta(CH_3)$	Leu	1359	--	--	--	--
$\delta(CH_3)$	Thr	1173	1173	1173	1178	1178
ν(C–OH)	Ser	1125	1118	1118	--	--
δ(C-C-N)	Gln	--	--	--	1109	1109
δ(C-C-N)	Arg	1086	1086	1086	--	--
asym $\delta(CH_3)$	Leu	1062	--	--	--	--
asym $\delta(CH_3)$	Val	--	1048	1048	1035	1035
$\nu(C_\alpha–C_\beta)$	Arg	973	979	979	979	979
$\nu(C_\beta–C_\gamma)$	Arg	930	934	934	945	945
COOH def	Glu	887	889	889	885	885

In the ν(C-H) region, two bands are seen in the 16E6 spectra at 2870 cm^{-1} and at 2936 cm^{-1}, the first can be assigned to symmetric ν(-CH) of Thr and Glu, whereas the second is originally from the contribution of the asymmetric ν(C-H) of Arg and Gln. A new band appears in the mutants which is not seen in the 16E6 peptide, at around 2977 cm^{-1} and it can be attributed to symmetric ν(C-H) of the additional Val side chain ($(CH_3)_2CH$-) contribution, which is present in all the mutants.

4.1.4 PDZ1 interaction with HPV16 E6 peptides

The structure of the PDZ domains displays very small conformational changes upon binding with the natural partner[77, 314]. However, when the binding partner is substituted by a

viral protein, the binding process does not follow the same rules[99, 315]. The first characteristic is that only four residues from the natural peptide are found to interact with the PDZ binding site, whereas in the viral proteins at least 6 residues are used to stabilize the complex and assure a high affinity[91, 104].

Figure 4.1-9 shows the titration of PDZ1 with different ratios of the16E6 L_0/V peptide in the MIR region. The spectrum at 1:1 ratio is dominated by bands from PDZ1 (Figure 4.1-2) whereas the spectrum at a ratio of 1:6 shows only the features of the 16E6 L_0/V peptide. The spectra at 1:2 and 1:3 ratios are very similar to each other. In this work the 1: 2 ratio is used as the spectrum representation of the interaction between PDZ1 and 16E6.

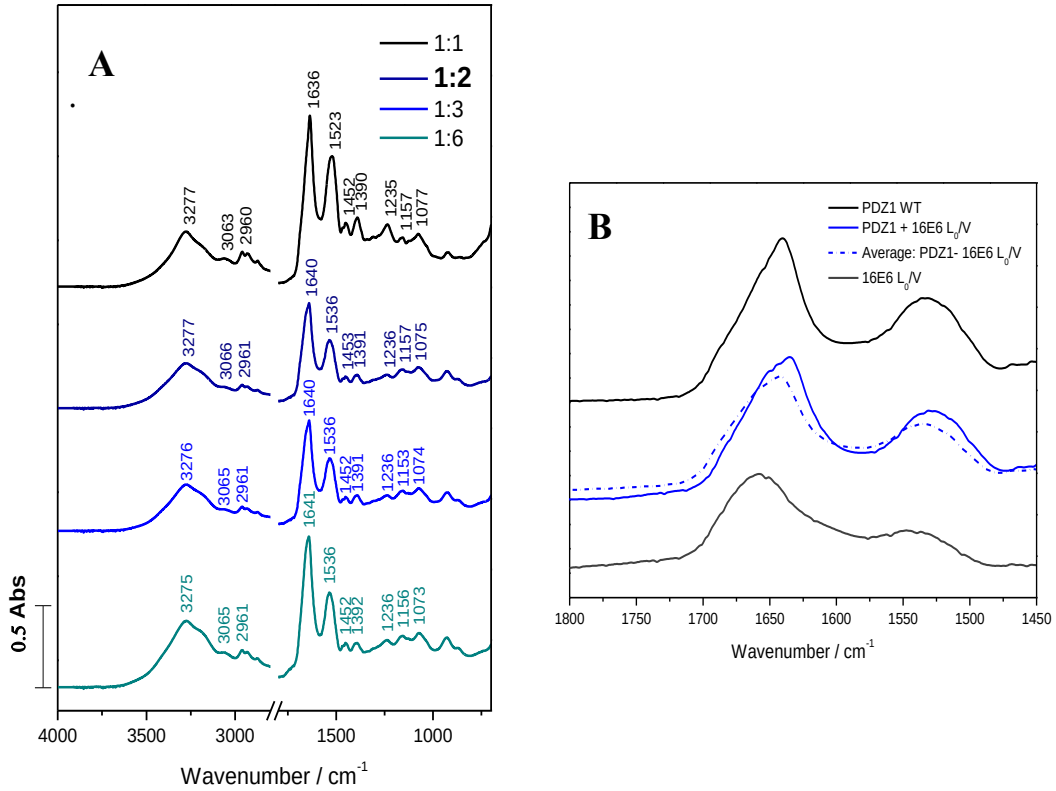

Figure 4.1-9. A. Infrared titration of PDZ1 in presence of 16E6 L_0/V. B. spectrum comparison between the average of the PDZ1 in its free form and the bound form.

As a control, to make sure that the spectra represent the protein-protein interaction, the PDZ1 and peptide spectra in their free form were averaged (1:2 ratio) (Figure 4.1-9. B dotted blue line) and compared with the spectrum obtained in the titration using at 1:2 ratio (Figure 4.1-.9.B solid blue line). The significant difference in the shape and wavenumber of between amide I and II is evident, indicating that the technique is valid to follow the conformational

changes upon complex formation. In the results presented here no subtraction was made of the original spectra of the complex between the protein and the peptide.

The titration was carried out in presence of the 16E6 L_0/V variation in order to compare the main backbone conformational changes to the properties of the complex formation already described by NMR[71].

4.1.4.1 Infrared spectra

Backbone conformational changes. The MIR spectra of the bound PDZ1 in the presence of the 16E6 peptide and its variations are displayed in Figure 4.1-10. In comparison to the spectrum of the PDZ1 free form (Figure 4.1-2) a shift in the amide I signal is observed, from 1636 cm^{-1} to ~1640 and 1641 cm^{-1} in presence of all the peptides. Upon binding an intense shoulder arises at 1658 cm^{-1}, this signal is associated with the contribution of α-helical component. Table 4.1-4 shows the relative percentage of the different secondary structure elements obtained by the deconvolution of amide I of the bound forms. For further details of the fitting see Figure 7.2-2 in the appendix.

Table 4.1-4. Amide I deconvolution from the spectra of the PDZ1 bound form in presence of the HPV16 E6 peptides (in parenthesis the frequency in cm^{-1} of the secondary structure component assigned)

(%)	PDZ1 free	PDZ1+ 16E6	PDZ1+ 16E6ct 5 L_0/V	PDZ1+ 16E6ct 6 L_0/V	PDZ1+ 16E6 L_0/V	PDZ1+ 16E6 R_{-5}/V
α-helix	19 (1657/ 1665)	12 (1657)	19 (1660)	19 (1662)	13 (1657)	12 (1657)
β-sheet	60 (1640)	61 (1641/1690)	61 (1623/1640/ 1685)	61 (1641/1688)	64 (1640/1686)	66 (1640/1689)
β-turns	11 (1668)	18 (1673)	7 (1673)	9 (1675)	14 (1676)	13 (1673)
Random coil	10 (1647)	9 (1649)	13 (1648)	11 (1648)	9 (1648)	9 (1649)

Upon the binding of the 16E6 peptide an increase in the percentage of β-turns is evident, this may indicates the β-augmentation process characteristic of the PDZ domains ligand binding[316]. These changes may reflect the structural rearrangement of the peptide more than the changes in the PDZ1 secondary structure. In presence of the 16E6 L_0/V and 16E6 R_{-5}/A, an increase in the percentage of β-turns and β-sheets is observed. In comparison to the results with the 16E6 peptide, the increase of β-sheets elements suggest that a different hydrogen bonding pattern is occurring in the binding process with the mutant where, as a

result, the peptide has a more pleated structure[77, 317]. With the 5 and 6 residues peptides the increase of the percentage of β-turns is not observed; indicating that, more than 6 residues are necessary to accomplish the complete β-strand addition. This is also confirmed by the increase of the percentage of random coils.

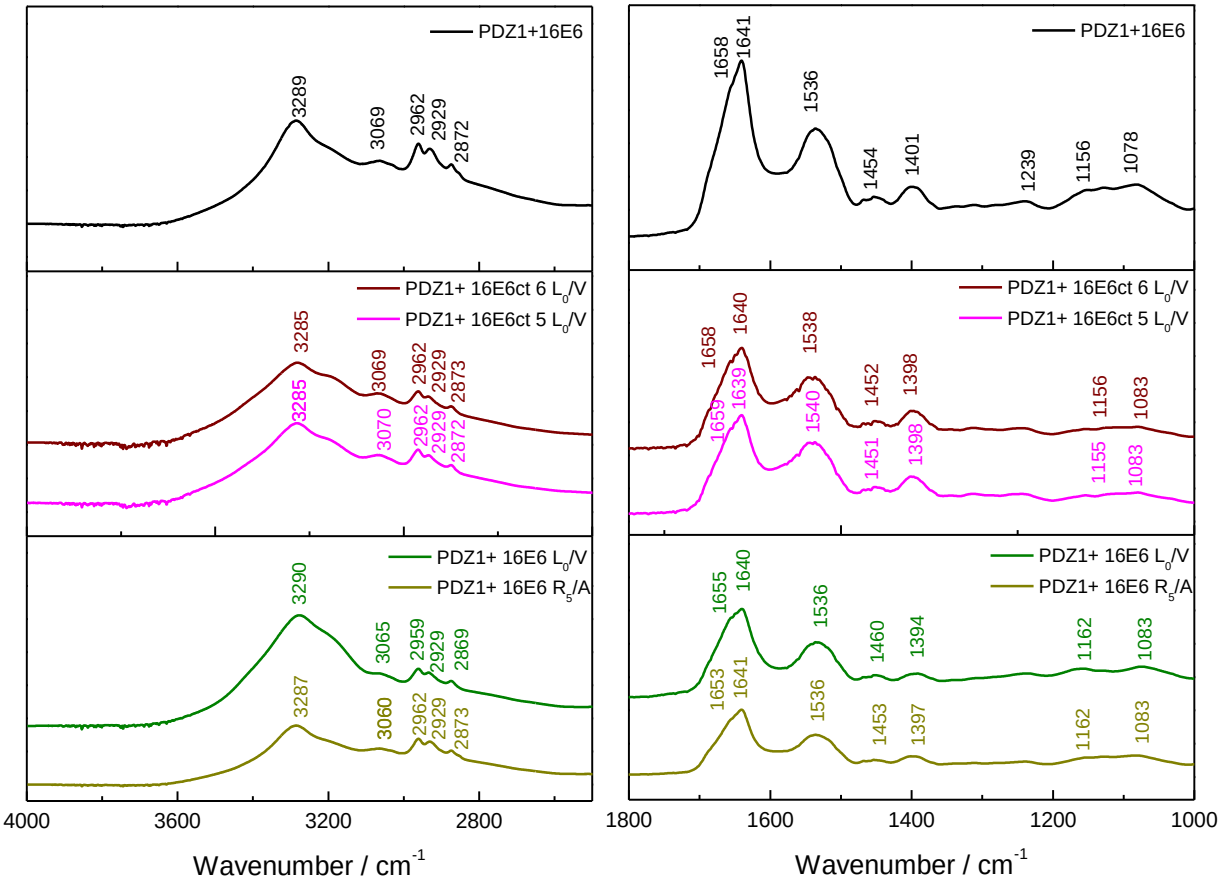

Figure 4.1-10. Mid infrared spectra of the PDZ1 interaction with the different HPV16E6 peptides.

The spectra in ^2H_2O (Figure 4.1-11) allows to depict the water contribution from the amide I region. It is evident that the amide I band has a similar behavior in ^2H_2O as in H_2O, it shows a displacement of 4 cm^{-1} upon the binding of WT 16E6 and the two short peptides (from 1631 cm^{-1} to 1635 cm^{-1}), whereas for the bound form with 16E6 L_0/V the band appears at 1644 cm^{-1} and with 16E6 R_5/A appears at 1647 cm^{-1}, which corresponds to a larger backbone conformational changes.

The amide II band arises at 1536 cm^{-1} in the bound form with the 11-residue peptides. The same displacement is observed for the shorter peptides, at 1536 cm^{-1} for $16E6_{ct}$ $6L_0$/V and at 1540 cm^{-1} for $16E6_{ct}$ 5 L_0/V; this indicates that the additional residue (P_{-6}) exerts an influence on the stability of complex formation via the ligation with the N-H and C-N groups.

The amide II displacements were confirmed in $^{2}H_2O$, where the amide II band (Figure 4.1-11) at 1518 cm^{-1} in the free form is shifted to a higher wavenumber arising at 1537 cm^{-1} with 16E6 and $16E6_{ct}$ 6 L_0/V, at 1544 for the 5 residue peptide and finally at 1546 and 1550 cm^{-1} for 16E6 L_0/V and 16E6 R_5/A, respectively.

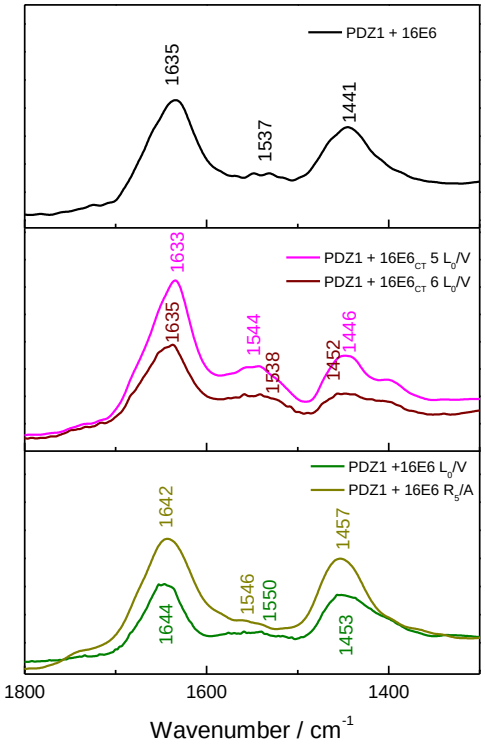

Figure 4.1-11. Mid infrared spectra of the PDZ1 interaction with the different HPV16E6 peptides in $^{2}H_2O$

On the other hand, the amide II' band has a displacement from 1459 cm^{-1} in the free form to lower wavenumbers in presence of 16E6 L_0/V, 16E6 R-$_5$/A and the peptide of 6 residues. However in the presence of 16E6 and the 5 residue peptide, this shift is even more pronounced corresponding to the signals arising at 1441 cm^{-1} and 1446 cm^{-1}. This points toward more prominent motions of the C-N groups in the protein backbone in presence of the 16E6 and $16E6_{ct}$ 5 L_0/V.

The FIR spectra (Figure 4.1-12) shows that upon binding Amide VI band shifts from 513 cm^{-1} (free form) to 518 cm^{-1} for 16E6ct 6 L_0/V and to 526 cm^{-1} with 16E6 R-$_5$/A. In presence of the shorter peptides the signal arises at 520 cm^{-1} with 16E6ct 5 L_0/V and to 518 cm^{-1} for 16E6ct 6 L_0/V. This indicates that residues P_{-5} and P_{-6} are relevant for the binding and the other residues in the peptide (P_{7-11}) may help to stabilize the backbone of the protein upon binding.

Amide VI is a coupled mode arising from the in-plane and out-of-plane δ(C=O) and the deformation of the (C-C-N) groups[259]. The small displacements of amide I indicate that the C=O groups are only slightly affected, then the perturbations of the C-C-N groups are most likely to be the reason behind the shift of the amide VI signal, these changes can also be associated with the shift of amide II and amide II'.

Additionally (Figure 4.1.12), the band at 256 cm^{-1} suffers a small perturbation going to lower wavenumber in the presence of the 11-residue peptides and to a higher wavenumber in presence of the short peptides. This band was attributed to the amide VII mode coupled to the torsion vibrations of several amino acid side chains and lattice modes. Due to the complexity of the vibrations arising in this region not much information can be deduced for the spectral differences observed for these vibrations.

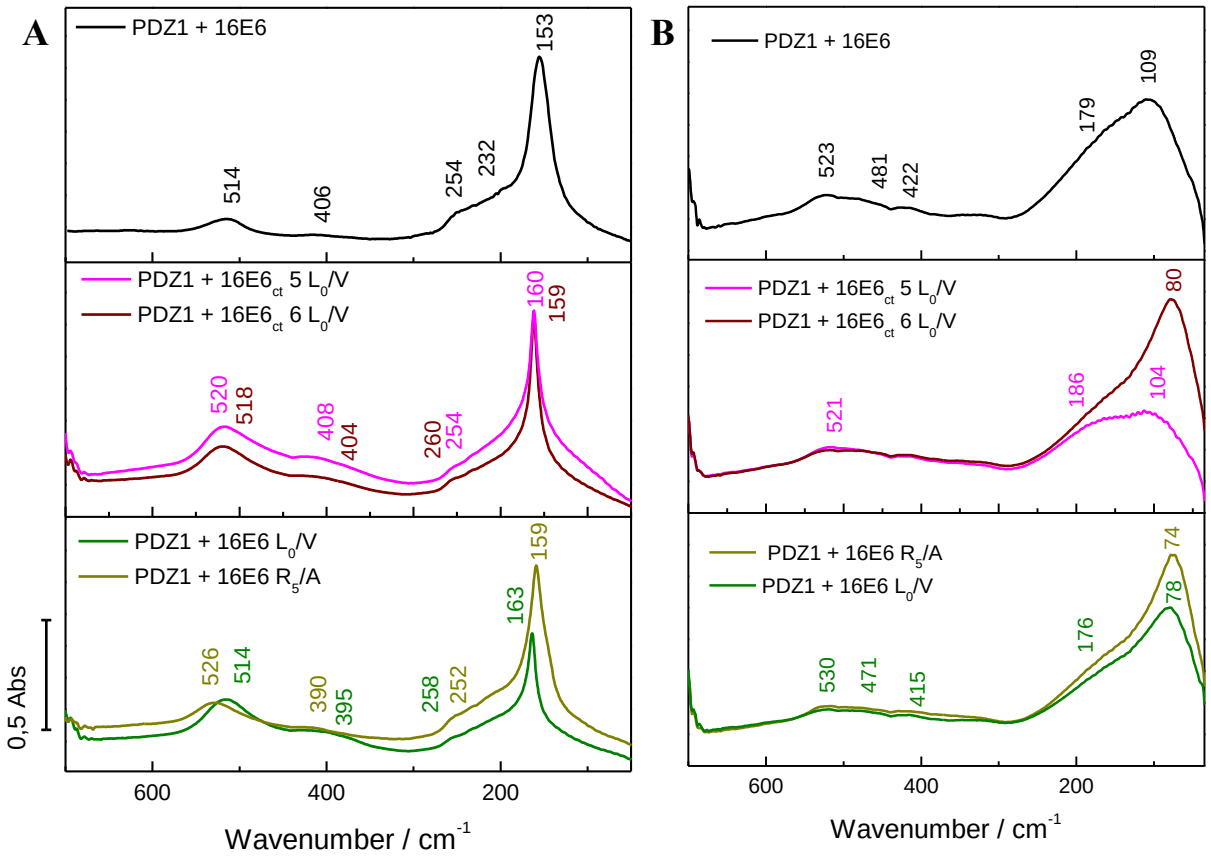

Figure 4.1-12. Far infrared spectra of the PDZ1 interaction with the different HPV16E6 peptides in A.H_2O and b. ^2H_2O

Amino acid side chains. In the MIR spectra the band corresponding to ν(C-O) vibration from Thr, Ser and Tyr, is barely affected in presence of the short peptides. The same occurs with the 16E6 peptide, appearing at 1156 cm^{-1}. On the other hand, with 16E6 L_0/V and

16E6 R_{-5}/V peptides, the signal arises at 1162 cm^{-1}. Higher wavenumber of this vibrational modes is associated with O-H groups been hydrogen bonded[300].

In the FIR region (Figure 4.1-12) the signal observed at 408 cm^{-1} in the free form corresponding to δ(N-Cα-Cβ) modes of Ala and δ(Cβ-Cγ-C) modes of Leu, upon binding shifts to a lower wavenumber in presence 16E6 L_0/V and 16E6 R_{-5}/A.

In general, it is evident that the 16E6 L_0/V and 16E6 R_{-5}/A peptides affect several side chains that with the WT peptide, 16E6 and the short peptides remain unaltered as in the free protein form.

Hydrogen bonding. As a general rule, hydrogen bonding lowers the frequency of stretching vibrations, since it lowers the restoring force, but it can also increases the frequency of bending vibrations since it produces an additional restoring force[247]. The backbone conformational changes described before may be directly correlated to the difference in the hydrogen bonding bands upon binding. The ν(C-N) vibrations are the most affected ones in presence of 16E6 L_0/V and 16E6. The frequency corresponding to this vibrational mode shifts to higher wavenumber when the band of the hydrogen bonding collective modes downshifts.

Nevertheless, the increase of the frequency of the δ(N-H) modes, indicates that the changes upon binding are influenced by other kinds of interactions besides the hydrogen bonding, as it was observed for the differences in the amide I and amide II band.

The MIR spectra of all the bound forms above 2800 cm^{-1} mainly show (Figure 4.1-10) changes in amide A and amide B. The amide A signal, observed at 3285 cm^{-1} in the free protein, does not present any shift in presence of the shorter peptides. However, in presence of 11-residue peptides a shift to high wavenumber is observed, this shift is more pronounced in presence of 16E6 L_0/V. A similar pattern is evident for amide B.

For the ν(C-H) region the band corresponding to the asymmetric ν(CH_3) vibration is perturbed only in presence of the 16E6 L_0/V peptide, going from 2962 cm^{-1} to 2959 cm^{-1}; this occurs also with the signals from symmetric ν(CH_3) mode, changing from 2874 cm^{-1} to 2869 cm^{-1}. The asymmetric ν(CH_2) modes at 2929 cm^{-1} do not present any perturbation.

In the FIR spectra (Figure 4.1-12.A) the signal corresponding to the collective vibrational modes of the hydrogen bonding undergoes important modifications, not only in the frequency but also in the band shape. In the bound forms the signal becomes sharper and

more narrow. The most pronounced effect is seen in presence of 16E6 L_0/V, where the band is displaced by ~20 cm^{-1} in comparison to the free protein, arising at 163 cm^{-1}. With 16E6 R_{-5}/A the signal appears at 159 cm^{-1} and with 16E6 at 153 cm^{-1}. With the short peptides the signal is observed around 159 cm^{-1}. The lower frequency indicates that stronger hydrogen bonding is occurring[318].

The broad band observed in the spectra in ^2H_2O (Figure 4.1-12.B) shows a different result. PDZ1-16E6 undergoes a displacement to higher wavenumber, seen at 109 cm^{-1}. The same is seen for PDZ1-16E6$_{ct}$ 5 L_0/V with a signal at 104 cm^{-1}. On the other hand, the signal coming from the other bound forms arises at lower wavenumbers; the most relevant effect is in presence of 16E6 L_0/V as it was also observed in the spectra recorded in H_2O. This may indicate that the hydrogen bonding not only depends on the P_0 and P_{-5} but also on the peptide length.

4.1.4.2 Raman spectra

Backbone conformational changes. In the backbone vibrations of PDZ1 observed by Raman spectroscopy (Table 4.1-5), the amide I band only shifts in the presence of the shorter peptides, from 1667 cm^{-1} in its free forms (Figure 4.1-5) to 1664 cm^{-1} with 16E6$_{ct}$6 L_0/V, and to 1661 cm^{-1} with 16E6$_{ct}$5 L_0/V.

The amide II band of the free form is a small shoulder at 1565 cm^{-1}. This band shifts to a higher frequency in the presence of 16E6 L_0/V (1569 cm^{-1}) and to a lower frequency in the presence of 16E6 R_{-5}/A and the shorter peptides (1563 cm^{-1}). The difference between this result and the shift observed in the infrared might be due to the broadness and low scattering of this amide mode in Raman.

Table 4.1-5. Backbone vibrational modes of PDZ1, in its free and bound form by Raman spectroscopy

PDZ1 free	Bound 16E6	Bound 16E6$_{ct}$ 5 L_0/V	Bound 16E6$_{ct}$ 6 L_0/V	Bound 16E6 L_0/V	Bound 16E6 R_5/A	Modes
1667	1667	**1661**	**1664**	1667	1667	Amide I
1565	1566	**1563**	**1569**	1563	1563	Amide II
1341	1340	1338	1340	1338	1340	δ(C-H)
1270	**1266**	**1263**	**1265**	**1265**	**1266**	Amide III β-turns
1243	1242	**1239**	1242	**1239**	**1239**	Amide III β-sheets

Following amide III in the Raman spectra of the bound forms (Table 4.1-5) gives the clue that the changes in the frequencies in amide I are more related to conformational changes in the β-turn elements than in the β-strands. Only with 16E6 L_0/V and the shorter peptides, changes of amide III in the β-strand are observed.

As a general rule, the mode's frequency decreases as the weakened water hydrogen bonding decreases the amide N-H bending and the C-N stretching force constants, as seen in the spectra of the bound forms with 16E6 L_0/V and the short peptides, the changes can be explained by the water hydrogen bonding impact on the N-H bend force constant more than the C-N stretch force constant [252].

The δ(Cα-H) modes in Raman spectra, arising at 1341 cm^{-1} and 1318 cm^{-1} in the free form, only displayed a relevant change in the bound form with 16E6 L_0/V and with the short peptide 16E6ct 5 L_0/V, with a signal at 1338 cm^{-1}.

Amino acid side chains. From the side chain contributions obtained from the Raman spectra (Table 4.1-6) the signal at 1410 cm^{-1} corresponding to the symmetric δ(CH_3) of Thr have a similar pattern as the signal described from the infrared spectra.

Table 4.1-6. Amino acid side chain vibrations of PDZ1 in its free and bound form by Raman spectroscopy

PDZ1 free	Bound 16E6	Bound $16E6_{ct}$ 5 L_0/V	Bound $16E6_{ct}$ 6 L_0/V	Bound 16E6 L_0/V	Bound 16E6 R_5/A	Amino acids	Modes
1605	1606	1606	1606	1606	1603	Tyr	Ring breathing
1449	1446	1446	1446	1449	1446	Ala, Leu, Phe	δ(CH_2)
1410	1409	1409	1409	**1407**	**1407**	Thr	δ(Cα-H)
1207	**1200**	**1205**	**1205**	**1200**	**1200**	Phe Tyr	δ(ring) ν(Ring –O)
1173	1172	1173	1172	1172	1172	Met	rocking (C-O(H))
1160	**1154**	**1154**	**1154**	**1154**	**1154**	Iso Leu	rocking $CH3^+$ δ(Cγ1–Cβ–Cγ2)
1128	**1125**	**1125**	**1125**	**1125**	**1125**	Arg Ser, Val	wagging N-H rocking CH_2^+
1032	1030	1030	1030	**1027**	**1027**	Thr Phe	OH def δ(C-H) def
1003	1003	1003	1003	1003	1003	Phe	Ring breathing
851 833	**860** 831	852 831	852 830	**860** 831	**859** 831	Tyr	Fermi doublet

In the PDZ1-16E6 L_0/V and PDZ-16E6 R-$_5$/A bound forms, this band goes to 1407 cm^{-1}. This is also supported by the displacement of the signal found at 1032 cm^{-1}, resultant from the OH deformation of the Thr. In this second band, the contribution from the δ(C-H) vibration of Phe is also expected, but comparing with the sharp band arising at 1003 cm^{-1} from the ring breathing modes of Phe, that is not perturbed by the binding, it can concluded that the spectral differences in this vibration reflect the changes in the Thr side chains.

The signal at 1160 cm^{-1} in the free form arising from the side chain motions of Iso and Leu seems affected upon the binding of all the peptides, shifting to 1154 cm^{-1}. The same is observed with the signal at 1128 cm^{-1} corresponding to the contribution of Arg, Ser and Val, shifted to 1125 cm^{-1} in the bound form.

Tyr side chains also seems affected by the peptide binding, with a representative signal arising at 1207 cm^{-1} that shifts to 1200 cm^{-1} in presence of the 11-residue peptides, but remains at the same position in the presence of the short peptides.This indicates theat the residues Tyr101 is only affected by the interaction between the residues upstream of the HPV16 E6 protein.

Hydrogen bonding. The ν(C-H) modes arising in the Raman spectra are described in Table 4.1-7. The difficulty in interpreting this area is that many vibrations are overlapping and the bands are typically broad. The bands in this region arise mainly from the fundamental C-H of the backbone; however, many studies have associated the frequencies in this spectral region with specific amino acid contributions. As the dihedral angle of the Cα shift due to the hydrogen bonding form in the near residues[237, 311].

Here, the main C-H bands perturbed upon binding are the signal at 2734 cm^{-1} assigned to the Met residues. This small shoulder is very well resolved and shifts to 2728 cm^{-1} in presence of the 16E6 and the small peptides to 2725 cm^{-1} with 16E6 L0/V and to 2730 cm^{-1} with 16E6 R_5/A.

The His C-H groups are also affected except for the bound from in presence of 16E6, the signal at 2773 cm^{-1} shift to 2768 cm^{-1}. This points toward an interaction between the P_0 residue and the His residues in PDZ1. Besides the Met and His groups the displacement of the signal at 2934 cm^{-1} to 2930 cm^{-1} in all the bound forms might indicate the perturbation of Arg residues due the binding process, the same is observed with the signal at 2970 cm^{-1} that shifts

to 2965 cm^{-1}. This signal corresponds to the contribution of the Ser and Thr. With 16E6 R_{-5}/A peptide the displacement is more pronounced, appearing at 2962 cm^{-1}.

Table 4.1-7. ν(C-H) region of PDZ1 in its free and bound form by Raman spectroscopy (Assignments are according to the studies of Howell *et al*[311] and Smith *et al*[237])

PDZ1 free	Bound 16E6	Bound 16E6$_{ct}$ 5 L_0/V	Bound 16E6$_{ct}$ 6 L_0/V	Bound 16E6 L_0/V	Bound 16E6 R_{-5}/A	Amino acids	Modes
2734	**2728**	**2725**	**2728**	**2728**	**2730**	Met	asymmetric ν(C-H)
2773	2772	**2768**	**2768**	**2768**	**2768**	His	asymmetric ν(C-H)
2875	2874	2874	2874	2874	2874	Ala, Val Ile Leu	symmetric ν(-CH_3)
2934	**2930**	**2930**	**2930**	**2930**	**2930**	Met, Arg,	symmetric ν(C-H)
2970	**2965**	**2965**	**2965**	**2964**	**2962**	Ser,Thr	symmetric ν(C-H)
3061	3060	3060	3062	3060	3060	Tyr	ν(α-CH)

4.1.4.3 Discussion

From the amide I and III modes it can be concluded that the main conformational changes upon binding are reflected in the β-turn elements of the secondary structure. This is in line with previous reports, that upon binding the βB suffers a structural modification as the binding sequence accommodates between αB-helix and this β-strand[319]. Nevertheless, from the fitting of the amide I band it seems that the structural changes reflect the structural rearrangement of the peptide more than the changes in the PDZ1 secondary structure.

The increase in the percentage of β-sheets beside the β-turns elements in presence of the 16E6 L_0/V and 16E6 R_{-5}/A peptide, suggests that a different hydrogen bonding pattern is occurring in the binding process with the mutant, as a result the peptide has a more pleated structure[77, 317]. This indicates that the non-covalent peptide–surface interaction involving the donation or addition of a β-strand in the ligand with a β-sheet as the receptor; the contact surface modulates the binding specificity and affinity.

SPR measurements, with a comparable dissociation constant in the micromolar range, of PDZ1 from MAGI-1 in presence of 16E6 and the same mutations analyzed here had

demonstrated that MAGI-1 PDZ1 shows a preference for C-termini with a Val residue at $P_{0.}$ Furthermore, SPR results made a relation of 16E6 L_0/V> 16E6 R_{-5}/A> 16E6[298].

Comparing these results with the hydrogen bonding collective modes in the FIR region, it is evident that the higher the affinity of PDZ1 for the peptide, the stronger the hydrogen bonding network. As a consequence, in the bound form with 16E6 L_0/V the pleated β-strand secondary structure of the peptide is directly modulated by this network.

In addition, FTIR Temperature dependence studies of PDZ2 from human protein tyrosine phosphatase 1E (hPTP1E) and the C-terminal of its cellular binder, the Fas receptor, have shown that the β-augmentation process is also reflected in the increase of the amide I absorption[320]. The same feature can be observed from comparison of the amide I intensity of bound forms and the free PDZ (Figure 4.1-13). It is important to state that the length of the peptide plays an important role in the intensity, which is almost twice in presence of the 11-residue peptides than in presence of the shorter peptides. This corroborates with what was observed by the amide I deconvolution, where in presence of the short peptide no relevant differences in the percentage of β-turns or β-sheets were observed.

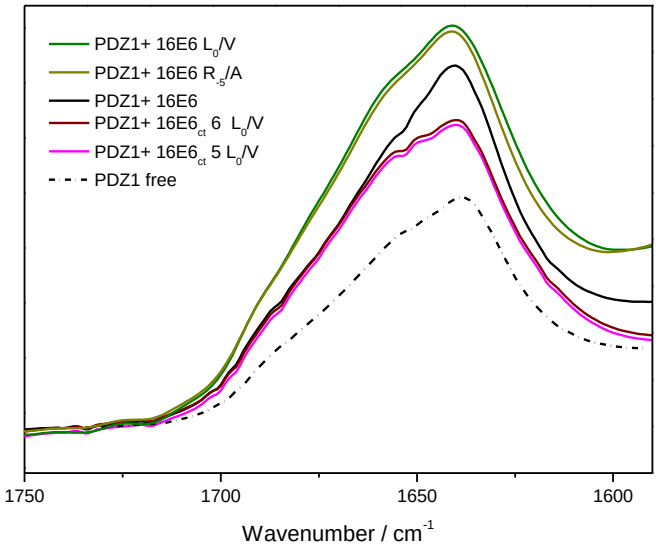

Figure 4.1-13. Amide I comparison of PDZ1 in its free form and bound form with the different 16E6 peptides

The summarized analysis of the amide II vibrations indicates that upon binding the PDZ1 backbone conformation changes in the presence of 16E6 and the 5 and 6 residue long peptides are similar, except for the C-N group; evident in the difference of the amide II' and amide VI band. In the presence of 16E6 peptide a different rearrangement of these groups is

evident. Furthermore, comparing the amide II vibration of the 16E6 R-$_5$/A and the 5-residue peptide bound form, it is clear that the N-H contribution is comparable. The main difference arises from the C=O as it is concluded from the changes in the amide I band, meaning that this residue helps as an anchor to maintain the backbone stability upon binding.

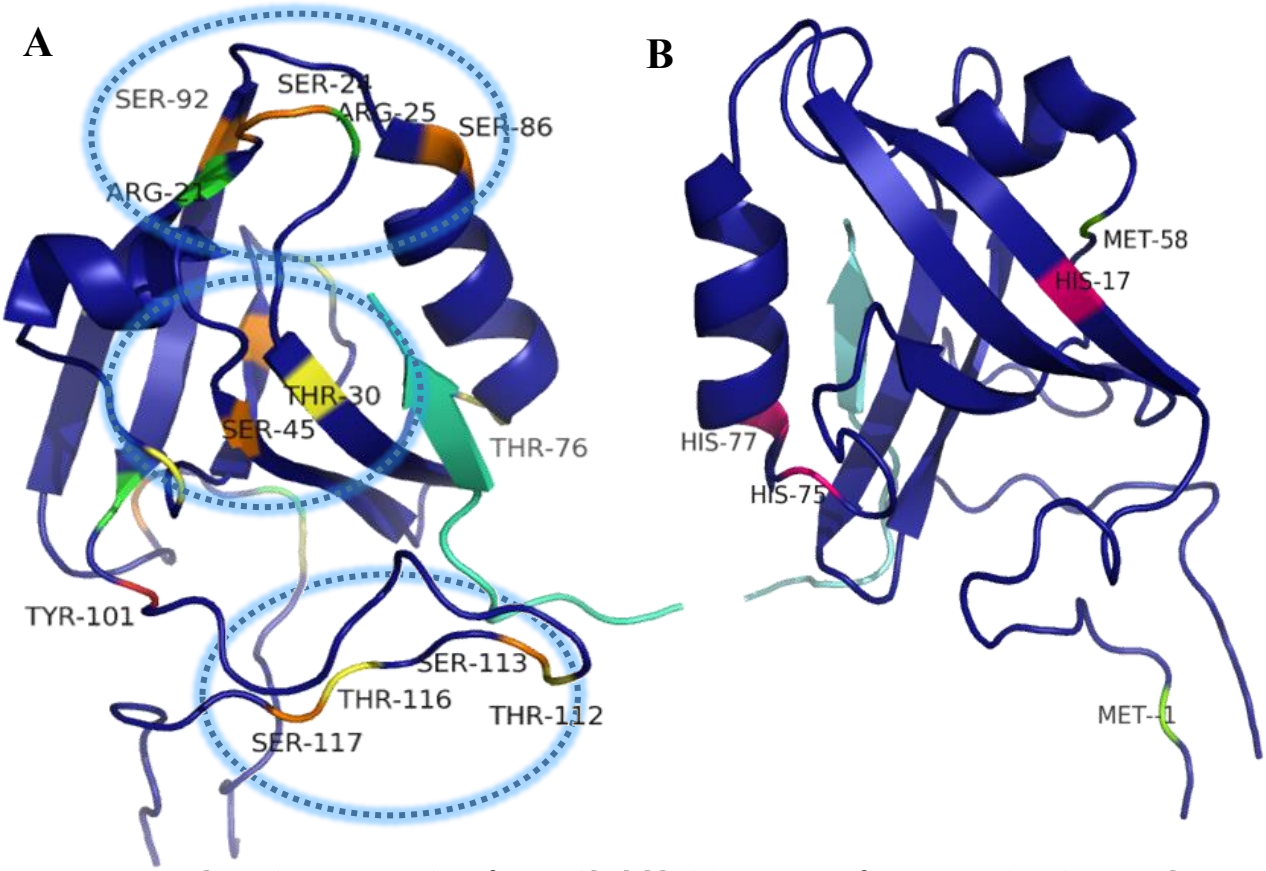

Figure 4.1-14. Schematic representation of PDZ1 (dark blue) in presence of 16E6 L0/V (cyan), In A. Thr (yellow), Ser (orange), Arg (green) and Tyr (red) residues are highlighted and in B. Met (green) and His (pink) and the probable candidates for the binding labeled.

According to the spectral differences of the amino acid side chains contributions, it is evident that Thr, Ser, Tyr and Arg residues play an important role in the binding process. The main differences of the Thr, Ser and Tyr indicate that most of these residues are hydrogen bonded in the bound form. For the Arg residues the changes are more related to different orientations of the side chain, as the vibrations affected were the ν(C-H) modes and the wagging of the N-H group.

On this basis, we can suggest the most probable candidate residues involved in the binding process. There are eight Thr residues in PDZ1 from MAGI-1 (Figure 4.1-14 highlighted in the yellow), from which the more proximal ones to the binding site are Thr30, Thr76 and Thr112 and Thr116. Only one Tyr, Tyr101 (marked in red). Four Arg residues, which Arg21 and Arg25 are the closest one to the binding area. There are nine Ser residues, which almost all are near the binding site, in Figure 4.1-14 they are highlighted in orange: Ser24, Ser45, Ser82, Ser96, Ser113 and Ser117.

Following the labeled residues it seems that there are three main regions where the residues hydrogen bonding seems to be the key role of the binding (Figure 4.1-14.A /blue circles) namely the C-terminal region, the connection between Thr30, Ser45, Thr60 and Tyr101 and the connection of the αB-βF loop and the βA-βB loop.

According to what was observed in the ν(C-H) region in the Raman spectra the Met and His residues present differences between the free and the bound form. In Figure 4.1-14.B three His residues are highlighted (pink), where the most probable ones to be involve in the binding are His75 and His77. However, for the Met residues the picture is not clear, as the only two Met residues present in the PDZ1 structure, Met1 and Met58, are far for the binding site.

4.1.5 The C-terminal of PDZ1 MAGI-1

In order to analyze the contribution from the C-terminus, three amino acids in this region (Ser113, Leu114 and Val115) were exchanged into three Gly. These residues had been proven to display intermolecular nuclear Overhauser enhancements (NOEs) with the 16E6 peptides[312]. SPR measurements showed that this mutation leads to a significant decrease in affinity in presence of the 16E6 peptide in comparison to the bound form of the WT protein. A 2.5 folds reduction affinity with 16E6 and five folds reduction with 16E6 L_0/V was reported[312].

The MIR spectra (Figure 4.1-15) of the GGG mutant show an amide I band at 1640 cm^{-1} and the amide II at 1541 cm^{-1} indicating small perturbations in the ν(C=O) vibration and a relevant conformational change in the (N-H)/C-N groups. In the spectrum of the mutant in ^2H_2O (Figure 4.1-16), amide II' arises at 1456 cm^{-1} showing to that ν(N-H) as well as the δ(N-H) are perturbed in the mutant.

The Amide III band in infrared is seen at 1240 cm^{-1}, the same wavenumber as in the WT and almost the same is observed for the amide III in the spectrum recorded by Raman (Figure 4.1-17). Only a slight shift is seen in the β-strand component at 1209 cm^{-1}. This indicates that no conformational changes are seen in these fragments of the secondary structure due to the mutation of these residues.

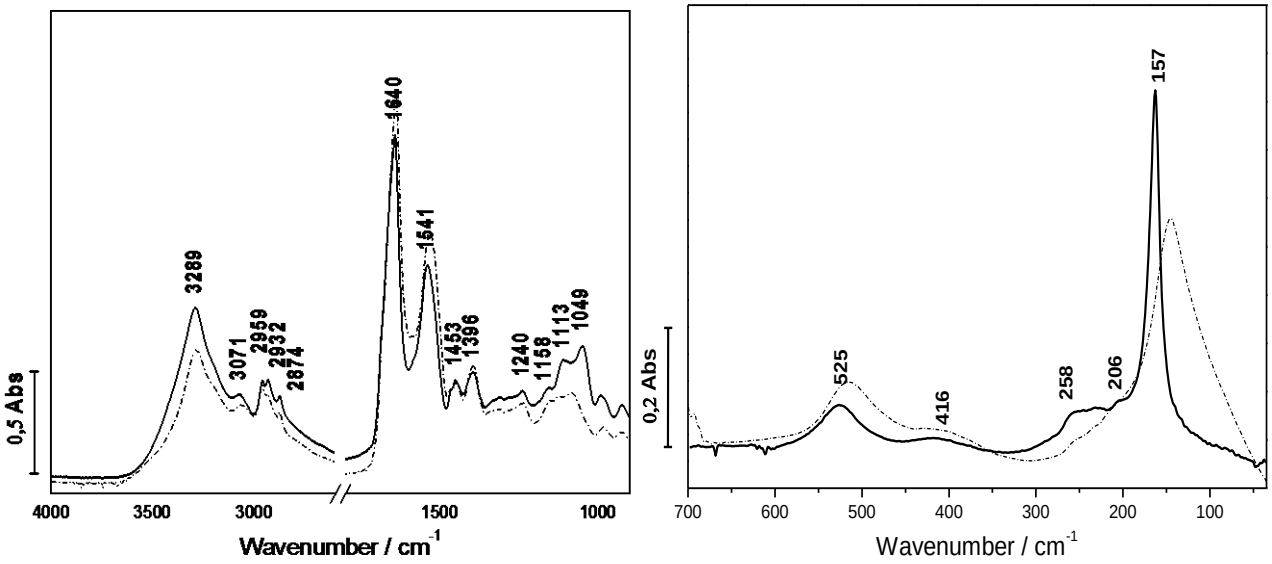

Figure 4.1-15. Mid and far infrared spectra of PDZ1 GGG (solid line) in comparison with PDZ1 WT (dotted line).

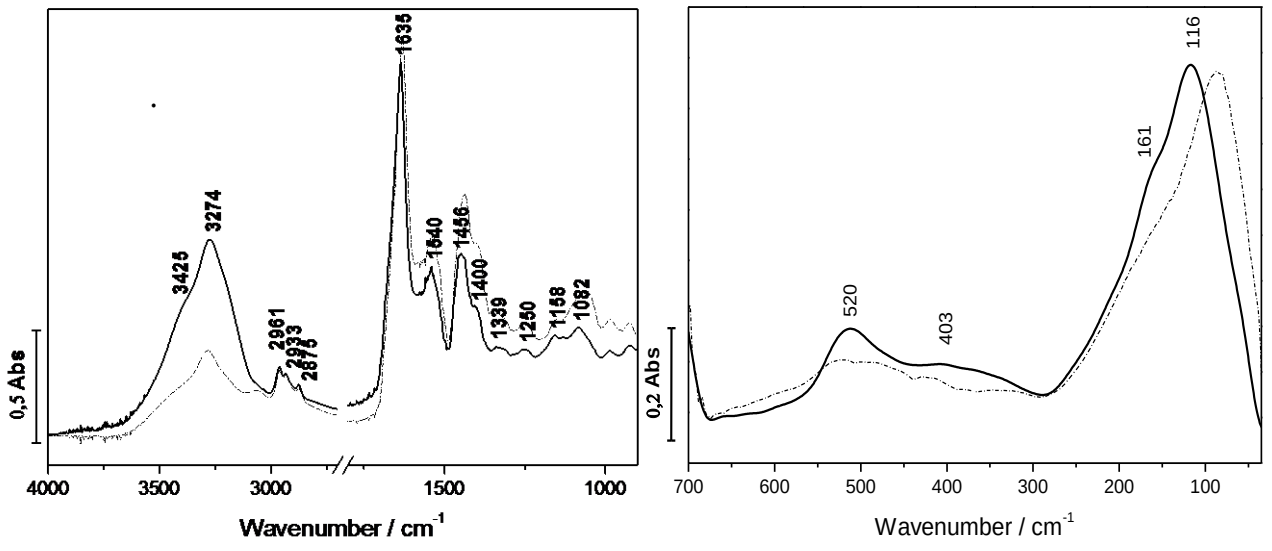

Figure 4.1-16. Mid and far infrared spectra of PDZ1 GGG in $^{2}H_2O$ (solid line) in comparison with PDZ1 WT (dotted line).

The main difference is that upon deuteration in the WT the signal shifts to 527 cm^{-1} and in the mutant in appears at 520 cm^{-1}, this suggests that the hydrogen bonding network is more affected by $H/^{2}H$ exchange in the WT (see Figure 4.1-16).

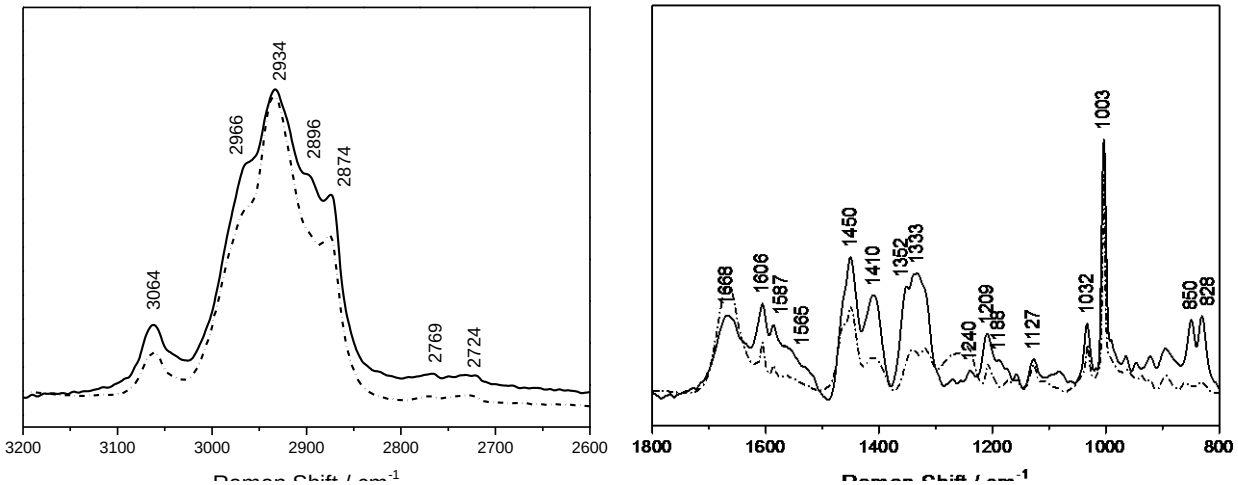

Figure 4.1-17. Raman spectrum of the PDZ1 GGG (solid line) in comparison to the PDZ1 WT spectrum (dotted line)

The signals at 1352 cm^{-1} and 1333 cm^{-1} in the Raman spectrum (Figure 4.1-17), corresponding to the symmetric and asymmetric deformation of the CH_3 and CH_2 groups, show not only changes in their frequency in comparison to WT but also a change in the intensity. Previous studies have related the intensity ratio between these signals (I^{1333}/I^{1352}) to an indication of the α-helix axis orientation, as the studies were made in *fd* filamentous viruses where the only secondary structure are α-helixes[321]. This is not the case of PDZ1. The difference in intensities may describe as a qualitative character of the conformational changes due to the mutated residues.

The amino acid chains perturbed by the mutations in the infrared spectrum are the vibrations of Thr, Ser and Tyr residues, whose signal arises at 1158 cm^{-1}. Beside this, two new signals arise at 1113 cm^{-1} and 1049 cm^{-1}, both had been assigned to the ν(C-O) modes of alcoholic group of Thr, Ser and Tyr[255, 299, 300]. In the Raman spectrum the contribution from the side chain of this amino acid can be confirmed by the band at 1400 cm^{-1} (Table 4.1-6).

The reason of how these mutations can have a direct effect on the Thr side chain can be described by Figure 4.1-18. From the eight Thr residues in the PDZ1 structure (marked in green), Thr112 and Thr 116 are located just in the vicinity of the mutated residues (black region); the changes to more mobile or flexible structure can shift the orientation and

interaction of the side chain of these residues, besides Thr30, Thr112 and Thr116, it cannot be ruled out that, through changes in the hydrogen bonding, Thr60 might be affected. In addition, the Ser113 was one of the mutated residues (see figure 4.1-14.A) and Ser117 is just next to it.-

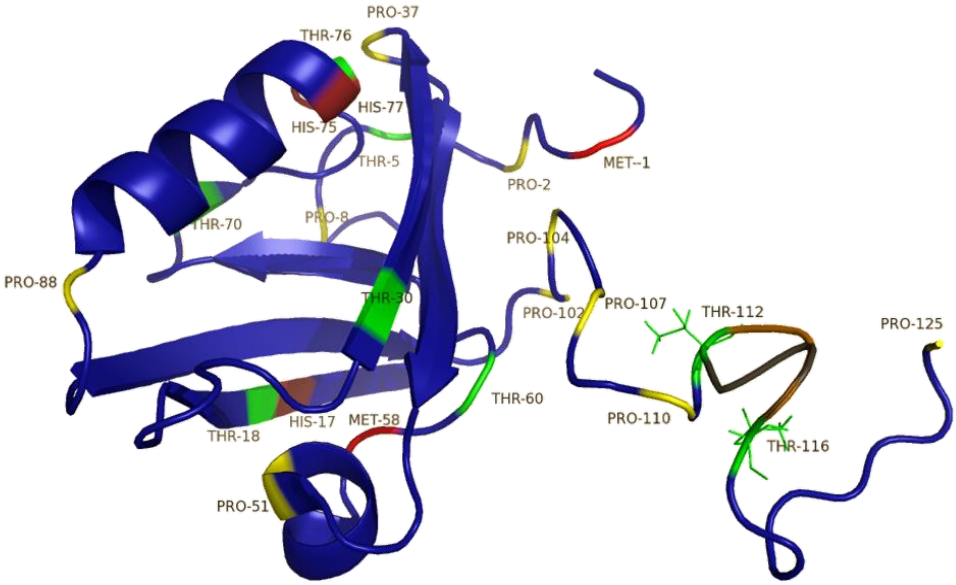

Figure 4.1-18. Schematic representation of PDZ1 GGG and simulation of the possible structural changes (black region) cause by the mutation

Another signal affected is the band in the Raman spectrum at 1188 cm^{-1} corresponding to the contribution of the rocking (C-O(H)) modes of Met residue. As it is shown in Figure 4.1-18 the most probable affected Met residues (marked in red) is Met1 located in the N-terminal region of the protein.

Beyond the effect on the backbone and the amino side chains contribution, the most outstanding differences are seen in the hydrogen bonding. In the infrared spectrum Amide A and amide B have changes of more than 5 wavenumbers going to higher frequencies, appearing at 3289 cm^{-1} and 3071 cm^{-1}, respectively. It is known that the frequency of these bands depend on the strength of the hydrogen bonding, the lower the frequency the higher the strength.[247]

The ν(C-H) region in the Raman spectrum shows variations from the vibrations of the WT in the Tyr vibrational modes, appearing at 3064 cm^{-1}, showing the effect on Tyr101. The Thr and Ser are seen at 2966 cm^{-1}, and His at 2796 cm^{-1}. It is important to remark that the three His residues (Figure 4.1-18 marked in pink) are located next to Thr residues, His17 –

Thr18 and His75-Thr76-His77. Nevertheless, these residues are located far from the mutated region. This suggests that small changes in the C-terminus can cause internal conformational changes the hydrogen network through the C-H groups. Another explanation could be that the changes the conformation are more related to the tertiary structure of the protein than to changes in the secondary structure.

Besides these bands, there is a new signal at 2896 cm^{-1}. It can be assigned to the symmetric ν(C-H) of Thr and Pro. In addition to the Thr residues already explained, there are five Pro residues that might be perturbed due to the mutation. In Figure 4.1-18 (marked in yellow) the positions of Pro102, Pro104 Pro107, Pro110 and Pro125 are shown.

In the FIR the spectral range corresponding to the hydrogen bonding shows a sharp band at 157 cm^{-1} that shifts upon deuteration to 116 cm^{-1} showing a second component at 161 cm^{-1}. As explained in previous paragraph the frequency reflect the strength of the hydrogen bonding[272, 305], as conclusion it can be seen that the strength of the hydrogen bonding network in the GGG mutant is weaker than in the WT. This new conformation of the hydrogen bonds may also be the cause of the conformational changes reflected in the shifts in Amide II and Amide II' band.

4.1.5.1 PDZ1-GGG and its interaction with HPV 16E6 peptides

The MIR (Figure 4.1-19), FIR (Figure 4.1-20) and Raman (Figure 7.2-5 and Figure 7.2-6) and spectra show several spectral changes upon binding of the PDZ1 GGG in presence of the different peptides, revealing the interaction between the C-terminus and the peptide sequence.

Backbone conformational changes. The amide vibrations are slightly affected, in comparison to what was described for the interaction between the different peptides and PDZ1 WT. In amide I a shift of 4-6 wavenumbers is observed in presence of the 11- residue peptides and a more significant shift is found with 16E6 L_0/V. Nevertheless is seems that interaction with the 5- and 6-residue peptides does not have the same effect on the protein, indicating that the upstream residues (P_{-7} –P_{-11}) are important in the interaction between the C-terminus and the HPV16 E6.

This is supported by the signals present in the Raman spectra (Table 4.1-8). Here, amide I only shifts in presence of 16E6 L_0/V from 1668 cm^{-1} to 1664 cm^{-1}, indicating that not only the peptide length have an effect on conformational changes but also the P_0 residue.

On the other hand, Amide II in the infrared spectra is shifted from 1541 cm^{-1} in the free form to 1536 cm^{-1} in presence of the shorter peptides. With the 11-residue peptides there is a slight shift to 1538 cm^{-1} in presence of 16E6 and 16E6 R_{-5}/A, a similar pattern is observed in the Raman spectra, where the signal shifts from 1565 cm^{-1} to 1560 cm^{-1}.

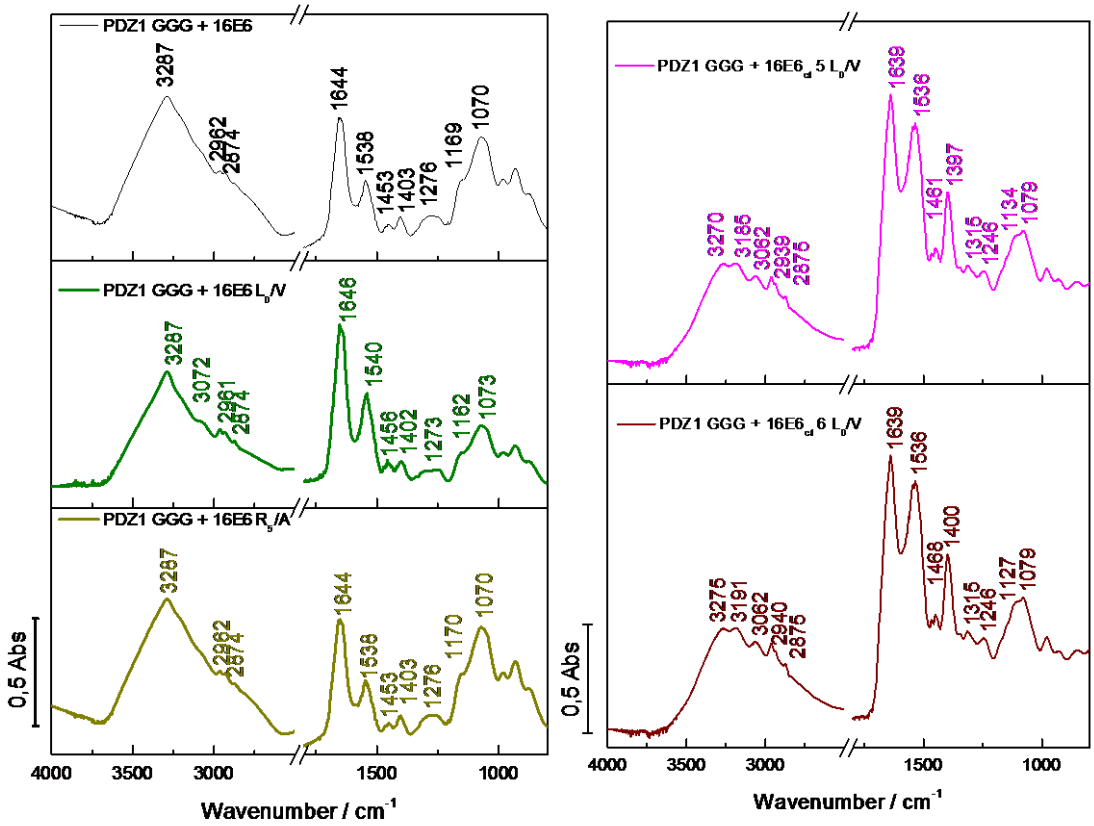

Figure 4.1-19. Mid infrared spectra of PDZ1 GGG interaction with the different HPV16 E6 peptides.

The amide III band in MIR shows a relevant displacement, in the case of the 11-residue peptides the signal shifts from 1240 cm^{-1} in PDZ1 GGG spectrum to 1276 cm^{-1} with 16E6 and 16E6 R_{-5}/A and to 1273 cm^{-1} with 16E6 L_0/V. For the spectra in presence of the short peptides the signal is visible at 1246 cm^{-1}, corroborating with what was observed with the amide I band. The residues (P_{-7} –P_{-11}) have an interaction with the C-terminus.

Table 4.1-8. Resume of the backbone vibrational modes of PDZ1 GGG in its free and bound forms by Raman spectroscopy

PDZ1 GGG free	Bound 16E6	Bound 16E6$_{ct}$ 5 L_0/V	Bound 16E6$_{ct}$ 6 L_0/V	Bound 16E6 L_0/V	Bound 16E6 R_{-5}/A	Modes
1668	1669	1669	1668	**1664**	1667	Amide I
1565	1565	**1560**	**1560**	1565	1564	Amide II
1352/ 1333	**1358/ 1332**	1352/ 1334	**1357/ 1332**	**1359/ 1335**	**1351/ 1338**	δ(C^{α}-H)
1268	**1270**	**1254**	**1271**	**1271**	**1270**	Amide III β-turns
1240	**1242**	**1236**	**1240**	**1241**	**1245**	Amide III β-strand

In Raman, the component corresponding to the β-turns in the amide III region is the most affected in presence of the 5-residue peptide going to lower frequency. However in presence of the other peptides the signal shows a small shift to higher wavenumbers.

For the amide III β-strand component, in presence of the 16E6 R_{-5}/A the perturbation is more pronounced than in presence of the other 11-residue peptides in the β-strand, where the signal shifts to higher frequency, namely to 1245 cm^{-1}. In comparison, in presence of the 5-residue peptide the signal appears at 1236 cm^{-1}, suggesting that the P_{-5} and P_{-6} are the main contact points between the C-terminus of PDZ1 and the viral protein. This is corroborated with the signals in the other bound forms, where no major changes are observed upon the binding for this vibrational mode.

In the Raman spectra the vibrations corresponding to the δ(Cα-H) modes, are not perturbed in presence of 16E6$_{ct}$ 5 L_0/V nevertheless in all the rest of the spectra the signal appear around 1358 cm^{-1} and 1332 cm^{-1}, but in presence of 16E6 R_{-5}/A the signals arise at 1351 cm^{-1} and 1338 cm^{-1}, so this peptide does not affect this vibration in the same way as the others.

In the FIR spectra (Figure 4.1-20) Amide VI shows a significant change to lower wavenumber with the 5-residue peptides as well as in presence of 16E6, though in presence of the rest of the peptides the signal shifts to higher wavenumbers. The more pronounced displacement is found in presence of 16E6 L_0/V, where the signal is detected at 531 cm^{-1}. These results are interconnected with the amide I and amide II band, indicating that not only the peptide length have an effect on conformational changes but also the P_0 residue.

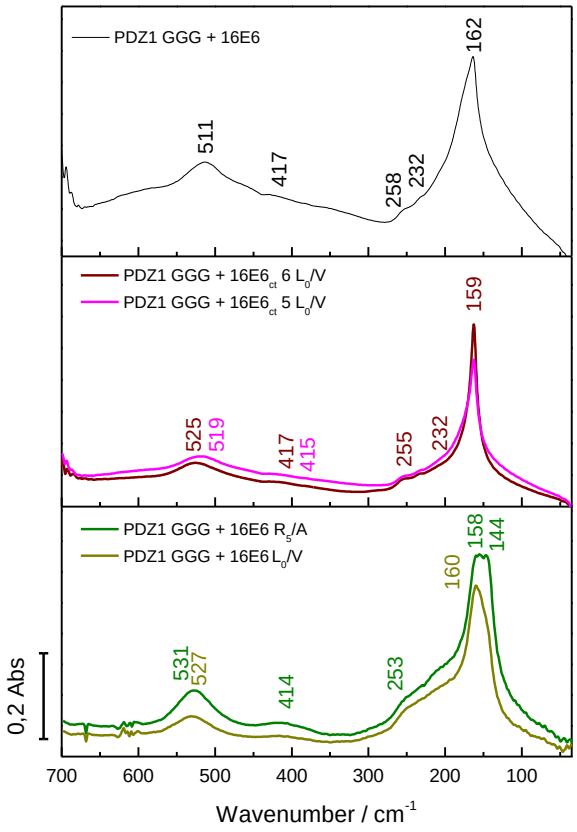

Figure 4.1-20. FIR spectra of PDZ1 GGG interaction with the different HPV16 E6 peptides.

Amino acid side chains. A complete description of all the contributions from the amino acid side chain vibrations observed in the Raman spectra of each of the bound forms is shown in Table 4.1-9. From this resume it is important to note that in all the bound forms perturbation of the Thr modes are observed, as it is also seen in their infrared spectra. The displacements are less pronounced in presence of the 16E6$_{ct}$ 5 L$_0$/V and 16E6 R$_{-5}$/A.

A similar pattern is seen with wagging NH_3^+ and rocking NH_3^+ modes coming from Arg, Ser, Val, that are only perturbed in presence of 16E6, 16E6 L$_0$/V and 16E6$_{ct}$ 6 L$_0$/V. This directly indicates that the Thr and Arg near the C-terminus and the Ser and Val residues, near or in the C-terminus have an interaction with P$_{-5}$ and P$_{-6}$.

In the presence of 16E6$_{ct}$ 5 L$_0$/V, perturbation of ring vibrational modes of Phe and Tyr are observed. Given that there is a relation between the C-terminus and the stability of the protein through these residues upon binding, as no changes in this band were observed upon binding in the PDZ1 WT.

Table 4.1-9. Amino acid side chain vibrations from the PDZ1 GGG interaction with HPV16E6 peptides

PDZ1 GGG free	Bound 16E6	Bound $16E6_{ct}$ 5 L_0/V	Bound $16E6_{ct}$ 6 L_0/V	Bound 16E6 L_0/V	Bound 16E6 R_{-5}/A	Amino acids	Modes
1606	**1608**	1605	1606	1606	1606	Tyr	Ring breathing
1450	**1447**	1450	1449	1449	1450	Ala, Leu, Phe	$\delta(CH_2)$
1410	**1419**	**1416**	**1416**	**1416**	**1415**	Thr	δ(Cα-H)
1209	1210	**1205**	1210	1210	1209	Phe Tyr	symmetric ν(Ring –O)
1171	**1175**	**1178**	1172	1170	**1168**	Met	δ(C-H)
1188	1188	**1183**	1186	1188	1188	Iso Leu	rocking $NH3^+$ δ(Cγ1–Cβ–Cγ2)
1127	**1120**	1127	**1121**	**1121**	1127	Arg Ser, Val	wagging NH_3^+ rocking NH_3^+
1032	**1037**	**1033**	**1037**	**1037**	**1036**	Thr Phe	OH def δ(C-H) def
1003	1003	**1001**	1003	1003	1003	Phe	Ring breathing
850 828	850 831	**847 828**	847 826	845 831	848 831	Tyr	Fermi doublet

Another important remark is that upon complex formation, the δ(C-H) modes of the Met residues undergo different displacements. In presence of the 16E6 this signal goes from 1171 cm^{-1} to 1175 cm^{-1}, in presence of $16E6_{ct}$ 5 L_0/V it arise at 1178 cm^{-1} and in presence of 16E6 R_{-5}/A it arises at 1168 cm^{-1}. For the other two peptides there are no relevant changes. The P_{-5} seems to have a direct interaction with the Met residues, probably Met1 (Figure 4.1-18). In the 16E6 R_{-5}/A as the amino acid side chain of the peptides is shorter; it might have an effect in the binding. In the WT bound forms the Met residues are affected in the same way upon binding.

Hydrogen bonding. In the MIR spectra (Figure 4.1-19) variations in the amide A and B as well as in the ν(C-H) region are remarkable. In case of the spectra in presence of the 11-residue peptides, upon binding amide B is barely visible due to the increase in the absorption intensity of amide A, even though there is only a slight shift in the frequency of this band, it shifts from 3289 cm^{-1} to 3287 cm^{-1}.

For the shorter peptides the spectra's characteristics are quite different. Amide A appears at 3270 cm^{-1} in presence of $16E6_{ct}$ 5 L_0/V and at 3275 cm^{-1} in presence of $16E6_{ct}$ 6

L_0/V. Amide B have a shift from 3071 cm^{-1} to 3062 cm^{-1}. Additional to these bands, a new signal arises at 3185 cm^{-1} for 16E6$_{ct}$ 5 L_0/V and at 3191 cm^{-1} for 16E6$_{ct}$ 5 L_0/V, this signal corresponds solely to the ν(N-H) vibrations that are usually coupled to the ν(O-H) vibrations in amide A.

In Raman, the signals arising in the ν(C-H) region are summarized in Table 4.1-10. The asymmetric ν(C-H) vibrational modes arising from the Met residues show a similar pattern of the side chain contribution already described before from this amino acid, in presence of 16E6 the signal goes to higher frequencies as well as in presence of 16E6$_{ct}$ 5 L_0/V but in presence of 16E6 R$_{-5}$/A the band arises at lower wavenumbers. But the symmetric ν(C-H) only shows a slight difference in presence of 16E6 R$_{-5}$/A.

For the rest of the signals in this region it is important to remark that only in presence of 16E6 and 16E6 R-$_5$/A a perturbation of the His vibrations in this spectral region is observed.

Table 4.1-10. ν(C-H) region of PDZ1 GGG in its free and bound form by Raman spectroscopy

PDZ1 GGG free	Bound 16E6	Bound 16E6$_{ct}$ 5 L_0/V	Bound 16E6$_{ct}$ 6 L_0/V	Bound 16E6 L_0/V	Bound 16E6 R-$_5$/A	Amino acids	Modes
2724	**2728**	**2732**	2725	2725	**2721**	Met	asymmetric ν(C-H)
2769	**2772**	2769	2769	2769	2767	His	asymmetric ν(C-H)
2874	**2869**	2873	**2869**	**2868**	**2868**	Ala, Val Ile Leu	symmetric ν(-CH_3)
2896	--	**2890**	**2890**	**2890**	2898	Thr, Pro	symmetric ν(C-H)
2934	2935	2935	2935	2935	**2932**	Met	symmetric ν(C-H)
2966	2966	2965	2965	2966	2966	Ser,Thr	symmetric ν(C-H)
3064	3063	**3060**	3064	3063	**3061**	Tyr	ν(α-CH)

For the hydrogen bonding collective modes in the FIR (Figure 4.1-20), with all the 11-residue peptides the band becomes broader in comparison to the free form of the mutant (Figure 4.1-20), which shows the contrary effect observed with the WT PDZ1 and its interaction with the peptides. With the shorter peptides no major changes in the shape or the frequency are seen.

For 16E6 bound form, the band arises at 162 cm^{-1}, the shape of the signal is very different from the other bound forms. With 16E6 L_0/V the signal arises at 160 cm^{-1}, while with 16E6 R_{-5}/A the signal splits into two peaks at 144 cm^{-1} and 158 cm^{-1}.

The spectral differences in this region indicate that, regardless of the affinity of the peptide, the effect of the mutation is similar upon binding. Nevertheless, the differences between the bound form of 16E6 and 16E6 L_0/V showed that the C-terminus of PDZ1 is a key region in the strength of the hydrogen bonding network upon binding. How a mutation in the P_0, that has a higher binding affinity, can be correlated to hydrogen bonding form by the residues of the C-terminus is still an open question.

However, it can be concluded, according to the results, that the interaction of $P(_{-5\text{-}11})$ residues with the C-terminus, are important for the strength of the hydrogen bonding upon binding, especially the P_{-5} residue.

4.1.5.2 Discussion

In summary, the changes in the backbone vibrations indicates that upon binding the dynamics of the protein are very different for the peptides of 6 and 11 residues than for the peptide of 5 residues. From the differences in the bands displacement, it can be concluded that the PDZ1 GGG-16E6$_{ct}$ 5 L_0/V has a complete different set of characteristics than the rest of the bound forms, showing that the interaction between the P_{-6} with the C-terminal has significance for the final conformation necessary to form the complex.

Furthermore, the amide III analysis shows that mutation in P_{-5} position has a larger effect on the β-sheet interactions between the protein and the peptide. Additionally, comparing the interaction between the bound form with 16E6 and 16E6 L_0/V, it is evident that variations in the P_0 position meaning changes in the secondary structure. These modifications are not only affecting the N-H and C-N groups, as it was seen in the interaction of the peptides and the PDZ1 WT, but also the C=O groups of the amide bonds. The C-terminus plays a role in maintaining the backbone groups in its place upon binding and also through a strong hydrogen bonding network with the P_{-5} and $P(_{-7\text{-}11})$ residues of the viral protein.

It is surprising how a mutation in the P_0 position of the peptide and its interaction with the binding loop can affect the C-terminal motions, this leads to conclude that not only the direct interaction between the αB and βB with the peptide is important to stabilize the binding

and form the complex. Comparing to what was observed in the interaction of the WT and the different peptides, the first difference is the broadness of the band, in the case of the WT the signal becomes sharper upon binding and in the interaction of the PDZ1 GGG the signal becomes broader, pointing towards that the C-terminal is a crucial of assembly of the hydrogen bonding network to stabilize the binding.

From the side chains vibrational modes, it is evident that the Thr, Ser, Val and Arg residues have a direct role in the interaction with the P_{-5} and $P(_{-7-11})$ residues while the Met and His residues do not seem perturbed in the mutant in presence of the peptides L_0/V and R_{-5}/A, as it was observed with PDZ1 WT. This suggests that the residues in the interaction between the C-terminus and the peptide have an effect on other areas of the protein besides the binding loop.

4.1.6 Variations in the βC-strand

By NMR spectroscopy the binding of the 16E6 L_0/V to the PDZ1 domain of MAGI-1 results in significant spectral changes, a part of the global response of the PDZ domain to the peptide binding besides the changes in the residues close to the binding site supplementary changes were observed around Lys44, a residue of the βC-strand sequence[312]. According to these results, the carboxylate group from the peptide C-terminal interacts with the backbone of the GFGF motif, and additional hydrogen bonds are formed between the backbone of βC-strand and the peptide. A similar result was obtained in X-ray structure of PDZ1 with HPV18 E6[98].

As a part of the conclusion of previous studies, the mutation of Lys44 residue against Glu (K44/E) or Ala (K44/A) residue does not affect the folding of the PDZ domain, these variants were classified as functional mutants[298], allowing them to be good candidates for the study of hydrogen bonding changes upon binding. The only important difference is seen in K44/A where the mutation causes chemicals shift on several residues of the C-terminal extension[312]. Additionally, the solution structure showed an interaction between P_{-3} and Lys44[298].

Backbone conformational changes. The MIR spectra of both variations (Figure 4.1-21) in comparison with the WT PDZ1 (Figure 4.1-2) show Amide I at 1636 cm^{-1}, which is at the same frequency and has the same characteristics (amide I fitting) as the WT spectrum. It is

also similar for amide II in the K44/E spectrum, while in the case of the K44/A mutant there is a slight shift in the frequency, where the signal arise at 1525 cm^{1}.

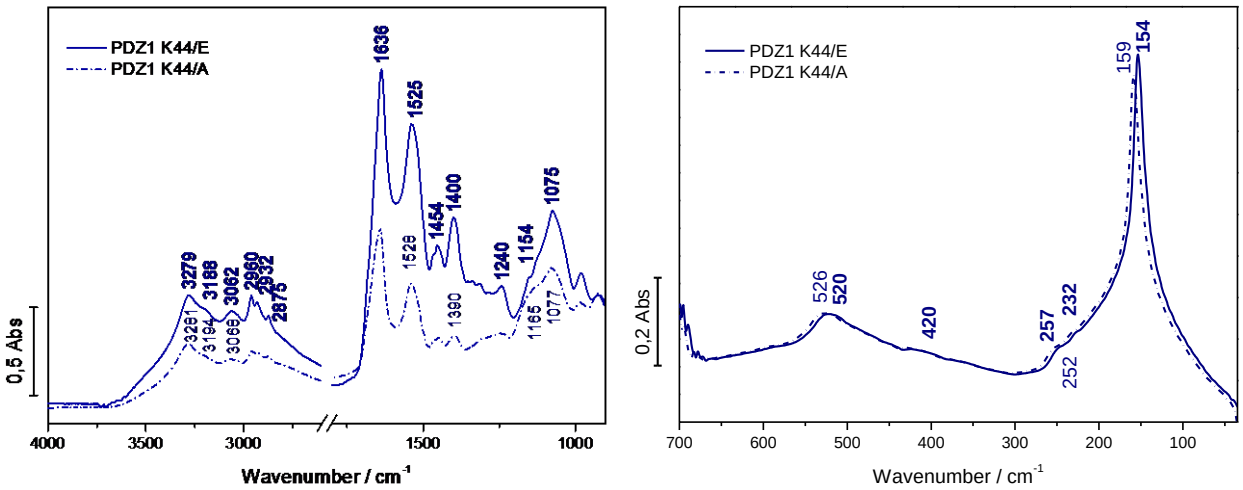

Figure 4.1-21. MIR and FIR spectra of PDZ1 K44/E (solid line) and PDZ1 K44/A(dotted line) in H_2O

The same can be seen for the amide I and amide II signals in the Raman spectra (Figure 4.1-22) were amide I is found at 1667 cm^{-1} for both mutants and amide II at 1565 cm^{-1} for K44/E and at 1570 cm^{-1} for K44/A.

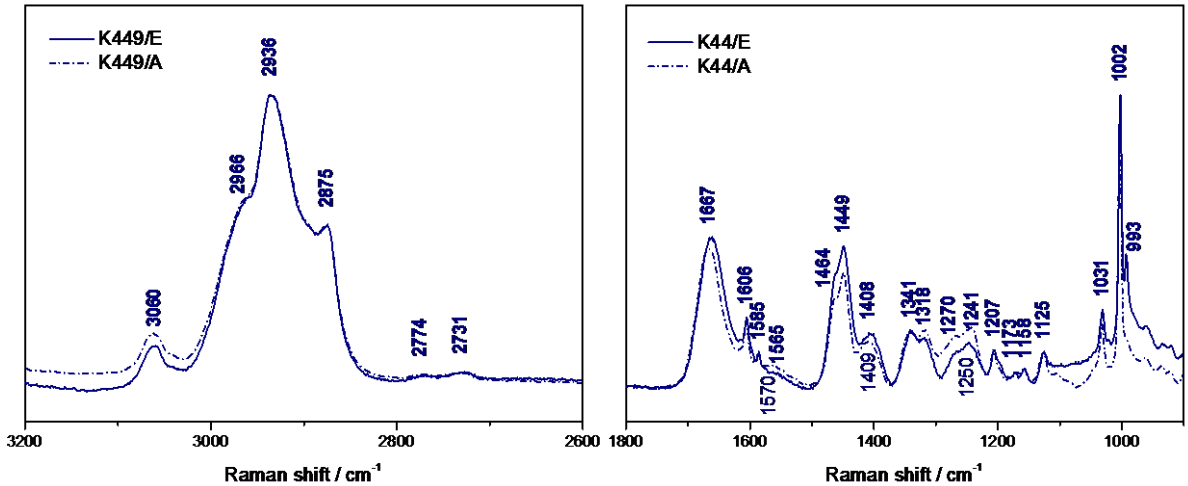

Figure 4.1-22. Raman spectra of PDZ1 K44/E(solid line) and K44/A(dotted line)

The amide III band arises at 1240 cm^{-1} for mutants in infrared and in Raman it is observed at 1241 cm^{-1} for the β-strand component and at 1270 cm^{-1} for the β-turn component. In the spectrum of K44/A a shift is seen in the first component where the signal arises at 1250 cm^{-1} points towards a different conformation of the β-strands.

The amide VI in the FIR region, however, shows a relevant shift in the frequency due to mutations. For K44/E the signal arises at 520 cm^{-1} and for K44/A at 526 cm^{-1}. Given that this vibrational mode is the combination of δ(C=O) in-plane and out-of-plane in addition to the (C-C-N) deformations modes; from amide I it is established that the C=O groups do not have any perturbation, therefore, the changes seen in amide VI are more probable to be caused by the changes in the C-C-N groups. This indicates that the mutation affects the dihedral angles of the amide bonds.

Amino acid side chains. From the amino acid side chain vibrations the main difference found in the Raman spectra is the signal at 1408 cm^{-1} corresponding to the δ(C-H) from the Thr residues in K44/E spectrum and the signal at 1125 cm^{-1} corresponding to the contribution of the wagging and rocking of the N-H groups from Arg, Ser and Val residues.

A feature that calls the attention is the appearance of a signal at 993 cm^{-1} for both mutations, this signal corresponds to the of the ν(C-C) and ν(C-N) vibrations of Ile residues.

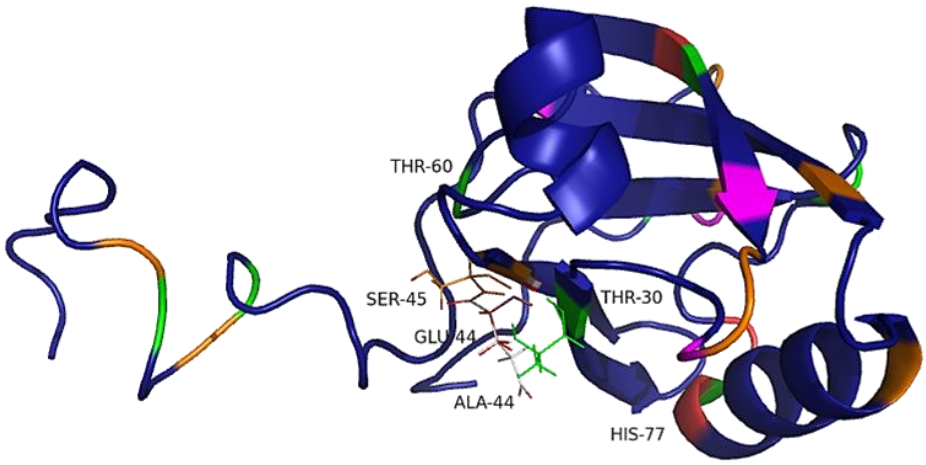

Figure 4.1-23. Schematic representation of the PDZ1 K44/E (red region) and PDZ1 K44/A (grey region) (PDB: 2KPK displaying His residues (soft red) Thr residues (green) and Ser residues (orange)

Hydrogen bonding. The more important modifications in comparison with the WT spectrum are seen in the bands related to the hydrogen bonding. Amide A (Figure 4.1-21) signal arising at 3279 cm^{-1} and 3188 cm^{-1} in the case of K44/E and at 3281 cm^{-1} and 3194 cm^{-1} for K44/A. Amide B only have a relevant displacement in the K44/A mutant arising at 3068 cm^{-1}.

In the ν(C-H) region in the IR spectra (Figure 4.1-22), a minor shift in the signals at 2960 cm^{-1}, 2932 cm^{-1} and 2875 cm^{-1} for both mutants is observed. In the Raman spectra the only perturbed vibration is the signal at 2966 cm^{-1} that in the WT was observed at 2970 cm^{-1}, this signal correspond to Ser and Thr symmetric ν(C-H).

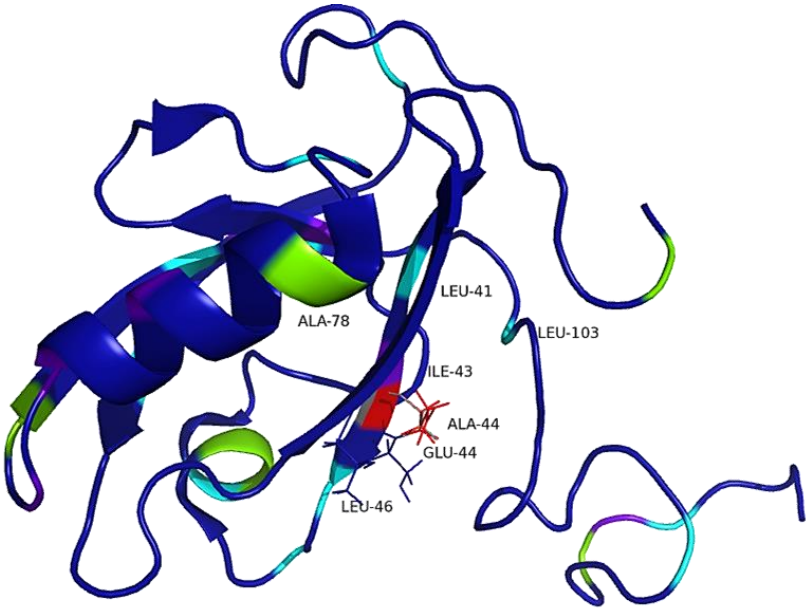

Figure 4.1-24. Schematic representation of PDZ1 K44/E superimpose with K44/A. (PDB:2KPK) displaying the Ala residues (green), Leu residues (cyan) and Ile residues (purple).

The FIR collective modes show a major change in the broadness and the frequency of the band, the band in the mutant's spectrum is sharper than the band observed in the WT spectrum. For K44/E the band arises at 154 cm^{-1} and for K44/A it arises at 159 cm^{-1}.

This difference in the hydrogen bonding vibrational modes can be directly correlated to the residue's position, the side chain of the amino acid is positioned on the most exposed part of the domain (Figure 4.1-23), it can be suggested that the interactions between the positively charged side chain like Lys44 been mutated to a neutral residue, as is the case of K44/A, or to a negative charged residues as is the case of K44/E, modify the electrostatic interactions between the protein and the solvent.

The small perturbation observed in the amino acid chain can be correlated to the interaction between Lys44, Thr30 and Ser45 (see Figure 4.1-23). According to the $H/^{2}H$ exchange by NMR this Thr30 has an group of hydrogen bonds with Lys44 and Ser45[312]. The

schematic representation in Figure 4.1-23 shows the possible amino acids affected by the mutation. From all the eight Thr residues (marked in green) present, the closest ones are Thr30 and Thr 60, given the orientation of the Glu or Ala side chain is more probable that the interaction is with the Thr30. For the Ser residues (marked in orange) the only residue close enough to the mutation site is indeed Ser45.

In general, the replacement of this residue with a neutral and negatively charged amino acid does not cause major backbone changes, but generates motions in specific amino acids around the mutated site. Besides this, it is evident that the hydrogen bonding of the protein does not have the same conformation as in the WT.

4.1.6.1 βC- strand variations and its interactions with HPV16 E6 peptides

By SPR it was shown that the interaction between PDZ1 K44/A and 16E6 L_0/V peptide has an affinity that is two folds attenuated as compared to the PDZ1 WT, in contrast the PDZ1 K44/E totally abolishes the interaction in presence of the 16E6 peptide[298, 322].

Congruently, even if the spectra of the mutants alone do not show many differences in comparison to the WT, spectral differences are observed in the behavior of the mutations in presence of the HPV16 E6 peptides. K44/A and K44/E do not present the same properties upon binding; variances in the amide vibrations as well as the hydrogen bonding are described.

***Backbone conformational changes*.** The MIR spectra of the interaction of K44/A with the HPV16 E6 peptides (Figure 4.1-25) show a displacement of amide I only in presence of the 11-residue peptides, the more pronounced shift is seen in presence of 16E6, where the signal arises at 1642 cm^{-1}. For the other bound forms with 16E6 L_0/V and 16E6 R_{-5}/A, the signal arises at 1640 cm^{-1}. In the Raman spectra of the bound forms with K44/A (Resume in Table 4.1-11), it is evident that there are no relevant changes in the Amide I vibration upon binding.

However, for the K44/E mutation, in the infrared spectra amide I shifts from 1636 cm^{-1} in the free protein to 1641 cm^{-1} in presence of all the peptides. In Raman, amide I shifts from 1667 cm^{-1} to 1670 cm^{-1} with the short peptides and to 1671 cm^{-1} with 16E6 and 16E6 L_0/V. For the bound form with 16E6 R_{-5}/A the signal is at 1672 cm^{-1}.

In summary, it can be concluded that, the mutation of Lys44 for a negatively charged residue, gives as a consequence changes in the C=O amide groups, and that these changes are more pronounced in presence of the 16E6 R_{-5}/A peptide indicating a different interaction between the Lys44 and the P_{-5} when this Arg residue is mutated of the HPV16 E6 peptide.

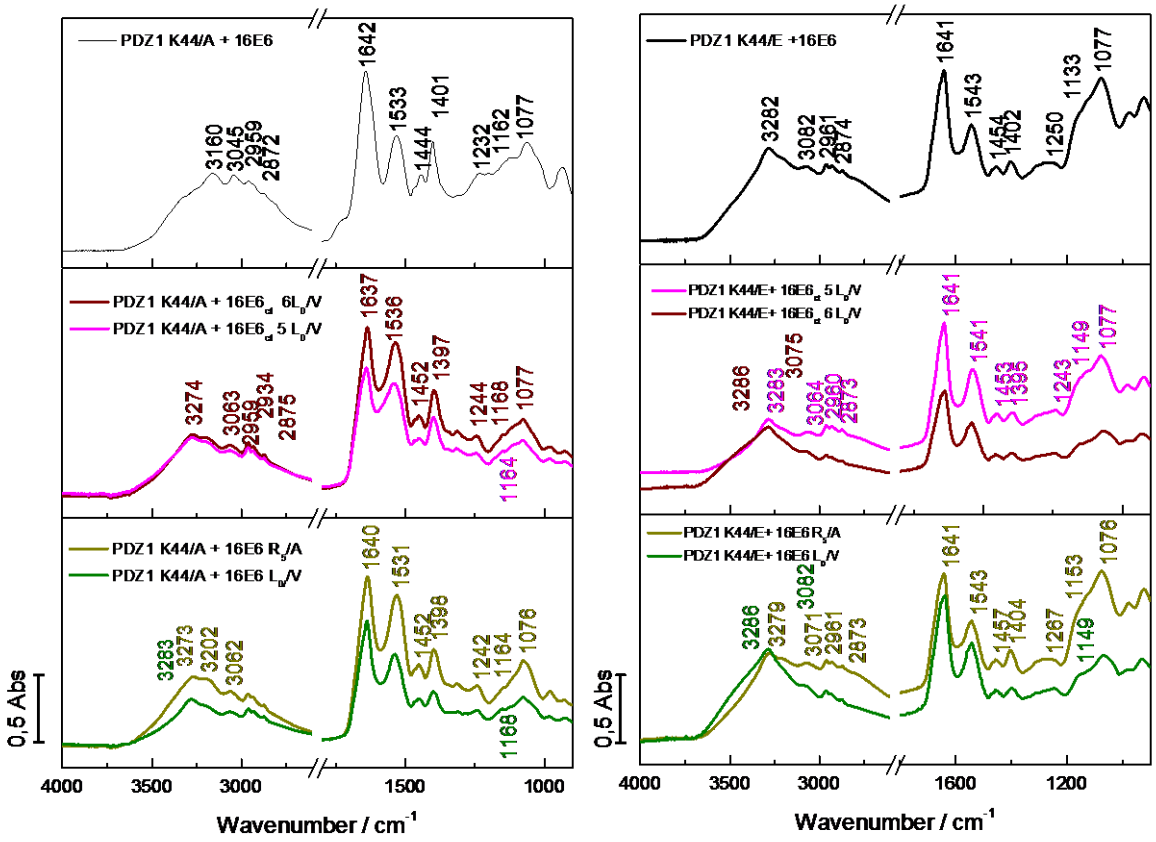

Figure 4.1-25. MIR spectra of the PDZ1 K44/A (right) and K44/E interaction with the different HPV16 E6 peptides

For amide II, the complex formation with K44/A in infrared displays a displacement of the signal to higher wavenumbers, this effect is more marked with the short peptide where the signal arises at 1536 cm^{-1}. Instead with 16E6 the band arises at 1533 cm^{-1} and with 16E6 L_0/V and 16E6 R_{-5}/A it arises at 1531 cm^{-1}. A similar pattern is seen in the amide II of the Raman spectra (Table 4.1-12), for the bound forms with the short peptides the signal appears at 1570 cm^{-1} and with 16E6 it appears at 1569 cm^{-1}. With the other two 11-residue peptides it appears at 1568 cm^{-1}. It seems that the lower the affinity for the peptide the larger the changes of this vibrational mode, similar patterns were observed in the interactions between the PDZ1 WT and the HPV16 E6 peptides.

For K44/E in infrared, the amide II arise at almost the same frequency in presence of all the peptides, for the bound form with 11-residue peptides it arise at 1543 cm^{-1} and with the short peptides at 1541 cm^{-1}.

In Raman (Table 4.1-11), amide II band shifts from 1570 cm^{-1} to ~1574 cm^{-1} in all the bound forms. It is important to notice that with K44/E the displacement of this signal upon binding in the infrared spectra is more pronounced than with K44/A, however in Raman the shift in the amide II band is more or less of the same magnitude for both mutations. This difference between both techniques is because in Raman amide II has a low scattering having a low resolution of the signal.

Table 4.1-11. Summary of the backbone vibrational modes of PDZ1 K44/A and K44/E in its free and bound forms by Raman spectroscopy

Modes (cm^{-1})	Amide I		Amide II		δ(Cα-H)		Amide III β-turns		Amide III β-sheet	
K44/X =	A	E	A	E	A	E	A	E	A	E
Free	1667		1565	1570	1408		1270		1241	1250
+ 16E6	1666	**1671**	**1569**	**1574**	1407	1407	**1267**	1268	**1246**	**1257**
+16E6$_{ct}$5 L_0/V	1666	**1670**	**1570**	**1573**	1408	1407	1270	**1266**	1242	**1255**
+16E6$_{ct}$6 L_0/V	1667	**1670**	**1570**	**1573**	1407	**1403**	1269	**1266**	1242	**1255**
+ 16E6 L_0/V	1667	**1671**	**1568**	**1573**	1407	**1402**	**1267**	**1263**	**1247**	**1259**
+ 16E6 R_5/A	1667	**1672**	**1568**	**1574**	1407	1407	**1267**	**1263**	**1246**	**1259**

The amide III band in the infrared spectra (Figure 4.1-25) of the bound form with K44/A displays a shift to lower wavenumbers is presence of 16E6, appearing at 1232 cm^{-1} and a shift to higher wavenumbers with all the other peptides, where it is observed at ~1242 cm^{-1}.

In Raman, the amide III component for the β-turn does not display any shifts in presence of the short peptides as well as the β-strand component. However in presence of the 11-residue peptides the band corresponding to β-turns component has a slight shift, from 1270 cm^{-1} to 1267 cm^{-1}. For the β-strand component the signal shifts from 1241 cm^{-1} to higher wavenumbers, arising at 1246 cm^{-1} for 16E6 and for 16E6 L_0/V and 16E6 R_{-5}/, at 1247 cm^{-1}.

On the other hand, infrared amide III of the bound forms with K44/E shows a shift to higher wavenumbers with the short peptides; arising at 1243 cm^{-1}. With 16E6 the band a more pronounced shift appearing at 1250 cm^{-1} and with 16E6 L_0/V and 16E6 R_{-5}/A it arise at 1267 cm^{-1}.

Amide III of the β-turns vibrational modes in Raman upon binding shifts to lower wavenumbers with 16E6 it shifts only to 1668 cm^{-1}, with the short peptides it arises at 1266 cm^{-1}, with 16E6 L_0/V and 16E6 R_{-5}/A in appear at 1663 cm^{-1}. For the β-strand component of this vibrational mode, the signal shifts to higher frequencies, with the shorter peptides it arise at 1255 cm^{-1}, with 16E6 appears 1257 cm^{-1} and with 16E6 L_0/V and 16E6 R_{-5}/A is at 1259 cm^{-1}.

The results of amide III suggest that the addition of the β-strand as part of the binding process is being perturbed due to the mutation, where in the case of the K44/A in comparison to the changes observed in K44/E upon binding, there is only a partial β-strand addition.

In the FIR spectra (Figure 4.1-25), amide VI of the K44/A-peptide complexes shows that with the short peptides the signal goes from 526 cm^{-1} to lower wavenumbers, arising at 518 cm^{-1} for 16E6$_{ct}$ 5 L_0/V and at 523 cm^{-1} with 16E6$_{ct}$ 5 L_0/V. With the 11-residue peptides no changes are detected in presence of the 16E6 peptide and a slight shift is seen with 16E6 L_0/V for the signal at 528 cm^{-1}. Nevertheless with 16E6 R_{-5}/A the signal has a pronounced displacement appearing at 535 cm^{-1}.

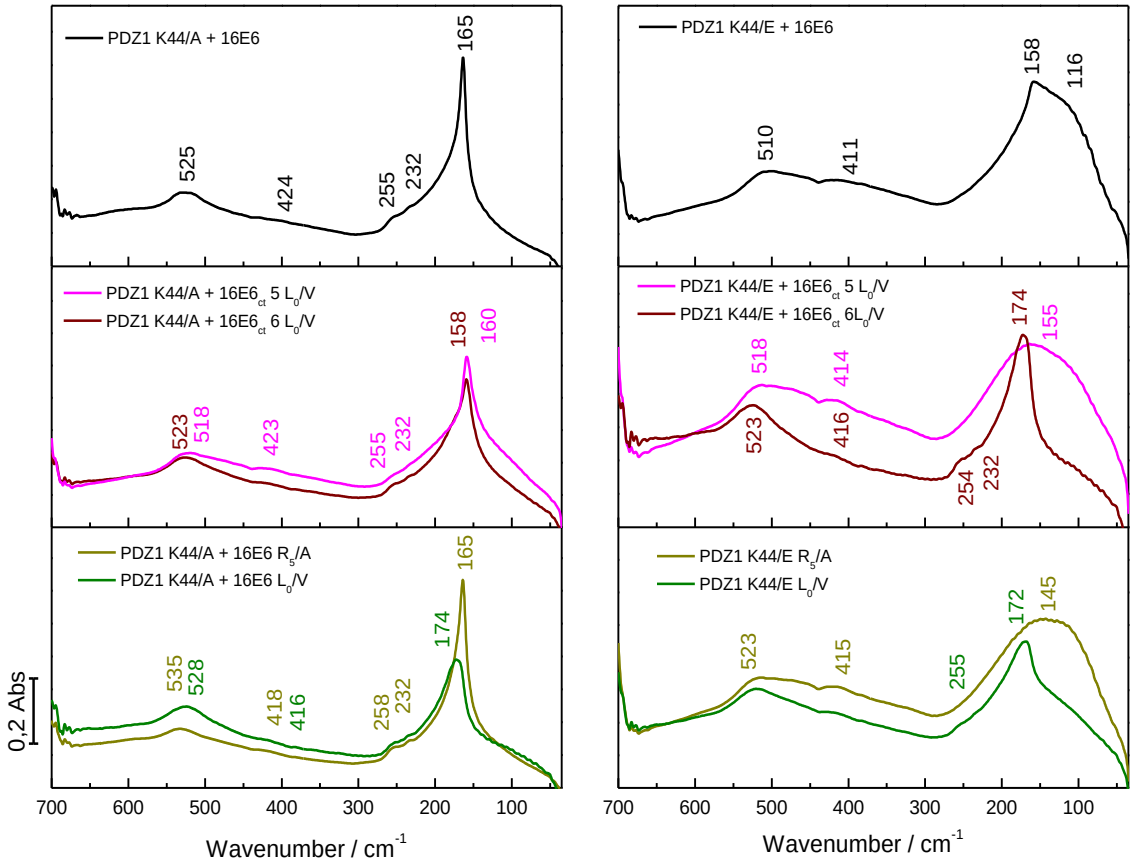

Figure 4.1-26. Far infrared spectra of PDZ1 K44/A and K44/E interaction with the different HPV16 E6 peptides

For the K44/E-peptide complexes, this signal shifts from 520 cm^{-1} in the free form, to 510 cm^{-1} in presence of 16E6, to 518 cm^{-1} with $16E6_{ct}$ 5 L_0/V and for the rest of the bound forms it appears at 523 cm^{-1}. Upon binding to the WT, a similar behavior is seen, as an exception with the WT in presence of 16E6 L_0/V the signal has the same frequency as in presence of the 16E6 peptide, which is not the case with K44/E.

In the case of the changes in amide VI with K44/A-peptides it is evident that a completely different conformation is seen in each one of the bound forms, the outcome from this signal can be compared as to the conclusions described for the amide III modes.

In addition to the amide vibrations, it is relevant to discuss that in the Raman spectra the δ(Cα-H) modes do not show any perturbation in the K44/A bound forms and in the K44/E there is only a shift in presence of $16E6_{ct}$ 6 L_0/V and 16E6 L_0/V where the signal appears at 1403 cm^{-1} and 1402 cm^{-1}, respectively.

Amino acid side chains. The MIR spectra (Figure 4.1-25) shows that upon complex formation the signal corresponding to the side contributions of the Glu residues, around 1077 cm^{-1}, is not perturbed, in K44/A or K44/E. Comparing to the interaction between the WT and the HPV16 E6, this signal has an important displacement in the presence of peptides with a Val residue in the P_0 position. Figure 4.1-14 shows the Glu residues, Glu36 and Glu39, in the loop between βB and βC strand that might be an important part of the interaction between both proteins, what is not evident from the structure and the position of the amino acids is how changes in the residue 44 are related to these Glu residues. It is more likely that the signal in this case is reflecting the motions of the Glu residue from the peptide.

Taking as a model the X-ray studies on PDZ1 MAGI-1 in presence of HPV18 E6 (7 residues peptide)[98], it is evident that Lys479, that correspond to the Lys44; and the Glu residue in the peptide (P_{-3}) has a direct interaction thought hydrogen bonds and indirect interactions through Ser, Thr and Val residues of the protein with the Thr(P_{-2}) from the peptide forming an intricate network.

The contribution from Thr, Ser and Tyr side chains vibrations, attributed to the signal at 1165 cm^{-1} in K44/A spectrum, shows no significant shift upon binding. In presence of 16E6 L_0/V and $16E6_{ct}$ 5 L_0/V the signal arises at 1164 cm^{-1}, for $16E6_{ct}$ 6 L_0/V and 16E6 R_{-5}/A it arises at 1168 cm^{-1} and in presence of 16E6 it arises at 1162 cm^{-1}. These differences can be due to the correlation between the hydrogen bonds of Thr465 in the βB-strand (Figure 4.1-27),

before named Thr30, and the Lys44 residue. Nevertheless, for K44/E this signal shows a significant shift upon binding, except in the presence of the 16E6 R_{-5}/A peptide, pointing towards a connection between the P_{-5} and Lys44 being needed for a proper binding.

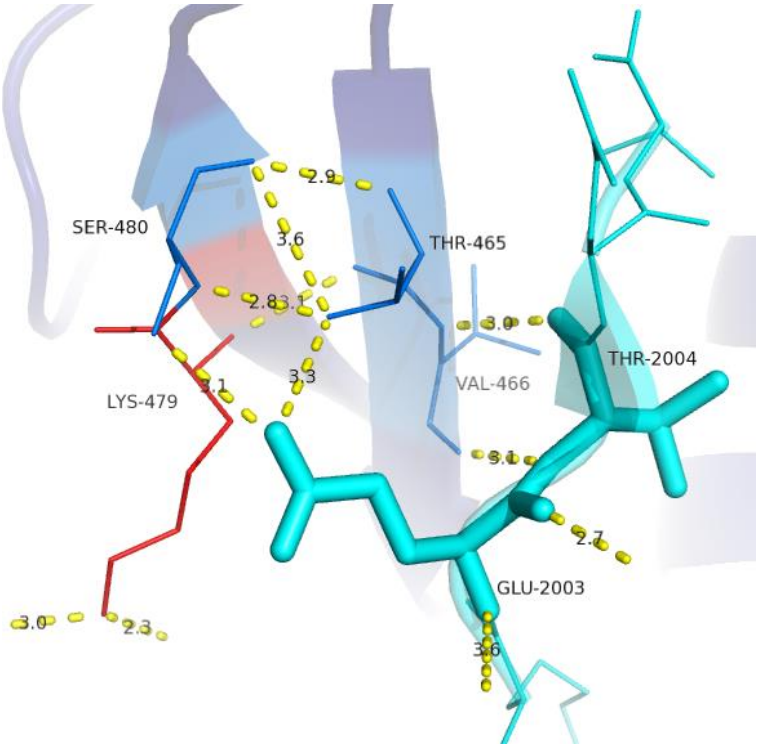

Figure 4.1-27. Schematic representation of the H-bonds between Lys479 from PDZ1 MAGI-1 and the Glu (P_{-3}) and Thr(P_{-2}) from the HPV18 E6 peptide (H-bonds in yellow). (PDB: 2I04)

Table 4.1-12 and Table 4.1-13 have a complete resume of all the amino acid side chains vibrations observed in the spectra of K44/A and K44/E in its free and bound forms.

It can be seen that the signal at 1408 cm^{-1}, attributed to the δ(C-H) of Thr does not present almost any shift upon binding, in contrast to what was observed in MIR, where the ν(C-OH) and the δ(O-H) modes are perturbed in the case of K44/E, suggesting that the changes observed in MIR are due to the Ser and Tyr residues.

For the signal at 1031 cm^{-1}, In comparison to the interactions of PDZ1 WT, where the signal shifts to higher wavenumbers upon binding; with the mutation to a neutral amino (K44/A) no changes are seen. With a negatively charged amino (K44/E), the displacement goes to lower wavenumbers. It is known that these vibrational modes are sensitive to hydrogen bonding, according to previous studies, higher value are related to hydrogen bonded OH group, lower values are related to the free group[250]. As a conclusion, it can be deduced

that upon binding in the WT there are new hydrogen bonds forming within the side chain of Ser and Tyr residues, and in K44/E the hydrogen bonds are disrupted due to the mutation.

Table 4.1-12. . Amino acid side chain vibrations of aromatic residues of PDZ1 K44/A and PDZ1 K44/E in its free and bound form by Raman spectroscopy

Modes (cm^{-1})	His		Tyr		Phe/Tyr		Thr/Phe		Phe	
K44/X =	A	E	A	E	A	E	A	E	A	E
Free	1585		1606		1207		1031		1002	
+ 16E6	1585	**1581**	1606	1606	**1203**	**1210**	1030	1031	1002	1001
+16E6$_{ct}$5 L_0/V	1585	1585	1606	**1609**	1207	1207	1035	1030	1002	**1005**
+16E6$_{ct}$6 L_0/V	1585	1584	1606	**1609**	1207	1207	1030	1030	1002	1002
+ 16E6 L_0/V	1585	**1580**	1606	**1609**	**1203**	**1204**	1029	**1038**	1002	1001
+ 16E6 R_5/A	1585	**1580**	1606	**1610**	**1204**	**1200**	1030	**1043**	1003	**1007**

Table 4.1-13. Other amino acid side chain vibrations of PDZ1 K44/A and PDZ1 K44/E in its free and bound form by Raman spectroscopy

Modes (cm^{-1})	Ala, Leu, Phe		Thr		Met		Iso/Leu		Arg, Ser, Val	
K44/X =	A	E	A	E	A	E	A	E	A	E
Free	1464/1448		1408		1173		1158		1126	
+ 16E6	1465/ 1448	1465/ 1448	1408	1407	1173	**1175**	**1155**	**1160**	1127	**1117**
+16E6$_{ct}$5 L_0/V	1464/ 1448	1465/ 1448	1407	1406	1173	**1181**	**1155**	**1168**	1126	**1118**
+16E6$_{ct}$6 L_0/V	1465/ 1448	1464/ 1448	1407	1408	1172	**1170**	**1154**	**1164**	1126	**1116**
+ 16E6 L_0/V	1465/ 1448	1464/ 1448	1408	1408	1173	**1177**	**1154**	**1164**	1126	**1116**
+ 16E6 R_5/A	1464/ 1448	1464/ 1447	1407	1407	1172	**1178**	**1154**	**1168**	1127	**1126**

For K44/A upon binding the RR spectra shows perturbation only in the symmetric ν(Ring–O) of Tyr and the δ(ring) of Phe, assigned to the signal at 1207 cm^{-1}. A similar behavior is seen with the K44/E mutation upon binding, except that in presence of 16E6 the signal has an upshift instead of a downshift as it was seen with the other peptides. This band is sensitive to hydrogen bonding in the case of the Tyr scattering but this is not valid for the Phe residues, due to the apolar character of this amino acid. As a general explanation the changes in the frequency might be due to displacement of the ring position caused by the electrostatic interactions in the surrounding of the residues.

In the case of the K44/E the effect upon binding in the ring breathing modes of Phe is also evident in presence of the $16E6_{ct}$ 5 L_0/V and 16E6 R_{-5}/A peptide, where the signal shifts from 1002 cm^{-1} to 1005 and 1007 cm^{-1} respectively.

Furthermore, a perturbation of the ring breathing modes of Tyr (Tyr101) is also present in K44/E RR spectra upon complex formation. The differences in the signal at 1606 cm^{-1}, are seen upon binding with all the peptides except with 16E6. In summary, it can be concluded that in K44/E Tyr101 ring is perturbed due to the formation of hydrogen bonds upon binding but in the K44/A this motion is not seen. Besides, for K44/E several spectral differences are observed. The first is the signal at 1585 cm^{-1} attributed to ν(C-C) modes of His residues, this vibration downshifts in presence of the 11-residue peptides. This motion is not observed in the spectra of the complex with the WT. There are only 3 His residues in the PDZ1 sequence, His75 and His77 are located in αB helix, the vicinity of Lys44, how changes in the mutations of this residue can perturb His residues upon binding is still an open question.

A possible explanation might be that, because of the mutation, many of the hydrogen bonds between Lys44 and the peptide, direct or indirect might be lost. The peptide forms a new hydrogen bond network with other residues around; the His residue involved might be His79. It is suggested from the shifts in the spectra that residues upstream (P_{-7}-P_{-11}) are the ones involves in this interaction.

For non-aromatic amino acids (Figure 4.1-27) in K44/E, perturbations of the rocking (C-O(H)) from Met residues are observed. Additionally, displacement in the signal attributed to the rocking CH_3 and δ(Cγ1–Cβ–Cγ2) from Ile and Leu residues are observed, likewise changes in the frequencies corresponding to the wagging N-H of Arg and the rocking CH_2 and CH_3 from Val and Ser, respectively, are observed upon binding. The effect over these residues is more pronounced in presence of $16E6_{ct}$5 L_0/V and 16E6 R_{-5}/A, pointing out to a different conformation than the one observed with the PDZ1 WT of the complex structure because of the lack of the P_{-7}-P_{-11} residues. For K44/A, only the Ile and Leu rocking CH_3 and δ(Cγ1–Cβ–Cγ2) were slightly perturbed.

Hydrogen bonding. In the FIR spectra (Figure 4.1-26), the hydrogen bonding collective motions show another property of these mutants. Upon peptide binding with K44/A the corresponding band has no importantl shift from 159 cm^{-1} to 160 cm^{-1} with the short

peptides. For the rest, in presence of 16E6 and 16E6 R_{-5}/A the signal arises at 165 cm^{-1} and in presence of 16E6 L_0/V the signal appears at 174 cm^{-1}.

The higher the affinity to the protein, the higher the frequency of the band, this is similar to the pattern observed in the WT interactions, the only difference in that case is the displacement of the signal was more pronounced and the shape of the signal had a tendency to be sharper, this last one is not seen in the spectral depiction of K44/A.

For K44/E the spectral differences are more prominent not only due to the shift but also to the shape of the band itself. In presence of $16E6_{ct}$ 5 L_0/V and 16E6 R_{-5}/A the signal is characterized by a broad band with a peak at 155 cm^{-1} and 145 cm^{-1} respectively. With 16E6 the band is also broader and has a prominent peak at 158 cm^{-1} and a shoulder at 116 cm^{-1}. At last in presence of $16E6_{ct}$ 6 L_0/V and 16E6 L_0/V the band gets a sharper shape it comparison to the rest, arising at 172 cm^{-1} and 174 cm^{-1} respectively.

Additionally, the ν(C-H) region in the Raman spectra (Table 4.1-14), shows that for K44/A only the Ser and Thr vibrations are perturbed upon binding; for K44/E instead, Met residues in the presence of the 16E6 and 16E6 L_0/v are influenced in a similar way, for His vibrations displacements are evident in the presence of the three 11-residue peptides and the more evident one is in presence of 16E6 R_{-5}/A.

Table 4.1-14. . ν(C-H) region of PDZ1 K44/A and K44/E in its free and bound form by Raman spectroscopy

Modes (cm^{-1})	Met		His		Ala, Val, Leu, Ile		Ser, Thr		Tyr	
K44/X =	A	E	A	E	A	E	A	E	A	E
Free	2731/2936		2774		2876		2968		3060	
+ 16E6	2731/ 2936	**2723/ 2930**	2774	**2270**	2876	2875	2869	2869	3061	**3065**
+$16E6_{ct}$5 L_0/V	2732/ 2935	2731/ 2936	2774	2773	2876	2876	**2870**	**2970**	3061	**3058**
+$16E6_{ct}$6 L_0/V	2732/ 2936	2728/ 2936	2774	2773	2875	2876	**2965**	**2966**	3060	**3065**
+ 16E6 L_0/V	2731/ 2935	**2723/ 2929**	2771	**2771**	2876	2876	**2967**	**2960**	3060	**3065**
+ 16E6 R_5/A	2731/ 2936	2731/ 2935	2774	**2781**	2876	2876	**2965**	**2975**	3061	**3056**

The Thr and Ser modes have an important shift upon binding. As with the His vibrations, the effect is more pronounced in presence of $16E6_{ct}$ 5 L_0/V and 16E6 R_{-5}/A, where

instead of going to lower frequencies the shift is to higher frequencies. The Tyr modes are the also affected in presence of all the peptides, what is interesting is that in presence of $16E6_{ct}$ 5 L_0/V and 16E6 R_{-5}/A the signal goes to lower frequencies and in presence of the rest of the peptides it goes to higher frequencies, pointing to the importance of the residues upstream and their interaction with Lys44.

4.1.6.2 Discussion

It is important to consider that Lys44 has a unusual set of spectral properties as the side chain of the amino acid is positioned in the most exposed domain. NMR structural studies suggested that the positively charged side chain of Lys44 interacts with the negatively charged side chain in the Pro rich sequence between Asp106-Asp109. Furthermore, it proposed that this interaction might restrict the motions and hence the conformation of the C-terminal extension[71].

In summary, the K44/A mutant losses of the ability to bind properly to the HPV16 E6 peptides. Nevertheless, changes in the hydrogen bonding and the amide were observed. In case of K44/E a different set of spectral characteristics were observed upon peptide binding, suggesting that changes in the charge of this specific residue might generate a new binding arrangement between both proteins.

From the changes of the amide III vibrations, it can be suggested that upon binding the K44/A mutant presents conformational changes in the β-turns and β-strand only in presence of the 11-residue peptides. However, with K44/E in presence of the short peptides there is already a conformational shift that begins to take place and becomes more pronounced in presence of the 16E6 and furthermore with 16E6 L_0/V and with 16E6 R_{-5}/A.

Other smaller characteristics that differ in behavior between these mutants and the WT PDZ1 is that upon binding with the K44/A protein the β-strand amide III vibration shifts to lower frequencies while for K44/E shifts to higher frequencies.

Comparing these results to the interaction between WT PDZ1 and the peptides, it is important to remark that in the WT in presence of all peptides a relevant shift to lower wavenumbers was observed in the β-turns contribution of the Amide III mode. This indicates that with K44/A, the β-turns components in the protein are not able to interact with the first residues of the peptide. In K44/E this effect is not detected, indicating how the change from a

charged amino acid, regardless if is positive (Lys) or negative (Glu), to a neutral one is a key for the interaction.

For the β-strand amide III modes, the behavior of K44/A and the WT are very similar. They both present a shift to lower wavenumbers of similar magnitude in presence of the 11-residue peptides. However with K44/E this shift goes to higher wavenumbers, indicating that instead of the bonds gaining strength upon binding as it happens with K44/A and the WT, mutation to negatively charged amino acid causes a loss in the strength of the bonds corresponding to this vibration (see Figure 4.1-21). As changes in amide I and II were seen, it is expected that the C=O, as well and the C-N and N-H groups, have a different conformation upon binding.

According to what was observed in the vibrations correlated to the hydrogen bonding vibrations, it seems that the complex formation, the mutation K44/A inhibited the hydrogen bonds formation seen in the WT, while in the case of K44/E, the mutation generates a new coordination of the hydrogen bonding network that it is completely different from the characteristics previously described in PDZ1-HPV16 E6 interactions. This demonstrates the importance of the electrostatic interactions between Lys44 and the HPV16 E6 to the binding affinity.

For the side chains contributions, changes in the Ser, Thr, Tyr, His and Met residues were described in the free protein as well as in the bound form with the different peptides. This corroborates with what was proposed in Figure 4.1-14, that the region around Lys44 is the region were the strength of hydrogen bonds defines the affinity and furthermore if the β-augmentation process occurs or not.

4.1.7 Conclusion

For a long time PDZ domains have been considered to have a passive function in comparison to others protein-protein binding domains[323], but their capacity to use multiple surface for docking a diversity of molecules, and their promiscuity have related the binding event to allosterically-regulated processes, through long-range energetic couplings that link the binding site to a distal region on the structure.

Previous studies of the interaction of PDZ1 from MAGI-1 with other viral proteins, like the cellular binder NET1[87] and HTLV1 Tax[89], have demonstrated that the oncogenic

effect of high risk HPV seems not to be driven by binding affinity competition with the host ligand. The majority of the data are *in vitro* assays mainly providing qualitative information. Initial structural insight into the targeting of PDZ domains by the HPV E6 proteins was described by Zhang *et al* [98]. The analysis of the crystal of a short peptide that mimics the C-terminal of HPV18 E6 bound to PDZ1 domain from MAGI-1 and SAP97/Dlg revealed that peptide residues outside the canonical PDZ binding motif were involved in direct contacts with the canonical core region of the PDZ domain.

Furthermore, the NMR structure of the free form of PDZ1 MAGI-1 and its bound form in presence of 16E6 L_0/V, indicates that the conformational changes outside the canonical core, that is not related to the carboxylate binding loop, might have an important role in the stability of the complex and the affinity in presence of different targets[71].

In the present work mutations of the 11-residue C-terminus of HPV16 E6 as well as mutation of PDZ1 domains were analyzed by infrared and Raman spectroscopy. The aim was to investigate the sequence requirements for the E6-binding specificity. The results show that this specificity is correlated to changes in the hydrogen bonding more than changes in the backbone.

The differences in the percentage of β-sheets beside the β-turns elements in the presence of the 16E6 L_0/V peptide in comparison with the 16E6, suggest that a different hydrogen bonding pattern is occurring in the binding process with the mutant, where as a result the peptide has a more pleated structure[77, 317]. This indicates that the higher the affinity the more pleated the structure of the peptide as the hydrogen bonding network is stronger between the peptide and the protein.

According to the results, the differences in affinity are directly correlated to the hydrogen bonding, suggesting that the pathogenicity and prevalence of a particular virus type[66, 324], as in this case HPV16, is in its ability to have a strong hydrogen network in comparison to the natural binder.

Based on the spectral differences of the amino acid side chains contributions, it is evident that Thr, Ser, Tyr and Arg residues play an important role in the binding process. The main differences of the Thr, Ser and Tyr indicate that most of these residues are hydrogen bonded in the bound form. For the Arg residues the changes are more related to different

orientations of the side chain, as the vibrations affected were the ν(C-H) modes and the wagging of the N-H group.

Besides, Met and His residues are also part of the setting for the peptide binding. Grouping these residues according to what was observed with PDZ1 GGG, PDZ1 K44/A and PDZ1 K44/E, two regions of the proteins can be highlighted as the main core of the hydrogen bonding network (see Figure 4.1-14.A).

From the study with the PDZ1 GGG mutant in the specific, it was demonstrated that the C-terminal is crucial for assembly of the hydrogen bonding network to stabilize the binding. The interaction between the P_{-6} and this region has significance for the final conformation necessary to form the complex. The P_0 position of the peptide and its interaction with the binding loop are also affecting the C-terminus which leads us to conclude that not only the direct interaction between the αB and βB with the peptide is important to stabilize the binding and form the complex. As a conclusion, the interaction between the C-terminus and the peptide has an effect on other areas of the protein besides the binding loop

Simulations of the PDZ1-HPV18 E8 exchanging Leu is the P_o had shown that the presence of the Leu weakens the β-sheet interaction between the peptide and the βB[322], the main chain of interactions of this β-sheet with the peptide backbone are responsible to for stabilizing an extended peptide in the binding groove, thus increasing or decreasing the affinity interaction, as it was shown in our results from the comparison between the short peptides and the eleven residues peptides.

The P_{-5} residue is usually a conserved positively charged residue (Arg). Many studies have suggested that this residue might be a key point for PDZ binding [325]; as a support *in vitro* and *in vivo* assays [326] and X-ray structures of several PDZ domain in presence of viral proteins [327] suggested that positions located upstream of the canonical four residue PDZ binding motif may also modulate the conformational changes upon binding[80, 328]. According to the results, the electrostatic interactions or a charged Lys44 have a key role in the binding affinity. The P_{-5} position has a larger effect on the β-sheet interactions between the protein and the peptide charge amino acid, regardless if is positive (Lys) or negative (Glu), to a neutral one is a key for the interaction. This means that the interaction is mediated by charged residues upstream of the PDZ-binding motif strongly contribute to binding selectivity.

As a resume of the interaction of PDZ1 with the shorter peptides, the binding of the HPV16 E6 is modulated by more than the last 6 residues of the C-terminal sequence. Studies with other viral and natural binders with PDZ1 MAGI-1 have demonstrated the importance of the R_0 and R_{-5} residues. Mutation in the P_{-5} this residue abolished the E6-mediated degradation of PAGI-1 and SAP97, this demonstrate the important role of these residues outside the canonical PDZ-recognizing sequence (only four amino acid), these additional interactions provide the viral protein with an upper hand in competing with cellular ligands.

The latest allostery model, the "shift population" model, proposed that upon binding, conformational changes distal to the carboxylate group might be the key to understanding the binding dynamics between the PDZ domains and the viral proteins. Ligand-dependent dynamics of this allosteric behavior and the inter-molecular signaling may be directly correlated to the methyl side chains. The β-augmentation upon binding triggers the C-H groups of specific amino acids makes the hydrogen network stronger, as was observed in our results. However, the molecular details of such intradomain allostery are still unclear.

As perspectives, site-direct mutagenesis of the Thr30, His75, His77 and residues in the αB-βF loop and the βA-βB loop corroborate the network proposed. Furthermore, extension of these studies to other PDZ domains that are known also to be target of viral proteins confirm that the hydrogen bonding pattern is not an isolated phenomena of the PDZ1 from MAGI-1 in presence of HPV16 E6 C-terminus.

4.2 Copper coordination with the A*β*16 peptide

4.2.1 Introduction

The participation of transition metal ions in the neurodegenerative process is highly discussed since Zn, Fe and Cu ions are found in amyloid plaques at significant concentrations and clearly seem to promote the aggregation of the isolated peptide[329-331]. Deciphering the redox characteristics of the copper A*β* peptides complexes is an important task in connecting the dots of the role they are assumed to play in Alzheimer's disease.

The metal-binding sites have been identified in the N-terminal hydrophilic region of the Aβ peptide[332]. The coordination environment of Cu(II) is defined by 3N1O, corresponding to 3 or 2 His[333] and the N-terminus together with an Asp or Glu residue. At pH 9 the amide bond of Ala2 is a binding partner (see Figure 1.2.3, section 1.2.1)[330, 334]. Residues His6, His13, His14 and Asp1 have been identified to be part of the coordination sphere by infrared spectroscopy[3] and other techniques[335]. The CuA*β* components present two conformers between pH 6 and 9, respectively, that have been described to be in equilibrium with each other at physiological pH[334, 336-338].

The focus of this work is to understand the reorganization of the A*β*16Cu-peptide upon redox reaction by means of electrochemically-induced FT-IR difference spectroscopy. With this technical approach, the analysis of both, the Cu(II) and the Cu(I) A*β*16 complexes, in a single difference spectrum was made. As the sample remained in solution under a controlled temperature, the problems related to a fast aggregation that is typically observed in the CuA*β*16 complexes[339] were overcame.

The difference spectra of CuA*β*16 samples were recorded at pH 8.9, with the aim to access separately the one of the CuA*β*16 complexes that occurs simultaneously at physiological pH. Differently labeled samples were studied for data analysis including ^{14}N to ^{15}N labeling of the discussed His residues and a change of ^{12}C to ^{13}C in addition to the ^{15}N labeling at the Asp1 residue. Furthermore, to corroborate the band attribution and the concluded properties from the spectra, the electrochemically-induced FTIR difference spectra of two model peptides DAHK (Asp-Ala-His-Lys) and GHK (Gly-His-Lys) in presence Cu were performed.

4.2.2 CuDAHK and CuGHK complexes

DAHK is the N-terminal metal-binding sequence of human serum albumin (HSA), and GHK is a copper binding growth factor in plasma. Their structure in presence of Cu(II)[4], their thermodynamics[5], and their function[340] have been widely studied and very well characterized, making them thus, a reference for the assignment and understanding of the Aβ redox behavior.

In previous experiments, Cu ions in DAHK and GHK showed a rather complex electrochemical behavior. For GHK not only Cu (I), but also Cu(0) was observed upon reduction depending on the applied potential. In DAHK the oxidation to Cu(III) was also described[4]. So both peptides react in a distinct way. In the experiments shown here, we could obtain reversible infrared difference spectra when cycling between the oxidized and reduced form for both peptides (Figure 7.2-7 appendix), suggesting that the redox reaction remain between Cu(II) and Cu(I).

The differences observed in the results could be due to the experimental approach: in cyclic voltammetry experiments, the kinetics of an electrochemical reaction are observed; while here a fully reducing or oxidizing potential was applied with a timing of several minutes in each step until the equilibrium was obtained. This allows the system to make the necessary conformational changes to accommodate Cu(I). The data was obtained by averaging several cycles of oxidized minus reduced difference spectra and vice versa. For each cycle the spectra were reproducible, indicating that the reduced form was stable.

The oxidized minus reduced FT-IR spectra at pH 6.8 and 8.9 are shown in Figure 4.2-1.A and Figure 4.2-1.B for DAHK and Figure 4.2-1.C and Figure 4.2-1.D for GHK. The positive signals correspond to the changes of the oxidized form and the negative signals to the reduced form. The FT-IR difference spectra of both peptides at pH 6.8 show the same general spectral features. Contributions from the peptide bonding are expected, the so-called amide bands and from the individual amino acids: His, Lys (C-terminal) and Asp (N-terminal) in the case of DAHK[341]. The summary of all bands analyzed here is presented in Table 7.2-1 (appendix).

Smaller but highly reproducible signals are seen around 1590-1570 cm^{-1} arising from the different protonation states of the imidazole in His indicated the change for the

coordination of the Cu(II) via the N^{π} changes to N^{τ} at pH 6.8 upon reduction. The negative signal at 1589 cm^{-1} is characteristic of the Nπ-H, present in the reduced state, and the positive signal at 1579 cm^{-1} from Nτ-H present in the oxidized state[261, 342].

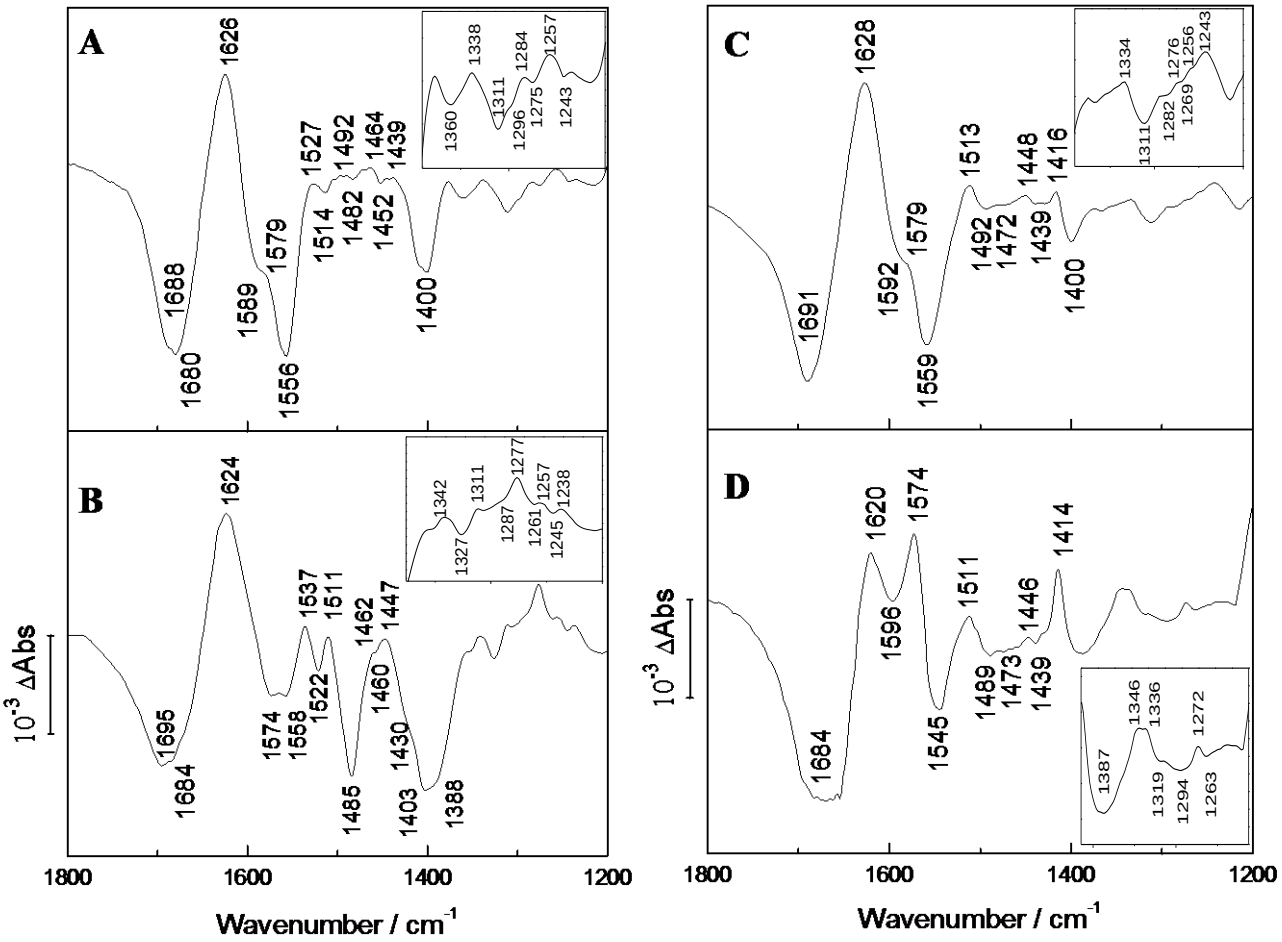

Figure 4.2-1. FTIR difference spectra of the Cu-DAHK complex. A. At pH 6.8. B. At pH 8.9 and Cu-GHK complex. C. At pH 6.8. D at pH 8.9

In the spectrum of DAHK at pH 8.9 (Figure 4.2-1.B) this signal only appears for the reduced form, indicating that at this pH, Nτ is protonated and that the Cu(I) coordination is made via Nπ. For GHK at pH 8.9 (Figure 4.2-1.D) the corresponding signal at 1592 cm^{-1} shifts to 1596 cm^{-1}, and the positive signal from 1579 cm^{-1} shifts to 1574 cm^{-1} upon reduction, indicating the same changes in the coordination of the imidazole as at pH 6.8.

One of the main difference between the two peptides is the position of the His residue, previous studies have proposed that this is an important factor that can regulate the coordination mode[119, 343]. The main spectral differences are observed in the deformation and

stretching of the His vibrational modes. For GHK, a positive signal is observed at 1416 cm^{-1} at pH 6.8 and 1414 cm^{-1} at pH 8.9. This band corresponds to the deformation of the Nτ-H[261, 342]. The signal gain intensity at high pH, changes in the dipole moment in this kind of modes are related to stronger hydrogen bonding.

For the DAHK at pH 6.8 a small shoulder is observed at 1482 cm^{-1} in the reduced state; at pH 8.9 this vibrational mode gains intensity and arises at 1485 cm^{-1}; this band corresponds to the ν(C_2=Nπ)[261, 342]. As it was concluded from the vibrational modes described before, DAHK coordination mode changes from Nπ to Nτ upon reduction at pH 6.8 while at pH 8.9 the same coordination with Nπ is observed. Nevertheless, the gain in intensity indicates that the dipole moment in both states is not the same, suggesting a change in the symmetry of the molecule.

It can then be suggested that according to the position of the His residues, when the His is in second position in the sequence, an exchange of the imidazole coordination is more probable than when the His is in the third position.

The signals at 1688 and 1691 cm^{-1} at pH 6.8 (and at 1695 and 1684 $cm^{-1}$for pH 8.9 include the contributions of the ν(C=O) vibration of the peptide bonding[247, 344] of the reduced form. The positive signal between 1628 and 1620 cm^{-1} in the different spectra reflects the signal of the oxidized form. The shift of the ν(C=O) vibration upon reduction can be explained by a change of the hydrogen bonding and thus the environment of the C=O group upon reduction of the Cu ion confirming a change of the coordination sphere upon reduction. Keeping in mind that the samples sequence are only three or four residues long, a change in the hydrogen bonding is unlikely to affect the secondary structure to an extent where the frequency of the amide vibration upshifts, from 1626 cm^{-1} to 1688 cm^{-1}, as seen in the difference spectra of DAHK at pH 6.8.

In addition, it is worth noting that in the GHK spectra at pH 6.8 a similar upshift (+63 cm^{-1}) is observed. This observation rules out the role of the hydrogen bonding changes as the cause of the upshift of the carbonyl vibrations. Therefore, the most probable reason may be that the amide carbonyl is coordinating Cu(I).

Besides the signals from the backbone and the His, the contributions from the Asp residue can be expected in DAHK. Protonated acidic residues typically display a ν(C=O) vibration around 1700 cm^{-1}, the exact position depending on the hydrogen bonding

environment. For deprotonated acidic residues the intense contributions of the $\nu(COO^-)^{as/s}$ can be found at positions close to 1560 cm^{-1} and 1400 cm^{-1} respectively[302, 345]. The difference signal of the COO^- can be due to a hydrogen bonding difference between the two forms (e.g. with the amino terminal group or due to an interchange between the amino terminal group and the COO^- (Rotation of the C-C bond)[250, 288]. This is more likely at pH 8.9 than pH 6.8. It is important to note that the signal upshifts upon reduction; therefore, the hydrogen bonding becomes weaker. The absence of difference signal indicates that the Asp side chain does not change environment upon reduction at higher pH.

Interestingly the changes become more pronounced at pH 8.9 and additional signals are present around 1574 and 1430 cm^{-1} in direct comparison to the GHK peptide. This suggests that at high pH the Asp may experience a change in environment upon reduction. In this case, it can be proposed that the amine becomes free and can form a hydrogen bonding with the carbonyl of the Asp. Thus, this may lead to a slight shift in the frequency of the carbonyl vibrations. The signals of the additional Ala residue cannot be at the origin of these differences, since the absorption coefficient of Ala is typically small and this amino acid has no significant absorption in this range.

Finally, signals from the Lys residue that is present in both, GHK and DAHK, are observed. In model compound studies the $\delta(NH_3^+)^{as}$ and the $\delta(NH_3^+)^{s}$ vibrational modes of the Lys side chain have been observed at 1650 and 1520 cm^{-1} [302]. Whereas the asymmetric mode may be overlapped by the broad differential amide I signals around 1688 and 1626 cm^{-1}, the symmetric mode is involved in the broad contribution of the $\nu(COO^-)^{as}$ vibration as well as the amide II signals at 1559 cm^{-1}[345].

4.2.3 The CuA*β*16 complex

Redox induced FTIR difference spectra of CuAβ16 pH 8.9: backbone and Asp1. The second conformer of CuA*β*16 that occurs physiologically can be obtained at pH 8.9. The oxidized minus reduced FT-IR difference spectra for the unlabeled sample at pH 8.9 (A), after $^1H/^2H$ exchange (B) and the Asp1 labeled peptide (C) can be seen in Figure 4.2-2.

The spectra show mostly negative signals, which points towards small modifications in the coordination sphere of Cu during the course of the redox reaction. This is confirmed by the changes in intensity of the ν(C=O) vibrations in the region between 1700-1600 cm^{-1}. The

amide I region includes a signal at 1665 cm^{-1} which shifts towards 1648 cm^{-1} upon $^{1}H/^{2}H$ exchange to 1648 cm^{-1}. In the amide II region corresponding to the negative signal seen at 1555 cm^{-1} shifts towards lower frequencies. The amide II' vibration is seen as a broad signal at 1485 cm^{-1}. These spectral differences point towards a rearrangement of the structure upon reduction.

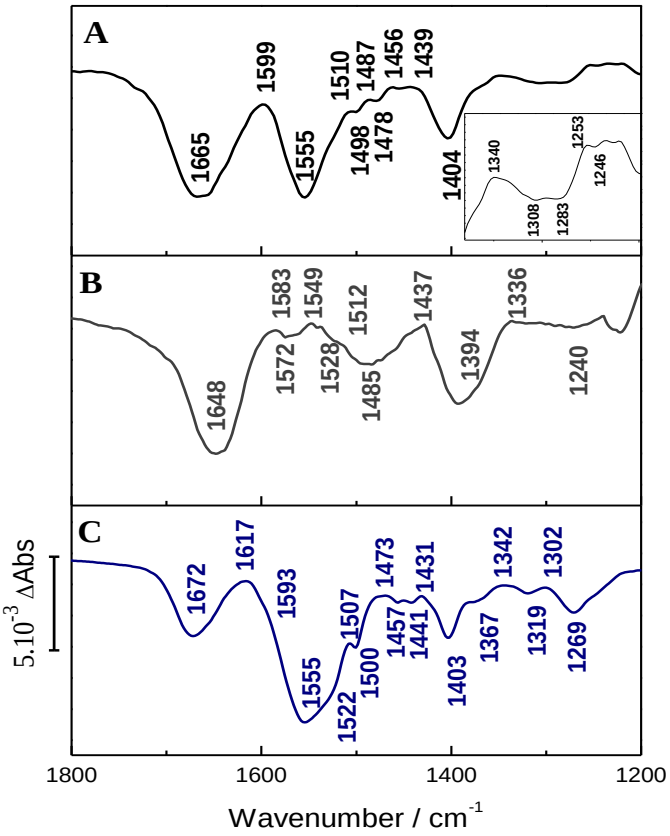

Figure 4.2-2. FTIR difference spectra of the CuA*β*16 complexes. A. unlabeled sample at pH 8.9, B. at pD 8.9 and C. Asp1 ^{13}C- and ^{15}N-labeled sample at pH 8.9

Asp1. Figure 4.2-2.C shows the oxidized minus reduced FT-IR difference spectra of Asp1 labeled by ^{13}C and ^{15}N at pH 8.9. The labeling of this residue decreases the signals including the ν(C=O) vibration at 1665 cm^{-1} confirming the involvement of the backbone group from Asp1 in the signal of the reduced form. Due to this shift, a peak at 1672 cm^{-1} becomes visible that can be attributed to the ν(C=O) vibration of the backbone in the typical β-sheet conformation adopted by the peptide at pH 8.9.

The labeling also affects the positive signal at 1599 cm^{-1} which is split in two signals at 1617 cm^{-1} and 1593 cm^{-1} respectively. Smaller signals like the scissoring vibration of the

$^{15}NH_2$ side chain of Asp1 may arise here; being redox active, more likely the side chain of Asp1 is participating in the binding.

Upon $^{1}H/^{2}H$ exchange the amide II vibration downshifts toward 1485 cm^{-1} (Figure 4.2-2.B) and other signals become visible in the 1600-1550 cm^{-1} range. Those signals can be arising from His and Asp. Upon labeling of Asp1, the contribution(s) of this residue downshift. This can be seen in the two shoulders that appear at 1593 cm^{-1} and 1525 cm^{-1}. Those vibrations can be assigned to the ν(C=O) and $\nu(COO^-)^{as}$ modes, respectively. With this in mind, the signal at 1672 cm^{-1} can be then assigned to the carbonyl groups of the backbone. In the amide II range, the broad negative signal centered at 1555 cm^{-1} shows a shoulder at 1522 cm^{-1} upon labeling, that involves coordinates of the Asp $\nu(COO^-)^{as}$ vibrational mode.

Tyr10. In previous data obtained at pH 6.8 by Youssef El Khoury in our laboratory, a negative signal at 1517 cm^{-1} was identified as the contribution of the ν_{19}(CC) ring mode of protonated Tyr (see Figure 7.2-8 appendix). In the A*β*16, there is only one Tyr residue, Tyr10. At pH 8.9, this signal is not evident anymore (Figure 4.2-2.A) and smaller signals at 1498 and 1487 cm^{-1} are seen. The position at 1498 cm^{-1} is typical for the deprotonated Tyr[346, 347]. Therefore, it can be suggested that the conformation of Tyr10 changes when the pH changes and its side chain moves from being buried away from the solvent to become more exposed to the solvent at pH 8.9. However, it is noted, that the intensity of this vibrational mode is typically higher than for the protonated form, which is not the case here and the assignment is thus not straightforward. The signal may be partially overlapped, as it is for example clearer in the data obtained for the Asp1 labeled compound, where the signal is observed at 1500 cm^{-1} (Figure 4.2-2.C).

It cannot be excluded that at pH 8.9, the Tyr residue is not participating in the conformational change that occurs upon redox reaction and is thus not visible in the difference spectra. In any case we can conclude that the Tyr is not showing the same features at the two pH values studied. In addition, the deprotonation of a few percent of Tyr in not excluded at pH 8.9. However, the Tyr signal is redox-active and the deprotonation seems to happen only upon reduction. Nevertheless, no clear statement can be made concerning the Tyr10 and further analysis by site-directed mutagenesis or labeled Tyr residue is recommended.

His6, His13 and His14. The comparison between the FT-IR difference spectra of the unlabeled sample and the His labeled samples is shown in Figure 4.2-3. Several small shifts

are seen in the amide I range at 1665/1670 cm^{-1} indicating that the vibrational modes of the backbone contributions involved here are coupled and shifted due to the isotopic labeling.

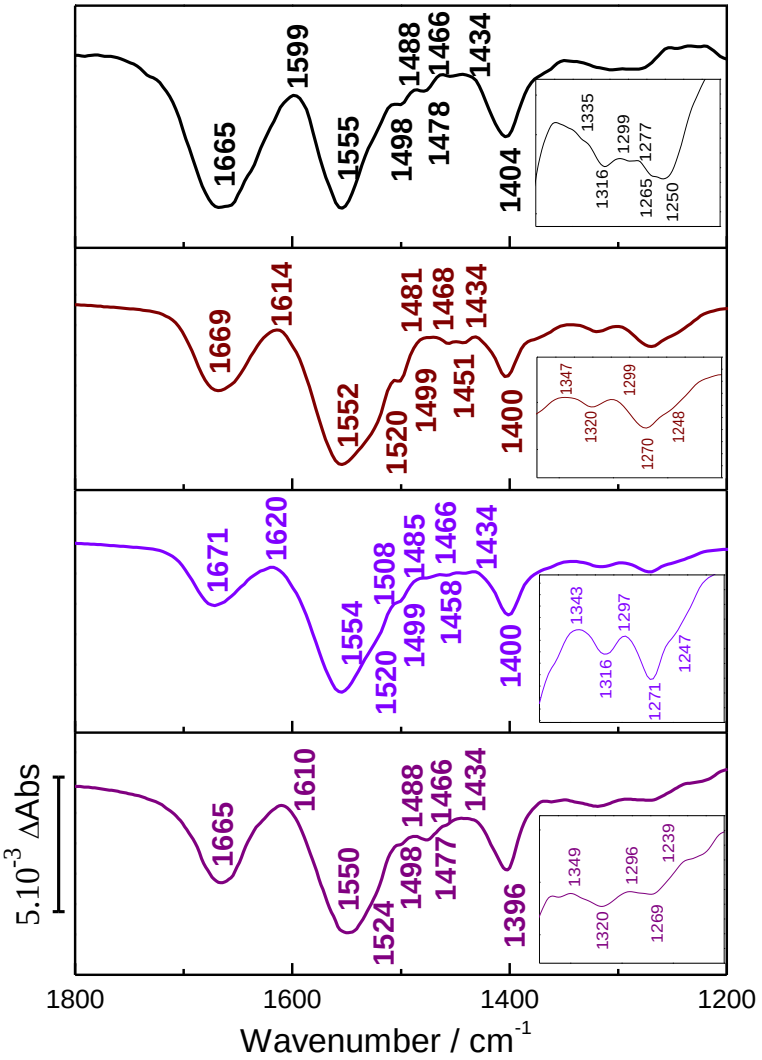

Figure 4.2-3. FTIR difference spectra of the CuA*β*16 samples recorded at pH 8.9. A. Unlabeled, B. His6-labeled, C. His13-labeled and D. His-14 labeled.

The slight downshift in the frequency upon reduction is an indicator of a geometrical changing of the complex; however the deprotonated amide remains a binding partner of Cu(II) and Cu(I). It should be noted that the frequency is unusually-high for a deprotonated amide[290, 344], however this particular deprotonated amide function is involved in the coordination of Cu(II) and Cu(I) which is expected to affect the frequency of this vibration. The Ala2 residue was shown to bind Cu^{II} at pH 9.0[3]. If this residue has any spectral contributions, they would appear in the 1500-1400 cm^{-1} region but difficult to assign because of the low extinction coefficient.

The negative signal seen at 1404 cm^{-1} in the spectrum of the unlabeled sample undergoes a slight downshift upon His6 labeling (i.e 1403 cm^{-1}) and a more pronounced one upon His13 labeling (i.e. 1401 cm^{-1}). This is an indication on the involvement of the His13 residue in the coordination of Cu^{I} at pH 8.9. Furthermore, the signal's frequency is typical of $\delta(N^{\pi}\text{-}H)$ vibration of N^{τ}-bound form of His. The sensitivity of this signal to the labeling of His by ^{15}N leads us to assign this signal to the υ(CN) vibration of the N^{π}-protonated form while N^{τ} binds Cu. Therefore, it is likely that both, His6 and His13, bind Cu(I) via N^{τ} at pH 8.9.

Between 1350 and 1200 cm^{-1} several small signals appear, that are highlighted in the insets. These signals in the fingerprint region include the overlapping contributions of the coupled ν(CN) and δ(CH) ring vibrations and reflect small but reproducible shifts of the His modes upon reduction, that can be confirmed in the labeled samples. Specifically, the positive signal observed at 1340 cm^{-1} can be attributed to the ν(C-Nπ) mode[302, 342]. It is important to note that in the His13 spectrum the signal arises at a similar frequency, while in the His6 and His14 spectrum the signal appears at 1347 cm^{-1}, changes in this vibrational mode have been associated with the hydrogen bonding of the Nπ, suggesting that in the oxidized state the Nπ of these residues are protonated.

4.2.4 Conclusion

The structures suggested for the model peptides on the basis of the obtained results are shown in Figure 4.2-4. The coordination sphere of the DAHK-Cu(I) displays a different His(N) coordination at the two pH values studied. In the case of GHK the same Cu(I) coordination can be expected at both pH values.

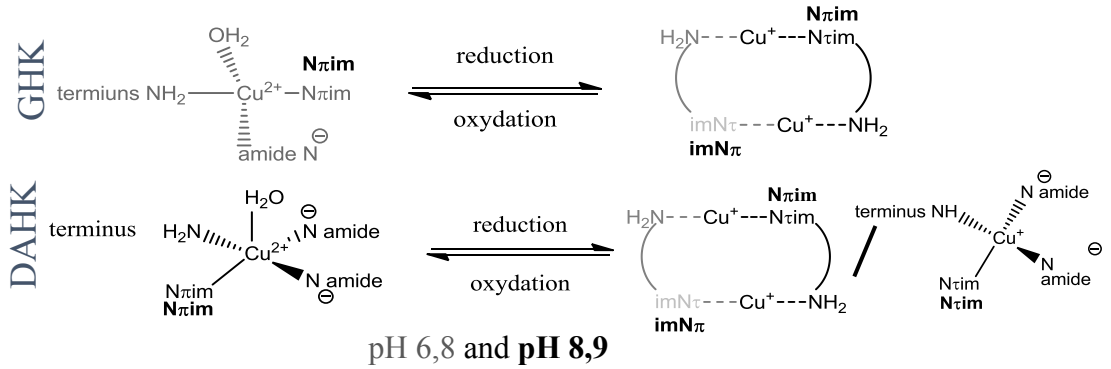

Figure 4.2-4. Suggested structure of the Cu (I/II) coordination of GHK and DAHK at pH 6.8 and 8.9

For the Aβ16 peptide, it can be concluded that the Tyr10 residue may undergo a deprotonation upon reduction at pH 8.9 whereas at pH 6.8 this residue remains in the neutral form. In the light of the previous findings concerning the role of Tyr10 in the formation of the Aβ plaques, our data suggest that the redox transition of the CuAβ16 at pH 8.9 may be a critical step in the pathway of the plaques formation.

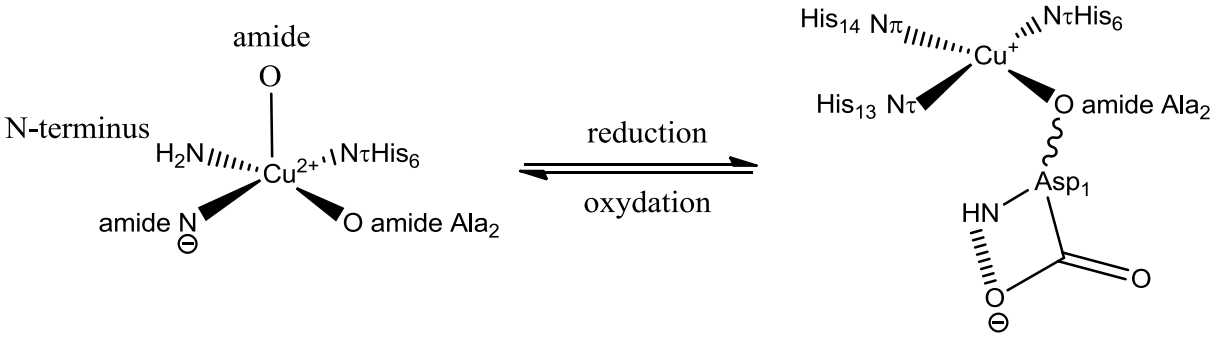

Figure 4.2-5. Suggested structure of the Cu (I/II) coordination of Aβ16 at pH 8.9

At high pH (8.9) Cu(I) has a coordination sphere formed by Asp1, His6 and H13 via Nτ, and H14 via Nπ as depicted in Figure 4.2-5. The major changes observed in the redox reaction are due to coordination with the N atom of the His residues and the Asp1, while the Ala2 contribution remains without changes. In comparison to the model peptides, the coordination sphere of DAHK seems to be the most similar one upon reduction.

The results showed a difference sphere of coordination between the Cu(II) and Cu(I) complexes, where the major changes in the structure will be dominated by the contribution of the imidazole ring of the different highlighted His residues, Asp1 and Tyr10. The FT-IR difference spectra showed that only negative signals appear in the Ox-Red difference spectra, pointing towards an important change in the transition dipole moments upon reduction. Furthermore, the coordination sphere of Cu(II) is conserved to a large extent when the reduction to Cu(I) occurs since the spectra do not show any positive signals that shift and become negative upon reduction.

It is believed that amyloid formation in AD and other amyloidogenic diseases such as prion disease are the result of protein or peptide misfolding[125, 348]. The Aβ peptide has a structural transition associated with amyloid formation, with conversion from random coil to an extended β sheet-like conformation in aqueous medium[142]. According to recent studies in presence of Cu, both monomeric and dimeric species have been proposed[349].

These results with CuAβ16 point towards a monomeric complex, as it was also observed for the model peptides. Changes in the structure were observed, where the C=O, N-H and C-N groups of the backbone are perturbed due to the Cu binding. In the reduced as well as in the oxidized CuAβ complex the structure seems to be formed by mostly β-sheet. Although copper reduction does induce a re-ordering of the main chain, as the rearrangement of the structure upon reduction is reflected in the displacements of the amide bands to lower wavenumber, comparing the difference spectra with the spectra of Cu^{II}Aβ16 complex of previous studies[3]. This indicates that the formation of the fibrils observed in AD patients is not only triggered by the presence of Cu and its redox process. It can be proposed that the effect of metal ions in AD pathology is a two-step process as it was described by Faller[145, 350] and by Hardy and Selkoe[351]. First, the development of the fibrils is pH-dependent and the contribution of the protonation of other amino acids is suggested. The second step will be production of ROS induced by Aβ.

It is important to note that the data shown here were obtained with the Aβ16 peptide, since the coordination takes place in the N-terminal region. For future studies, it can be suggested to follow the same line as here in order to investigate how other transition metals, such as Zn or Fe, bind to the Aβ16 peptide. The deep understanding of the transition metals coordination spheres in the Aβ16 would open new possibilities in the application of this aforementioned technique on the full-length Aβ peptide.

4.3 The metal-ligand vibrations in Complex I

4.3.1 Introduction

Complex I is a very complex metalloprotein, it contains between 5–9 Fe-S clusters, according to the different organisms[196]. In the last 20 years, studies on complex I involved mainly EPR measurements[169, 188, 216]. The reduced state had been widely described by EPR and other spectroscopic techniques, the properties of the cluster in their oxidized state had been deduced according to the paramagnetic properties of the clusters and to the recently resolved structure[183].

In this study the aim is to describe the RR bands of complex I in the oxidized and reduced states. This study focuses mainly on the assignments of the RR bands of the Fe-S cofactors observed in the low frequency range where a systematic investigation of the Fe-S cluster is undertaken by investigating several subunits of the complex I as well as the complete one. Together with the isotopic labeling of the Fe iron atoms with ^{54}Fe, this approach allows an accurate assignment of the RR bands to the individual clusters which later will be used in the analysis of the roles of the cofactors in the electron transfer chain. Furthermore, site-directed mutations of some amino acids present around the N1a and N2 clusters can help a better understanding of the roles of the amino acids in the tuning of the cluster redox properties.

As the structure of complex I from *E. coli* or *A. aeolicus* is not yet resolved, we rely on the *T. thermophilus* published structure [183] as well as on the sequence alignment between the different species. This comparison allows to suggest which are the specific amino acids involved in the clusters' environment beyond the cluster motifs and which might be they contribution in the electron transfer process.

Besides the Fe-S cluster, attention has been given to the assignments of RR bands of the remaining known cofactor, namely the FMN as well as the elucidation of a newly discovered quinone cofactor which is investigated by means of electrochemistry coupled to fluorescence spectroscopy where UQ models included in the study for comparison.

The obtained results are shown below, starting with the fully oxidized state, the fully reduced state and finally the reduction by addition of NADH, the effect of other nucleotides as NADPH and NAD^+ was also investigated.

4.3.2 The oxidized state

The Raman spectra of Complex I, QRF and NDF from *E. coli*, as well as the spectrum of NuoEF from *A. aoelicus* were recorded after the excitation with a 514.5 nm laser. The spectra can be classified in three regions according to the nature of the observed vibrational modes. First, the metal-ligand vibrations and their overtones can be seen in the range 100 - 700 cm^{-1}. Between 700 - 1800 cm^{-1} the FMN vibrations can be observed additionally to the amide modes and the amino acid side chain vibrations related to the environment of the cofactors. The last region, between 2700 and 3200 cm^{-1}, corresponds to the ν(C-H) vibrations of the carbon-α (Cα) of the backbone.

Fe-S modes. The low frequency region in the Raman spectra (Figure 4.3-1) is characterized by the Fe-S vibrational modes. The selective enhancement of Fe-S vibrations is based on the excitation of the Fe-S bonds between the iron and the sulfur from the coordinating Cys residues and the sulfide ions within the cluster. A charge transfer (CT) band arises when the transition from the ground to the first excited state takes place. Fe-S clusters exhibit identifiable RR spectra using excitation into the intense $S \rightarrow Fe^{3+}$ CT bands. [352]

Small Fe-S proteins have been extensively studied by RR spectroscopy[353, 354]. Here, the assignments were made with respect to the previously reported studies on [2Fe-2S] and [4Fe-4S] model complexes and their excitation profiles [355,12,164]. The assignments were also supported by isotopic labeling. The shifts are in line with other isotopic labeling studies as well as normal mode calculations[356, 357,358].

There are nine well-described stretching modes arising from the Fe-S clusters[359] (Figure 4.3-1). An overview of all the Fe-S modes observed in the different samples is depicted in Table 4.3-1.

The main Fe-S stretching modes of the [2Fe-2S] and the [4Fe-4S] clusters are clearly distinguishable, since the D_{2h} distortion only applies for [2Fe-2S] clusters. In contrast, the [4Fe-4S] clusters have a T_d symmetry that seems to be very often distorted, as reported previously[355, 356, 360]. This leads to a signature that is more precisely fitted by a D_{2d} compressed distortion. According to this coordination geometry, four "short" and eight "long" Fe-S bonds can be described, the arrangement is based on the benzyl cube model for protein bound clusters[12, 270]. The eight long bonds are in parallel and perpendicular direction with

respect to an idealized fourfold axis. These characteristics only apply to clusters that have only Cys ligands[355]. The signals in this region are further discriminated in bridging (Fe-S^b) and terminal (Fe-S^t) modes.

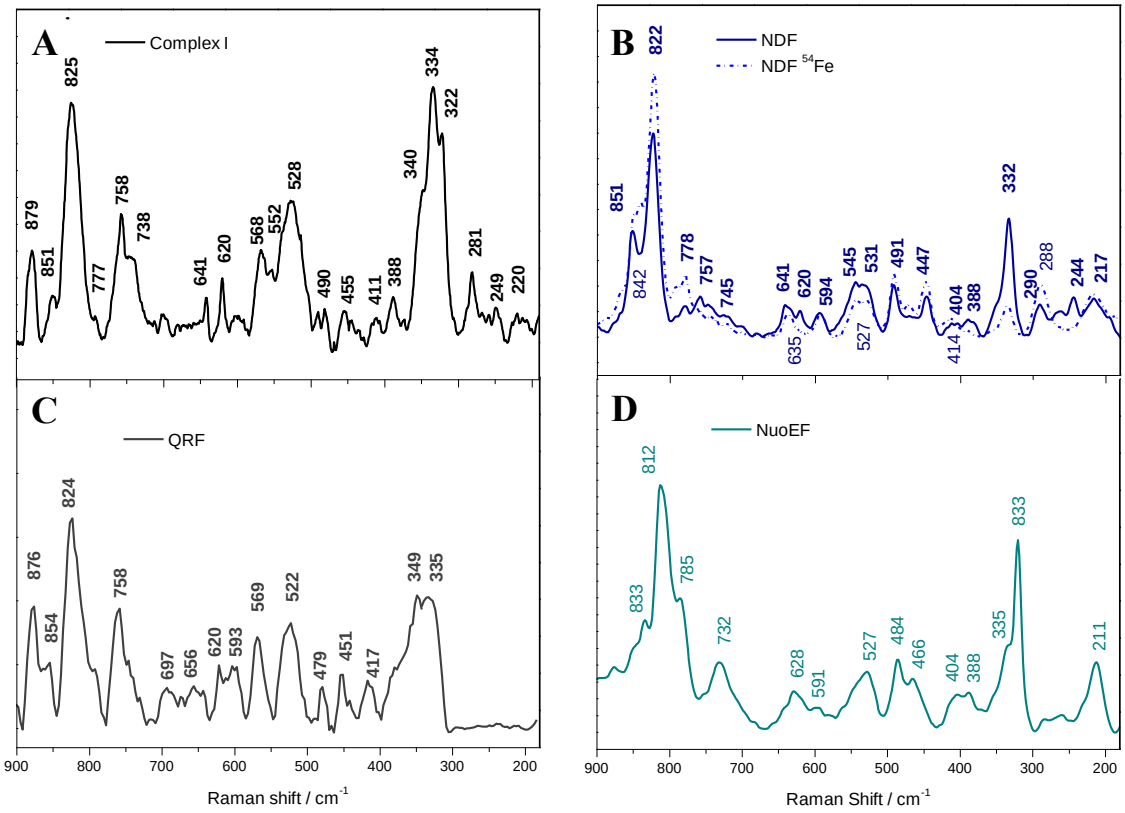

Figure 4.3-1. Low frequency RR spectra enhanced by an excitation of 514.5 nm. A. *E. coli* complex I. B. The NADH dehydrogenase fragment (blue solid) and the ^{54}Fe-enriched NADH dehydrogenase fragment (dotted line) of the *E. coli* complex. C. Quinone reductase fragment and D. *A. aeolicus* Subcomplex NuoEF.

The spectrum of NuoEF allows describing the properties of the N1a and N3 clusters. In the spectrum of NDF the signals arising from N1b, N4, N5 and N7 are observed and the spectrum of QRF supports the assignment for the N6a, N6b and N2 clusters. Due to the complementary of all these spectra, a full assignment of the metal-ligand vibrations of Complex I was achieved.

Identification of the [2Fe-2S] clusters. The spectrum of the NuoEF subcomplex (Figure 4.3-1. D) includes the modes of the binuclear cluster N1a and the tetranuclear cluster N3. The signal at 211 cm^{-1} corresponds to the A_g mode of the Fe-Fe interaction, typical for [2Fe-2S] clusters[12]. The strength of the Fe-Fe interaction within the [4Fe-4S] clusters is lower than in the [2Fe-2S] clusters, and thus, the resonance of this vibration is expected to be weak in the case of the [4Fe-4S] cluster.[12, 359]

In the spectrum of the dehydrogenase fragment this RR band is present at 217 cm^{-1} in the NDF spectra (Figure 4.3-1. B), and at 220 cm^{-1} in complex I (Figure 4.3-1.A). The frequency's upshift (6-9 cm^{-1}) in comparison to the NuoEF spectra is related to differences in the interaction between the Fe orbitals[12, 359] arising from the contribution of N1b in the NDF and complex I samples.

Table 4.3-1. Metal-ligand vibrations of Complex I and its fragment by Raman spectroscopy. (Assignments are mainly according to the studies of Moulis *et al.*[270], Czernuszewicz *et al.*[355] and Han *et al.*[12, 359])

Modes		QRF	Complex I	NDF	NDF ^{54}Fe	NuoEF	Type of cluster	Cluster contribution
Fe-S stretching	A_g Fe-Fe	--	220	217	217	211	2Fe-2S	N1a, N1b
	Bridging (T_2: B_2/E)	--	249	244	--	--	4Fe-4S	N4,N5,N7
	Terminal(B_{3u})	--	281	290			2Fe-2S	N1b
	Bridging (T_1:A_2/E)						4Fe-4S	N4,N5,N7
	Bridging (B_{1g})	--	322	OV	OV	319	2Fe-2S	N1a
	Terminal ($A_{1\ breathing}$)	333	334	332	--	335	2Fe-2S	N1a, N1b
							4Fe-4S	N3,N4,N5, N6a,N6b,N7, N2
	Terminal Fe-S (Cys)	349	340	--	--	--	4Fe-4S	N2
	Bridging(A_g)		388	388	414	388	2Fe-2S	N1a
	Bridging(B_{2u})			403		404		
	Bridging (B_{2u})	417	411	--	--	--	4Fe-4S	N2
Bending motions	C_α-C_β-C + C_α-N-C	451	455	447	446	--	2Fe-2S	N1b, N4,N5,N7
							4Fe-4S	
	C_α-C_β-N	479	--	--	--	466	2Fe-2S 4Fe-4S	N1a, N2
	Fe-S-C + A_1 overtone		490	492	491	484	4Fe-4S	N3,N4,N7
Fe-S Overtones	2 x T_1(A_2)	516	--	--	--	--	4Fe-4S	N2, N6a,N6b
	2x T_1 (E)	522	528	531	527	527	4Fe-4S 2Fe-2S	All
	2X B_{3u}	547	552	544	545	--	2Fe-2S	N1b
	T2 x υ(Fe-S-Fe)	569	568	--	--	--	4Fe-4S	N2,N6a,N6b
	A1 x υ(Fe-S-Fe)	--	--	593	594	591	4Fe-4S	N3,N4,N5, N7
C-S Stretching		621	620	620	--	628	4Fe-4S	All
			641	641	--	--		N5
	Cysteinate group	758	758	757	--	--	4Fe-4S	N2,N6a,N6b

Cluster N1a of NuoEF is coordinated by a Cys-$(Xxx)_{12}$-Cys-(Xxx)-Cys-$(Xxx)_3$-Cys motif, that is also present in the [2Fe-2S] ferredoxin from *Clostridium pasteurianum* and *Azotobacter vinelandii*.[361]. This type of ferredoxin has a thioredoxin-like ligation, where the cluster has a motif formed by two loops (Figure 4.3-2.A). The unique features of this cluster are the Fe-S^b modes (Ag, B_{2u}) of the $Fe^2(\mu 2\text{-}S)^2$ unit which appear at 388 cm^{-1} and 404 cm^{-1}, respectively. These signals have been also described for the 25 kDa subunit of the *Paracoccus denitrificans* complex I[226, 362]. Although the signal is a shoulder, it remains present in the spectra of the full complex and its fragment (NDF) (solid line Figure 4.3-1.B). In the ^{54}Fe labeled fragment, this signal shifts towards 414 cm^{-1} supporting the assignment of this signal to cluster N1a.

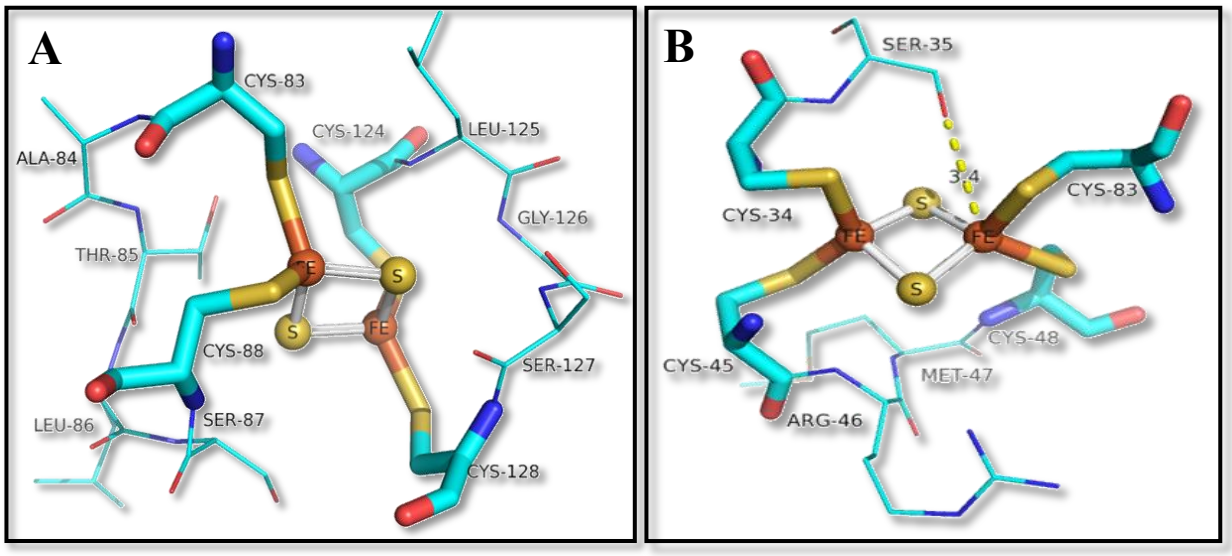

Figure 4.3-2. Schematic representation of the [2Fe-2S] clusters present in Complex I and their motif A.N1a and b. N1b. The dashed yellow line represents a hydrogen bond, its length is shown in Å. (PDB: 4HEA)

Besides the previous modes, the signal at 319 cm^{-1} can be attributed to a Fe-S^b mode (B_{1g}), observed before in the "red paramagnetic protein" in *C. pasteurianum*[363], Rieske proteins[353] and mitoNEET[364], it had been described only for [2Fe-2S] cluster, therefore it is related to the N1a cluster in the NuoEF spectrum. This signal is not detectable in the spectrum of NDF, most likely due to an overlap with the more intense signal around 330-340 cm^{-1} arising from [4Fe-4S] clusters. In complex I the Fe-S^b mode (B_{1g}) is seen at 322 cm^{-1}. It can be concluded that the clusters contributing to this spectral range have different environments in complex I from *E. coli* and NuoEF from *A. aeolicus*.

In summary, the binuclear cluster N1a is found to exhibit similar characteristics as a thioredoxin-like [2Fe–2S] Ferredoxin. The RR of the N1a cluster, assigned to the fundamental Ag Fe-Fe of the N1a Cys motif points towards a weak connection of the cysteine ligands between each other and overlap of the Fe orbitals and weak Fe-Fe interactions. The cluster motif can also influence the distortion of the cluster; as can be seen in Figure 4.3-2. N1a and N1b motifs have a completely different arrangement. While the Fe atoms in N1b are connected through 3 amino acids between their Cys ligands, in N1a the Cys ligands form two loops leaving both Fe atoms "free" and not directly connected.

Besides the normal modes, Fe-S overtones can be identified in the spectra. From previous studies it is expected to observe the overtones between 500 and 800 cm^{-1}[357, 365, 366]. For the [2Fe-2S] and [4Fe-4S] clusters, the bands are assignable to overtones of the fundamentals of Fe-S stretching modes. There are two possible quantum transitions ν_1 and ν_2, and the intensity of the overtones and the frequency should be proportional to the squares and products of the corresponding fundamentals[359].

An overtone seen in all spectra is caused by the ν_1: Fe-S^t (B_{3u}) and ν_2: Fe-S^b modes present in the region of 275-290 cm^{-1}. This overtone is expected to be in the spectral region of 500-550 cm^{-1}. The Fe-S stretching modes in this area are coupled; however, their overtones are typically uncoupled[367, 368]. The signal at 545 cm^{-1} present in the spectra of complex I and the NADH dehydrogenase fragment was described for the [2Fe-2S] clusters, specifically for adrenodoxin-type clusters[359], leading to the conclusion that N1b could have the type of distortion described for ferredoxins[369]. The increase of its intensity in the spectrum of complex I may be explained by the C-S stretching vibrations probably contributing to the signal[370].

The four C-S stretching modes from [2Fe-2S] clusters are expected at 650-670 cm^{-1} [12] however, they are not detectable in any of the spectra because, most likely, they are too weak to be seen under the experimental conditions applied.

The main difference between N1a and N1b, observed in the RR spectra, can be attributed to the ligation of the clusters. The spectral characteristics of the cluster N1b reveal that the frequencies related to the B_{3ut} mode and the Ag, B_{1ut}, B_{2gt} and B_{3ub} modes differ

significantly from N1a. The data for N1b reveals a distorted symmetry as described previously in adrenodoxin-type clusters[359, 369].

This is in line with EPR data, redox titrations and the energy profile for electron transfer[18, 216]. N1a has a lower midpoint potential than N1b[371]. EPR spectroscopy characterizes N1a as a signal of rhombic symmetry ($g_z,_y,_x$ = 2.00,1.94, 1.92), while N1b exhibits an axial symmetry ($g_z,_y,_x$=2.02, 1.94, 1.94)[134]. This suggest that, the differences in the geometry, due to the effect of ligation of the cluster motif are the cause of the dissimilarities of their redox and paramagnetic properties.

In addition, it has been suggested that redox interactions of N1b with the other clusters further change the environment and therefore the shape of the cluster itself, even though its function is to be a single electron carrier[12, 216]. As explained above (see section 1.4.3) the function and the properties of N1a are still a matter of controversy, including the understanding of the structure of the cluster motif, the pH-dependency of the *Em* and the role during the electron transfer.

Identification of the [4Fe-4S] clusters. In the spectrum of the NuoEF subcomplex the contributions of the tetranuclear clusters derive only from N3, in the NDF the signals derived from N4, N5, and N7. In complex I the additional vibrations from clusters N6a, N6b and N2 are seen; the QRF fragment will only give rise to the contributions from N6a, N6b and N2.

In the spectra of the NDF and of complex I (Figure 4.3-1. A and B), a RR band is evident at 244 cm^{-1} and 249 cm^{-1}, respectively. This signal is assigned to the Fe-S^b vibration from [4Fe-4S] clusters, not present in NuoEF. This RR band had been described as a T_2 mode including two components, B_2 and E[355]. The average of the vibrations will be E type at lower frequencies around 242 cm^{-1} as in the spectrum of the fragment. For complex I the average will be B_2 near 250 cm^{-1}. Since this signal is only present in the spectra of the NDF and the complex I, it can be assigned to the contribution from the clusters N4, N5 and N7.

The differences in the frequency between the various samples may be caused by the change in the environment, especially in the case of N5. It should be mentioned that cluster N5 being close to the protein surface[183] in the fragment will have a different environment in the complex inducing small shifts. The T_2(E) and T_2(B2) bridging modes involve small amplitudes of Fe motions[355] that may be due to the longitudinal movement of the T_2(E)

stretching and the latitudinal movement of T_2(B2), giving evidence for the influence of the ligation of the Cys residues that form part of the cluster motif. As can be seen in Figure 4.3-3.C, all the Cys residues of N5 are connected through the motif while in the other [4Fe-4S] clusters only three of the Fe atoms are connected.

The spectral region around 275-290 cm^{-1} includes the Fe-S^t vibrations from the [2Fe-2S] clusters according to the B_{3u} mode[12] and Fe-S^b vibrations of the [4Fe-4S] clusters according to the T_1 mode. This mode also has two components: A_2 and E[164]. The signal is only detectable in the spectra of the NDF and the complex, arising at 290 and 281 cm^{-1}, respectively (Figure 4.3-1. A and B), suggesting that the vibrations of the [4Fe-4S] clusters N4, N5 and N7 have the major contributions to this signal. The shift of 9 cm^{-1}, also reflects that the environment of the cluster is not the same in both proteins.

The 330-340 cm^{-1} region contains the bridging modes of the clusters. One of the strongest bands around 336 cm^{-1} was described for [4Fe-4S] clusters as a total symmetric A1 breathing mode, primarily from Fe-S^b stretching[356, 372]. In the case of NuoEF this vibration is seen at 335 cm^{-1} corresponding to the contribution of N3. This band is known to be characteristic of the intermediate state of the [4Fe-4S] clusters, in which the Fe atoms move away from each other, while all the S atoms move towards the center[355, 373]. For NDF the signal is broad and appears at 332 cm^{-1}. In the case of the complex it is seen as an intense peak at 334 cm^{-1} and for QRF this signal is seen at 333 cm^{-1} (Figure 4.3-1.C).

This band is also an indicative of a full cysteinyl coordination of the cluster in oxidized Fe-S proteins[374]. Several studies have correlated the intensity of this band with the overlapped bridging modes and their coupling with the S-C-C modes (AgSCC). The frequency of this band is linked to the dihedral angles[270, 355, 359, 375]. The relationship can be summarized as follows: when the angle of the AgSCC decreases, the frequency of the mode increases demonstrating the interaction between the S^t-C-C bending motions and two stretching Fe-S terminal modes. Details of this coupling are evident in the spectrum of the ^{54}Fe labeled fragment where the signal upshifts to 338 cm^{-1} from 332 cm^{-1} in the unlabeled sample (Figure 4.3-1, solid and dotted line).

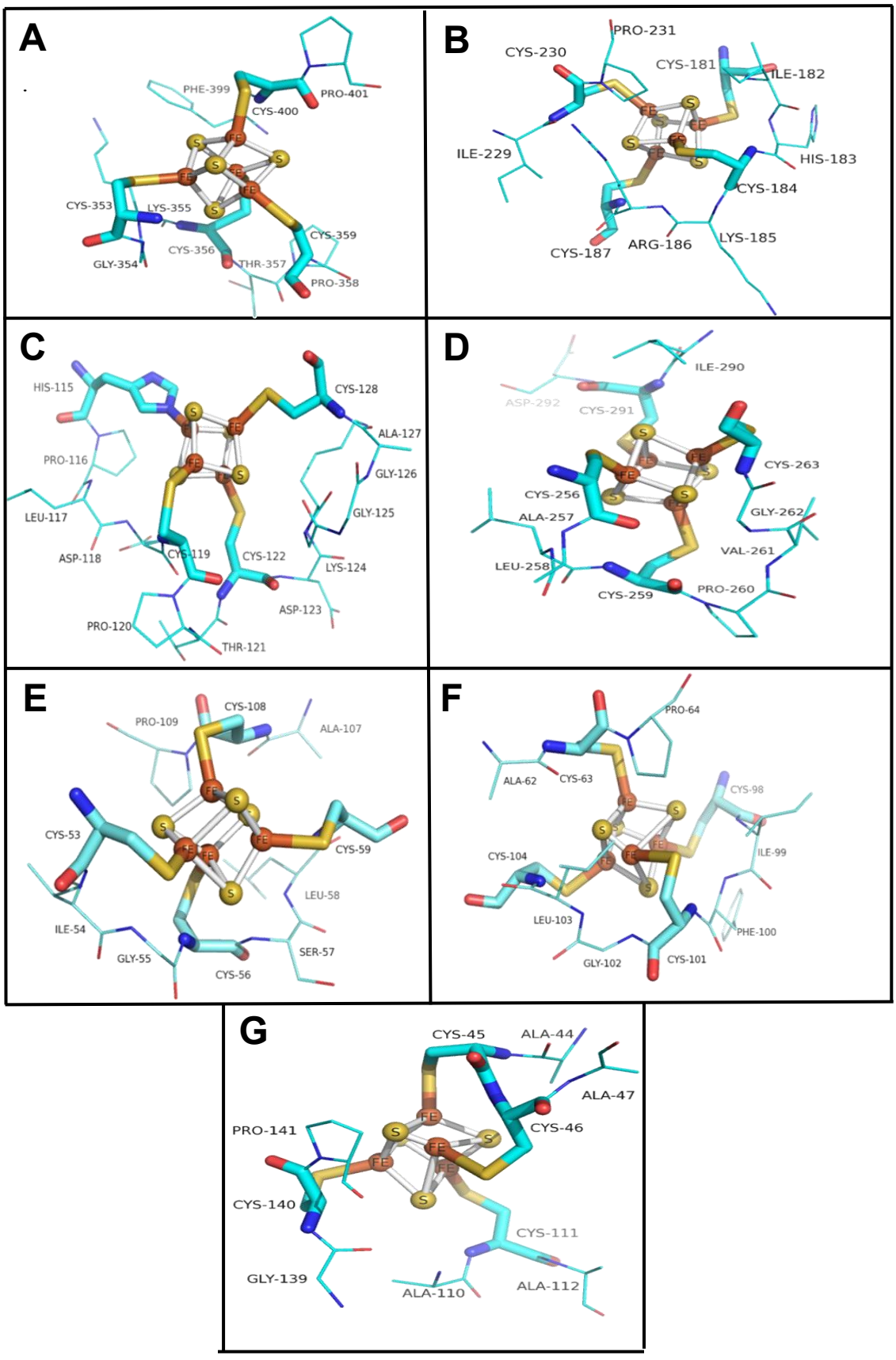

Figure 4.3-3. Schematic representation of the [4Fe-4S] clusters present in Complex I and their motif A.N3 B. N4 C. N5 D. N7 E. N6a F. N6b and G. N2 (PDB: 4HEA)

The RR bands at 340 cm^{-1} and at 411 cm^{-1} in the spectrum of complex I (Fig. 4.3-1.A), and 349 cm^{-1} and 417 cm^{-1} in QRF (Figure 4.3-1.C) are assigned to the Fe-S^b (B_{2u}) mode of a [4Fe-4S] cluster. At 411 cm^{-1} in the spectrum of complex I, this band is mainly the contribution of the Fe-S^b modes. Similar features have been described in a native 2[4Fe-4S] cluster in ferredoxins[270].

More specifically this vibrational mode is a characteristic signal of hybrid clusters, or clusters that have a non-cysteine amino acid as ligand, as for example the ferredoxin from *Pyrocuccus furiosus,* from *Chromatium vinosum* or *C. pasteurianum*[356, 376]. It was proposed that the differences are caused by the degree of splitting of the vibrational modes attributed to the Fe-S(Cys) (Fe-S^b) that change the vibration depending on the various distortions experienced by the Fe-S(Cys)/ (Fe-S^b) bonds.

In summary, this signal reveals the unusual ligand coordination for one of the tetranuclear clusters. In complex I, there are two clusters that have these characteristics, namely N5 and N2. Whereas N2 is coordinated by two neighboring cysteine residues, N5 is ligated by a histidine residue. Since this vibration is only visible in the spectra of the QRF fragment and complex I (Figure 4.3-1. A and C) and not found for the NDF, it can be unambiguously assigned to the N2 cluster.

In another study using the benzyl cube model in solution[355] it was shown that this vibration has two components with a regular cysteinyl ligand at 340 cm^{-1} and 367 cm^{-1} attributed to a Fe-S^t vibration described by a T_2(E) mode. Since the two components are not visible in the spectra of complex I, the vibration shows a distinct conformational relaxation due to different cysteinyl coordination. A lower symmetry of cluster N2 can be concluded from the band position at 411 cm^{-1} band in the complex I.

As shown is Figure 4.3-3.G there are two main differences between N2 and the others [4Fe-4S] clusters that can be the cause of the variations in the Fe-S stretching vibrations. First in N2, two of their Cys ligands are joind (Cys44-Cys45), which will cause a difference in the dihedral angles of the cluster motif in general. Second, usually three of the Cys ligands are connected through the motif while here only two of them have this property.

The region between 450-500 cm^{-1} is characterized by a mixture of bending modes: S-Cα-Cβ, Cα-Cβ-C and Cα-N-C[377]. These modes directly depend on the Fe-S-Cα-Cβ dihedral

angle, the coupling strength between the Fe-S stretching and the Fe-S-Cα vibrational mode with S-Cα-Cβ bending displacement[164]. The spectrum of the fragment (Figure 4.3-1.B solid line) shows a band at 447 cm^{-1}, which is not susceptible to the ^{54}Fe substitution (491 cm^{-1}; Figure 4.3-1.B dotted line) in the spectral region dominated by the Cα-Cβ-C and Cα-N-C bending. The clusters contained within the fragment display different bending vibrations than clusters N1b and N3 in NuoEF again indicating that the environment of the clusters is different in *E. coli* and in *A. aeolicus*. The signal at 466 cm^{-1}, dominated by the Cα-Cβ-N bending modes[356] is only seen in the spectra of and NuoEF (Figure 4.3-1.D).

The frequency and the intensity of this band directly reflect the core symmetry depending on the hydrogen bonding of the Cys side chains. The Fe-S/S-C-C coordination mixing has been extensively studied[377]; which helps to account for the variability in the spectral pattern of the Fe-S (Cys) modes and the intrinsic properties of the clusters observed in the samples. This vibration indicates a skeletal deformation confirming the unique environment of cluster(s), probably N1a, that may be stabilized by strong hydrogen bonds.

The signals at 484 cm^{-1} and 492 cm^{-1} in the spectrum of the fragment and that at 490 cm^{-1} in the spectrum of complex I include the bending of T_2 modes in T_d symmetry[377]. This mode is a Fermi resonance composed by a Fe-S-C bending mode and the A1 components of the Fe-S stretching overtone of the [4Fe-4S] clusters (described below). The frequency is influenced by the average strength of the Fe-S stretching force constant[378]. This signal is the consequence of the contribution of all the clusters except N6a, N6b and N2, as they are not present in QRF.

The RR band at 568 cm^{-1} in the spectrum of complex I and at 569 cm^{-1} in the spectrum of the QRF fragment, arises from the combination of the $Fe\text{-}S^b$ T_2 mode (the signal at 249 cm^{-1} described above) and the Fe-S-Fe bending modes. The signals at 591 cm^{-1} and 593 cm^{-1} in the spectra of NuoEF and the fragment, respectively, are caused by the combination of the symmetric A1 breathing mode seen at 335 cm^{-1} for NuoEF and 332 cm^{-1} for the fragment and the Fe-S-Fe bending modes of the [4Fe-4S] clusters.

For the [4Fe-4S] clusters signals between 620-650 cm^{-1} are expected as a contribution of the ν(C-S) modes[356, 373]. The spectrum of NuoEF contains a broad band with a maximum at 628 cm^{-1} corresponding to the N3 ν(C-S). In the spectra of the complex and the fragment a

signals is present at 620 cm^{-1} and it contains the overlapping C-S stretching modes of all [4Fe-4S] clusters. The shift in this signal is directly correlated to changes in the dihedral angle between the Fe-S-Cα[355].

The signal at 641 cm^{-1} that can be found in the spectra of the NDF and complex I also corresponds to the C-S stretching modes. This signal was previously described for [4Fe-4S] clusters with three Cys ligands and as a fourth ligand a different amino acid like Asp, His or Glu[270, 372, 375]. The number of possible orientations of the Cys side chain carbons and the Fe-S-C-C dihedral angles lowers the true site symmetry and there is evidence of the deformation of the tetranuclear symmetry and the length of the bonds[270, 374]. In the data shown here, the signal most likely arises from the contribution of cluster N5 since it is the only cluster with an incomplete Cys ligation (Figure 4.3-1.B) in NDF.

A broad signal is present at 758 cm^{-1} in the spectrum of QRF and of complex I. Bands at this position are usually assigned to C-S stretching vibrations from the cysteinate group. The same assignment can be made in the spectra of the complex I and the fragment for the signals at 757 cm^{-1} and 756 cm^{-1}, respectively. The high frequency of these modes is also related to the contribution of the CH_2 rocking mode[356, 374]. This signal arises from the contribution of all the [4Fe-4S] clusters except the N3 cluster, since this signal is absent the spectrum of NuoEF.

FMN modes. In addition to the Fe-S clusters, signals from the flavin cofactor may be expected in the RR spectra. The main contributions from flavin typically originate from the isoalloxazine ring (Figure 4.3-4)[379]. Several studies have demonstrated that the spectra from FMN, FAD and riboflavin include the same modes[380]. Raman lines have been assigned to each of the three rings[381] and to each of the carbonyl groups or nitrosyl moieties[382].

Previous studies with free and protein bound flavin demonstrated that the interactions between the protein and the cofactor might weaken bonds leading to decreased force constants and hence to a shift of many of the signals of protein-bound FMN[383-385].

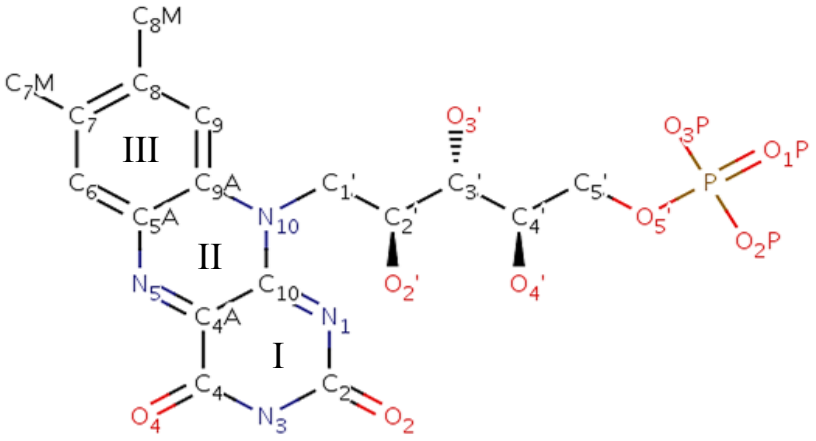

Figure 4.3-4. Structure of Flavin Mononucleotide. Adapted from the ligand explorer data bank (RCSB, PDB:4HEA)

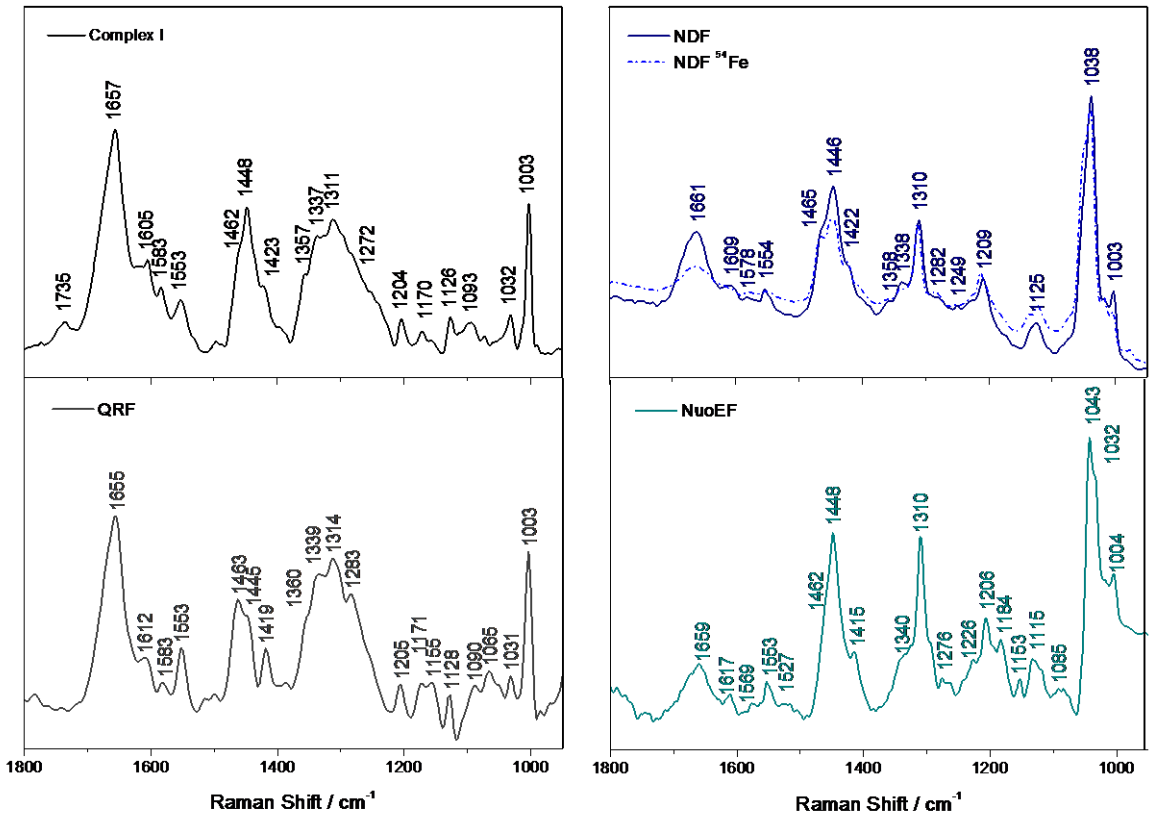

Figure 4.3-5. Mid frequency RR spectra enhanced by an excitation of 514.5nm. A. *E. coli* complex I. B. The NADH dehydrogenase fragment (blue solid) and the ^{54}Fe-enriched NADH dehydrogenase fragment(dotted line) of the *E. coli* complex. C. Quinone reductase fragment and D. *A. aeolicus* Subcomplex NuoEF.

According to these studies, the breathing-like mode of ring III (see Figure 4.3-4) [387] is involved in the band at 732 cm^{-1} for the NuoEF (Figure 4.3-1.D), in the broad signal around 745 cm^{-1} in the spectrum of the fragment (Figure 4.3-1.B), and in the signal seen at 738 cm^{-1} in the spectrum of the complex (Figure 4.3-1.C). A complete assignment of all the FMN modes and their frequencies from the NuoEF, NDF and complex I spectra is summarized in

Table 4.3-2. The assignments was also compared to the normal modes described by simulations and analysis of the spectra of similar proteins[388].

Table 4.3-2. Comparison of the frequencies of FMN normal modes between the analyzed samples and previous studies.

Band number [386]	FMN [379]	FMN H_2O [380]	FMN bovine heart[388]	NuoEF	NDF	Complex I	Assignments
	--	742	--	732	745	739	Ring breathing of ring I [380].
	--	788	--	785	778	777	$\upsilon(C_7\text{-}N_{7m})$, $\upsilon(C_6\text{-}C_7)$ [380]
XIII	1162m	1158	--	1153			υ_{33}: $\upsilon(C_2N_3)$, $\upsilon(C_{4a}\text{-}C_4)$, $\upsilon(C_{4a}\text{-}C_{10a})$, $\upsilon(C_7\text{-}CH_3)$, $\delta(C_6\text{-}H)$
XII	1182sh	1183	--	1184			υ_{32}: $\upsilon(C_4\text{-}C_{4a})$, $\upsilon(N_3\text{-}C_4)$, $\upsilon(C_2\text{-}N_3)$, $\upsilon 5N_1\text{-}C_2)$
XI	1232m	1228	1226	1226			υ_{30} : $\upsilon(C_8\text{-}CH_3)$, $\upsilon(N_3\text{-}C_4)$
X	1256m	1256	1251	1276			υ $(C_9\text{-}N_{10a})$, $\upsilon(C_6\text{-}N_1)$, $\delta(N_3\text{-}H)$, $\delta(C_2{=}O)$, $\delta(C_4{=}O)$,$\delta(C_5{=}H)$, $\delta(C_6{=}H)$
VI	1410s	1407	1407	1415	1422	1423	υ_{22} : $\upsilon(N_1\text{-}C_2)$, υ $(C_{5a}\text{-}C_6)$, υ $(C_8\text{-}C_9)$, υ $(C_{5a}\text{-}C_{9a})$
V	1467s	1462		1462	1465		υ_{21} : υ $(C_6\text{-}C_7)$, υ $(C_8\text{-}C_9)$, υ $(C_9\text{-}C_{9a})$, δ (CH_3)
II	1585s	1581	1586	1569	1578	1584	υ_{16}: $\upsilon(C_{4a}\text{-}C_{10}$), $\upsilon(C_{10a}\text{-}N_{10})$

Furthermore, above 1000 cm^{-1} (Figure 4.3-5) vibrations that have strong or medium scattering have been detected. In the case of NuoEF, a complete fingerprint from the normal modes previously described is observed. It should be noted that these modes overlap with each other in the case of NDF. This overlapping is even more evident in the spectrum of Complex I. Even if the RR scattering of the flavins is viable at all UV wavelengths, the contribution from aromatic amino acids might be stronger depending on which wavelength the enhancement is made. Since the excitation wavelength (514.5 nm) is closer to the electronic transitions of the Fe-S cluster, the signals from the amino acids in the environment are more intense than the vibrations of the FMN.

Contributions from amide vibrations and amino acid side chains.

Tyr. The first two signals above 800 cm^{-1} are characterized by a Fermi doublet from Tyr residues that have two components, the first one around 820-830 cm^{-1} corresponding to

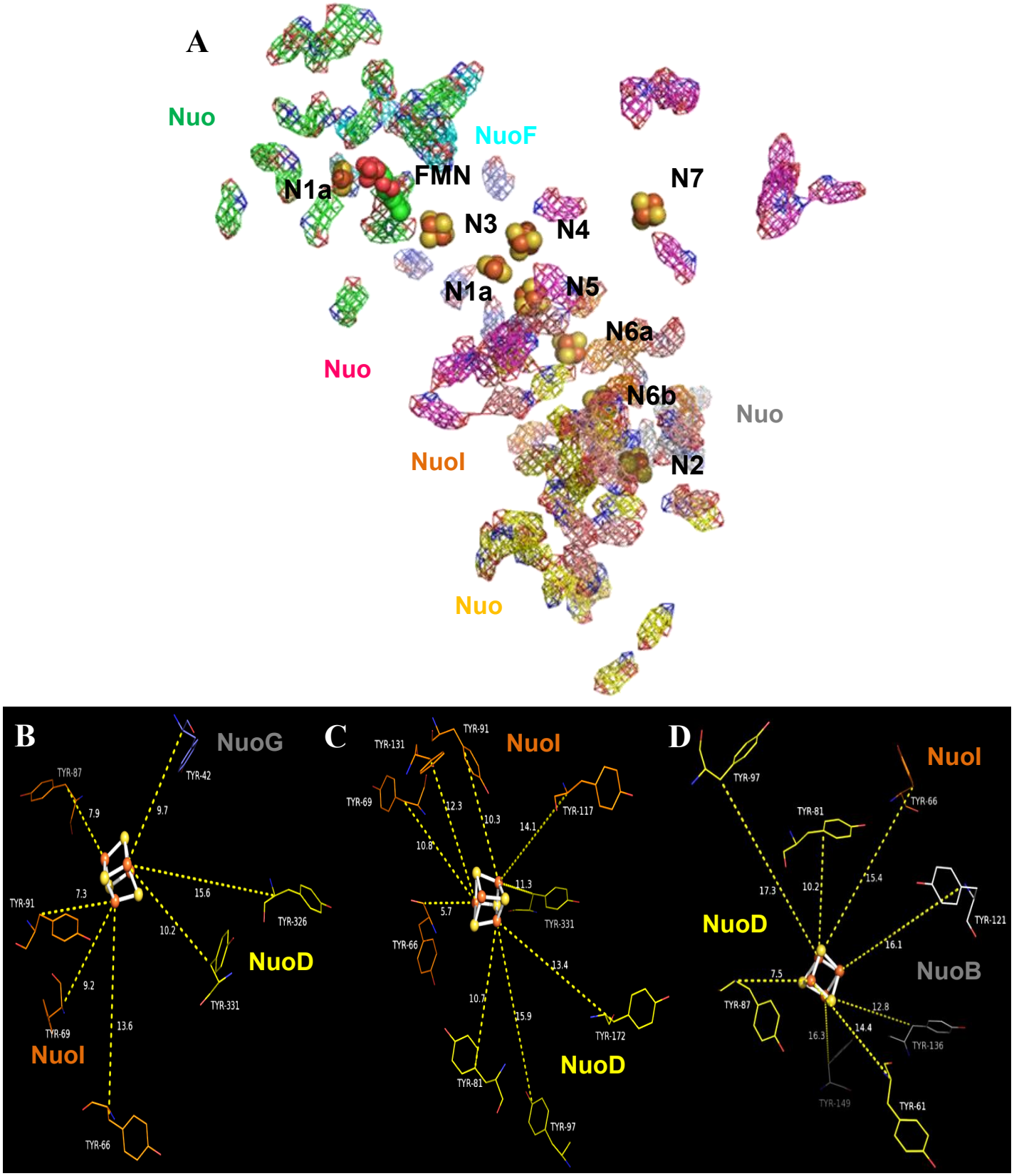

Figure 4.3-6. Schematic representation of Tyr residues around the Fe-S clusters. A. Complex I B. N6a C. N6b and D. N2

the overtone from the out-of-plane ring bending of the para-substituted benzene (ν_{16a} mode). The second signal observed around 840-855 cm^{-1} originates from the resonance between the symmetric ring breathing vibrations (fundamental mode ν_1)[389].

The intensity ratio between the two signals ($I\nu_{16a}/I_{\nu 1}$) reflects the average of the "exposed" or "buried" tyrosine residues present near the cofactors. If the ratio is high the Tyr residues are exposed and if the ratio is low, the Tyr residues are exposed[390]. Typically residues up to about 20 Å away from the cofactors are considered to be possibly contributing to the spectra[357, 391, 392].

In this spectral region each sample exhibits a particular signature. The spectrum of NuoEF has a doublet formed by two signals at 812 and 833 cm^{-1} with $I\nu_{16a}/I\nu_1$: 0.3. The spectrum of the fragment has a doublet at 822 and 851 cm^{-1} with $I\nu_{16a}/I\nu_1$: 0.5, the QRF fragment at 824 and 854 cm^{-1} with $I\nu_{16a}/I\nu_1$: 0.9 and that of complex I has a doublet at 825 and 851 cm^{-1}, $I\nu_{16a}/I\nu_1$: 0.3. The factors that influence the ratio of the tyrosine signal are among others, pH, solvent effects influencing the environment of the benzene ring and the conformation of the amino acid side chain. Is also important to consider that, ratio is the average among the population of the different Tyr residues in the protein.

In the case of the NuoEF, the NDF, and the complex I the $I\nu_{16a}/I\nu_1$ ratio indicates that most of the Tyr residues in the vicinity of the clusters are "buried", the hydroxyl group acting as a donor of a strong hydrogen bond to a negative acceptor group. On the contrary, the average of the tyrosine signals indicate that most of the Tyr are "exposed" in the QRF and the hydroxyl group acts as an acceptor of strong hydrogen bonding from a positive donor group. The latest may be account for tyrosine residues in the vicinity of cluster N2, N6a or N6b [183, 210, 231, 295, 393]. In general, the Fermi doublet observed in NuoEF, NDF and QRF spectra gives an idea of differences in the distribution of the Tyr residues around the cluster in each subunit.

As can be seen in the schematic representation of all the Tyr residues in the membrane part of complex I from *T. thermophilus* (Figure 4.3-6.A), the Tyr residues per subunit are more abundant around the clusters N6a, N6b and N2. On the basis of the recently published crystallographic data[183], residues in the vicinity of the cofactors can be discussed. In the case of the N2 cluster, Tyr81 and Tyr87 from NuoD (conserved as Tyr 267 and 273 in *E. coli*) and

Tyr87 from NuoI (Tyr 86 in *E.coli*) can be identified to be located at distances below 10 Å from the cluster (Figure 4.3-6.B).

Further residues like Tyr91 from NuoI in the case of N6a and Tyr66 and Tyr69 also from NuoI in the case of N6b are seen in the structure from *T. thermophilus* are not conserved in *E. coli* and will thus not be involved in the spectra reported here. Highly conserved Tyr residues located in the vicinity of the N2 cluster have been previously studied by means of electrochemically-induced FTIR difference spectroscopy, revealing that the redox reaction is perturbing the environment of these Tyr residues notably Tyr 114, 19 and 154 in *E. coli* that correspond to Trp95, Phe119 and Tyr136 in *T. thermophiles* [1, 230]. Tyr136 (in *T. thermophilus*) is located about 12 Å from the N2 cluster and thus it is a possible candidate for the resonance Raman signature described here.

Trp. The signals at 879 and 876 cm^{-1}, present only in the spectrum of complex I and the QRF can be attributed to the υ_{10a} vibrational mode of tryptophan residue(s). Typically this mode is expected to arise between 870 and 880 cm^{-1}. The frequency of the band reflects the strength of hydrogen bonding at the N^1H site of the indole ring (υ_{10a}); the lower the frequency, the stronger the hydrogen bonding[394, 395]. The 876 cm^{-1} signal is typical for strong hydrogen bonding; this environmental feature can be correlated with clusters N6a and N6b present in NuoI and N2 in NuoB.

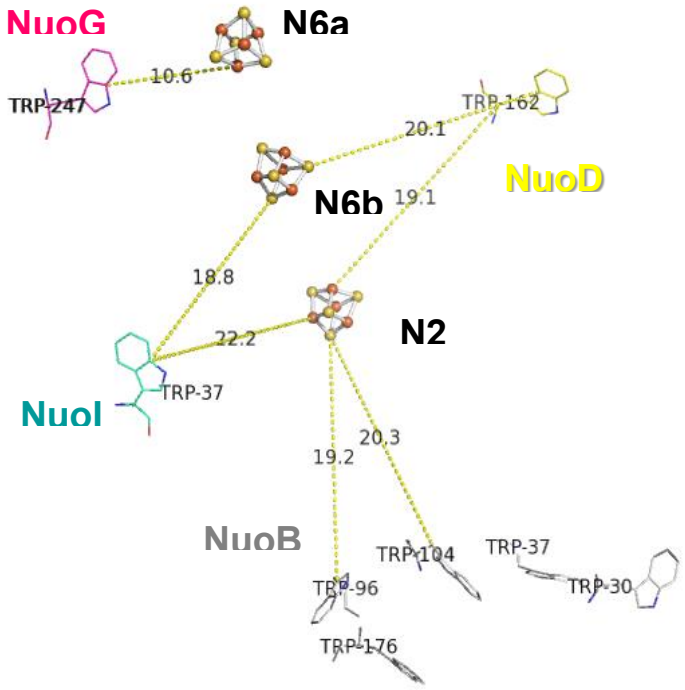

Figure 4.3-7. Scheme of the closest Trp residues around N6a, N6B and N2 in *T. thermophilus* complex I. (PDB: 4HEA)

In the spectrum of complex I (Figure 4.3-2) the presence of the Trp contribution could be indicating that in the oxidized state, there are at least two Trp residues around the clusters N6a, N6b or N2; one of the residues being highly hydrogen bonded. Studies in photosystem I have revealed that these Trp signals can be used as structural markers for the determination of the environment and solvent exposure of Trp residues[392, 395]. When the signal is observed, the indole side chain is located less than 20 Å from the electron transfer cofactor and may follow the structural changes around the cofactors during the electron transfer reactions[392].

One residue that can be suggested to be involved in the RR data on the basis of the *T. thermophilus* structure[183] is for example Trp 247 in NuoG, which is found at position 219 in *E. coli*. It is located about 11 to 13 Å from N6a and N6b, respectively, and according to the structure it seems to be the closest Trp to the cofactors (Figure 4.3-7). Further amino acid side chains, like Trp37 in NuoB in *T. thermophilus*, conserved at position 55 in *E. coli*, is found around 22 Å away from N6b and N2. Several further residues are indicated in Figure 4.3-7, but they are not conserved in *E. coli*.

Other amino acids. Table 4.3-3 resumes a full description of the entire amino acid side modes, the amide vibrations and the ν(C-H) modes above 1000 cm^{-1} found in the RR spectra of complex I, QRF, NDF and NuoEF (Figure 4.3-5). The main differences between them are marked in blue.

From the signals above 1000 cm^{-1}, the contribution from His (Nt-H asym rocking) and Ala (ν(C-C)) present a lower frequency in the NuoEF spectrum, this indicates that the position and interactions of these residues have a different pattern in NuoEF. Also in the NuoEF, the spectrum presents three signals, 1141, 1184 and 1527 cm^{-1}, that are not visible in the rest of the samples, this may be due to differences in the sequence of the structure, as NuoEF subcomplex is from *A. aeolicus* and the rest of the samples are from *E. coli*.

The δ(Cα-H) modes of the Cys residues in each of the samples exhibits a different frequency. In NuoEF the signal arises at 1415 cm^{-1}, shifting to higher frequencies in the other samples. In NDF the signal is seen at 1446 cm^{-1} and at the complex I spectrum it appears at 1423 cm^{-1}, while in the QRF two components are observed at 1419 cm^{-1} and 1447 cm^{-1}. The dihedral angle of the Cα with the C=O (ψ) influences the position of the signal. The broader the angle the lower the frequency will be[310], indicating that the Cys residues in NuoEF and

Table 4.3-3. Amide vibrational modes and amino acid side chain contributions from Complex I and its fragments by Raman Spectroscopy.

(Assignment were done based on the studies of Jenkins *et al.*[309] and Ianoul *et al.* [13])

Modes		Complex I	QRF	NDF	NDF ^{54}Fe	NuoEF
Fermi doublet	Tyr	**825** **851**	**824** **854**	**822** **842**	**822** **851**	**812** **833**
δ(ring)	Trp	**879**	**876**	--	--	--
Ring breathing	Phe	1003	1003	1003	1003	1004
ν(C-C) δ(ring)	Arg,Lys Phe	1032	1031	1038	1038	1032
ν(C-N)	Met	**1093**	**1087**	--	--	**1085**
Nt-H asym rocking ν(C-C)	His Ala	**1126**	**1128**	**1125**	**1125**	**1115**
Cβ-twist δ(Cϒ1-Cβ-Cϒ2)	Ile, Leu	--	--	--	--	1141
Cβ-twist δ(Cϒ1-Cβ-Cϒ2)	Iso	--	1155	--	--	1153
δ (C-H)	Phe	**1170**	**1174**	--	--	**1184**
symmetric ν(Ring –O)	Phe, Tyr, Trp	1204	1205	1209	1209	1206
Amide III δ(N-H) ν(C-N) δ(C=O) ν(C-C)	β-strands	1240	--	1249	1249	1226
	β-turns	1272	1286	1282	1282	1276
	α-helix	1311	1314	1310	1310	1310
ν(C-Cα) δ(Cα-H)	Backbone	**1337**	**1339**	--	--	---
Cα-Cβ-twist	Ala,Met,His,Lys	1357	1360	1358	1358	1340
δ(Cα-H)	Cys	**1423**	**1419** **1447**	**1446**	**1446**	**1415**
δ(CH_2)	Methylene group (side chain)	**1448**	**1460**	**1467**	**1467**	**1448**
CH_3 asym def	Met	--	--	--	--	1527
δ(N-H), ν(C-N)	Amide II	1553	1553	1554	1554	1553
ν (C=O) ν(C-C)	Phe His	**1583**	**1584**	**1578**	**1578**	**1569** --
Ring breathing	Tyr	1605	1605	1609	1609	--
δ($NH3^+$)	Lys	--	--	--	--	1611
υ(C=O)	Amide I	1657	1655	1661	1661	1659
ν(COO^-)	Asp, Glu	1735	1784	--	--	--
ν(C-H)	Cys, Met	--	**2723** **2741**	**2717**	**2717**	**2738**
	His	--	--	**2782**	**2782**	--
	Met	**2838**	**2826**	--	--	--
	Gly,Asp, Glu	**2857**	--	--	--	--
	His	**2869**	**2872**	**2874**	**2874**	**2880**
	Leu, Lus, Ile	**2882**	--	--	--	--
	Thr, Pro	**2933**	**2937**	**2940**	**2940**	**2935**
	Cys, His, Ser, Leu,Trp, Gly, Lys	2977	2968	2964	2964	2966
	Phe,Tyr, Trp	3062	3061	3061	3064	3062

some of the QRF have a larger angles than in the rest of the samples. The difference in the frequency of this vibrational mode had been also associated with the formation of disulfide bonds[396], but usually the disulfide bonds, also should give rise to signal between 2600-2700 cm^{-1}, as no signal are observed in this spectral range (Figure 4.3-8), this vibration can be attributed only to the changes in the dihedral angles of the Cys residues.

In addition, in the complex I and QRF a signal between 1730 and 1780 cm^{-1} arises. This signal can be attributed to the symmetric ν(C=O) modes from amino acids as Asp and Glu residues[310, 313], which are in proximity of the N6a, N6b and N2 clusters.

Backbone vibrations. All amide bands are resonance enhanced by the first dipole-allowed π→π* transition if the enhancement is made by a laser wavenumber in the UV region. Using an excitation laser with a frequency higher than 250 nm, as in our case, the ground state involves a dominating C-N bond elongation, with smaller C-C and N-C bond contractions and a more modest C-O bond expansion. The C-N double bond character decreases to the point where free rotation occurs so the scattering is lower[397].

Changes in amide I, II and III are observed in the different samples. These differences were expected, pointing to a different secondary structure in each one of the samples. The amide I signal involves the ν(C=O) vibration, it is found at 1657 cm^{-1} in complex I, at 1655 cm^{-1} in QRF and it goes to higher frequencies in the NDF and NuoEF, namely towards at 1661 and 1671 cm^{-1}, respectively.

Amide II vibrations appears around 1553 cm^{-1} in all samples, mainly involves the in-plane δ(N-H) and ν(C-N) vibrational modes. The low intensity of this signal is due to the small change in polarizability associated with this vibration[10].

The amide III range (Table 4.3-3) can be described as a multiband vibrational mode[308]. As general rule, the mode frequencies decrease as the weakened water hydrogen bonding decreases the amide N-H bending and the C-N stretching force constants and changes in water hydrogen bonding impact the N-H bend force constant more than the C-N stretch force constant[246, 252]. The α-helical component has the highest intensity in all the spectra seen here as expected from the already resolved structure[183]. The random coil component has a lower frequency in NuoEF. This indicates that in *A. aeolicus* the random coils have a weaker hydrogen bonding. In contrast to what it happens with the α-helical component in NuoEF and

NDF arises at the same frequency but a higher frequency in complex I and QRF spectra. These changes may also reflect the difference in the interaction between the structure and the environment, due to the absence of the subunits, as is the case of QRF, NDF and NuoEF.

The ν(C-H) region. Comparing with the ν(C-H) modes, arising above 2700 cm^{-1} (Figure 4.3-8) gives a general idea on the functional hydrophobic interactions in the proteins can be made. The potential information that can be obtained by RR is based on the fact that both the relative intensity and the frequency of the vibrational motions of amino acids side chains and the backbone are sensitive to the changes in the micro-environment, in this case around the cofactors.

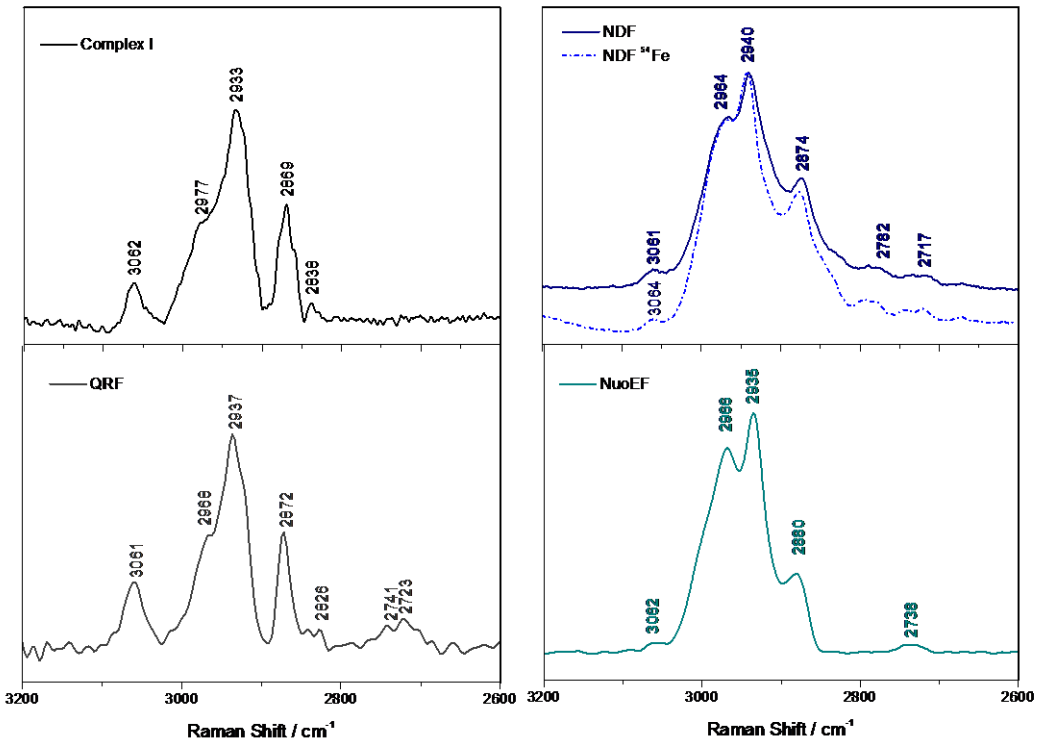

Figure 4.3-8. ν(C-H) stretching region of the RR spectrum of complex I, NDF and QRF from *E. coli* and NuoEF from *A. aeolicus*.

An example is the Met contribution at 2838 cm^{-1} and the Leu, Lys and Ile contribution, this band is observed only in the spectra of complex I, which may indicates that in the fragments and in the subcomplex some of the amino acids around the clusters have a different positions. A similar conclusion can be summarized for the signals around 2715-2740 cm^{-1} corresponding to the contribution of the Cys and Met residues. This set of signals is only observed in the NuoEF, NDF and QRF spectra. Due to the complexity of the complex I structure the signals above 2800 cm^{-1} may have a higher scattering than the signals observed

for the other samples, an assignment of the contribution of the different amino acids is not possible.

In addition, the signal at 2782 cm^{-1}, corresponding to the asymmetric modes of the His is only observed in the NDF spectrum indicating that many His residues are closed to the N1a, N4, N5 and N7 clusters.

In summary, the difference of the cluster motif between N1a and N1b are described and in addition, changes in cluster motif can be described and assigned in the case of N2 and N5. The biochemical approach, where the different subunits can be differentiated, allowed separating the vibrational modes of each one of the cluster as well as the backbone vibrations and the amino side chain contribution that surround them. The characterization of the Fe-S properties in their oxidized form is the basis for further studies in order to follow the changes of the clusters upon reduction. This is the aim of the next sections.

4.3.3 Spectroelectrochemistry

Coupling electrochemistry to FIR and RR allows recording the motions of the metal-ligand vibrations upon electron transfer and it becomes possible to analyze changes in the properties of the Fe-S cluster upon reduction. In analogy to the previous section (i.e. Section 4.3.2) a complete assignment of the vibrations corresponding to each one the clusters will be made together with a full description of the changes in the cluster geometry upon reduction in far IR.

The FIR and RR electrochemically-induced difference spectra can provide valuable information of the metal-ligand vibrations of both, the oxidized and the reduced forms of the protein. In the FIR region, the analysis of the spectra represents a challenge due to the high water absorption; Although RR and IR optical activity of the vibrations are not always similar for symmetry reasons, yet they can be complementary to each other. Therefore, the signals described are the ones that matched with the signals obtained in the differential RR spectra.

For the RR ν(Fe-S) modes two different sets can be distinguished according to the oxidation state of the Fe atom, Fe(III)-S^t, Fe(II)S^t, Fe(II)-S^t and Fe(II)-S^b, the assignment

and properties were compared to the theoretical calculations and experimental approach of the studies of Yachandra *et al*[357], Moulis *et al* [270], Han *et al*[12, 359]and Staples *et al*[370].

The full reduction of a Fe-S cluster is usually accompanied by the rigidity of the cluster in this case the polarizability is lower and the Fe-S stretching modes have a tendency not to be enhanced as in the oxidized[12, 398, 399]. The reason for this is that the RR band depend critically on the symmetry and structural distortion in the electronic excited states, hence the changes in the intensity reflect the changes in the energy of the CT of $S \longrightarrow Fe^{+2}$ in the excited state[12]. In general the bands corresponding to the $\nu(Fe\text{-}S)^t$ lose intensity while the bands corresponding to the $\nu(Fe\text{-}S)^b$ gain intensity. In order to calculate the ox-red RR spectra normalization was perform, taking as reference the band of the ν_1 fundamental mode from Tyr around 820 cm^{-1} for NuoEF and from Phe at 1003 cm^{-1} for the rest of the samples.

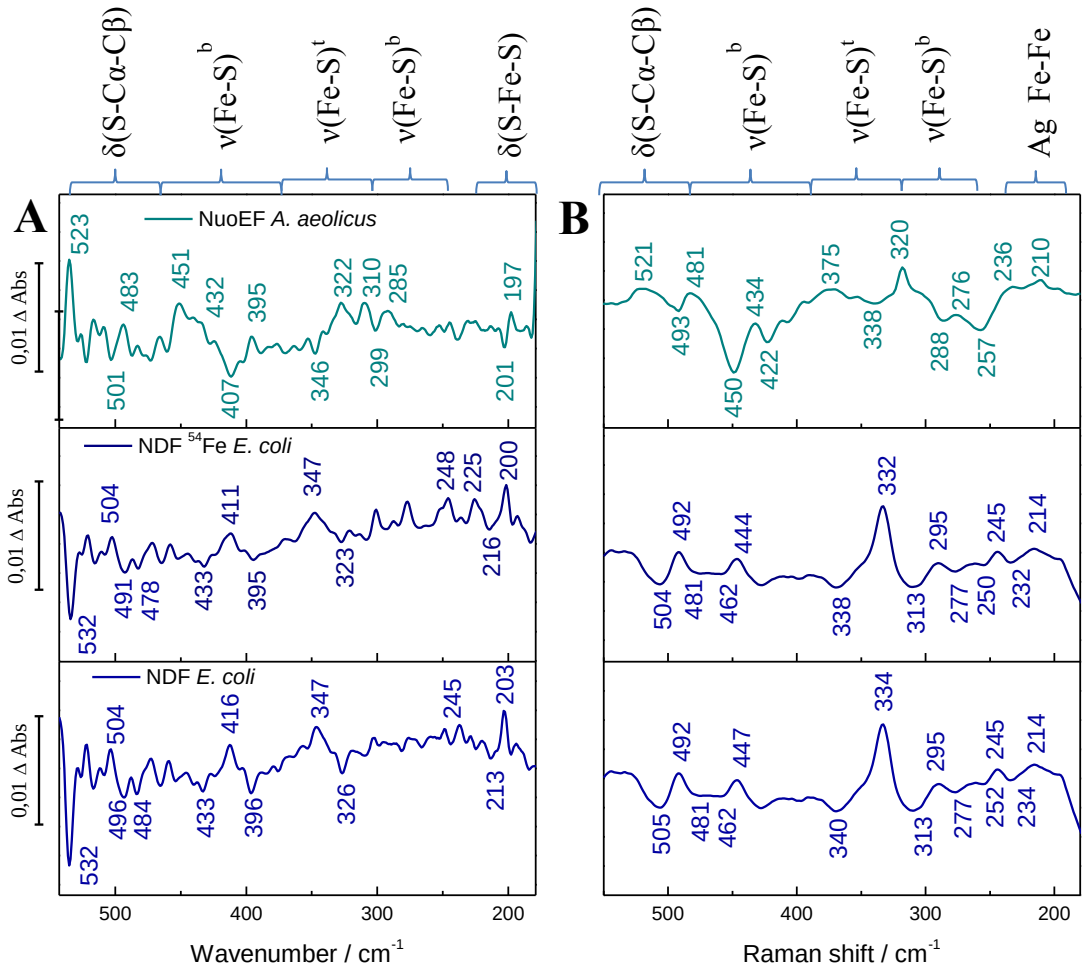

Figure 4.3-9. Spectroelectrochemistry (Ox-red) of NuoEF from *A. aeolicus*, NDF from *E. coli* in its ^{54}Fe isotopic label and unlabeled form recorded by A. Infrared and B. Resonance Raman.

Figure 4.3-9 shows the comparison between the ox–red spectra of the NuoEF subcomplex from *A. aeolicus* and the NDF from *E. coli* in its ^{54}Fe label and unlabeled form recorded by FT-IR and RR in the low frequency region where the metal-ligand vibrations are expected. In the Figure 4.3-9, the bands are classified in the bending motion of the Cys residues that form the cluster motifs, the $\nu(Fe\text{-}S)^t$, and $\nu(Fe\text{-}S)^b$; in the FIR spectra below 210 cm^{-1} the δ(S-Fe-S) motions that are observed but also the contribution from the hydrogen bonding collectives modes are expected to contributed in this area[272].

The FIR and RR difference spectra shows several similarities, especially in the ν(Fe-S) vibrations region. The complementarity of the data allows to confirm many of the vibrations in the FIR, where only metalloproteins with one or two Fe-S clusters had been described up to date[265, 266, 272].

In general, in RR, the negative signals corresponding to the reduced state, are lower in intensity than the positives ones, corresponding to the oxidized state. It has been previously described that the absorption coefficient of the ν(Fe-S) modes are weaker for the reduced form due the change of the iron center symmetry upon reduction[266, 270]. As the bonds get closer the cluster have a tendency to have a "rigid" structure[163, 166].

NuoEF Fe-S clusters (N1a and N3). In the NuoEF subcomplex ox-red spectra, the moieties of the reduced and oxidized states of N1a and N3 clusters are observed. For the bending vibrations (Figure 4.3-9.A), two signals are observed in the oxidized state, at 523 cm^{-1} corresponding to N3 and the second at 483 cm^{-1} corresponding to N1a. In the reduced state the first arises at 501 cm^{-1}, whereas the second band is not differentiable due to noise in the spectra. Nevertheless, in the RR differential spectrum (Figure 4.3-9. B), both signals are also seen in the oxidized state. In the reduced state the second band, corresponding to N1a is observed at 450 cm^{-1}.

The gain in intensity in comparison to the reduced state indicates different conformation of the cysteinyl coordination where an elongation of the Fe-S bonds has been proposed by previously studies[399, 400]. However, since drawing conclusions according to the difference in intensity is not straightforward other characteristics of the signal had to be taking into account. Typically, the frequency of this band is associated to the dihedral angles, where shifts to lower frequencies indicate narrower Fe-S-C dihedral angles, as in the case for both reduced clusters.

It can be notice that also the $\nu(Fe\text{-}S)^b$ vibrations have shifts to lower frequencies for both clusters upon reduction, suggesting the lengthening of the Fe-S bond. These modes are also affected by the dihedral angles[12, 399] corroborating with what was concluded from the spectral differences in the bending motions. However, in the RR spectrum, the signal at 276 cm^{-1} for the oxidized state corresponds to a mixture of $\nu(Fe\text{-}S)^b$ and $\nu(Fe\text{-}S)^t$ modes of N3. In the reduced state this signal splits into two components, at 288 cm^{-1} and 257 cm^{-1} indicating a decoupling of bridging and terminal modes upon reduction, where the first signal corresponds to the terminal mode and the second to the bridging modes. This vibration is observed in the FIR differential spectra at 285 cm^{-1}, and in the reduced state only the contribution of the terminal modes is observed at 299 cm^{-1}, based on its asymmetric nature of the vibration. The displacement of the $\nu(Fe\text{-}S)^b$ modes corresponds to what was already described for ferredoxin [4Fe-4S] clusters[270, 356, 401].

For the terminal mode, the same behavior is observed in the signal in the region 320-390 cm^{-1}. It is interesting to note, that in the FIR differential spectra the $\nu(Fe\text{-}S)^t$ are better resolved than in the RR differential spectra. This difference is due to the $Fe\text{-}S^t$ bonds having more possible normal modes as asymmetric vibrations than the $Fe\text{-}S^b$ modes[164, 359, 399, 400]. The $\nu(Fe\text{-}S)^t$ of both clusters are represented in the FIR differential spectra. The N1a contribution is observed at 310 cm^{-1} in the oxidized state and at 317 cm^{-1} in the reduced state, whereas for N3, the signals at 322 and 346 cm^{-1}, correspond to the vibrations of terminal coordination in the oxidized and reduced state, respectively.

Below 220 cm^{-1} in the FIR spectrum the S-Fe-S bending modes are expected[265, 266]. In the oxidized state this signal is observed at 197 cm^{-1} and in the reduced state at 201 cm^{-1}, the displacement to higher frequencies is associated with the Fe(II) oxidation state[265].

NuoG clusters (N1b, N4, N5 and N7). In Figure 4.3-9 the difference FIR and RR spectra of NDF can be observed. The difference between the signals already described for N1a and N3 can be attributed to the metal-ligand vibrations of the Fe-S cluster in the NuoG subunit.

For the bending motions, the clusters present in this subunit have a different cysteinyl coordination compared to N1a and N3. In the FIR spectra only one signal was reproducible at 504 cm^{-1}, whereas in the reduced spectra three signals arise at 532 cm^{-1}, 491 cm^{-1} and 478 cm^{-1}. As in NDF there is a major contribution from [4Fe-4S] clusters, the oxidized band can be

attributed to contribution of N3, N4, N5 and N7. In the reduced state, the first two signals had only been described for [4Fe-4S][270, 402, 403], while the third can only be assigned to [2Fe-2S][12, 164, 359].

This suggested that the [4Fe-4S] cluster N4 and N7 in NDF have a similar behavior described for the N3 cluster of the NuoEF subcomplex, where the reduced component arises at lower frequencies (See Figure 4.3-3.A/B/D), while N5 (see Figure 4.3-3.C) have a more rigid structure where all the Cys coordinating residues are connected to each other. The signal at 491 cm^{-1} can be assigned to the reduced component of the first type of clusters. The signal at 532 cm^{-1} can be assigned to the bending motions of N5, indicating that upon reduction, the dihedral angles of the cluster are broader. A similar behavior had been observed for **Hi**gh-**P**otential **I**ron-Sulfur **P**rotein (HiPIP) from *Chromatium vinosum*[376, 404, 405], where a small distortion from T_d symmetry was proposed, compared to the typical ferredoxin [4Fe-4S] cluster. This symmetry alteration is caused by a distortion of the Fe-S(Cys) bonds due to the high hydrophobic environment that surrounds the cluster, as is the case of N5. In the reduced state an upshift of this vibrational mode of this type of clusters had been attributed to a weaker hydrogen bonding.

The third signal at 478 cm^{-1} in the NDF spectra, corresponding to [2Fe-2S] clusters, indicates that N1b does not show the same elongation of the Fe-S bond as seen for N1a. According to this, it can be suggested that the changes in the dihedral angle are more pronounced in N1a than in N1b. It can be concluded, that these [2Fe-2S] have different redox properties.

In the spectrum recorded by FIR and for the $\nu(Fe\text{-}S)^b$ modes, the band at 411 cm^{-1} in the oxidized state was attributed (see Table 4.3-1) to [4Fe-4S] clusters. This bands splits into two components upon reduction, observed at 433 cm^{-1} and 395 cm^{-1}, indicating that some of the [4Fe-4S] cluster have an increase in the dihedral angle and others a decrease. As was described before, a decrease in intensity was observed for N3 which is also expected for N4 and N7, suggesting that the signal at 395 cm^{-1} corresponds to these clusters. An increase of the dihedral angle of N5 was concluded from the spectral differences in the bending motions, this suggests that the signal at 433 cm^{-1} can be attributed to the $\nu(Fe\text{-}S)^b$ of the reduced N5.

From the RR difference spectrum, one positive and one negative signal can be observed at 444 cm^{-1} and 431 cm^{-1}, respectively. These signals were described for the $\nu(Fe\text{-}S)^b$

modes of ferredoxin [4Fe-4S] clusters, attributed to N3, N4 and N7. Besides, the positive bands observed at 295 cm^{-1} and 245 cm^{-1} correspond to the $\nu(Fe\text{-}S)^b$ modes of [2Fe-2S] cluster. The splitting indicates that N1a and N1b differ in their geometry in their oxidized state as well as in their reduced state where the corresponding negative bands are observed at 277 cm^{-1} and 250 cm^{-1}.

For the $\nu(Fe\text{-}S)^t$ modes in the FIR spectra, one positive and one negative band are observed at 347 cm^{-1} and 323 cm^{-1} respectively, this terminal mode has been attributed to [4Fe-4S] and [2Fe-2S] clusters, the displacement to lower frequencies was expected in the reduced cluster as explained before for N3 and N1a from the NuoEF difference spectra. The shift in frequency, with respect to what is observed in the NuoEF difference FIR spectra, suggest that the cluster in NuoG has different cysteinyl coordination. As this band contains the contribution of all the clusters in the protein, not much information can be concluded about it, more than the complete reduction of the cluster.

The $\nu(Fe\text{-}S)^t$ modes in the RR spectrum show only one positive band at 332 cm^{-1}, described for the [4Fe-4S] cluster, and two negative bands, at 338 and 313 cm^{-1}, the first corresponds to the reduced [4Fe-4S] cluster and the second to the reduced [2Fe-2S] cluster. Below 220 cm^{-1}, in the FIR spectrum, a similar differential signal is observed in the NuoEF spectrum, corresponding to the S-Fe-S bending modes.

NuoB and NuoI clusters (N2, N6a and N6b). The difference between the NDF spectra and the complex I spectra (Figure 4.3-10) allows to assign the contribution from the cluster present in the NuoB (N2) and the NuoI (N6a and N6b). It is clear that due to the large number of Fe-S clusters in the sample, the bands previously described in NuoEF and NDF are broader, increasing the complexity of the spectrum interpretation.

In the region of the bending motion, the spectral differences described for N5 and the rest of the [4Fe-4S] clusters are also present in the ox-red FIR spectra of complex I. It can be suggested that the N2, N6a and N6b clusters behave, upon reduction, in the same way as the rest of the [4Fe-4S] clusters.

However, in the $\nu(Fe\text{-}S)^b$ vibration region, in the FIR difference spectra, a positive signal at 468 cm^{-1}, attributed in the oxidized state description of the N2 cluster (see section 4.3.2), shows a shift to lower frequencies in the reduced state arising at 447 cm^{-1}. In ferredoxin [4Fe-4S] clusters the downshift of this band upon reduction is not more than 10

cm^{-1}, while here only one of the clusters (N2) shows a downshift of ~20 cm^{-1}, indicating a strong change of geometry of the cluster (and perhaps hydrogen bonding). As the geometry of the cluster is severely affected, other vibrations present several shifts as well.

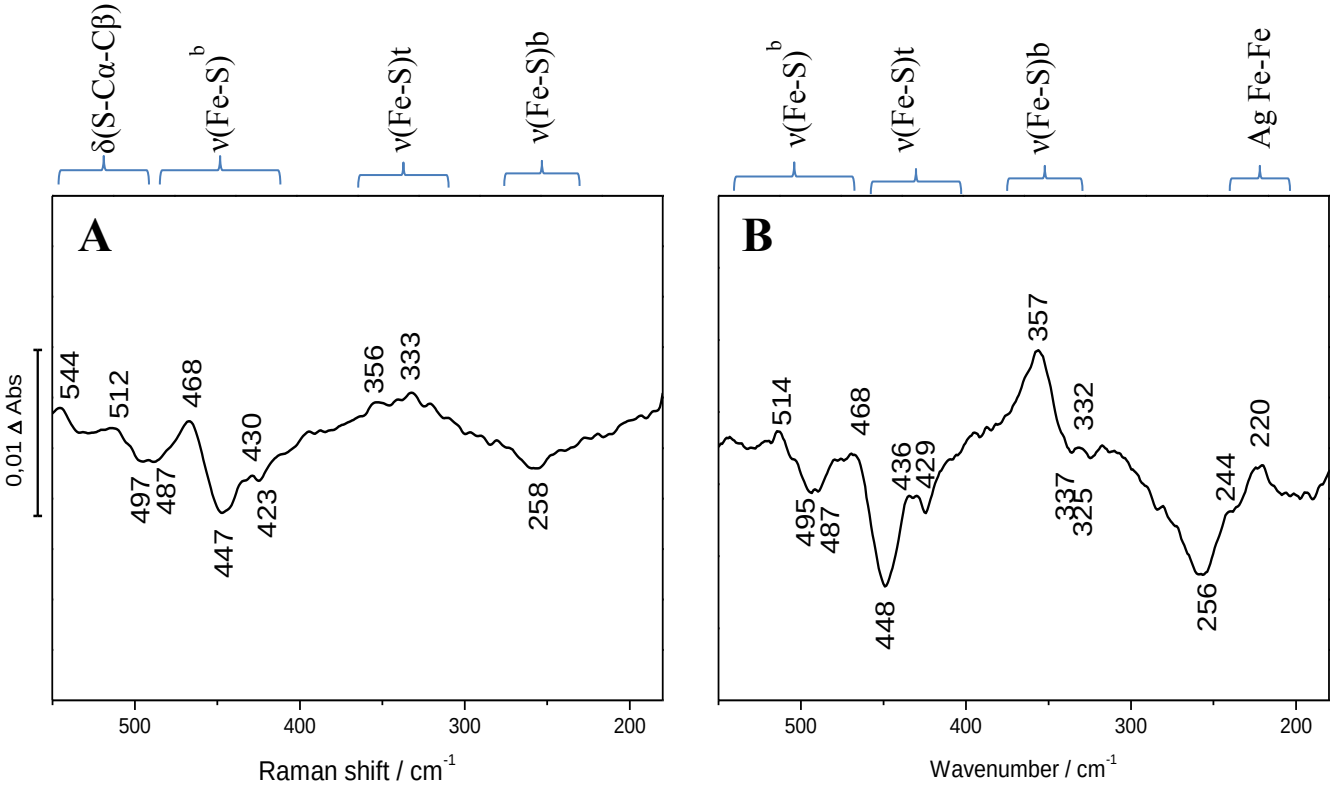

Figure 4.3-10. . Complex I ox-red difference spectrum recorded by A. Infrared and B. Resonance Raman.

For example, the signal at 357 cm^{-1} in the RR difference spectrum, assigned to the $\nu(Fe\text{-}S)^t$ modes N2 in the oxidized state, shows a negative counterpart at 337 cm^{-1}. This suggests that instead of the Fe-S^t bonds getting shorter as it is typically observed in the ferredoxin [4Fe-4S] clusters[223, 401], the Fe-S^t bonds of N2 are elongated upon reduction. A similar pattern of what was observed for the reduced N1a. It seems that this property can be related to their pH-dependent character, this behavior had been described before for cluster that have the ability of slower rates of electron transfer.

For the rest of the bands observed in the RR and FIR ox-red difference spectra all the assignment are according to what was observed in the NDF and NuoEF spectra. This suggests that N6a and N6b clusters have very similar properties to N3, N4 and N7.

Tyr. Besides the metal ligand vibration in the low frequency region of the RR difference spectra, important change are observed in the Fermi doublet corresponding to the Tyr residues (Figure 4.3.11).

For NuoEF, two positive signals described the Fermi doublet in the oxidized state, at 805 and 815 cm^{-1}, while in the reduced state an upshift is observed for both of the signals arising at 810 and 824 cm^{-1}. As explained above (see section 4.3.2 pg 159) the difference in frequency and intensity of this doublet is reflection of the hydrogen bonding and the exposure to the environment of the Tyr residues. The shift to higher frequencies suggests a weaker hydrogen bonding. The difference in intensity, between 815 cm^{-1} and 824 cm^{-1} suggest that many of the residues that were buried in the oxidized state are now exposed to solvent in the reduced state.

In the case of NDF two positive signals are observed at 823 cm^{-1} and 851 cm^{-1} and two negative, at 840 cm^{-1} and at 863 cm^{-1}. As for NuoEF, the average of the Tyr residues around the clusters in the reduced state are weakly hydrogen bonded in comparison to the oxidized state. The difference in intensity between the signal at 851 cm^{-1} and at 863 cm^{-1}, indicates that in average the Tyr residues are more buried within the structure in the reduced state than in oxidized state.

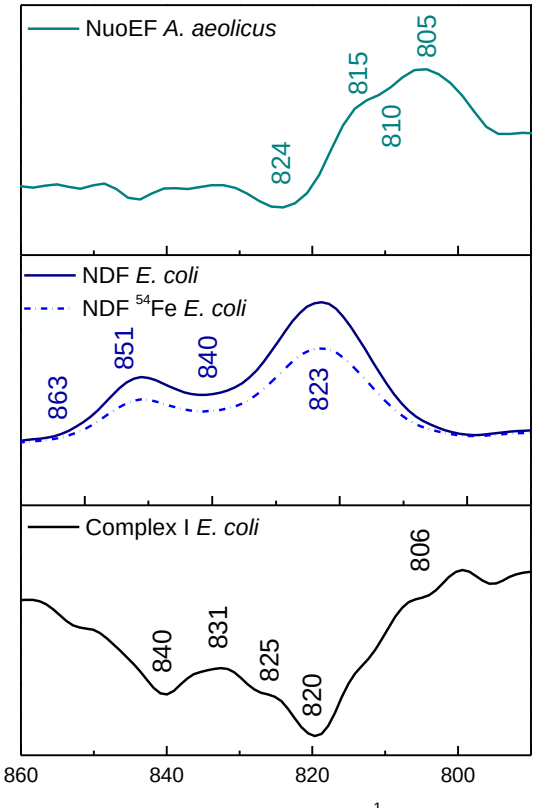

Figure 4.3-11. RR difference spectra (Ox-red) in the fermi doublet region of NuoEF from *A. aeolicus*, NDF from *E. coli* in its ^{54}Fe isotopic label and unlabeled form.

For the complex I difference RR spectrum, two positive signals are observed at 825 and 831 cm^{-1} and two negatives at 820 and 840 cm^{-1}. As both of the signals do not have the same shift to higher frequencies, it can be said that on average some of the Tyr residues have now a weaker hydrogen bonding, mostly the Tyr surrounding the subunits NuoEFG, as it was observed in the NDF, and some of the Tyr residues around the NuoBI have a strong hydrogen bonding in the reduced state. As the intensity of the both of the signals are higher in the reduced state, it can be suggested that on average the Tyr residues are more buried within the structure in the reduced state.

Even though the Fermi doublet gives an average about the state and the disposition of the Tyr residues in the sample, it is evident that upon reduction the Tyr residues are an important key in the description of the conformational changes in complex I. The Tyr residues around N1a and N3 do not have the same behavior as the Tyr residues of the NuoG subunit. This can be due to the differences in their position between the *A. aeolicus* and the *E. coli* protein, or their distribution around the cluster.

4.3.3.1 Conclusion

In conclusion, the FIR difference spectra are suitable of the $\nu(Fe\text{-}S)^t$ vibrations while RR is more appropriate for the $\nu(Fe\text{-}S)^b$ vibrations. Both techniques are complementary, helping to obtain a proper assignment and description of the redox active vibrational modes and the properties of the Fe-S cluster present in the protein. An assessment of the changes in the metal-ligand vibrations facilitates the comprehension of the molecular changes occurring in the cofactors upon reduction.

It can be seen that N1a and N1b show a different set of redox properties. This was also proposed in the studies of Ohnishi *et al.* and Hirst *et al.*[216, 217] The main difference is that N1a binding length of the cluster ligation increases upon reduction, given by the changes in transfer of the S to the Fe(II), where the dihedral angles are narrower and the $Fe\text{-}S^t$ and $Fe\text{-}S^b$ are elongated. In contrast, N1b the $Fe\text{-}S^b$ bonds are kept in the same geometry upon reduction,

this characteristic had already been described by several [2Fe-2S] clusters like the one present in adrenodoxins[357, 359].

N3, N4, N6a, N6b and N7 display a similar redox behavior. Similar redox characteristics had been described for ferredoxin [4Fe-4S] clusters[374, 403]. Here, narrower dihedral angles and shorter $(Fe\text{-}S)^t$ bonds are seen upon reduction. The opposite can be said for the behavior of N5, where longer $(Fe\text{-}S)^t$ bonds and wider dihedral angles are the major characteristic of the cluster upon reduction. Several studies in similar Fe-S clusters indicate that these changes are related to a highly hydrophobic environment, where the hydrogen bonds involved with the cluster motif are weaker after reduction[356, 404, 406].

In general, according to the difference in the $Fe\text{-}S^t$ and $Fe\text{-}S^b$ bonds, the clusters N1a, N5 and N2, showed an expansion of their geometry upon reduction. According to the redox properties described for similar clusters[352, 364, 406], these are metal centers whose function is related to the need to stabilize a high-energy electron and/or an electron that will not be transferred very fast, the changes in the geometry allowed a fast recovery to the oxidized state. It is noted that these clusters play a crucial role in the timing of the electron flow and hence the coupling of the electron and proton transfer reaction as well as the rate-limiting step in the kinetics of the electron transfer reactions. On the other hand, the cluster with an unchanged geometry upon electron transfer can be suggested to function as a stabilizer of an additional electron since this cluster does not hold the electron for a long time because its electron transfer rate is much faster than the clusters described before[166, 407].

4.3.4 The effect of substrate binding

As the reduced state obtained by electrochemistry is not the natural equilibrium process observed during catalysis, the effect of complex I substrate, NADH, was studied. The NADH reduces several of the Fe-S clusters, transferring the electrons from the FMN (see section 1.4.2.2). In general the spectra of the reduced proteins are an order of intensity lower than the oxidized protein. The effect is more pronounced in the NDF spectra than in the other samples.

In order to determine if the nucleotides are bound, the bands at 1010 cm^{-1} and 1378 cm^{-1} corresponding to the adenine moieties, were followed[411]. The decrease of these signals

reflects their bound state. The same protocol was described in the RR studies of substrate binding of dehydrogenase enzymes[412-414].

The full reduction of a Fe-S cluster is usually accompanied by a change in the rigidity of the cluster[12, 165, 385]. The polarizability is lower and the Fe-S stretching modes are less enhanced[165]. Beside this, it is important that these metal centers have a different electronic state upon reduction[266, 415] which is reflected in the frequency and the intensity of the obtained spectra.

NAD^+, the oxidized form of NADH, is known to interact directly with the flavin when no other nucleotide is bound[191, 416]. Its effect had been described for the moieties of the FMN[417, 418], but so far the conformational changes or the influence in the properties of the Fe-S cluster have not been noticed. In addition, the interaction between complex I and NADPH it still a source of controversy, for example Albracht[419, 420] had proposed that this nucleotide does not react in the same site as NADH giving to the mechanism another route to electron transfer. Li *et al.*[421] followed by many others[422-425] had proposed that NADPH can act as a kind of inhibition of the ROS production. Brandt *et al.*[426] have also proposed that its binding is not necessary for the catalytic activity but it stabilizes the complex in the reduced state.

Besides the metal-ligand vibrations the contribution from specifical side chains amino acids perturbed upon the substrate binding the ν(C-H) modes above 2700 cm^{-1} will be discussed.

4.3.4.1 Metal-ligand vibrations

The Ag Fe-Fe modes. As explained above (section 4.3.3) this vibrational mode is expected to be enhanced only for the [2Fe-2S] clusters[12, 361]. This mode allows a correlation measurement of the distance between the two Fe atoms, as the vibration arises from the motion of the Fe atoms towards each other (Figure 4.3-12)[12].

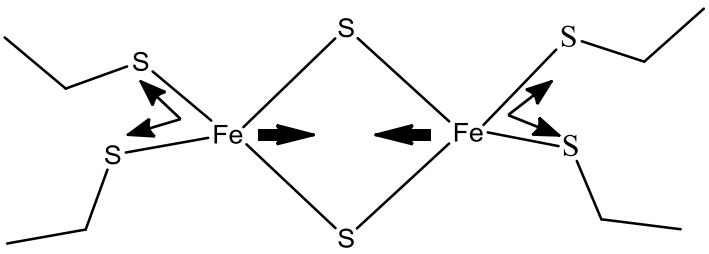

Figure 4.3-12 . Eigenvector for the normal mode of the Ag Fe-Fe vibration. Adapted from Han *et al.*[12]

The frequency itself is not an indication of the metal-metal bond strength, but higher frequencies suggest a stronger Fe-Fe interaction[359]. In NuoEF (Figure 4.3-13. A), upon the binding of NAD^+ a small shift to higher wavenumbers is observed, whereas in presence of NAPDH and NADH, the band shifts towards lower frequencies; the effect is more prominent in with the latter one. For NDF (Figure 4.3-13.B) and complex I (Figure 4.3-13.C) the same shift is observed upon the reduction with NADH; suggesting that in N1a and N1b Fe orbitals are more distant upon reduction, whereas in presence of NADPH and NAD^+ no major changes occur.

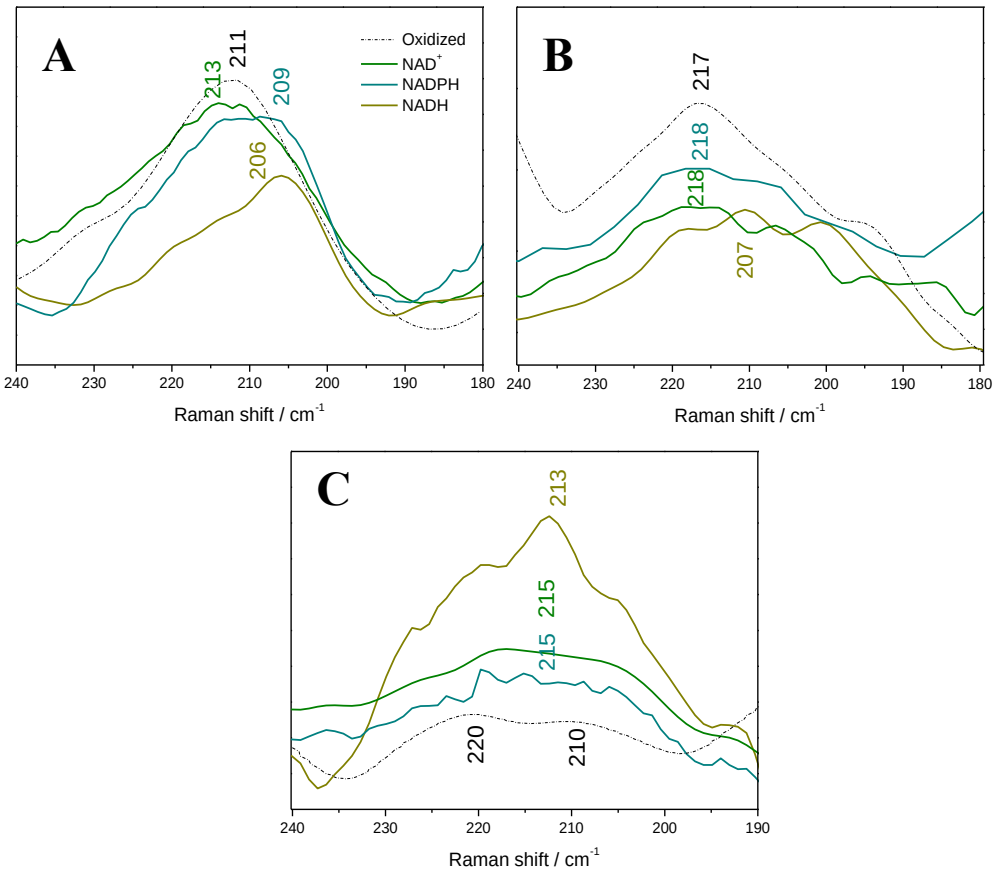

Figure 4.3-13. Resonance Raman spectra of A. NuoEF, B. NDF and C. Complex I in presence of NAD+, NADPH and NADH in the Ag Fe-Fe vibrational mode region.

These results can lead to the conclusion that Fe-S coordination where the enhancement in the electron donation from the ligands to the Fe-S cluster core results in an elongation of the Fe-Fe distances and to a more distorted structure of the proximal Fe-S cluster. This had been previously proposed by electron tunneling[164, 214, 410] and broken symmetry DFT

calculations[427], where upon reduction the cluster provides a pathway for inner sphere of electron transfer.

The ν(Fe-S)^t and ν(Fe-S)^b . The first ν(Fe-S)^b mode arises at ~260 cm^{-1} in the spectra of NuoEF (Figure 4.3-14.A), NDF (Figure 4.3-14.B) and complex I (Figure 4.3-14.C). This band can be attributed to the B_2 (Fe(III)-S)^b modes of [4Fe-4S] clusters[270]. The shift of these modes is related to narrower cysteinyl Fe-S-Cβ-Cα dihedral angle.[12, 165] As the shift is observed in all the samples it means that all the [4Fe-4S] clusters (N3, N4, N5, N6a, N6b and N2) have the tendency to display the same change in the cysteinyl coordination.

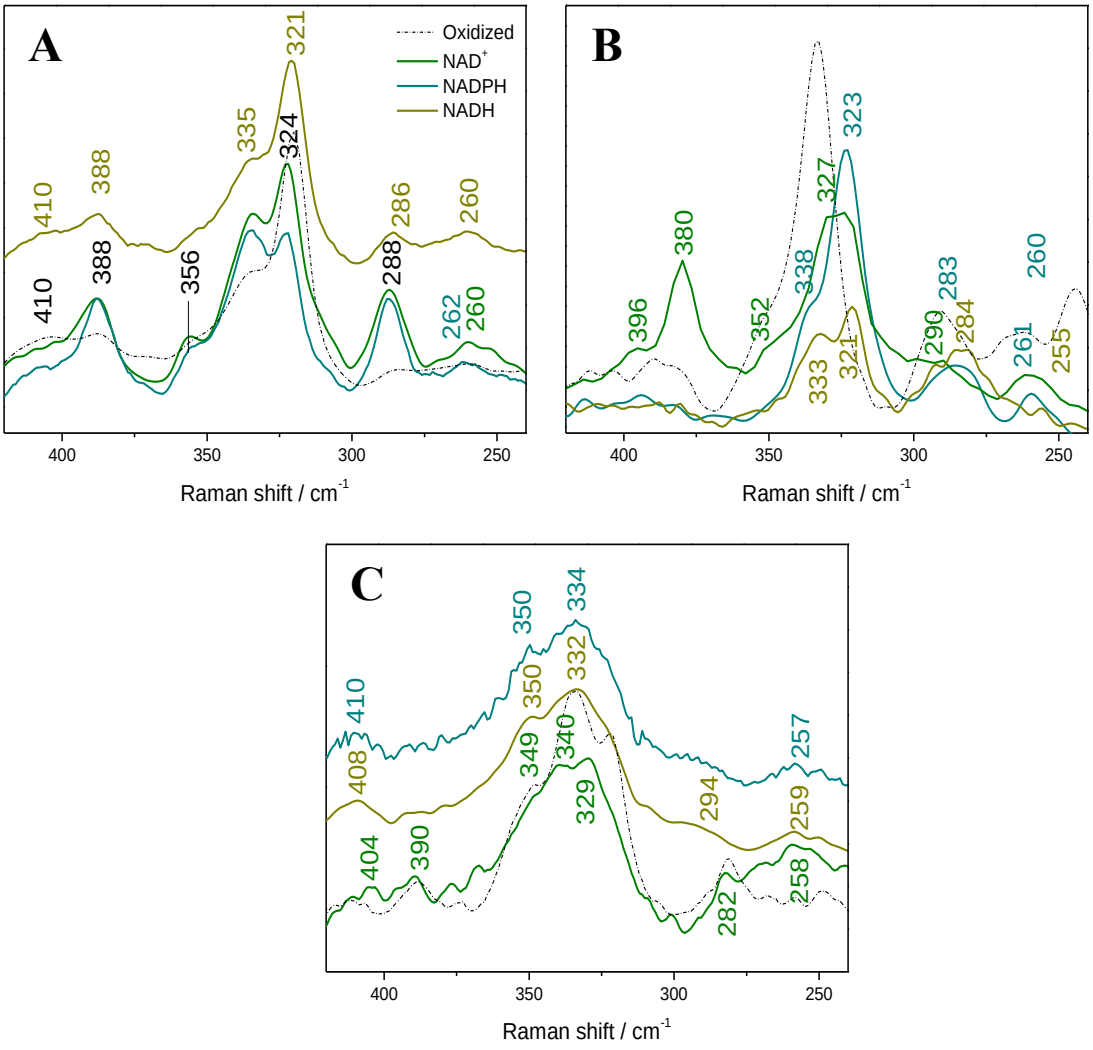

Figure 4.3-14. Resonance Raman spectra, in ν(Fe-S) stretching region of A. NuoEF B. NDF and C. Complex I in presence of NAD+, NADPH and NADH.

In the spectra of NuoEF subcomplex (Figure 4.3-14.A) three ν(Fe-S)^t modes are observed in the ν(Fe-S) region . The first, arising at ~286 cm^{-1}, which was not observed in the

spectra of the oxidized form (Figure 4.3-15.A dotted line), it can be attributed to the B_{3u} ν(Fe(II)-S)^t, this mode is expected for [2Fe-2S] as well as for [4Fe-4S][12, 428], suggesting that N1a and N3 are reduced. However, some contribution from the T_2 ν(Fe(III)-S)^b from [4Fe-4S] clusters can be also be expected in this area[428, 429]. The gain in enhancement supports the contribution of ν(Fe(III)-S)^b as this kind of mode had been described to lose enhancement upon the reduction of the Fe atom . In general, changes in intensity suggest that the Fe-S^b bond is weaker[270].

This indicates that in N3, in presence of all the nucleotides the coordination of the Fe-S^b changes to a more "relaxed" state. In the spectra of NDF (Figure 4.3-14.B), the same is observed in presence of NADH and NADPH, whereas for NAD^+ no changes are observed in comparison to the oxidized state. This suggests that for the [4Fe-4S] clusters N4, N5 and N7 in presence of NADH and NADPH the same effect is observed.

In the spectra of complex I (Figure 4.3-14.C) the signal is only observed in presence of NAD^+, while for NADPH and NADH the signal is observed as a broad shoulder where is not possible to assigned a specific frequency. It can then be proposed that N6a, N6b and N2 are likely to have "rigid" Fe-S^b bonds[355, 358].

In the RR study of a pure S=3/2 ferredoxin cluster from *Pyrococcus furious*[409], the Fe-S^b signals of "rigid" bonds have a tendency to arise at higher frequencies and lower intensity than the "not rigid" counterpart. According to the simulations, electron tunneling studies[214, 410, 430] and broken symmetry calculations[164], "relaxed" centers likely allow a faster electron transfer than the "rigid" centers, where as in the "rigid" the reversibility to the oxidized state is slower due to the change in the energy of the Fe-S bridging bonds[167]. Nevertheless, upon addiction of NAD^+ no electron transfer is expected and the changes in the cluster's geometry are most related to conformational changes of the protein upon the substrate binding.

The vibrational mode, B_{1u} ν(Fe(III)-S)^b of [2Fe-2S] cluster, arising at 321 cm^{-1} (NADH) and 324 cm^{-1} (NADPH and NAD^+) in the spectra of NuoEF, is assigned to N1a. This band shifts only slightly upon reduction in comparison to the oxidized state (319 cm^{-1}). This indicates that the bridging bonds of the metal center are not perturbed upon substrates binding. Thus, it can be suggested that upon binding of the substrate, N1a is not fully reduced.

In the spectra of NDF, this band was overlapped by the ν(Fe-S)^t modes of the [4Fe-4S] cluster, however upon binding a band arises at 321 cm^{-1} (NAD^+), 323 cm^{-1} (NADH) and 327

cm^{-1} (NADPH). From the shape of the band, it is more probable that it corresponds to the A_1 $\nu(Fe\text{-}S)^b$, where some of the $Fe\text{-}S^t$ display a narrower cysteinyl Fe-S-Cβ-Cα dihedral angles[12, 263, 401] and some remain in the same symmetry as in the oxidized state, corroborating the observation of the previously described vibrations. For the rest of the signals in this spectral region, some of the $Fe\text{-}S^t$ bonds keep the same cysteinyl geometry upon the binding of the substrate attributed to the signal at 333 cm^{-1} which is the case in presence of NAD^+. Nevertheless, upon binding of NADH, a second signal arises at 338 cm^{-1}, and with NADPH at 352 cm^{-1}, suggesting that some of the clusters have wider dihedral angles upon reduction. It is interesting to keep in mind that the effect is more marked with NADPH.

In complex I, with NAD^+ no major spectral differences are observed. Furthermore with NADH and NADPH the $\nu(Fe\text{-}S)^b$ modes do not seem perturbed indicating that no changes in the geometry of N6a and N6b are occurring. However, with NADH and NADPH the most important spectral difference is observed in the signal at 340 cm^{-1} attributed to the $\nu(Fe\text{-}S)^t$ modes of N2, this band is no longer visible, this indicates that the dihedral angles of the cysteine coordination is perturbed, where the cluster is fully reduced and must present a different geometry[165, 358].

The last bands observed in the NuoEF spectra corresponds to the $\nu(Fe\text{-}S)^b$ modes of N1a and N3 (see Table 4.3-1). No difference is observed in the frequency with respect to the spectra of the oxidized state, nevertheless the loss in intensity in presence of NADH indicates that the clusters might be partially reduced. In the spectra of NDF with NAD^+ two signals arise at 380 cm^{-1} and 396 cm^{-1}, indicating that N1a have a displacement to narrower dihedral angles[12,361]. Nevertheless, in presence of NADPH and NADH the signals are no longer visible suggesting that the cluster is completely reduced. A similar behavior is observed in the spectra of complex I, with the difference that second signal at 410 cm^{-1} does not change upon substrate binding.

According to these results, it can be proposed that the N1a in *A. aeolicus* and the N1a in *E. coli* do not have the same reduction mechanism. This dissimilarity might be due to the structural changes due to the missing subunits in the subcomplex or to differences in the hydrophobicity, typically observed in the protein core of thermophilic organisms as *A. aeolicus*.

The bending motions of Cys. Between 420 and 500 cm^{-1} the bending motions are expected[12, 401, 431]. In the oxidized state three bands were attributed for all the samples (see Table 1.1-1). In general, for NuoEF, upon the binding of NAD^+ many spectral differences are observed, while in presence of NADPH and NADH the spectra are similar to each other and to the band described in the spectrum in the oxidized state. This implies that no difference in the Cys residues of the cluster motif change upon reduction in the N1a and N3 cluster motif.

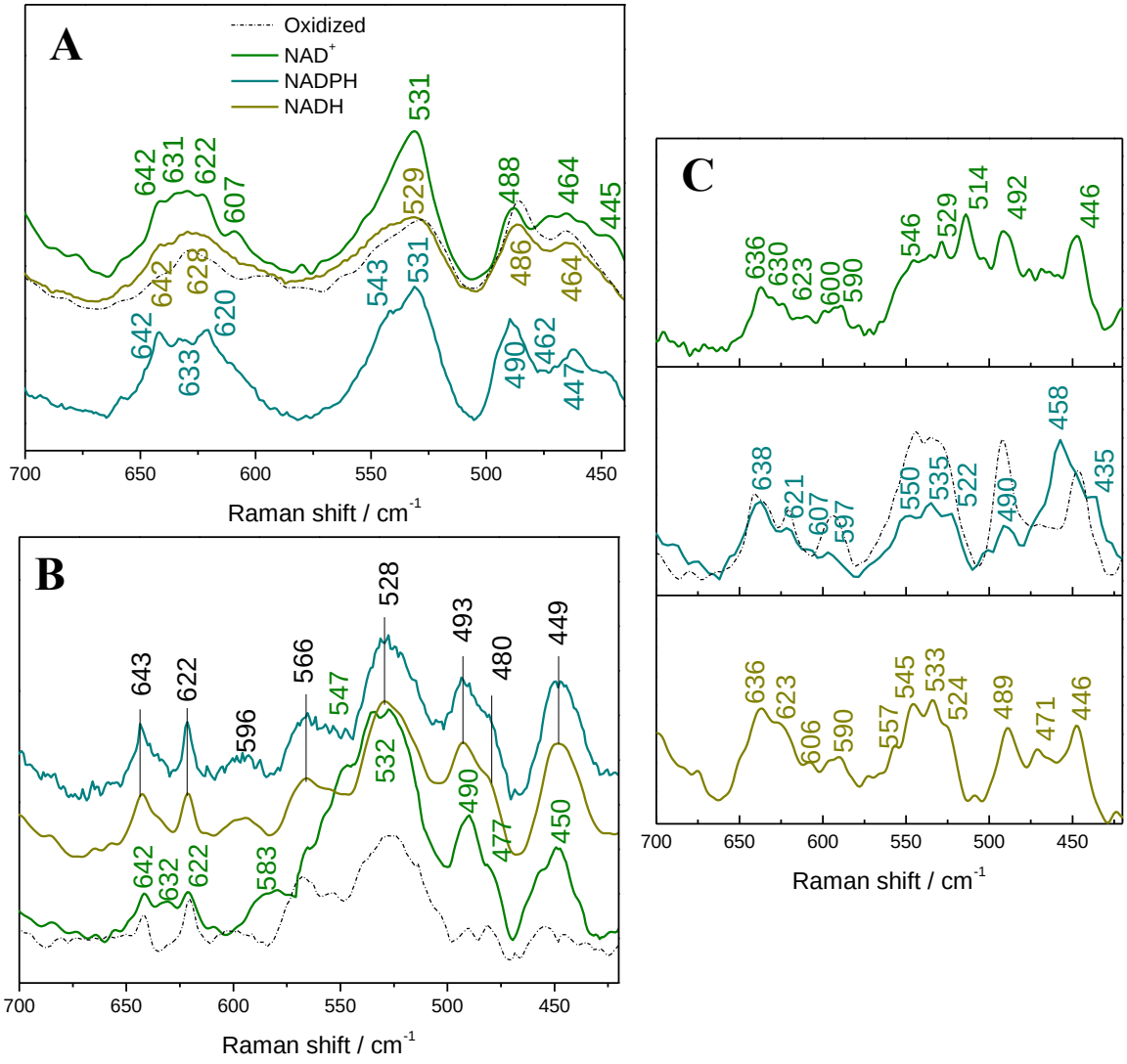

Figure 4.3-15. Resonance Raman spectra of A. NuoEF B. Complex I and C. NDF in presence of NAD+, NADPH and NADH. The spectra shows the region of the bending motions, the overtones from the ν(Fe-S) and the ν(C-S)

Specifically, the presence of NAD^+, the spectrum of NuoEF (Figure 4.3-15.A) shows a well-resolved band at 488 cm^{-1} and a broad band with several peaks where two are more distinguishable from the rest at 464 and 445 cm^{-1}. The last band was not present in the spectra of the free form and it was attributed to the cluster in the NuoG subunit (N1b, N4, N5 and

N7). This vibration was assigned to the coupling of the δ(Cα-Cβ-C) and δ(Cα-Cβ-N). It seems that upon binding, the N1a and N3 clusters display characteristics observed before in the cluster of the NuoG subunit. Nevertheless, the band is too broad indicating the presence of a different conformation. A similar conclusion can be said for the peak at 464 cm^{-1}.

In the NDF and complex I spectra with NAD^+ (Figure 4.3-15.C) no major changes are observed. Nevertheless, in presence of NADPH and NADH, the NDF spectrum (Figure 4.3-15.C) presents three bands in which all of them exemplify a different conformation of the Cys residues. The differences in intensity and frequency are related to the displacement in the dihedral angles, confirming the conclusions made from the differences of the $\nu(Fe\text{-}S)^b$. According to Han *et al.*[12] and Czernuszewics *et al.*[165], the signal at 435 cm^{-1} is only observed in fully reduced [4Fe-4S] cluster.

The overtones from ν(Fe-S) modes. In the spectral region between 500 and 600 cm^{-1} the overtones form the Fe-S stretching are observed (Figure 4.3-15). Due to the complexity of the possible combinations between the Fe(III)-S^t, Fe(II)-S^t, Fe(II)-S^t and Fe(II)-S^b modes a full assignment of this area will require the support of theoretical calculations. Nevertheless, it is evident from a qualitative approach that the this spectral range reflects the changes observed in the already described $\nu(Fe\text{-}S)^t$ and $\nu(Fe\text{-}S)^b$.

The ν(C-S) modes. This particular mode is sensitive to motion of the Cα-H and the Cα-N group[432], while perturbation in the Cα-N group lead to lower frequencies, motions in the Cα-H leads to higher frequencies[432, 433]. In the spectrum of NuoEF in the oxidized form, only one broad band was observed in this region at 628 cm^{-1}, while in presence of NADH two bands are observed, with NADPH three and with NAD^+ four. The lower frequency bands, between 600 and 620 cm^{-1}, correspond to the ν(C-S) modes of [4Fe-4S] cluster, while the higher frequency bands, between 620 and 640 cm^{-1}, of the [2Fe-2S] clusters. In summary, upon the binding of NADPH, N3 and N1a have a typically C-S coordination where the Fe-S-Cα dihedral angle is between 90-170°[270, 434], whereas in presence of NADPH, in N1a, it seems that at least one of the C-S bond has a different coordination due to motions in the Cα-N group, and in presence of NAD^+ the same effect is observed for N3.

In NDF (Figure 4.3-15.C), a similar behavior is observed, although with NADH the [4Fe-4S] clusters (N4, N5 and N7) exhibit two different C-S coordination while the [2Fe-2S] clusters (N1a and N1b) are similar to their oxidized state only in the lower frequency

suggesting minor motions of the Cα-N groups. Instead with NADPH and NAD^+, four bands are observed. In the case of NADPH the [4Fe-4S] clusters display three different coordination, this is also observed with NAD^+, whereas the [2Fe-2S] cluster displays three different conformations.

4.3.4.2 FMN vibrations

In the spectra of the reduced form, many of the contribution from the FMN isoalloxazine ring are combined with the contribution from the amino acid side chains or with amide vibrations. There are two main bands at ~732 cm^{-1} and ~785 cm^{-1}, observed in all the protein spectra. These bands are FMN vibrational modes. These bands will be taken as markers of the changes in the bonds around the isoalloxazine ring of the FMN upon reduction.

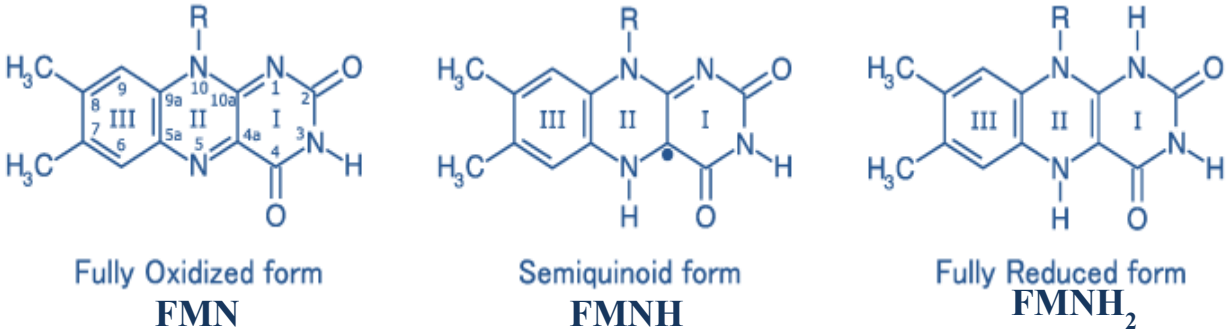

Figure 4.3-16. Isoalloxazine structures in the fully oxidized, semiquinoid and full reduced states. The nomenclature of the bond is shown in the fully oxidized state. R=ribose-5-phosphate

The isoalloxazine moieties of FMN can exist in three different oxidation states, the fully oxidized (quinoid), the semiquinoid, and fully reduced states (See Figure 4.3-16). In general, upon reduction with NADH the vibrational modes corresponding to the carbonyl and nitrosyl moieties of the ring I, II and III are observed[435-437].

The signal at 735 cm^{-1} (NuoEF), 745 cm^{-1} (NDF) and at 739 cm^{-1} (complex I) in the oxidized state, shows a shift to lower frequency in presence of NADH, NAD^+ and NADPH (Figure 4.3-17), furthermore in the spectra of NDF (Figure 4.3-17.B) and complex I (Figure 4.3-17.C) with NAD^+ the vibration have a decrease in the enhancement, whereas in presence of NADPH and NADH the opposite is observed. For NuoEF (Figure 4.3-17.A), the behavior is different from the other proteins: the signals have a tendency to gain intensity in presence of NAD^+, while in the presence of the other two nucleotides no changes in the intensity are observed.

This band corresponds to the contribution of ring breathing modes of ring I[385, 437]. As the resonance enhancement of FMN bands is expected only for the modes in which the atoms are displaced within the molecular plane of vibration, a gain in intensity means that changes upon the substrate binding, cause a major displacement of the vibrational mode of ring I, furthermore a lower frequency implies a lower energy of the bonds. Previous theoretical and experimental comparison of different flavin samples in the semiquinone state had related changes in the frequency and the intensity of this mode to changes in the electronic density of the ring I[388] .

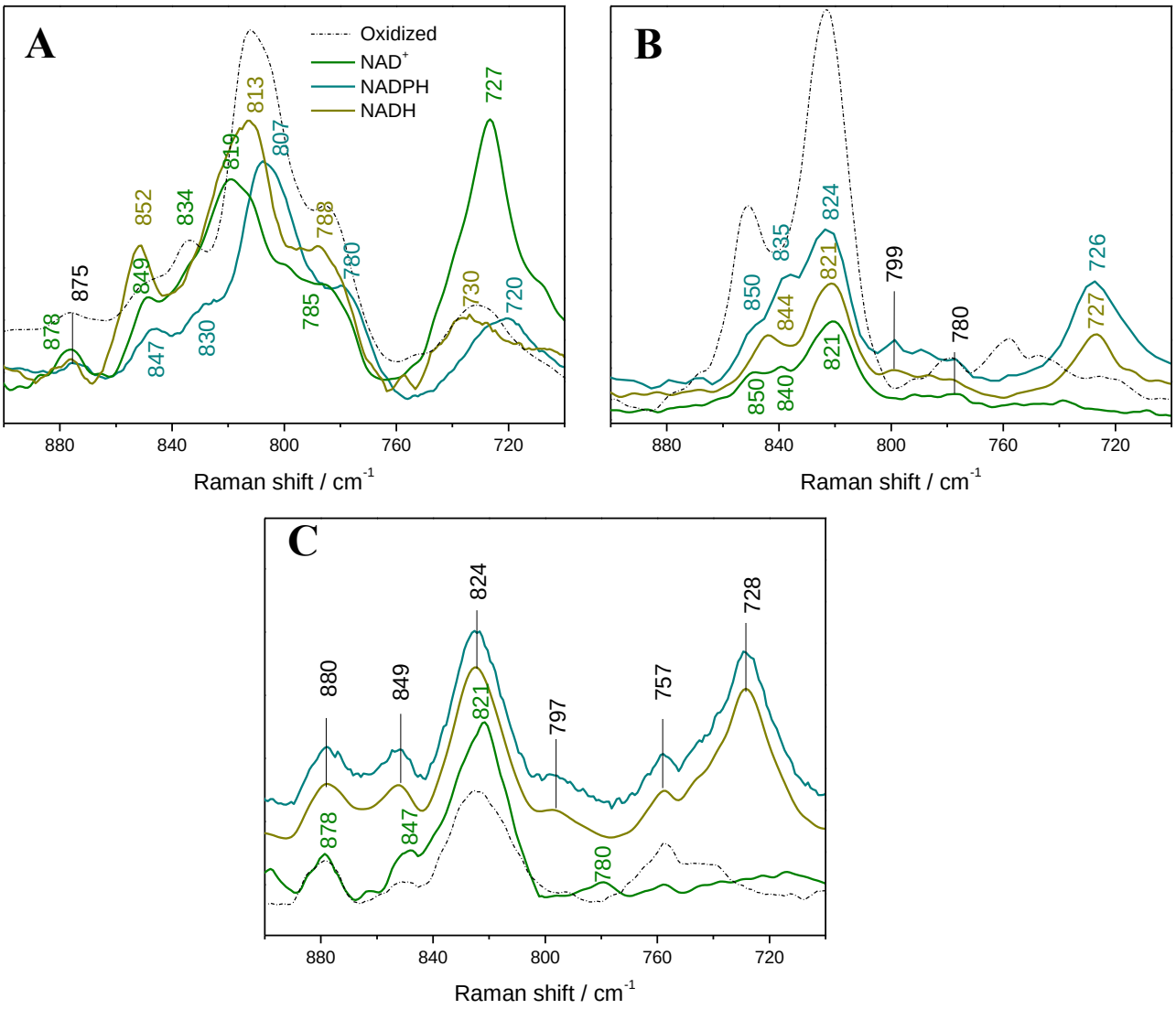

Figure 4.3-17. Resonance Raman spectra of A. NuoEF subcomplex B. NDF and C. Complex I in presence of NAD^+, NADPH and NADH

The band at 785 cm^{-1} (NuoEF), 778 cm^{-1} (NDF) and 777 cm^{-1} (complex I) in the oxidized state corresponds to the $\upsilon(C_7\text{-}N_{7m})$, $\upsilon(C_6\text{-}C_7)$ modes of ring III[388, 438]. In NuoEF-

NAD^+ spectra this signal shows a decrease in the frequency arising at 780 cm^{-1}, while for NDF and complex I higher frequency is observed (~798 cm^{-1}). This indicates that the delocalization of the electron is density in the ring III NuoEF subcomplex from *A. aeolicus*, which seems perturbed only in presence of NAD^+, while in complex I and NDF from *E. coli* it is the binding of NADPH and NADH that causes the perturbation.

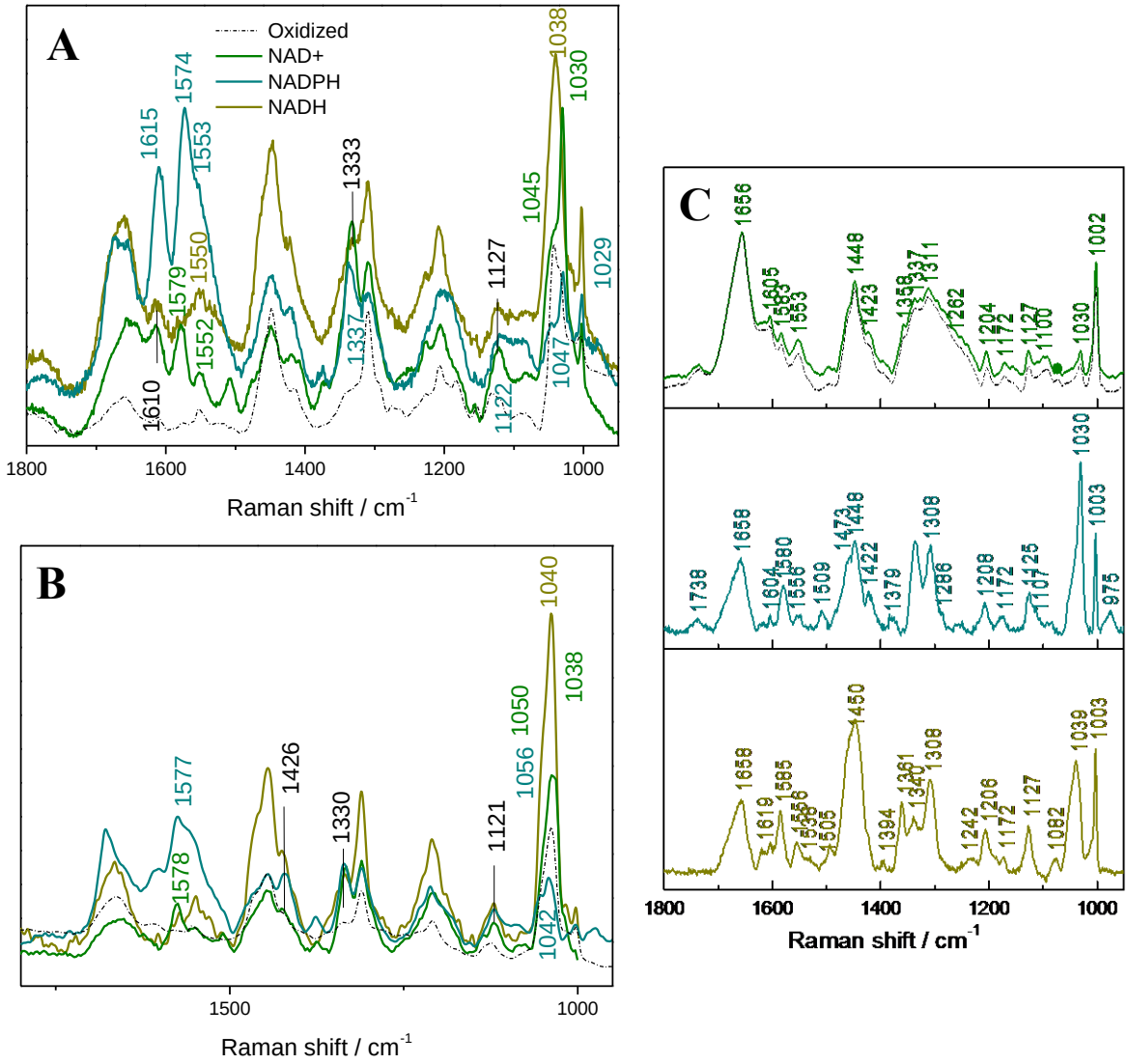

Figure 4.3-18. Resonance Raman spectra in the mid frequency region of A. NuoEF, B. NDF and C. Complex I in presence of NAD^+, NADPH and NADH.

The signal at 1153 cm^{-1} and 1184 cm^{-1} in the oxidized state, are mostly attributed to the $\nu(C_2\text{-}N_3)$ and to $\nu(C_4\text{-}C_{4a})$, respectively (see Table 4.3-1). Upon binding of the three nucleotides these signal are no longer observed in the spectra (Figure 4.3-18). The loss of intensity suggests a significantly weaker hydrogen bond to the NH group (N_3-H) of the isoalloxazine ring[385, 439] (see Figure 4.3-4). This result, together with the reported X-ray

structure, where the N_3-H group is surrounded by a negatively charged surface without hydrogen bond formation, suggests that N_3-H is weakly polarized. A similar result as observed in the studies of Hikita *et al.*[390] in bovine heart complex I. This corroborated the assignment of these two bands to only FMN vibrations.

It is important to note that the same changes are observed in the presence of NAD^+ and NADPH, indicating that even if the electron transfer might not be occurring, the binding to any of the nucleotides has the same effect over these bonds in the isoalloxazine structure.

Furthermore, the band V ($\nu(N_1\text{-}C_2)$), observed at ~1415 cm^{-1} (NuoEF) and 1422 cm^{-1} (NDF) in the oxidized spectra and the band II ($\nu(C_{4a}\text{-}C_{10})$), observed at 1569 (NuoEF), 1578 cm^{-1} (NDF) and at 1584 cm^{-1} (complex I) in the oxidized state (Figure 4.3-5), are empirical markers for the dielectric environment of the isoalloxazine moiety[440]. Upon reduction with NADH the first band disappears. This loss of enhancement had been associated with the hydrogen bonding of the C_2=O[439].

For the second band, an important gain in intensity is observed in presence of NAD^+ and NADPH for all the proteins, besides, the band shifts toward lower frequencies. In the case of the proteins with the bound NADPH, the shift to lower frequencies is more pronounced for NuoEF and NDF and the gain in intensity is no longer observed. These spectral differences are related to different electronic distribution in the ring I, lower frequencies point towards the formation of the fully reduced state, while the gain in intensity indicates an alternation between the oxidized and the semiquinone state[385, 440].

In summary it can be said that the polarized N_3-H, adjacent to the C_2=O group may stabilize the polarized state of C_2=O to strengthen the hydrogen bond of the C_2=O. This could be the reason of a stronger hydrogen bond of this oxygen atom. The results indicate that both N_1 and N_3 are protonated upon reduction. In addition to this, changes in the electronic density of ring I can be suggested to occur upon binding of any of the nucleotides.

4.3.4.3 Contribution from amino acid side chains

In general, NuoEF side chains show more manifest spectral differences in presence of the different nucleotides than NDF and complex I. In this part only the bands perturbed upon binding will be discussed.

Tyr -Fermi doublet. In the low frequency region the contribution from Fermi doublet attributed to the Tyr residues shows spectral differences upon the binding of the nucleotides in comparison to the oxidized state.

Upon binding of NAD^+, in the NuoEF (see Figure 4.3-17.A) and NDF (Figure 4.3-17.B) spectra in principle no changes are observed, in comparison to the oxidized state, except for the new band arising at 849 cm^{-1} in NuoEF at 850 cm^{-1} in the NDF spectrum. In complex I with NAD^+ Figure 4.3-17.C), both bands that represent the Fermi doublet arise at lower frequencies, the v_1 fundamental mode at 847 cm^{-1} and the v_{16a} mode at 821 cm^{-1}.

Upon binding of the NADPH, in NuoEF the two bands have a slight shift to lower frequencies while in NDF only the v_1 fundamental (850-830 cm^{-1}) is observed at lower frequencies, where in complex I no changes are observed. In addition, in NuoEF and NDF the v_1 fundamental band gains intensity changing the I_{v16}/I_{v1} ratio. It is important to note, that in addition to these two proteins a second signal is observed, at 847 cm^{-1} in NuoEF and at 850 cm^{-1} in NDF.

The new band observed in the NuoEF and NDF spectra in presence of NAD^+ and NADPH corresponds to the same vibrational modes. Site-direct mutagenesis in Tyr residues of viral proteins[441, 442] showed that when a population of deprotonated residues is embedded in a highly hydrophobic environment, they are able to give rise to an enhanced second component of the v_1 fundamental mode that is usually at higher frequency in comparison of the main doublet. This suggests that, upon binding of NAD^+ and NADPH to the NuoEFG subunit (clusters N1a, N1b, N3, N4, N5 and N7), a motion of Tyr residues occurs where many of the exposed residues will the buried within the structure. Furthermore, many Tyr will be in the deprotonated state.

Upon binding of NADH, a minor displacement of the v_1 fundamental mode to lower frequencies is observed in the NDF and complex I spectra, in comparison to the spectrum of the oxidized form (see Figure 4.3-1.D). However in the spectrum of NuoEF this signal has an important shift to higher wavenumber (~20 cm^{-1}), which points towards weaker hydrogen bonding in the case of complex I and NDF upon the reduction with NADH and the contrary can be suggested for the NuoEF subcomplex.

Besides this, in the three proteins, an increase in intensity is observed for the v_1 mode. Changes in the intensity are reflected in the I_{v16}/I_{v1} (I_{850}/I_{820}) ratio, where a higher ratio, as is the case, indicates changes in the environment between the "exposed" and "buried" Tyr residues, suggesting a higher quantity of exposed residues, where many of hydroxyl groups become a donor of a strong hydrogen bond to a negatively charger acceptor[289].

Trp - δ(ring). In the spectra of complex I (Figure 4.3-17.C), the signal corresponding to the δ(ring) mode at 876 cm^{-1} of Trp residues does not present any significant shift upon the binding of the nucleotides. This band corresponds to the Trp residues around N6a, N6b and N2, suggesting that upon binding none of the Trp residues surrounding the clusters are perturbed.

However, in the spectra of NuoEF (Figure 4.3-17.A) a new signal corresponding to this vibrational mode arises upon binding, indicating the proximity to the clusters of Trp residues upon binding. In general the frequency of the band reflects the strength of the hydrogen bonds of the N_1H site of the indole ring, in presence of NAD^+ the signal is observed at 878 cm^{-1}, while in presence of NADPH and NADH at 878 cm^{-1}, this frequency is related to strong hydrogen bonding[355, 443].

Arg, Lys - ν(C-C)/ Phe - δ(ring). The band corresponding to these vibrations was observed in the oxidized state spectra (see Figure 5.2-5) at 1043 cm^{-1} for NuoEF, 1038 cm^{-1} for NDF and at 1032 cm^{-1} in the complex I. With the binding of NADPH, the signal loses intensity and in the case of NuoEF it arises at lower frequency (1029 cm^{-1}) where in NDF and complex I it arises at higher frequencies, at 1050 cm^{-1} and 1039 cm^{-1}, respectively. Furthermore, a shoulder is depicted in the NuoEF and NDF spectra, arising at 1047 cm^{-1} and 1056 cm^{-1}, respectively; this shoulder can be attributed to the Arg and Lys ν(C-C) modes. This shoulder suggests that many of Arg and Lys residues display different motions, while some of them just remain unchanged.

As the ring breathing modes of the Phe (~1001 cm^{-1}) are not perturbed upon binding in any of the samples, it can be depicted that the changes of this vibration is due to changes in the side chain of Arg and Lys residues. The loss of intensity may be due to changes in the position of the residues according to the cluster or, more probably to changes in polarizability with respect to the distance between the atoms[310].

With NAD^+ and NADH, the signal arises at lower frequencies for NuoEF and the shoulder at 1045 cm^{-1} is observed, for complex I with NAD^+ the band is observed at 1056 cm^{-1} while for NDF and no major spectral differences are observed.

In summary, it can be suggested that the Arg, Lys residues around the N1a and N3 clusters in the NuoEF subcomplex are having some motions upon the binding of the nucleotides, where with NAD^+ and NADPH the perturbation is more pronounced. The same is observed in NDF upon the binding of NADPH, indicating that the Arg and Lys around the clusters except N6a, N6b and N2 display different motions.

His –asym rock/ Ala – ν(C-C). This mode was observed in the oxidized state at 1115 cm^{-1} in NuoEF and at ~1125 cm^{-1} in NDF and complex I. Upon the binding of NAD^+ and NADH in NuoEF the band shift to 1127 cm^{-1}, while for NDF it shift 1121 cm^{-1}. No shift is observed in complex I. In the presence of NADPH, for NuoEF the signal arise at 1122 cm^{-1}, for NDF at 1121 cm^{-1} and for complex I at 1126 cm^{-1}.

For NDF the effect of the binding of the nucleotides is the same, a small perturbation of this residues can be suggested, while for complex I this perturbation is only observed in the presence of NADPH. However, the spectral differences in NuoEF upon the binding suggest that the His and Ala residues are more affected in the NuoEF subunits than in the rest of the protein, where the effect is more pronounced in presence of NAD^+ and NADH.

ν(C-Cα)/ δ(Cα-H). The frequency of this vibration is directly related to the dihedral angle of the backbone, the lower the frequency, the lower the angle, the band is only the reflection of the most populated conformation.[13, 246, 249]. With the binding of all the nucleotides the band arises at lower frequencies, except in complex I. In the case of NuoEF the shift is more pronounced in presence of NAD^+ and NADH. Furthermore, a gain of intensity is observed is all the samples, reflecting the general conformational changes due to the binding.

Lys - δ(NH_3^+)/ Tyr – ring breathing. The gain of intensity of this band is only observed in the NuoEF spectra, in the oxidized state it was seen as a small shoulder at 1617 cm^{-1}, that was attributed to the δ(NH_3^+) modes of Lys. The enhancement of the vibration is more pronounced in the presence of NADPH, while the shift in frequency is more relevant in presence of NAD^+ and NADH, where the signal arises at 1610 cm^{-1}, at this frequency also the

contribution of the ring breathing modes of Tyr are also expected. The gain in intensity usually is related to changes in the pKa of the side chain[310].

4.3.4.4 The ν(C-H) region

In region above 2700 cm^{-1}, in NuoEF spectra in presence of three nucleotides (Figure 4.3-19.A), the band corresponding to the His, Leu and Ile residues observed at 2880 cm^{-1} in the oxidized state presents a shift to lower frequencies in presence of the three nucleotides. For NDF (Figure 4.3-19. B) no major shift is observed for this band.

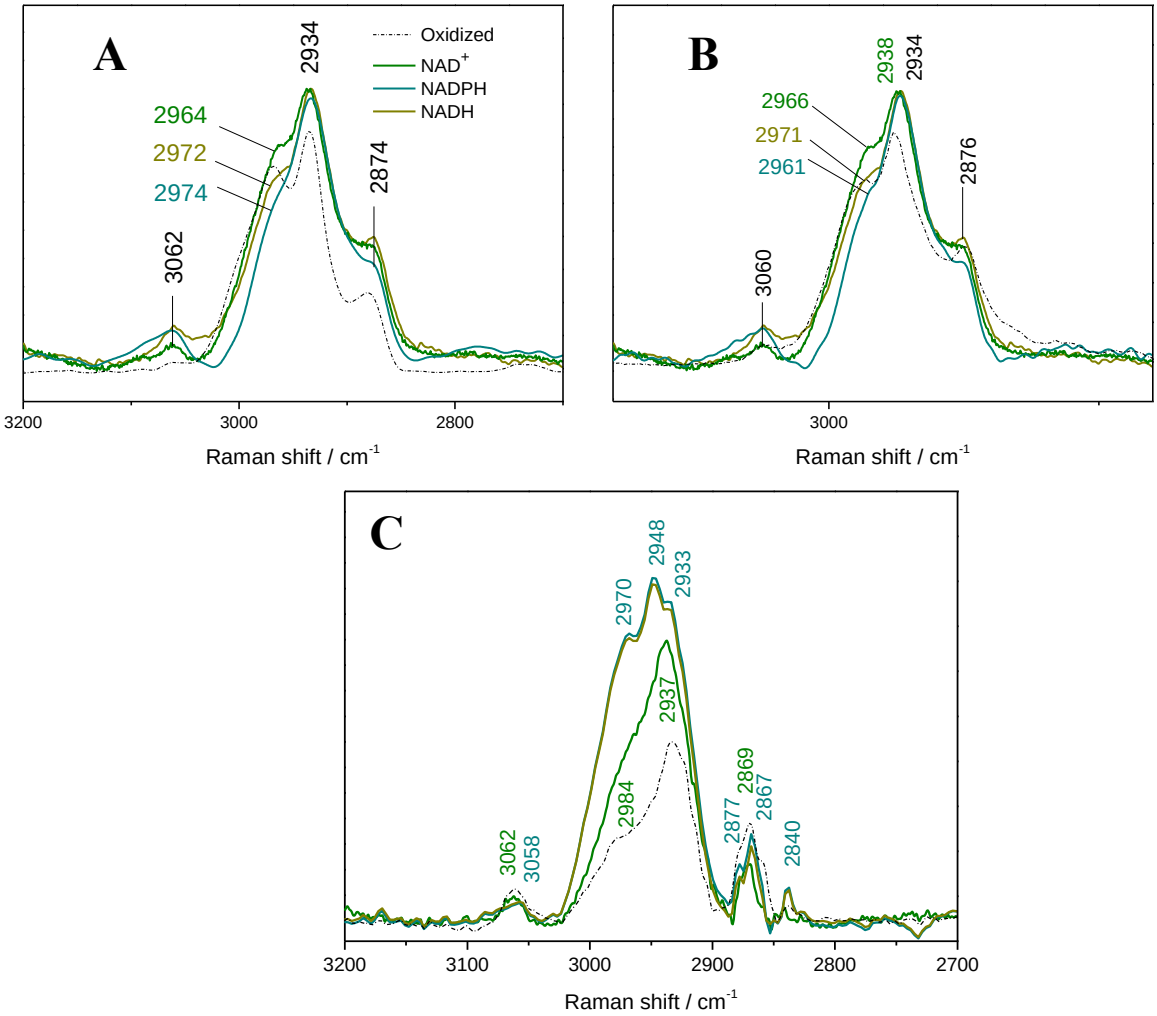

Figure 4.3-19. Resonance Raman spectra of A. NuoEF subcomplex, A. NDF and C. Complex I in presence of NAD^+, NADPH and NADH.

The main alteration from the effect of each one the nucleotides is evident in the signal attributed to the combination of the His, Ser and Cys residues where of the NuoEF the difference in frequencies lead to the relation: NuoEF-NAPH > NuoEF-NADH > NuoEF-NAD^+, where the frequency of the NuoEF-NAD^+ is identical to the one observed in the

spectrum of the oxidized form. However, in the NDF spectra the relation can be described as: NDF-NADH > NDF-NADPH > NDF-NAD^+, which the frequency of NDF-NAD^+ is almost the same as in the spectrum of the oxidized form. From these results it can conclude that, in the case of the NAD^+ no changes in the dihedral angle of these amino acids are observed, whereas in NuoEF the effect of the NADPH is more prominent than in the case of NADH. This can be due to the difference in quantity of these residues in each one of protein, making the effect more evident for the NuoEF subcomplex than in the fragment.

In complex I this contribution was observed in the oxidized state at 2977 cm^{-1}, where in presence of NAD^+ it arises at 2984 cm^{-1} and with NADH and NADPH it arises at 2970 cm^{-1}. This indicates that the residues around N6a, N6b and N2 have very different behavior to what was observed for NDF and NuoEF.

In addition to this, in the complex I spectra (Figure 4.3-19.C) the band arising from the contribution of Leu, Lys and Leu, observed in the oxidized state at 2882 cm^{-1}, in presence of NADPH it arises at 2877 cm^{-1}, whereas in presence of NAD^+ and NADH no changes are observed. A similar pattern is observed in the band corresponding to the contribution of Phe, Tyr and Trp arising at 3062 cm^{-1}.

The last variation in the contribution from the Thr and Pro, described in the oxidized form at 2933 cm^{-1}, in the presence of NAD^+ the signal arises at 2937 cm^{-1}, whereas with NADH and NADPH a second signal is observed at 2948 cm^{-1}. This suggest that in presence of NAD^+ all the Thr and Pro residues in average have a different conformation while in presence of NADPH and NADH some of them remain in the same conformation as in the oxidized state.

These vibrational modes, for the analysis of protein, reflect changes in the micro-environment. It is important to consider that due to the overlapping of several contributions not much information can be deduced from their analysis[289, 311]. Nevertheless, it is typically accounted that the lower frequency of the bands reflects narrower dihedral angles of the amino acids involve in the backbone structure[13, 443].

In summary, from these vibrational modes, it can be concluded that for all the samples NAD^+ does not exert any influence, whereas for NuoEF in presence of NADH; His, Leu and Ile may have a narrower dihedral angle, and the Ser and Cys residues broader ones, where for this second one the effect is more pronounced in presence of NADPH.

For NDF, only major changes of His, Ser and Cys are observed, which in presence of NADH the perturbation is more marked. In the complex I samples Thr and Pro residues are perturbed in presence of NADPH and NADH, whereas in presence of NADH perturbation of His, Tyr, Trp and Met were observed.

4.3.4.5 Conclusion

The reaction between the FMN and NADH is a two-electron reaction which is very likely to be a hydride transfer reaction[444, 445]. The reduced flavin is re-oxidized by electron transfer to the iron-sulfur clusters, presumably in two one-electron steps. However, further knowledge of both the kinetics and thermodynamics of NADH oxidation is required to understand how NADH oxidation is linked to energy transduction, conserving essentially all the free energy[17, 191].

Efremov *et al.*[224, 446] showed the structures of the hydrophilic domain of complex I from *T. thermophilus* with nucleotides bound. This study had revealed a juxtaposition of specific interactions between the protein and the nucleotide, in specific stacking interactions between three Phe residues and the adenine ring, besides a number of hydrophobic interactions, and hydrogen bonds to the nicotinamide carboxyamide.

Upon binding, the nicotinamide ring of NADH forms a stacking interaction with the isoalloxazine ring of FMN, this interaction provides a favorable geometry for fast hybrid transfer between the C_4-N of NADH and N_5 of FMN,[15] which is also observed in our results. Alternatively, it can been proposed that NADH and NAD^+, form an hybrid mechanism, where the turnover of the protein is directly regulated to the concentration of NAD^+ in the environment and the ROS production. This is reflected by the differences first in the $\upsilon(C_4{=}O)$, in the oxidized state the oxygen molecule is externally weak, taking in count the state of the protein as, a steady state, each reaction functions as a two-substrate reaction except in the case of NAD^+. That kind of reaction is already achieved by the substrate given to the protein. Furthermore, the result points towards N_3-H groups surrounded by a negatively charged surface without hydrogen bond formation and the hydrogen bonding of the $C_2{=}O$.

From the metal-ligand vibrations the results suggest that the reduction of the [2Fe-2S] clusters have as consequence the distancing of the Fe orbitals, whereas in presence of NAD^+

changes in the geometry of the cluster are more associated with narrower dihedral angles and with NADPH, wider ones. As it was shown, N1a in the NuoEF subcomplex was partially reduced or not reduced at all, suggesting that N1a in *A. aeolicus* and the N1a in *E. coli* do not have the same reduction mechanism.

For the [4Fe-4S] clusters, N3, N4 and N5 N5 in presence of all the nucleotides, the coordination of the Fe-S^b changes to a more "relaxed" state, while N6a, N6b and N2 are likely to have "rigid" Fe-S^b bonds. The "relaxed" centers are likely to be faster electron transfer than the "rigid" centers, where in the latter ones, the reversibility to an oxidized state is slower due to the change in the energy of the Fe-S bridging bonds.[167]

In summary, it can be concluded that the conformational changes that follow the substrate binding have a great effect on the cysteinyl coordination of the Fe-S cluster even if there is no electron transfer. Moreover, the redox properties of the cofactor modulate the changes in the protein structure and the changes in structure have a modular effect in the metal coordination of the Fe-S clusters.

Even if the electron transfer takes route defined by the successive sites of redox centers, the electrons do not go directly from NADH towards the ubiquinone molecule; they frequently jump back and forth between neighboring redox centers with the result that net flux of electron through Complex I (net number of electrons reducing a ubiquinone) is far smaller than the number of redox reactions that actually occur.

The reduction potential of the FMN in the enzyme's active site is lower than that of free FMN (thus, the oxidized state of the FMN is most strongly bound) and close to the reduction potential of NAD^+. Consequently, the catalytic transformation is reversible. The conformational changes observed with the bound NAD^+ in all the samples around the cluster environment may reflect the effect of this process. It may be the cause why, in the presence of NADPH, these changes are not seen. Due to the environment of the protein, many hydrophobic residues complement the electron charge occasioned by the NADPH to NADH reduction. In this case, the protein in all the states presents a kind of inhibition, and this effect is especially enhanced for N1a.

4.3.5 Site-direct mutagenesis in NuoEF and NuoB subunits

According to previous studies, there are certain amino acids that can have an important effect on the midpoint potential of the cluster[6, 188, 230]. In eukaryotes, neutral residues as Val, Ser and Pro, even if they are not part of the Fe-S cluster motif have been considered to be involved in crucial hydrogen bonding[6, 445]. This hydrogen bonding network can influence the pH-dependent redox reaction in the case of N1a and N2 clusters, in contrast to the other clusters.

Site-directed mutagenesis allows the examination of the possible influence of several amino acids around the cluster motif. Previous studies have presented a series of residues that are conserved among several species in complex I[1, 196, 229]. In this section mutation of conserved residues around the N2 and N1a cluster will be analyzed in order to learn more about their special properties and crucial roles.

4.3.5.1 Studies in NuoE variations in *A. aeolicus*

A.aeolicus NuoEF subcomplex is part of the NADH dehydrogenase fragment. It has a molecular mass of 66 kDa and contains three cofactors: FMN, N3 and N1a. In previous studies the structure of this subcomplex was solved to 1.9 Å[201].

As explained above N1a has its binding motif in the NuoE subunit (See section 1.4.2.2-Figure 1.4-3). The motif of this cluster has a special feature, the Cys are connected into two loops (See Figure 4.3-20.A), loop 1, between Cys83 and Cys88 (*T. thermophilus* nomenclature) and loop 2 between Cys123 and Cys128. Another important region to consider is the C-terminal β-strand (CT-β), previous structural studies revealed that this region shares secondary structural elements among several species and might be part of the loop that regulates the potential of the cluster[6]. Furthermore, the amino acid residues responsible for substrate binding as well as the cluster motif are conserved in both subunits of the protein, making this subcomplex a suitable structural tool to serve as model for the studies of the site of input of the first electron in complex I.

The midpoint potential varies with the species; by protein film voltammetry the *E. coli* and *A. aeolicus* N1a cluster showed a midpoint potential between -280 to -240 mV (vs. SHE); for *B. taurus, P. dentrificans* and *T. thermophilus* it is between -420 to -370 mV (vs. SHE). It

can be noted that *E. coli* and *A. aeolicus* have a higher redox potential, making them "high-potential" cluster in comparison to the complex I of the rest of the species studied that can be classified as "low-potential" clusters.

CT-β of the *A. aeolicus* NuoEF contains a Val residue (Val136) which was exchanged against Met. As seen in *B. taurus* and *Y. lipolitica*, the loop 1 contains a Val residue (V90 corresponding to Ser86 in *T. thermophilus*) that was exchanged against a Pro residue. These mutations were done in order to incorporate residues that belong to the "low-potential" N1a cluster (Pro and Met) hence attempting to modify N1a from being a "high-potential" cluster to a "low-potential" cluster.

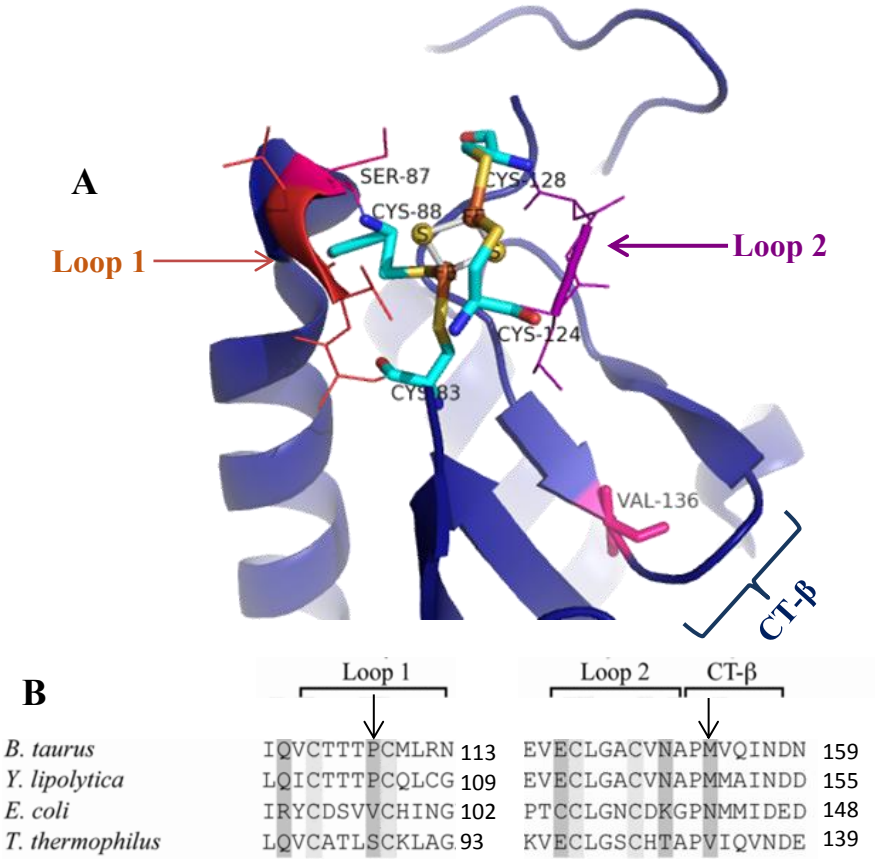

Figure 4.3-20. A N1a cluster motif, loop1 labeled in red and loop2 labeled in purple, mutated residues (*T. thermophilus* nomenclature) are labeled in pink. (PDB:4HEA) B. Alignment of the sequences of the 24 kDa subunit (*B. taurus*, UniProt code P04394), NUHM (*Y. lipolytica*, UniProt code Q9UUT9), NuoE (*E. coli*, UniProt code P0AFD1) and Nqo2 (*T. thermophilus*, UniProt code Q56221), indicating important features (yellow and grey). The arrows indicated the mutated residues. Adapted from Birrell *et al.* [6]

Martha Vranas from Prof. Friedrich's group (Institut für Biochemie, Albert-Ludwigs-Universität Freiburg im Breisgau) performed kinetic and EPR measurements besides X-ray crystallography as a collaboration in the aim to characterize this subcomplex. In our group

UV/visible titration were done in order to determine the midpoint potential of these variants as well as a complete spectroscopic characterization by FT-IR and RR of the oxidized and reduced states.

Table 4.3-4. Characterization of the *A. aeolicus* variants and the N1a redox properties.

NuoEF	K_M [µM][201]	EPR (detectable)[201]		N1a E_m
		N1a	N3	(mV vs. SHE)
WT	0,9 ± 0,1	+	+	-254[226]
V136M	0,8 ± 0,1	+	+	-241 ± 4,3
V90P	0,55 ± 0,05	-	+	-192 ± 5,1
V90P/V136M	0,1 ± 0,05	-	+	-202 ± 5,3

Table 4.3-4 shows an overview of the midpoint potentials, it can be seen that the NuoEF-V136M mutant has a similar properties as the ones displayed by the WT. NuoEF-V90P displays 50% less activity compared to the WT whereas the activity of NuoEF-V90P/V136M is completely abolished; the midpoint potential of both variations shifts to more positive value. The details of the titration as well as the Nernst curve fitting can be found in the appendix Figure 7.2-8.

Birrel *et al.*[6] performed site-direct mutagenesis of the conserved residue Val against Pro in the *E. coli* NuoE subunit and Pro against Val for the homologue NUHM subunit in *Y. lipolitica* and the 24 kDa from *B. Taurus*. As a result, N1a from *E. coli* was transformed into a "low-potential" cluster and N1a from *Y. lipolitica* and *B. taurus* were transformed into "high-potential" clusters. Exchanging both residues (Val90/Val136) increases the potential in the *B. taurus* and *Y. lipolytica* proteins by ~160 mV, and decreases the potential in the *E. coli* protein by 100 mV.

In this work, the mutations V90P and the double mutant, V90P/V136M give rise to more positive midpoint potential. This may indicate that in NuoE from *A. aeolicus* the residues have a different influence that in the N1a cluster from previously described organisms.[6] The different sphere of coordination shows that a third hypothesis should be made. In thermophilic organisms usually the structure is more rigid as part of a setup to the

adaption to an extreme environment. In the case of N1a in *A. aeolicus* the environment of the cluster is highly hydrophilic in comparison to its *E. coli* counterpart, for example. This difference in the environment may be the cause of the differences between what was expected and what was obtained.

The crystal structure of NuoEF V90P revealed a conformational change at the loop that coordinates the N1a cluster (Figure 4.3-21). In this variant the main carbonyl chain of some residues (Ile89, His92 and Leu93) shift towards the Fe-S cluster binding site, causing a conformational change in the second coordination sphere of N1a (residues Glu333 and Asp330).

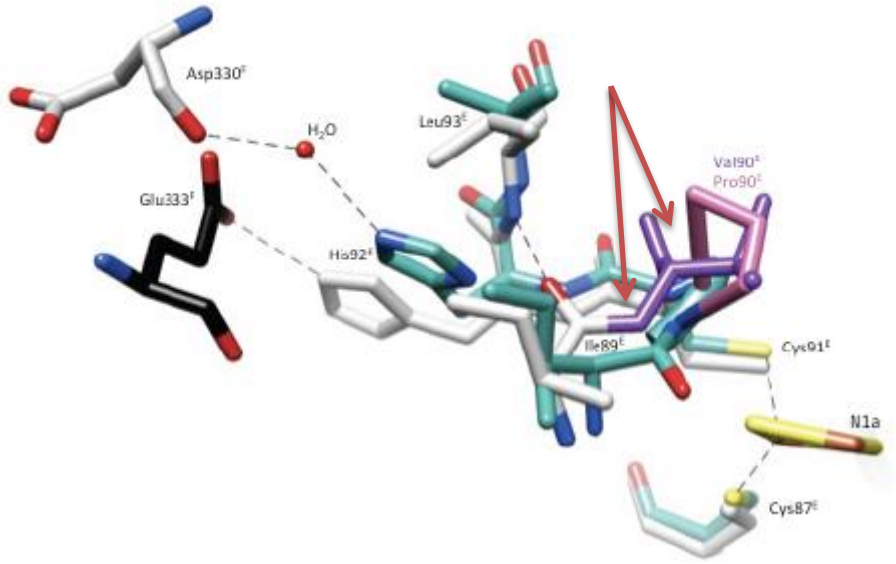

Figure 4.3-21. Structure comparison of NuoEF V90P (cyan) and NuoEF WT (grey) from *A. aeolicus*. Red arrows show the conformational changes of the main chain. Relevant residues are labeled. Adapted from Vranas.[201]

4.3.5.1.1 Infrared spectra

ATR-MIR spectroscopy (Figure 4.3-22) showed that V136M has the same spectral characteristics as the WT, except in the ν(C-H) region (signal at 3068 cm^{-1}). On the other hand, NuoEF-V90P and NuoEF-V90P/V136M showed changes in amide A, amide B and the ν(C-H) indicate the possibility of perturbation in the hydrogen bonding of the protein.

Besides, changes in amide II are seen in NuoEF-V90P indicating a perturbation of the protein backbone, in the case of NuoEF-V90P/V136M a similar shift of amide II is observed

but also amide I is displaced, indicating that in the double mutant not only the N-H and C-N motions are changed due to the mutations but also the C=O backbone.

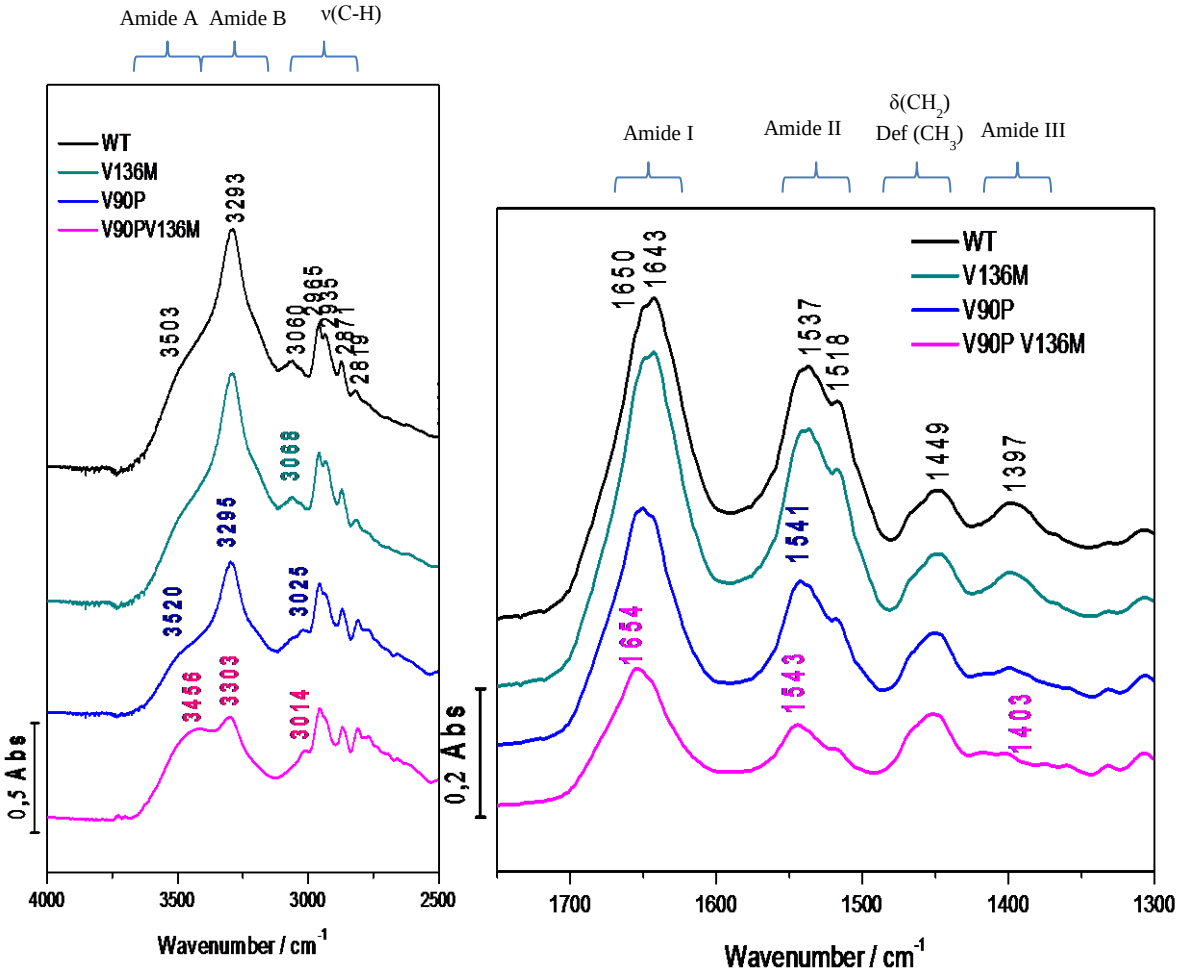

Figure 4.3-22. ATR-MIR spectra of NuoEF WT and NuoEF mutants. The differences between the WT and the mutants are highlighted in colors.

The deconvolution of amide I (Figure 7.2-9 appendix) showed that NuoEF-V136M has the same secondary structure composition as the WT sample, whereas NuoEF-V90P (Table 4.3-5) presented changes in the percentage of all the components as well as the NuoEF-V90P/V136M. This suggests that these mutants have very different structures in comparison to the NuoEF-WT.

In Figure 4.3-23 the spectra of the NuoEF WT and the different mutants are displayed, the complete assignment of the observed bands can be seen in Table 4.3-6, where the main shifts between the proteins are highlighted in bold blue.

Table 4.3-5. Amide I deconvolution from the spectra of the NuoEF WT and its mutants (in parenthesis the frequency of the secondary structure component assigned)

(%)	WT	V136M	V90P	V90P/V136M
α-helix	30,9 (1657/1649)	30,9 (1657/1649)	26.1 (1667/1657)	41,3 (1668/1655)
β-sheet	28,5 (1618/1630)	28,5 (1618/1630)	36,6 (1629/1642)	37,4 (1629/1642)
β-turns	21,9 (1674)	21,8 (1674)	10.1 (1681)	21,3 (1681/1673)
Random coil	18.7 (1643)	18.6 (1645)	27,2 (1650)	--

From the metal-ligand vibrations the main perturbation due to the mutations are around the ν(Fe-S) terminal modes; the shifts are more pronounced in the case of NuoEF-V90P and NuoEF-V90P/V136M. Displacements of the δ(C-C-N) and δ(C-S) modes are also seen for these two mutants. This indicates that these mutations have a direct effect on the Cys coordination, but the perturbation does not influence the shape and orientation of the cluster, as it does not affect the bridging modes.

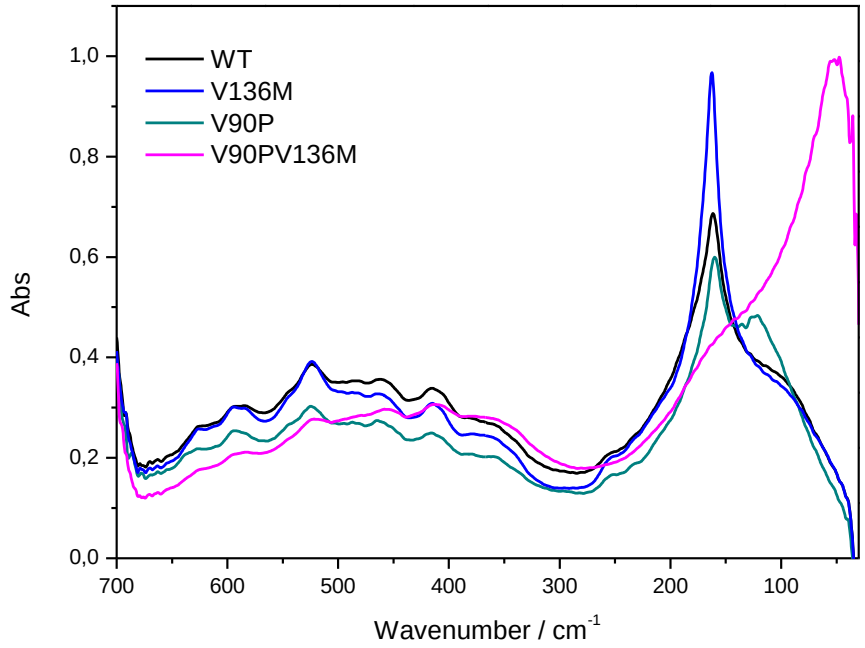

Figure 4.3-23. ATR-FIR spectra of NuoEF WT and the different NuoEF mutant of *A. aeolicus*.

The most relevant spectral difference between the WT and the mutants is the hydrogen bonding collective modes. This vibrational mode is characterized by a band with two peaks. As seen in MIR and the metal-ligand vibrations, the NuoEF-V136M spectrum is very similar to the WT. For NuoEF-V90P, the first peak seen at 161 cm^{-1} in the WT, arises now at 159 cm^{-1}, whereas the second peak at 97 cm^{-1} in the WT appears now at 119 cm^{-1}; not only the frequency changes but also the shape of the band. In the WT the first peak has a higher intensity than the second one; in this spectrum the second one changes from being a shoulder to become a well-defined peak. For NuoEF-V90P/Va136Met this characteristic is even more pronounced, where the second peak now has higher intensity and lower frequency, arising at 54 $cm^{-1,}$ and the first peak becomes a shoulder arising at 159 cm^{-1}.

Table 4.3-6. FIR modes of the NuoEF WT and the different mutants.
(Highlight in bold blue are the modes shifted in the variations)

Modes	Fe-S cluster	WT	V136M	V90P	V90P/V136M
δ(C-S)	All	**627**	**627**	**630**	**632**
ν(Fe-S) Bridging	N3	595	595	595	596
Amide VI	--	525	525	525	527
δ(S-Cα-Cβ)	N3	488	488	489	488
δ(C-C-N)	All Cys side chains.	**466**	**463**	**464**	**461**
ν(Fe-S) Bridging T1	N3	413	414	413	415
ν(Fe-S) Bridging T1	N3	375	374	374	374
ν(Fe-S) terminal	N1a	**352**	**351**	**358**	**361**
ν(H…O) Collective modes	--	**161** **97**	**161** **97**	**159** **119**	**159** **54**

As a general rule for this vibration, the lower the frequency, the stronger the hydrogen bonding. One of the plausible explanations is that more water molecules gain access to the inner part of the protein, therefore interact with the backbone of the protein and further

stabilize the structure. This stabilization can also be reflected by the higher midpoint potential of the Fe-S cluster.

4.3.5.1.2 RR spectra

In Figure 4.3-24 the RR spectra in the low frequency range represent the symmetric and asymmetric metal-ligand vibrations of N1a and N3, the main shifts of N1a in the vibrations corresponding to N1a are highlighted. A comparative overview of all the observed bands, according to the assignment made before for N1a and N3 (see section 4.3.2) can be seen in Table 7.2-2. (Appendix). As the aim is to compare the effect of the mutations around N1a, Table 4.3-7 shows a summary of the metal-ligand vibrational modes corresponding only to this cluster.

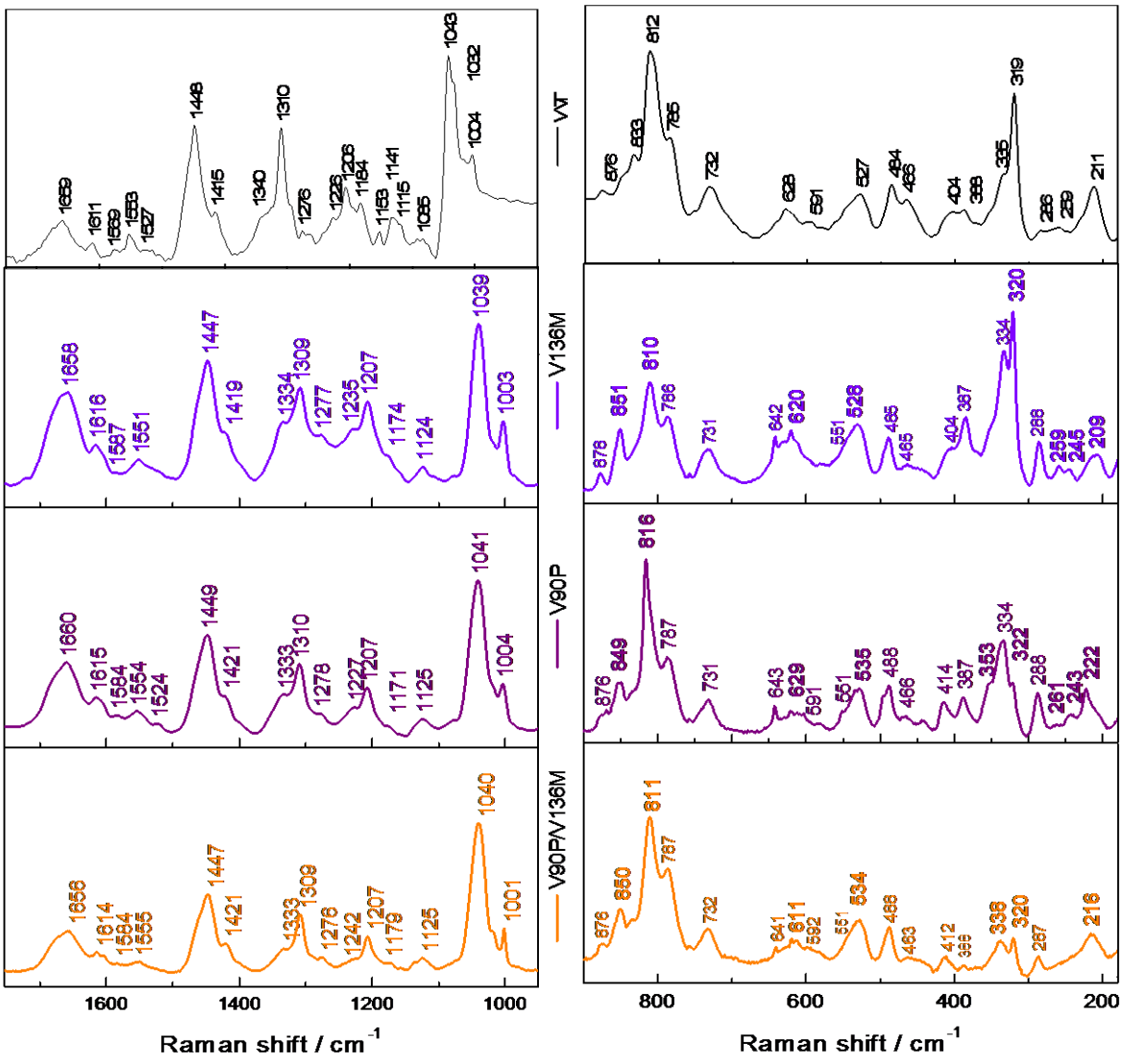

Figure 4.3-24. RR spectra of the NuoEF mutants. The vibrational modes highlighted are the ones affected by the mutations.

In general, a decrease in the intensity of the signals corresponding to the metal-ligand vibrations is observed in the NuoEF-V90P spectrum and the effect is more pronounced for NuoEF-V90P/V136M, this indicates that the mutations destabilize the CT transfer that give rise to the enhancement of the of Fe-S vibrations, where the transition from the ground to the first excited state takes place. This is in line with the UV/Vis spectrum described by Vranas[201].

An important vibration is the fundamental Ag Fe-Fe. This mode is a correlation measurement of the distance between the two Fe atoms, as the vibration arises from the motion of the Fe atoms toward each other[12]. In NuoEF-V90P and NuoEF-V90P/V136M the signal arises at 222 cm^{-1} and 216 cm^{-1} respectively, in comparison to the WT at 211 cm^{-1}, indicates an overlapping of the Fe orbitals.

Table 4.3-7. N1a metal ligand vibrations by RR spectroscopy of the NuoEF subcomplex WT and its variants from *A. aeolicus* (laser: 514.5nm)

Modes		WT	V136M	V90P	V90PRO/ V136M
Fe-S stretching	A_g Fe-Fe	**211**	**209**	**222**	**216**
	Bridging(B_2)	--	**243**	**245**	--
	Terminal(B_{3u})		**261**	**259**	
	Terminal(B_{1g})	**319**	**320**	**322**	**320**
	Bridging(A_1)	335	334	334	**338**
	Bridging(A_g)	388	387	387	388
	Bridging(B_{2u})	404	404	**414**	**413**
Bending motions	Fe-S-C + A_1 overtone	484	485	488	488
Fe-S Overtones	2x T_1 (E)	527	528	535	534
C-S Stretching		621	622	**629**	**611**
		--	642	**641**	**641**

The frequency itself is not an indication of the metal-metal bond strength, but higher frequencies suggest a substantial Fe-Fe interaction[12]; nevertheless, weak bonds are found to give larger intensities because of their dependence on the polarizability on the cube bond distance[361]. Not only changes in the frequency are observed, the shape of the band becomes

broader in the spectra of the mutants, this indicates a decrease of the intensity that involves mutual displacement of the Fe atoms (see Figure 4.3-12).

In addition, In the NuoEF-V90P and NuoEF-V136M spectra two signals arise at ~243 and 261 cm^{-1} that are not seen in the WT nor NuoEF-V90P/V136M spectra. In the WT, as the bands have a low intensity they could not be correctly assigned; although in the NuoEF-V90P/V136M spectrum these band are not enhanced at all, indicating that this protein is more photosensitive than the other samples, this can also be observed from the intensity of the metal-ligand vibrations with respect to the amino acid vibrations, where the first are half of the intensity observed in the NuoEF WT and NuoEF-V136M

Besides, it is evident that the mutants NuoEF-V90P and NuoEF-V90P/V136M present differences in the ν(Fe-S) terminal modes more than the ν(Fe-S) bridging modes. In these mutations the terminal modes arise at higher wavenumber, indicating a loss of energy by the bonds that coordinate the metal center, this corroborates with the results observed in FIR. Nevertheless, for the ν(C-S) modes above 620 cm^{-1}, the symmetrical vibrational mode in NuoEF-V90P goes to a higher frequency while in NuoEF-V90P/V136M it shifts to lower frequency. The effect of the mutation on the vibration is more pronounced in the later one where the signal is observed at 611 cm^{-1}.

Another important characteristic in the RR spectra of the mutants is that the three variations affect the Fermi doublet attributed to the contribution of Tyr residues in the same manner. These vibrational modes were seen in the WT at 812 and 833 cm^{-1}, the second component corresponding to the symmetric ring breathing vibrations (fundamental mode ν_1) arise at ~850 cm^{-1} in the three mutations. It may be noted that the fundamental mode ν_1 is sensitive to changes in the environment; conformations of the surrounding amino acid chains are usually the cause of these changes. A higher frequency indicates that many of the Tyr residues are now exposed to the solvent, whereas in the WT structure they were interacting with other side chains.

In the WT the ratio between these modes was $I\nu_{16a}/I\nu_1$: 0.3, indicating that the hydroxyl groups of several Tyr residues present in the structure act as donors forming strong hydrogen bonds, these Tyr residues are described as “buried” within the structure. For the mutants NuoEF-V90P and NuoEF-V90P/V136M as the intensity of the ν_{16a} mode is higher, the $I\nu_{16a}/I\nu_1$ is 0.35 and for NuoEF-V136M is $I\nu_{16a}/I\nu_1$: 0.45. However, it is important to note

that for the NuoEF-V136M this is the only spectral characteristic that differs from the spectrum of the WT.

Table 4.3-8. Amide vibrational modes and amino acid side chain contributions of NuoEF WT from *A. aeolicus* and its variants by Raman Spectroscopy.(Assignment were done based on the studies of Jenkins *et al.*[309] and Ianoul *et al.* [13])

Modes	Amino acids/ amide	WT	V136M	V90P	V90P/V136M
Fermi doublet	Tyr	**812** **833**	**816** **851**	**816** **849**	**811** **850**
		876	878	876	876
δring	Phe	1004	1003	1004	1001
ν(C-C) δring	Arg, Lys Phe	**1032**	--	--	--
OH-def motion	Thr	1043	1039	1041	1040
Nt-H asym rock ν(C-C)	His Ala	**1115**	--	--	--
NH_3^+ asym rocking	Lys	**1141**	**1124**	**1125**	**1125**
Cβ-twist δ(CΥ1-Cβ-CΥ2)	Ile	**1153**	--	--	--
δ (C-H)	Phe	**1184**	**1174**	**1171**	**1179**
υ (ring-O)	Tyr, Phr, Trp	1206	1207	1207	1207
Amide III δ(N-H) ν(C-N) δ(C=O) ν(C-C)	β-sheet	**1226**	**1235**	**1227**	**1242**
	Random coil	1276	1277	1278	1276
	α-helix	1310	1309	1310	1309
	δ(Cα-H)	**1340**	**1334**	**1333**	**1333**
δ(Cα-H)	Cys	**1415**	**1419**	**1421**	**1421**
$\delta(CH_2)$	Leu, Lys	1448	1447	1449	1447
CH3 asym def	Met	1527	--	1524	--
υ(C-N)+ δ(N-H)	Amide II	1553	1551	1554	1555
ν(C=0) ν(C-C)	Phe His	**1569**	**1587**	**1584**	**1584**
$\delta(NH3^+)$	Lys	1611	1616	1615	1614
υ(C=O)	Amide I	1659	1658	1660	1656
υ (C-H)	Lys, Leu, Ile	**2880**	**2880**	**2876**	**2873**
	Ile,Ser	**2935**	**2929**	**2930**	**2934**
	Cys, His, Ser, Leu,Trp, Gly, Lys	**2966**	**2973**	**2980**	**2973**
	Trp, Phe, Tyr	**3062**	**3062**	**3057**	**3059**

Above 800 cm^{-1}, a summary of all the bands and their assignments can be seen in Table 4.3-8. Three new bands arise in the mutants' spectra, at 1032, 1115 and 1153 cm^{-1}. As seen in the crystal structure (Figure 4.3-21) Ile 89, His92, Leu 93 have different orientation in NuoEF-V90P, this change in orientation in some amino acids may be reflected in the enhancement of their vibrations.

Additionally, changes in the δ(C-H) and the ν(C=O) modes of Phe are observed. For the first vibrational mode, in the WT the band arises at 1184 cm^{-1}, in NuoEF-V90M it is seen at 1174 cm^{-1}, in NuoEF-V90P at 1171 cm^{-1} and in the doubled mutant at 1179cm^{-1}. Changes in the frequency of this vibration are related to the dihedral angle motions (Figure 2.4-2), indicating that in the mutation the Phe residues have a different orientation. A similar pattern is seen for the band of the ν(C=O) modes, where for the WT the signal arises at 1569 cm^{-1}, for the mutants it is seen at 1584 cm^{-1}.

The Cys δ(Cα-H) modes are also perturbed, whereas for the NuoEF-V136M the signal arises at 1419 cm^{-1} for NuoEF-V90P and NuoEF-V90P/V136M it arises at 1421cm^{-1}, for this vibration, the dihedral angle of the Cα with the C=O (ψ) exerts an influence, where the broader the angle the lower the frequency will be[310], indicating that the Cys residues in the WT have a broader angles than in the rest of the samples. The difference in the frequency had been also associated with the formation of disulfide bonds[399].

From the amide vibrations, changes in the amide III corresponding to the β-strand component present an upshift in the case of NuoEF-V136M and NuoEF-V90P/V136M. Additionally, a slight shift of amide II and amide I is evident in NuoEF-V90P/V136M spectra, corroborating the observed changes in MIR, pointing towards important changes in the secondary structure in the case of the double mutant.

Furthermore, the modes corresponding to the δ(Cα-H), present a downshift, from 1340 cm^{-1} in the WT to ~1333 cm^{-1}, indicating motions of dihedral angle of several residues, as it was seen for the Phe and Cys residues.

In the υ(C-H) modes above 2700 cm^{-1} (Figure 4.3-25), changes are observed in the contribution from His, Leu and Ile, the band the NuoEF WT arises at 2880 cm^{-1} in the WT and NuoEF-V136M, whereas for the NuoEF-V90P it arises at 2876 cm^{-1} and for NuoEF-V90P/V136M at 2873 cm^{-1}. A similar displacement is seen for the band corresponding to the His, Phe and Tyr contribution, where shifts are only seen for NuoEF-V90P and NuoEF-

V90P/V136M. Nevertheless, for the contribution of Cys, His, Ser, the signal presents a shift for the three mutants, going from 2966 cm^{-1} in the WT to 2973 cm^{-1} for NuoEF-V136M and NuoEF-V90P/V136M and for NuoEF V90P the band is observed at 2980 cm^{-1}.

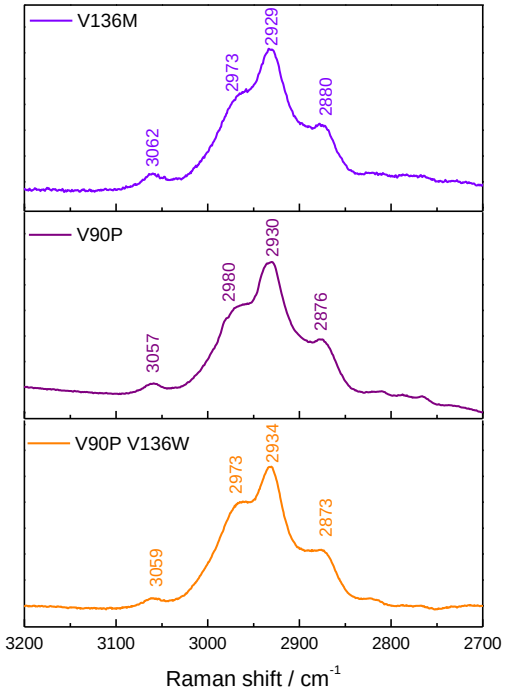

Figure 4.3-25. ν(C-H) region of the RR spectra of NuoEF mutants from *A. aeolicus*

Changes in this region indicate variations of the hydrophobic groups. As described before, many of the shifts reflect changes in the dihedral angles of the structure; even if the motions in the angles are small the enhancement given by the resonance effect of the technique provides an amplification of the bonds perturbed.

4.3.5.1.3 RR spectra – reduced state

In order to obtain the reduced state, dithionite and NADH were added to the samples according to the conditions explained in section 4.3.4. The spectra shown in Figure 4.3-26 correspond to the reduced state of N1a and N3 clusters with dithionite and NADH in low frequency region. In order to assure the reduced state of the samples, the band at 732 cm^{-1} and 788 cm^{-1} corresponding to the isoallazine ring of the FMN were monitored, as seen in the complex I, NDF and NuoEF WT samples (see section 4.3.2 and 4.3.4.2).

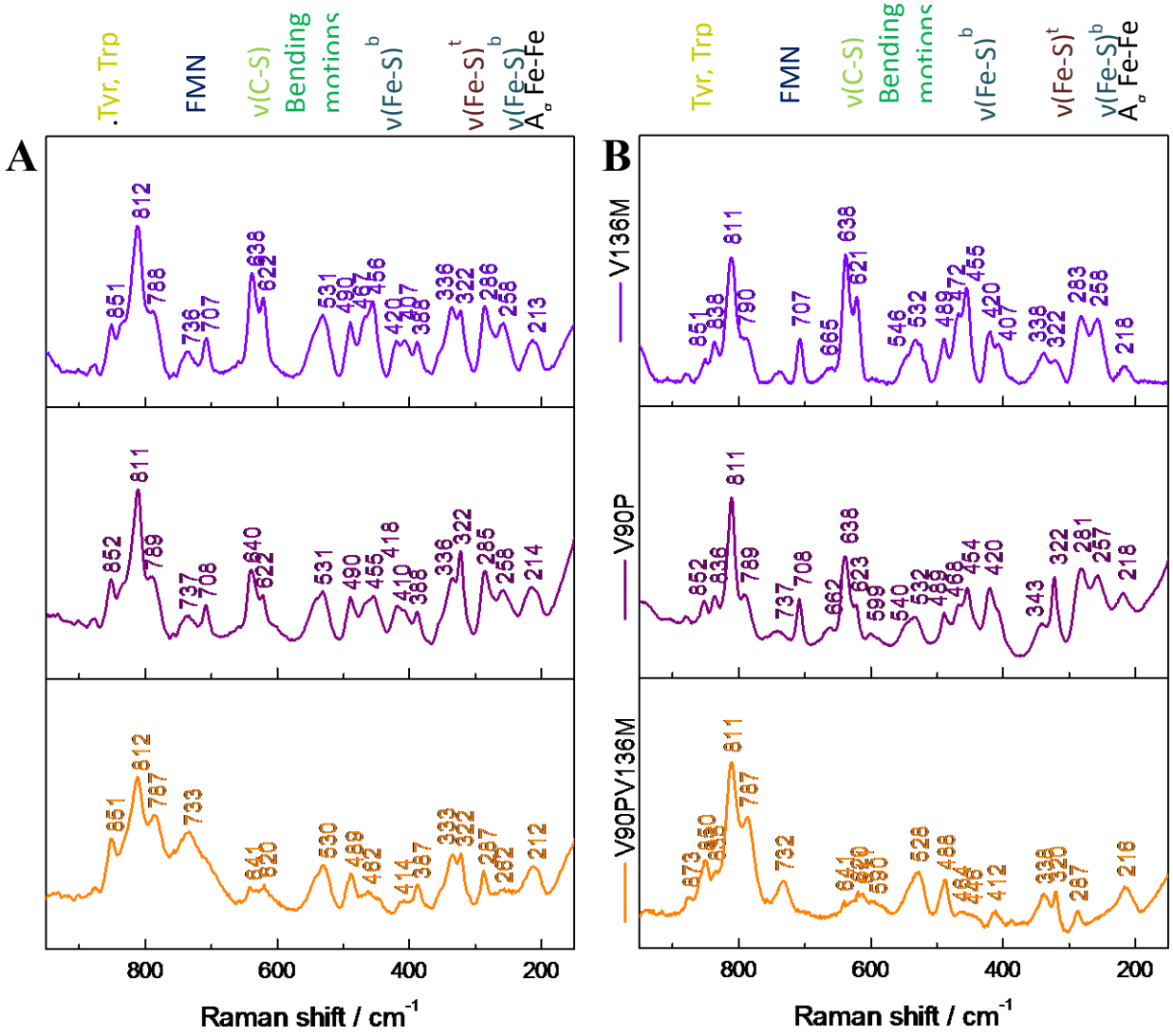

Figure 4.3-26. Resonance Raman spectra of NuoEF mutants in the reduced state. A. with NADH and B. with dithionite

The first characteristic that is evident from the spectra, is the change in intensity (see section 4.3.4.1), the spectra obtained in the reduced state are an order of magnitude less than for the oxidized proteins. RR band depend critically on the symmetry and structural distortion in the electronic excited states, hence the changes in the intensity had to do with changes in the energy of the CT of S⟶ Fe^{+3} in the excited state[12]. In general the bands corresponding to the ν(Fe-S)^t lose intensity while the bands corresponding to the ν(Fe-S)^b gain intensity. In order to better compare the spectra, normalization was made taking as reference the contribution from the signal at ~812 cm^{-1}.

For the ν(Fe-S) modes two different sets can be distinguish according to the redox state of the Fe atom, Fe(III)-S^t, Fe(II)S^t, Fe(II)-S^t and Fe(II)-S^b, the assignment and

properties was compared to the theoretical calculations and experimental approach of the studies of Yachandra *et al.*[359], Moulis *et al.* [270], Han *et al.*[12, 361] and Staples *et al.*[372].

The Ag Fe-Fe modes. Comparatively, the band corresponding to the Ag Fe-Fe vibration (210-220 cm^{-1}) (Figure 4.3-27), in the spectrum of the reduced NuoEF-V136M (Figure 4.3-27.B), goes to higher wavenumber. However, for NuoEF-V90P, in both reduced samples, the band shifts towards lower frequencies, where the effect is more pronounced in presence of NADH arising at 210 cm^{-1} (Figure 4.3-27.C). For NuoEF-V90P/V136M, the spectrum in the reduced form with NADH, this band presents a slight shift to lower frequency, from 216 cm^{-1} to 212 cm^{-1}, whereas in presence of dithionite no displacements are observed.

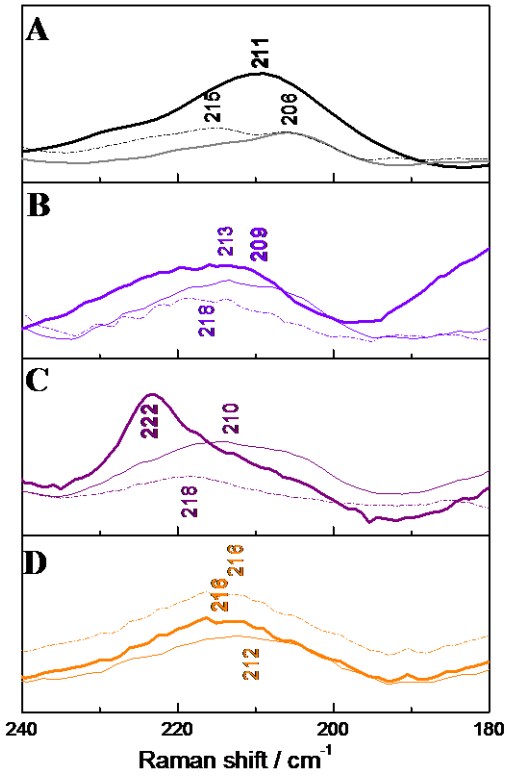

Figure 4.3-27. Comparison of band corresponding to the Ag Fe-Fe mode in the oxidized state (bold line) and in the reduced state with NADH (solid line) and with dithionite (dotted line) of NuoEF-WT(A), NuoEF-V136M(B), NuoEF-V90P(C) and NuoEF-V90P/V136M (D).

In NuoEF-WT (see section 4.3.4.1), the reduction with NADH slightly affects the frequency of the signal, going from 211 to 206 cm^{-1} (Figure 4.3-27), but the shape of the band changes and it loses intensity upon reduction and becomes broader. In comparison, each one of the mutants presents a particular behavior. As explained above (section 4.3.4.1) a lower frequency of this vibrational mode implies less Fe-Fe interaction; implying

lower energy of the vibration itself[12]. This is the case of the NuoEF-V90P, whereas for the NuoEF-V136M the opposite can be suggested.

With dithionite, a stronger reducing agent, a higher interaction between the Fe atoms is seen on the NuoEF-V136M mutation, this might indicate that in presence of NADH the cluster it is partially reduced whereas with dithionite a complete reduction of the cluster is achieved.

Additionally, what is intriguing is that in the case of the NuoEF-V90P/V136M in presence of dithionite, Ag Fe-Fe the vibration does not present changes and for NuoEF-V90P the displacement of the signal is smaller than in the reduced state with NADH. An explanation might be that as in the oxidized state NuoEF-V90P/V136M, the frequency and shape of the signal suggested that the Fe orbitals are overlapped; in presence of a strong reduced agent as dithionite no electron transfer is observed.

The ν(Fe-S)^b modes. For the bridging modes, a general shift to higher wavenumbers is observed in all the samples. The B_2 mode (245-265 cm^{-1}) (see Figure 4.3-28) from ~243 cm^{-1} in the oxidized state of NuoEF-V136M and NuoEF-V90P it arise at ~258 cm^{-1} in all the reduced samples. The increase in intensity and the shift of the band to higher frequency indicate a major contribution of Fe(II)-S^b modes.

It is important to remark that in NuoEF-V90P/V136M this band is not observed, this indicates that the double mutation changes the characteristics of the cluster, for instance the symmetry of the cluster, where a C_{2h} symmetry may no longer describe the properties of the metal-ligand vibrations. As it was observed during the experiment, from the three samples, this mutant was the most photosensitive, it might be that damage in the protein due to the laser exposure affected the enhancement of the metal-ligand vibrations.

The A_1 mode, ~ 335 cm^{-1}, in the reduced state with NADH presents a slight shift to higher wavenumbers, whereas in the reduced state with dithionite the signal presents a decrease in the intensity. This mode does not present contribution from the Fe(II)-S^b, the loss of the signal indicates a complete reduction of the cluster. This indicates that in presence of NADH, only the protein in only partially reduced.

The B_{2u} modes of NuoEF-V136M were similar to the NuoEF-WT in the oxidized state, upon reduction the bands have a shift to higher wavenumbers, arising at 408 and 420

cm^{-1} for NuoEF-V136M spectra, a similar pattern is observed in the reduced spectra of NuoEF-V90P. These vibrations arise from the motion of the S^b atoms pointing to one direction and the Fe atom toward the opposite direction, the splitting of the signal points out that ~~of~~ each set of Fe-S has a different orientation upon reduction. While lower frequencies are associated with Fe(II)-S^b and higher with Fe(III)-S^b[12, 356].

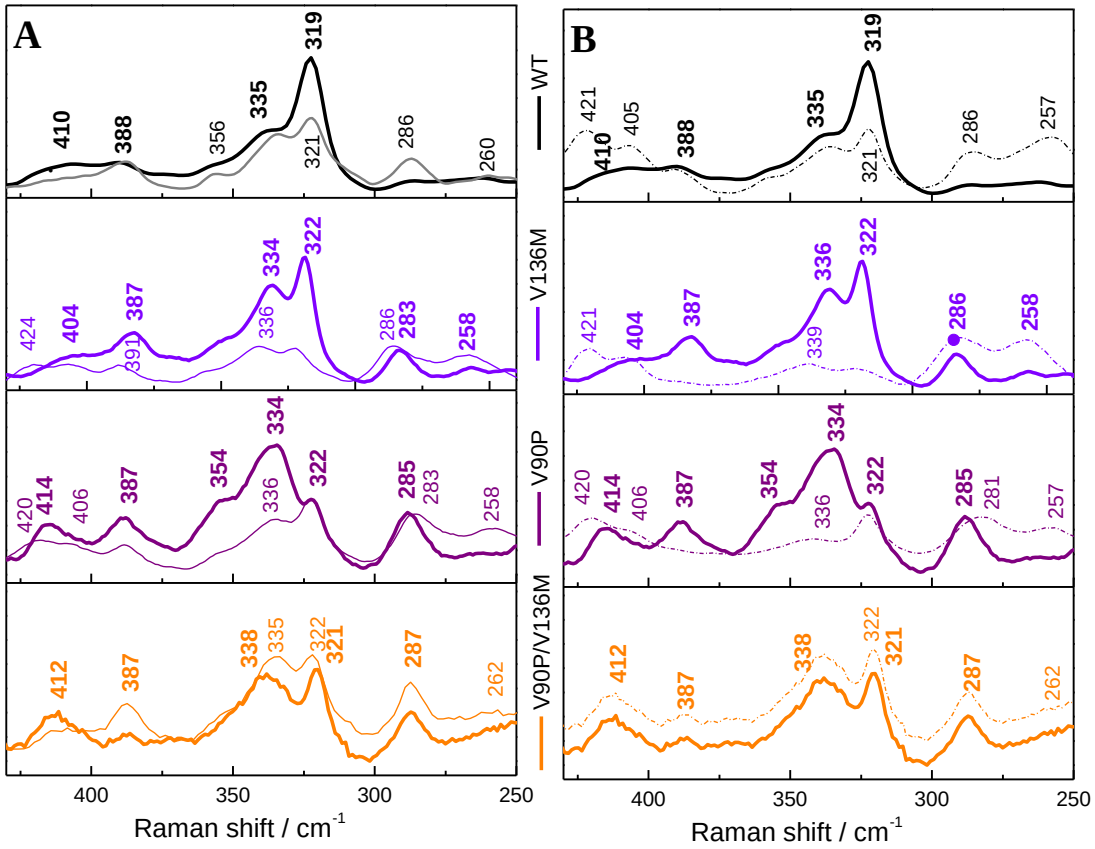

Figure 4.3-28. Contribution from the ν(Fe-S)b and the ν(Fe-S)^t modes of NuoEF variants in their reduced state with A. NADH and B. dithionite. The bolded lines in each spectrum correspond to the oxidized state.

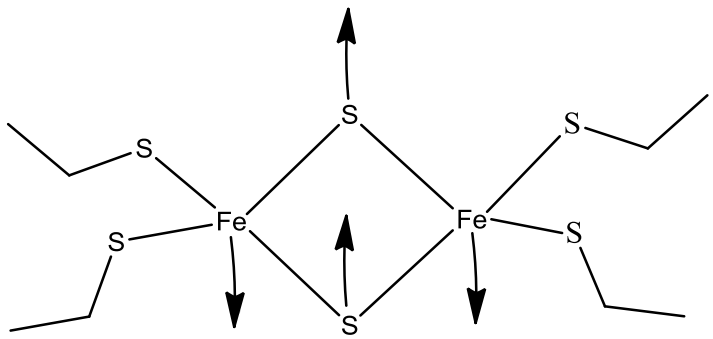

Figure 4.3-29. Eigenvector for the normal mode of B_{2u} ν(Fe-S)^b. Adapted from Han et al[12].

The v(Fe-S)^t modes. The B_{3u} modes of in all the samples have their corresponding symmetric component (~287 cm^{-1}). The first component has increased in the intensity upon reduction, whereas the second has decreased (see Figure 4.3-28). An increase of intensity to the symmetric component is associated with modes primarily involving v(Fe(II)-S)^t [223] this indicates that at least one of the two Fe atoms in reduced. These changes are more visible in the reduced NuoEF-V136M spectrum than in the reduced NuoEF-V90P, whereas in the reduced NuoEF-V90P/V136M no changes are observed.

The B_{1g} v(Fe(III)-S)^t mode, ~319 cm^{-1}, is a useful indicator of the conformation and hydrogen bonding interaction of the cysteinyl residues ligating the localized valence of the Fe(III) site. Hydrogen bonding to a metal-coordinated S ligand usually results in a decrease of intensity, as they reflect differences in the Fe-S^t-C-C dihedral angles of the coordinated cysteines. It is evident that in NuoEF-V136M and NuoEF-WT a decrease of the intensity is observed, this effect if even more prominent in the second, indicating a stronger hydrogen bonding upon reduction. Furthermore, for the reduced NuoEF-V90P, the shift to higher frequency points toward an increase in the energy of the bond. This suggested that as general rule that the Fe (III)-S bonds strength varies as a result of protein conformational difference.

The bending motions. Above 420 cm^{-1} change in the bending motions are represented by three bands (Figure 4.3-30), whereas only one of them was observed in the oxidized state (~485 cm^{-1}). This band corresponds to the coupled vibration of Fe-S-C + A_1 overtone (Table 4.3-7). Upon reduction for NuoEF-V136M, this band presents a higher enhancement and a slight shift to higher frequencies, indicating a wider dihedral angle[223]. Nevertheless, in the reduced NuoEF-V90P spectra the opposite is observed, the band decrease in intensity and no significant changes in the frequency are observed.

Furthermore, upon reduction two other bands appear or gain enhancement. The first, arising at 467 cm^{-1} and 472 cm^{-1} in the reduced spectra of NuoEF-V136M corresponds to the C_α-C_β-N modes from the N3 cluster, as for NuoEF-V90P, a similar pattern is observed of the for the reduce NuoEF-WT. The second band arises at 455 cm^{-1} both reduced spectra of NuoEF-V136M and NuoEF-V90P, where in the first the enhancement is higher. This band can be assigned to the C_α-C_β-N modes of N1a. The C_α-C_β-N modes of [2Fe-2S] are only enhanced when the Fe-S^t-C-C dihedral angle is higher or equal to 190^0, this can be caused by changes in the force constant of the cysteinyl coordination. Typically, changes in

the dihedral angles are the cause of the pattern observed in the displacement of the bridging vibrational modes, as the ones observed before.

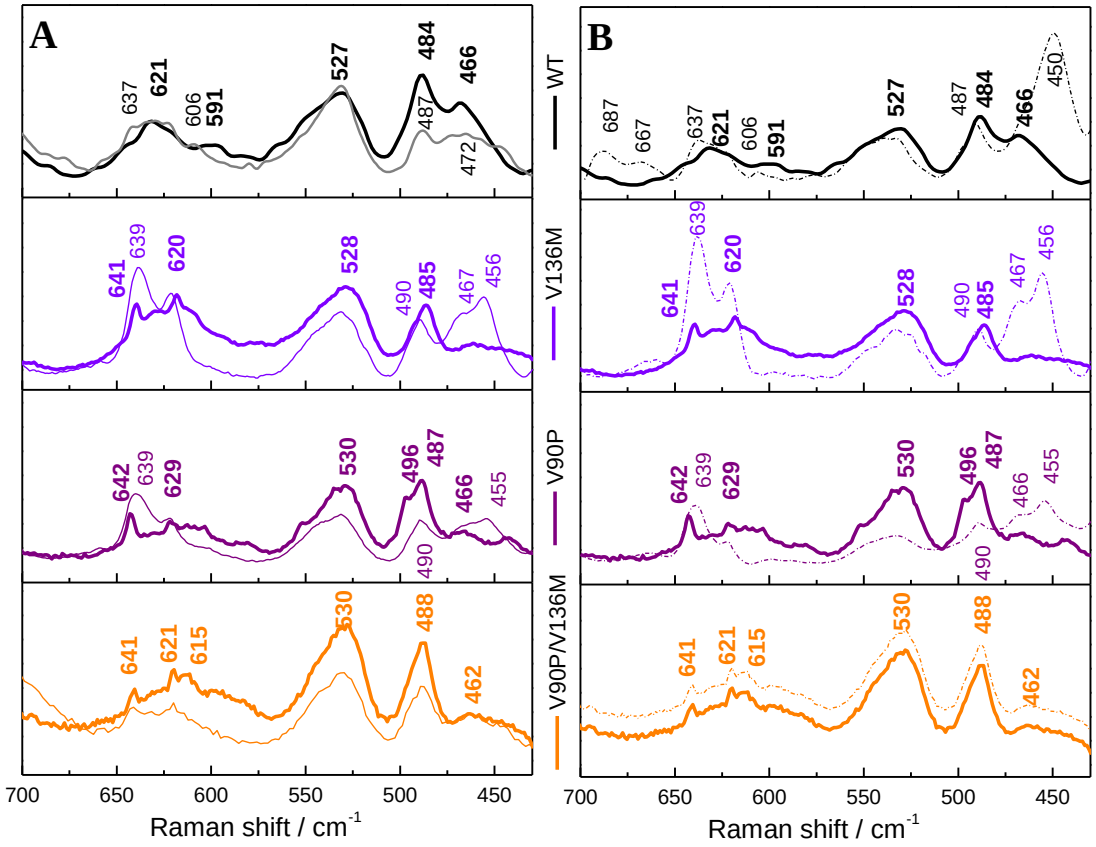

Figure 4.3-30. ν(C-S) stretching and bending motions of of NuoEF variants in their reduced state with A. NADH and B. dithionite. The bolded lines in each spectrum correspond to the oxidized state.

It seems that the ability of the N1a cluster to be reduced has to do with the ability of Cys to change coordination where the interaction between the cluster motif and the metal center exerts a constant force making the dihedral angle higher than 180^0. However it is very unlikely that the four Fe-S-C-C dihedral angles change uniformly from one state to the other, the V90P gives the idea which that the Cys residues which changes are Cys87 and Cys91 (Figure 4.3-21) in Loop 1 (Figure 4.3-20).

The C-S stretching. Above 600 cm^{-1} the two bands corresponding to the C-S stretching modes present a higher enhancement in comparison to the bands observed in the oxidized state, these bands are observed at ~622 and 640 cm^{-1}. This behavior is observed for the reduced spectra of NuoEF-V136M and NuoEF-V90P, as well as it was for the NuoEF-WT. Nevertheless in the reduction with dithionite in both spectra a new signal is observed ~667 cm^{-1}. This signal indicates that one of the Cys residues upon reduction

presents a different coordination from the rest. This leads to deduce that the reduction with dithionite has further effects on the coordination than what is observed with NADH. It is important to recall that this vibrational modes are a combination of the [2Fe-2S] and [4Fe-4S], so the contribution of N1a from N3 cannot be distinguished.

Amino acid side chains contribution. Following the observed pattern in the metal-ligand vibrations the spectra of the reduced state of NuoEF-V90P/V136M (Figure 4.3-31) do not present any changes in comparison to the oxidized form.

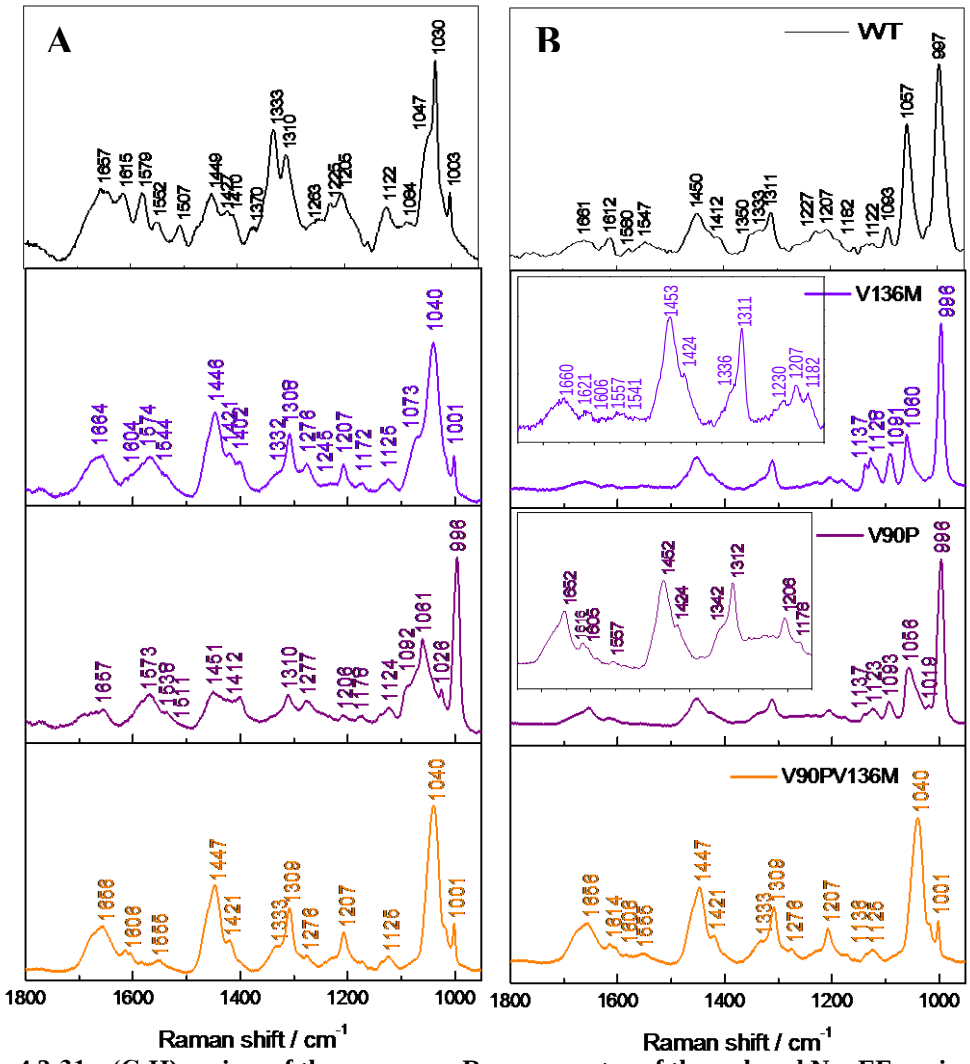

Figure 4.3-31. ν(C-H) region of the resonance Raman spectra of the reduced NuoEF variants with A. NADH and B. dithionite

Nevertheless, for the other two mutants, the δ(ring) mode of Phe shows an important perturbation upon reduction, in the case of reduced NuoEF-V136M with NADH no changes are observed but in the reduced form with dithionite the signal gains intensity and arises at

996 cm^{-1}. A similar behavior is observed in the spectra of both reduced NuoEF V90P for the band corresponding to this vibrational mode.

The other signal corresponding to the δ(C-H) modes of Phe, seems perturbed only in the reduced NuoEF-V90P, where it shows an upshift (from 1171 cm^{-1} to 1178 cm^{-1}). This indicates that in the NuoEF-V90P not only motions of the side chain are observed but also changes in the dihedral angle.

The Thr contribution from the OH-def motions, does not present any changes in the reduced NuoEF-V136M but in the reduced form with dithionite it appears at higher frequencies arising at 1060 cm^{-1} (oxidized: 1039 cm^{-1}), for NuoEF-V90P in both reduced spectra the signal arises as well ~1060 cm^{-1}.

The Cys δ(Cα-H) modes also present a displacement. A similar pattern is seen for the reduced NuoEF-V136M. With NADH no changes are observed but with dithionite the signal arises at higher frequencies, appearing at 1424 cm^{-1}. For the reduced NuoEF-V90P the changes display a different behavior, where in presence of NADH the signal is at 1412 cm^{-1} whereas with dithionite it arises at 1424 cm^{-1}. This points towards a difference in the dihedral angle upon reduction, where in the case of NADH the Cys residues have a tendency to have wider angles with dithionite the dihedral angles, becomes narrower.

Amide vibrations. Changes in the α-helix component of Amide III are observed in all the samples, this signal loses intensity whereas the β-strand component gains intensity in comparison to the oxidized state. Amide II also gains enhancement upon reduction, whereas amide I loses intensity. Changes in the amide vibrations may be related to the conformational changes around the clusters. In general, upon reduction the Fe-S clusters have a tendency to have a more rigid structure. If this is case, changes in the symmetry and furthermore in the polarizability are expected.

The ν(C-H) modes. In the reduced state two vibrations are arising in comparison to the spectra of the oxidized state. In the reduced spectra with NADH, the signals at 2736 cm^{-1} and 2790 cm^{-1} in NuoEF-V136M and NuoEF-V90P are observed, corresponding to contribution of Met and His respectively; in the spectrum of NuoEF-V90P/V136M, at 2767 cm^{-1} and 2817 cm^{-1}, these signals correspond to the asymmetric stretching of His and Ile. Their arising might be due to the motions in the structure upon reduction, in this way these residues can be closer to the cluster and therefore their vibrational modes are enhanced.

In the reduced state with NADH, the contribution from the Met and His is seen at higher frequencies and with higher intensity for NuoEF-V136M and NuoEF-V90P, it appears at 2744 cm^{-1} for the first and at 2740 cm^{-1} for the second, been less intense in the latter one.

The signal at 2885 cm^{-1} in the NuoEF-V136M spectrum in the dithionite-reduced state corresponding to the His, Leu, Ile contribution present a displacement of 8 wavenumbers in comparison to the oxidized state. For the rest of the mutations no changes are seen in any of the reduced spectra.

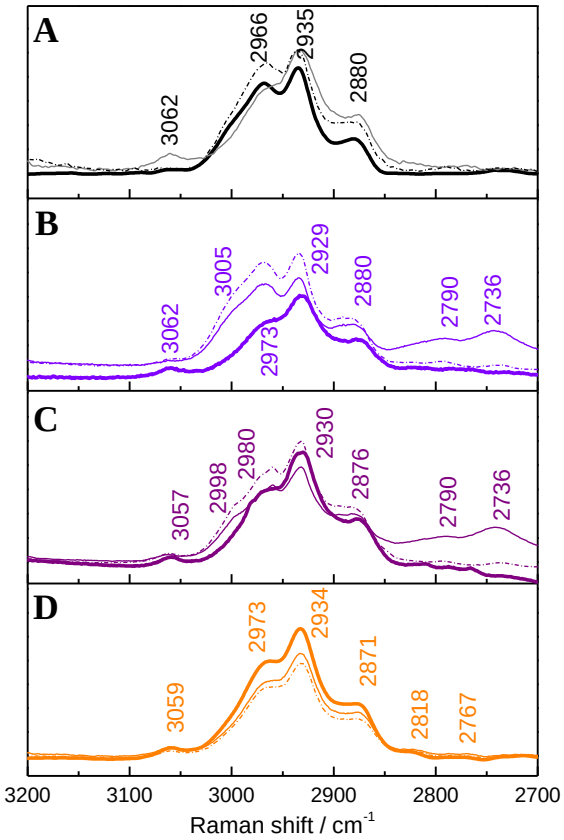

Figure 4.3-31. Contribution from the ν(C-H) modes of the oxidized (solid line) and reduced with NADH(grey line) and dithionite (dotted line) of NuoEF-WT(A), NuoEF-V136M (B), NuoEF-V90P(C) and NuoEF-V90P/V136M (D).

The band corresponding to the Cys, His and Ser symmetric stretching in the NuoEF-V136M reduced spectra with NADH is observed at 2969 cm^{-1} whereas in presence of dithionite the band arises at 2966 cm^{-1}. It is important to note that this band presents a negative displacement of around 6 to 9 wavenumbers, whereas in the oxidized state the signal was observed for this mutant at 2973 cm^{-1}. For the reduced NuoEF-V90P the signals are observed at 2970 cm^{-1} in the presence of NADH and at 2960 cm^{-1} with dithionite, while

in the oxidized state the signal was at 2980 cm^{-1}. For NuoEF-V90P/V136M the signal in the oxidized state was seen at 2973 cm^{-1} and in both reduced spectra is arises around the same frequency, at 2968 cm^{-1}.

A shoulder is evident in the reduced NuoEF-V136M and NuoEF-V90P that is not observed in the reduced state of the NuoEF-V90P/V136M nor in the oxidized state of any of them. With NADH the band arises at 3005 and 2998 cm^{-1} respectively and with dithionite at 2995 and 2999 cm^{-1}, respectively. This band is a contribution from the symmetric stretching of Thr and Pro residues.

In summary, it can be seen that in the case of NuoEF-V136 motions of the Cα-H groups of the Met, Ile, His, Cys, Ser, Thr and Pro are observed upon reduction, the effect is more pronounced in presence of dithionite, comparing to the frequencies observed in the oxidized state. A similar pattern is observed for NuoEF-V90P, whereas for the NuoEF-V90P/V136M motions are only evident from Cys, His and Ser residues upon reduction, in comparison, no difference in this perturbation is observed between the reduction with NADH or dithionite.

4.3.5.2 Conclusion

Within all the spectral characteristics, it seems that the changes in the redox midpoint potential are correlated to changes in the intramolecular hydrogen bonding network in the protein. These changes exert an effect of the terminal modes of the cluster, as the bands corresponding to the vibrations presented a displacement to higher frequency in NuoEF-V90P and NuoEF-V90P/V136M. This indicates a decrease in the bond strengths between the Cys residues and the metal center.

In the Fe-S cluster from the ferredoxin family, within the cluster motif there is usually an amino acid that forms a hydrogen bond with one of the Fe atom, e.g. N1b, where a Ser residue has a hydrogen bond with one of the Fe atoms (Figure 4.3-2.B). This allows the cluster to keep their structure “unchanged” upon reduction, even though the conformational changes happening in the close environment are considerable, the motions of the metal center behaves as an entire module. But when these Fe-H bonds are not present, the cluster depends on the hydrogen bonds formed by the side chains around the cluster within the structure, this

prompted that upon reduction the conformational changes perturbed or can disrupt the hydrogen bonds, having a new arrangement in each redox state.

Changes in residues in the Loop 1 and the CT-β region form a part of the extended hydrogen bonding that maintain the stability N1a. As observed in RR results, changes in this hydrogen bonding have as consequence an overlapping of the Fe orbitals and displacement of the dihedral angles of the Cys residues coordinating the metal center. As can be seen in Figure 4.3-32) these differences in bond length and strength may be the cause why for example neither in the NuoEFV90P/V136M the cluster cannot be reduced, nor in presence of NADH or with dithionite.

Besides, it seems that the mutations also exert an effect on the Thr, Phe and Cys residues upon reduction. Many of these residues form part of the second sphere of coordination of the cluster; in the WT no motions are observed in these residues upon reduction, indicating that these residues are a structural support for the proper electron transfer.

In the case of N1a, it is possible to relate the pH-dependency of its midpoint potential to changes in the hydrogen bonding, the lower the energy of the hydrogen bonding the more positive the potential.

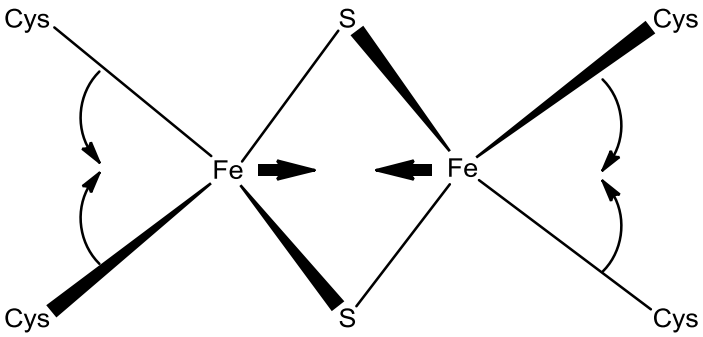

Figure 4.3-32. Schematic representation of the changes in bond strength and length due to the mutations around the N1a cluster motif.

It had been discussed in many studies that the Fe-S cluster N1a, is not directly involved in the electron transfer to the quinone and acts as an antioxidant to prevent the formation of ROS[447]. According to the obtained results, it can be concluded that the N1a cluster motif not only acts a regulator of the cluster but also exerts an influence in the geometry of the cluster itself. By homology with the function of other thioredoxin-like

proteins[363], it seems that the vicinity of the loops and the [2Fe-2S] clusters, together with the demonstrated versatility of the polypeptide chain in that region[6] may then suggest the possibility of a redox switch regulation[448-450]. Further studies of the mutation at different pH in their reduced and oxidized state are recommended as next steps, besides calculations of the electron transfer rate are suggested to clarify how much these residues can regulate the function of the cluster.

4.3.5.3 Studies on NuoB variations in *E. coli*

In the NuoB, the subunit that bears the N2 cluster, many residues are conserved among several species, an example can be seen in the alignment of five different sequences shown in Figure 4.3-33. According to what was proposed by Flemming *et al*[1] , if N2 participates in proton pumping, its redox reaction probably is coupled to a protonation/deprotonation of the cluster itself and/or of surrounding amino acids. There are six main residues that call the attention according to what was reported in previous studies, Glu67, Asp77 Asp94, Tyr114, Tyr139 and Tyr154.

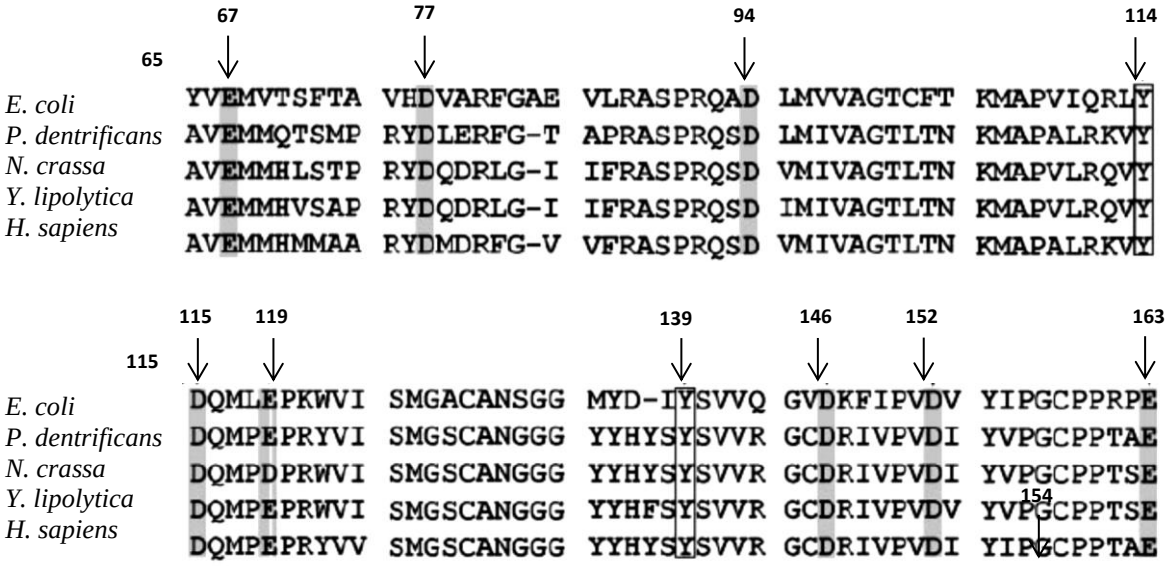

Figure 4.3-33. Alignment of the homologues of NuoB from different species [1]. The positions are numbered according to the *E. coli* sequence. The conserved amino acid of interest are highlighted.

Figure 4.3-34 shows their position according to the structure from *T. themophilus*[183], the only one that it was not possible to locate is Glu67, due to the limitation in the resolution of the available structure. In this study the aim was to compare the results obtained by EPR

and FTIR in the MIR range to the metal ligand vibrations coming from the N2 cluster by RR spectroscopy.

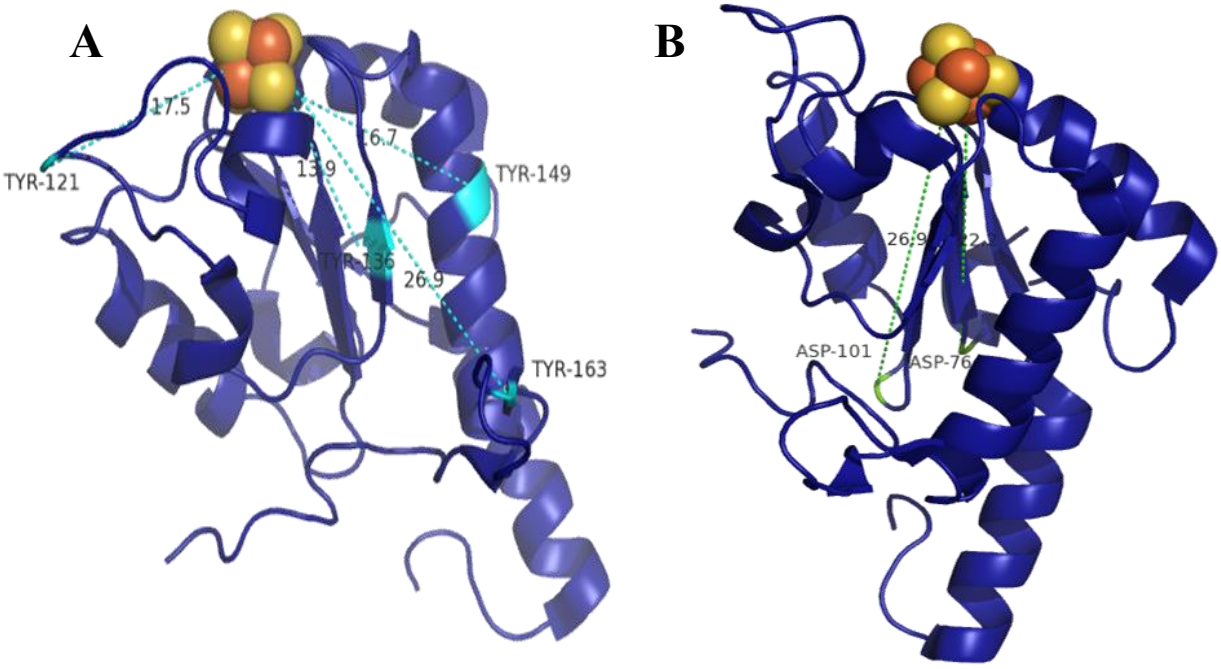

Figure 4.3-34. Schematic representation of Nqo4 (NuoB) subunit from *T. thermophilus.* N2 cluster is represent in spheres (Fe: orange/S: yellow) and the key residues mutated are higlited in cyan (Tyr) and green (Asp).

The spectra of the oxidized state of the mutant E67Q and E67D is presented in Figure 4.3-35, in Figure 4.3-36 the spectra of D77N and D94N mutations are shown and in Figure 4.3-37 are the spectra of the Tyr variations (Y139C, Y154H and Y114H/Y139C).

In the low frequency region, corresponding to the metal ligand vibrations is important to remark that all of the mutations have an effect on the fundamental Fe-S stretching of the Fe-S(Cys) vibrational modes of the N2 cluster previously assigned to the signal at 340 cm^{-1} (see section 4.3.2), the only exception is the E67D variation.

It was described that this variation does not exert any effect on complex I activity, unlike E67Q, D77N and D94N were the electron transfer activity was completely abolished[1]. For the mutation of the Tyr residues, only with the double mutant, Y114H/Y139C the enzymatic activity was reduced in 80% compare to the WT strain[229].

In the variants E67Q, D77N and D94N the signal showed a tendency to arise at higher frequencies. The major displacements of this vibrational mode are seen in the D77N and D94N mutations, where the signals arise at 352 and 356 cm^{-1}, respectively; furthermore the

intensity of the signal had decreased compare to the wild type, indicating not only that the mutation have a direct influence in bond length but also in the enhancement of the vibration. This is surprising as these residues are the furthest from the cluster.

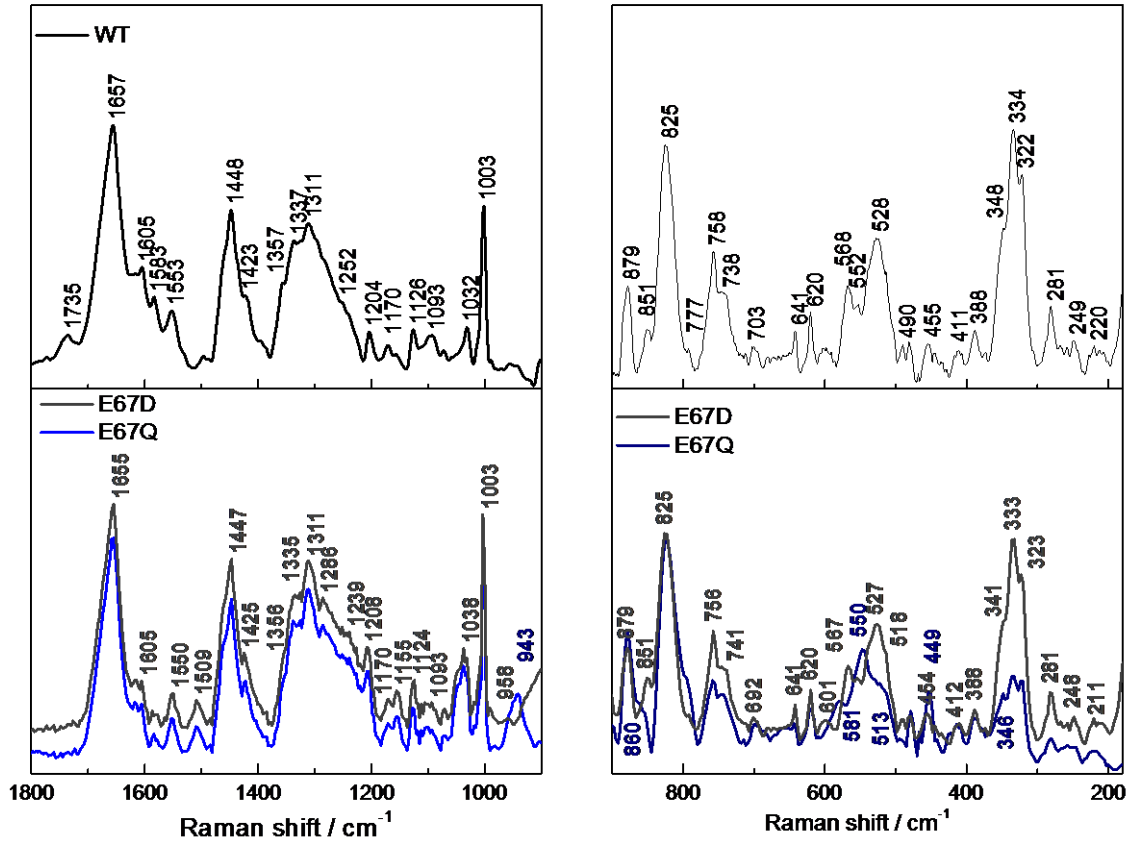

Figure 4.3-35. RR spectra of complex I WT and complex I/ NuoB variations of the E67 residue into Asp (E67D- grey line) and Gln (E67Q-blue line)

As can be seen in Figure 4.3-34, the distance between this residues and the N2 cluster is more than 22 Å. The closest Cys residue from the cluster motif is Cys 46 (~22.3 Å). Changes in the Cys modes could be correlated to motions of this specific residue, nevertheless is not clear how from such a distance any influence might be exerted.

Abnormally high frequencies (above 336 cm^{-1}), as is case of N2, for this totally symmetric terminal vibration had been described to be a characteristic of $[4Fe\text{-}4S]^{+2}$ clusters that are site differentiated via their terminal ligation in only an specific Fe atom, this gives the idea that the mutation have a direct effect in the dihedral angle of only one of the Cys residues [451]. This indicated that the different mutations are affecting a singular Cys residue and its ligation.

Additionally, as can be seen in Figure 4.3-36, changes in the Fe-S overtones related to the Fe-S-Fe modes coupled to bridging vibrations are affected by the D77N and the D94N mutation, for both proteins the signal arise at 580 cm^{-1}, instead of 568 cm^{-1} as it was seen in the wild type. The same signals are observed for the E67Q and E67D spectra, but in this case the signals are at 581 cm^{-1} and 601 cm^{-1} respectively. It seems that the lower the frequency of this mode more affected, is related to the stability of the protein.

Shifts in the ν(C-S) more are also observed, a new signal appears at 670 cm^{-1}, for D77N and D94N, at 689 cm^{-1} for E67D and 692 cm^{-1} for E67Q, indicating a new C-S conformation between the clusters.

Besides this, the signal corresponding to the cysteinate group is also shift to lower frequencies, appearing at 751 cm^{-1}, only in the case of the D77N and D94N mutations. This vibrations was assigned before to the cysteinate group of the clusters present in the quinone fragment (see section 4.3.2), N6a, N6b and N2. It is sure that it can only correspond to the N2 cluster. The displacement of the signal to a lower frequency indicates a rigid cluster ligation[12]
.

By EPR, the spectral position and line with of the signals of the N2 cluster remained unchanged in the D77N mutant, nevertheless their Fe-S vibrations showed that the cluster motif is perturbed; this effect is even more pronounced in the D94N mutant. In previous studies the D94N mutation, was not stable enough to perform EPR or difference FTIR analyses; comparing D77N and D94N spectra is evident that the main difference between them is the arrangement of the Fe-S(Cys) terminal modes of N2 are the same can be said for E67Q.

By difference FTIR an effect in the Tyr residues around N2 was observed due the D77N and E67Q mutations. Above 800 cm^{-1}, the Fermi doublet corresponding to the ν_{16a} and ν_1 modes from Tyr, present some displacement. Specifically in the ν_1 corresponding to the ring bending mode. The signal arises at 855 cm^{-1} for D77N, at 860 cm^{-1} for D94N and E67Q. A higher frequency of this mode is related to a weaker hydrogen bonding. Furthermore, the intensity ratio between the two signals ($I\nu_{16a}/I_{\nu 1}$) for D77N and E67Q is 0.2, as well as for D94N 0.1, comparing to the WT ($I\nu_{16a}/I_{\nu 1}$:0.3). It can be summarized that in the case of D94N some of the "buried" tyrosines that were strongly hydrogen-bonded in the interior of the protein are now exposed.

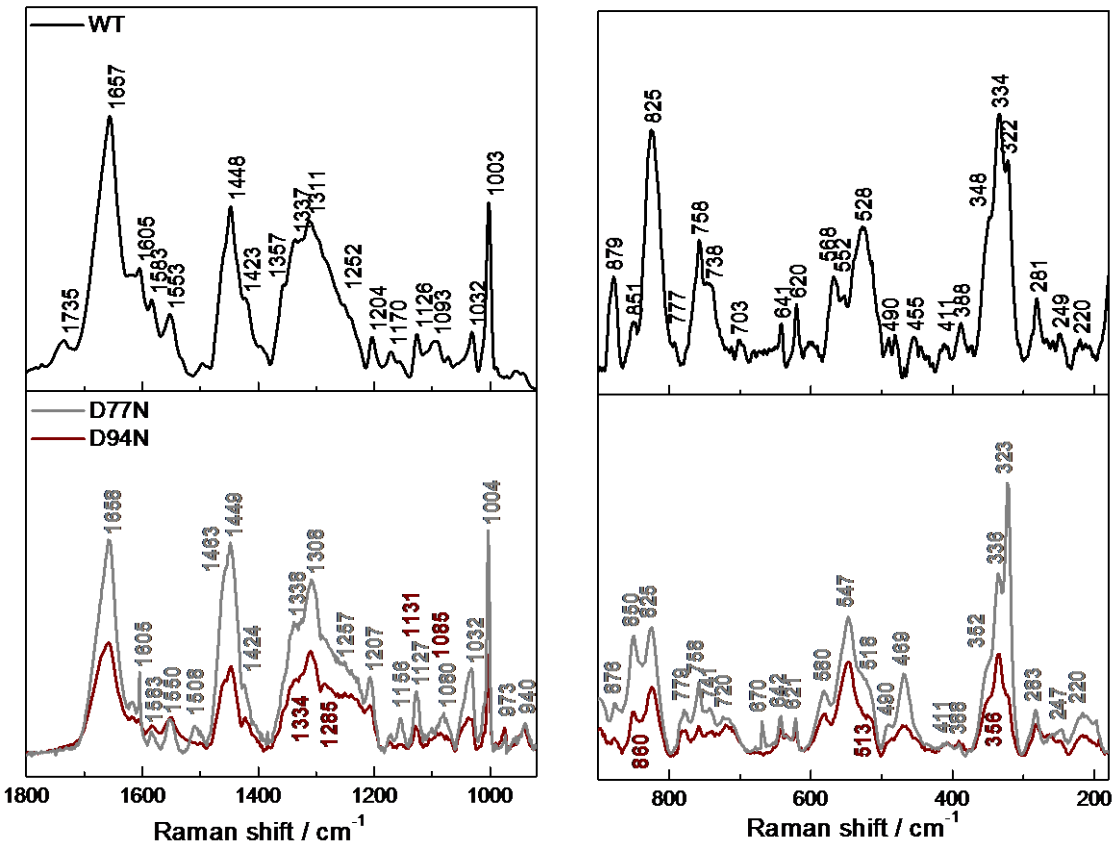

Figure 4.3-36. RR spectra from NuoB variations of the Asp77 (D77N) and Asp94(D94N) residues

The ν(C-H) (see Table 4.3-9) corresponding to the Tyr, Phe and Trp contribution also present a shift, where in the WT the signal is at 3058 cm^{-1}, for D77N is at 3060 cm^{-1} , at 3062 cm^{-1} for E67Q and in the D94N spectrum is at 3064 cm^{-1}, corroborating that in the mutants the position of these residues is perturbed. In this region, also the vibrational modes of Met are affected for these three mutations.

In summary, a comparison of E67D and E67Q spectra (Figure 4.3-35) against the WT spectrum of complex I (Figure 4.3-5.A), the mutation E67Q reveals several spectral differences, while E67D spectrum is almost the same as the wild type.

For the E67D the only differences arose in the ν(C-H) region above 2700 cm^{-1} (see Table 4.3-9), where the contribution from the Met, Trp and Tyr are perturbed. It was proposed before that mutation of the Glu67 can change the p_{Ka} of the side chain. As the mutation E67D conserves the characteristic of an acidic chain, the mutation does not exert major changes in the complex I structure; nevertheless there is a change in the enhancement of certain metal ligand vibrations. On the other hand, E67D, being charged amino acid, not only having an effect of the cluster structure but also in the activity of the protein, it seems that changes in the

hydrogen bonding next to the loops that the cluster motif shapes it can have a relevant modification in their mid-point potential as it was proposed by Flemming *et al*[1].

For the variants of the Tyr residues, as it was described before, changes in the Fe-S terminal bridging modes are seen, in the single mutants the displacement of the signal is more pronounced, arising at 349 cm^{-1} for Y193C and Y154H and at 345 cm^{-1} for Y114H/Y139C.

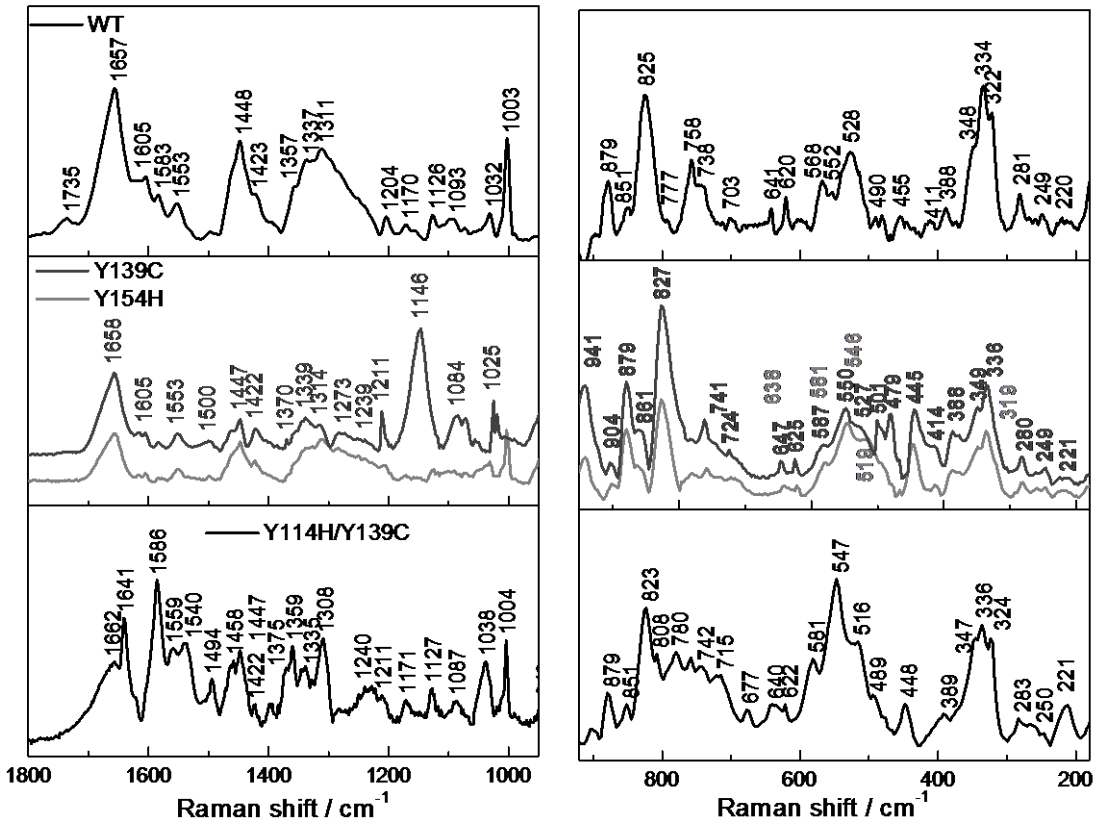

Figure 4.3-37. RR spectra of the NuoB variations of the Tyr139 (Y139C), Tyr154 (Y1524H) and the double mutant Tyr114/Tyr139 (Y114H/Y139C).

Another overtone (T_2 Bridging + Fe-S-Fe) is also shifted, for Y154H and Y114H /Y139C the signal arises at 581 cm^{-1} and for Y154H at 587 cm^{-1}. In the mutations of the Glu67, Asp77 and Asp94 a similar signal is observed, which was not present in complex I and the QRF spectra; this means that the mutation gives rise to a different conformation of the N2 cluster.

The differences in the ν(C-S) modes between the three mutations a better light on their effect in the N2 cluster. In case of Y139C and Y154H the ν(C-S) arises at 628 cm^{-1} and 638 cm^{-1}, respectively, while no major change of this vibration is seen in the double mutant. Instead, the cysteinate group vibration in the single mutant arises at 724 cm^{-1} and for the

double mutant it appears at 715 cm^{-1}, pointing that in the different mutations the effect in the cluster motif is due the relation between the Fe atom an their Cys ligands and in the case of the double mutant the main perturbation has to do with orientation of the Cys ligand respect to the structure of the protein.

Table 4.3-9. ν(C-H) region of the RR spectra of complex I and the mutations in the NuoB subunit.

Modes		WT	E67D	E67Q	D77N	D94N	Y139C	Y154H	Y114H/ Y139C
ν (C-H)	Met	2838	2843	2825	--	--	2841	--	--
	Gly, Asp, Glu	2857	--	--	2855	2860	--	--	
	His	2869	**2871**	**2871**	**2868**	**2873**	**2868**	**2868**	**2876**
	Leu, Lys, Ile, Val	2887	2881	2881	--	--	2880	2880	--
	Thr, Pro	--	2922	2922	2925	2920	2924	2924	2921
	Ile, Ser	2933	2934	2934	**2937**	2937	2934	2934	**2939**
	Cys, His, Ser, Leu,Trp, Gly, Lys	**2977**	**2965** **297**	**2965** **2978**	**2964**	**2969** **2981**	**2971**	**2978**	**2974**
	Tyr, Trp, Phe	**3062**	**3060**	**3060**	**3064**	**3060**	**3060**	**3060**	**3065**

In the E67Q, D77N and D94N changes in the Fermi doublet from Tyr was observed. A similar behavior is seen in the single mutations where the signal of the v1 mode arises at 861 cm^{-1}, indicating a weaker hydrogen bonding of the Tyr residues that were buried in the wild type. In the case of the double mutant no changes were observed. This gives the idea that the residues that change the status from buried to exposed due to the mutation in the Glu67, Asp77 and Asp94 might not as part of the NuoB subunit.

On the other hand, as it can be seen in Figure 4.3-34, where Tyr114 (in *E. coli* position) correspond to Tyr121, Tyr139 to Tyr136 and Tyr154 to Tyr149; Tyr114 is always close to the solvent, but Tyr139 and Tyr154 are "cover" by the surrounding subunits. When Tyr139 and Tyr154 are mutated separately, the perturbation is observed, but when Tyr114 is mutated the effect is no longer seen, adding that Tyr114 form a bridge between the Tyr residues affected in other subunit and the Tyr residues in NuoB, this bridge is made by Tyr139 and Tyr154, when one of them is no longer there the connection between the two subunits (or more) is missing.

This might be the reason why in previous studies of this mutation, NuoB of the *E. coli* complex I induce a protonation/deprotonation of specific tyrosine side chains according to Flemming *et al*[229]. It was shown that even though the single mutations did not alter the electron transport activity of complex I, the EPR signal of cluster N2 was slightly shifted. Nevertheless, FT-IR difference spectra of the double mutant revealed a complete loss the modes characteristic for protonation reactions of tyrosines. It was proposed that Tyr114 and Tyr139 in NuoB were protonated upon reduction of cluster N2 and were thus involved in the proton-transfer reaction coupled with its redox reaction.

4.3.5.4 Conclusion

In summary, previous studies have shown that Glu67, Asp77and Asp94 are essential for electron transfer. The role of Glu67 is most likely protonated by the oxidation of N2 and might be involved in the proton translocation. The analysis of the RR spectra in their oxidized state revealed that the mutations are able to affect the terminal ν(Fe-S) modes, changes in dihedral angle between the Fe-S-C on the Cys residues belonging to the cluster motif were proven and furthermore, perturbation in the hydrogen bonding of several Tyr residues, which one of them is Tyr154 and Tyr139.

4.3.6 Study of quinones in Complex I

Two quinone radicals have been detected during the catalytic turnover of complex I[295, 450, 451]. These radicals seem to be essential for the enzyme's mechanism; however, the molecular identity of these radicals remained unclear. It is known that complex I bears one binding site for a quinone located at the interface between the membrane and the soluble domains of the enzyme [183]. The presence of an additional, quinoid-type cofactor probably involved in quinone reduction, was previously suggested on the basis of UV/vis, EPR and FT-IR experiments[220, 243].

In previous studies, preparations of the mitochondrial complex I from *Neurospora crassa* and of the bacterial one from *E. coli* were spectroscopically analyzed under anaerobic conditions in various redox states. From UV/vis redox difference spectra signals were obtained that neither derived from the FMN nor from the EPR-detectable Fe/S clusters. The midpoint potential of this group in the *E. coli* complex I was determined to be approximately -150 mV at pH 6 and able to transfer two electrons (vs. SHE)[295].

The mechanism of quinone reduction is not fully known, as explained before (Section 1.4.2). The Fe/S clusters acts as one-electron donors and the ubiquinone (UQ) is a two-electron acceptor. A sequential reduction of the substrate by the most distal Fe/S cluster N2 would lead to the formation of a quinone radical. If not tightly bound by the protein, this radical might escape the complex and contribute to the production of ROS.

Here, the fluorescence emission of the complex I from *E. coli* was investigated as a function of oxidation-reduction state of the protein; the aim was to substantiate the presence of quinoid cofactors in the membrane arm of complex I. The excitation wavelength (λ_{ex}) was 295 nm (Trp contribution), 365 nm (FMN contribution) and 420 nm (other chromophores).

The spectra were recorded between potentials ranges, going from the fully oxidized state to the fully reduced state of the sample. In the case of complex I and NDF samples, the measurements were performed between 0 and -700mV (vs. Ag/AgCl), with steps of 20-30mV at the time, with an equilibration time of 10-30 min. At each potential applied a spectrum was taken with an integration time of 0.3s.

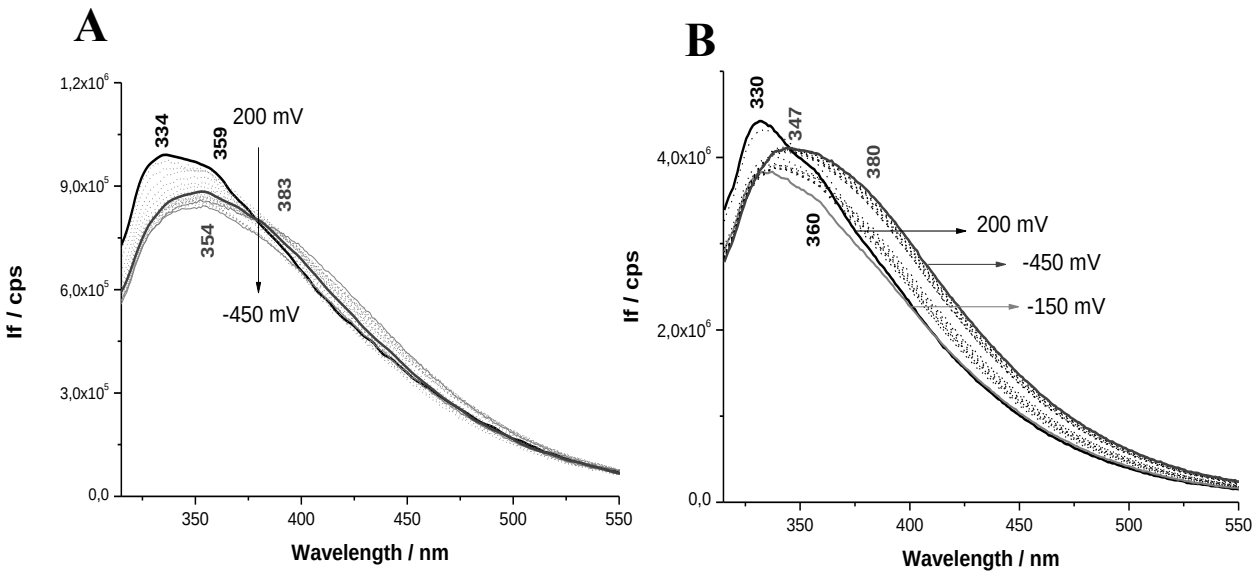

Figure 4.3-38. . Electrochemically controlled fluorescence emission spectra of A. complex I and B. NDF for the potential step from -450 to 200 mV (vs. SHE) λ_{ex}: 295 nm

The electrochemically controlled fluorescence emission spectra of complex I and of the soluble fragment were obtained in the potential range from –450 mV to 200 mV (vs. SHE), with a λex: 295nm (Figure 4.3-38). The complex I spectra in the oxidized state (black solid line Figure 4.3-38.A) showed two emission signal, one at 334 nm is characteristic of Trp residues buried in an hydrophobic environment and the second at 359 nm corresponds to the Trp residues exposed to the polar aqueous environment. The intensity and bandwidth of these signals showed that in both proteins there is a similar ratio of buried and exposed Trp residues. In the NDF spectra (Figure 4.3-38.B), these signals arose at 330 and 360 nm.

Upon reduction, in complex I, the spectra showed a decrease in fluorescence intensity and a red shift of the emission of about 20 nm of both signals (gray line), as Trp fluorescence is extremely sensitive to the environment, these changes indicate a further accessibility of the buried Trp residues. The signal arising at 383 nm, points toward to an unfolding process, where the exposed residues move to a more flexible structure.

In the case of NDF a similar red shift is seen in both signals, the difference is that upon reduction two steps can be described, the first until -150 mV (vs. SHE) where the fluorescence intensity decrease as in complex I, but no major shift in the frequency is detected; followed by an increase of the wavelength where the signal at 330 shift to 347 nm, and from 360 nm to 380 nm. In the first step a quenching of the signal can be suggested and in the second step, it

can be concluded that many of the buried Trp residues become exposed, and the protein adopts a more flexible structure, as observed for complex I.

Using an excitation of 365 nm (Figure 4.3-39), the fluorescence emission band specific for the flavin, can be seen in the signal at 442 nm and 532 nm for complex I and at 440 nm and 539 nm for the fragment. These bands decrease upon reduction and a slight blue shift as previously reported for other flavin carrier protein, which is associated with the bending motions of the isoalloxazine ring[452, 453]. No major changes in the frequency indicate that even in the reduced state the FMN remains in a stacked conformation[454].

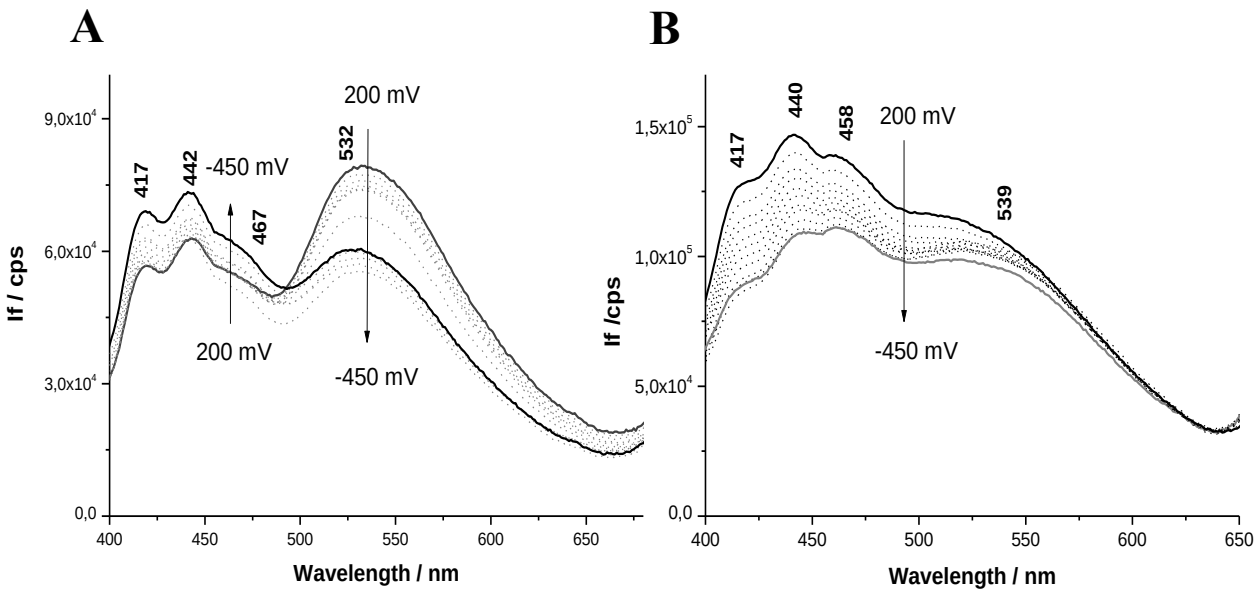

Figure 4.3-39. Electrochemically controlled fluorescence emission spectra of A. complex I and B. NDF for the potential step from -450 to 200 mV (vs. SHE) λ_{ex}: 365 nm

In the spectrum of complex I, a signal at 467 nm, not seen in the fragment's spectrum, shows the opposite behavior, where the fluorescence intensity increases with reduction of the enzyme. In a characterization study of Complex I from *Rhodothermus marinus*, an unidentified chromophore was depicted to have the same behavior. In that case, the signal was attributed to menaquinone. [228]

Furthermore, the spectra of complex I using an excitation of 420 nm are shown in Figure 4.3-40.A. The emission of the chromophore in question is involved in the large structure at 475 nm in the spectrum of complex I. The Nernst fit of the redox dependent intensity changes lead to three redox transitions. The potential at -337 mV (vs. SHE) corresponds to the midpoint potential of the FMN cofactor. This result is in line with previous

reports and confirms the reliability of the approach[443, 455]. Two additional transitions are observed at -37 and -235 mV (vs. SHE). In the fragment, this redox dependent change is not detectable and only the change of intensity corroborating with the flavin signal can be depicted. These redox transitions might indicate either the presence of two compounds with similar spectral properties or two distinct transitions of the same compound.

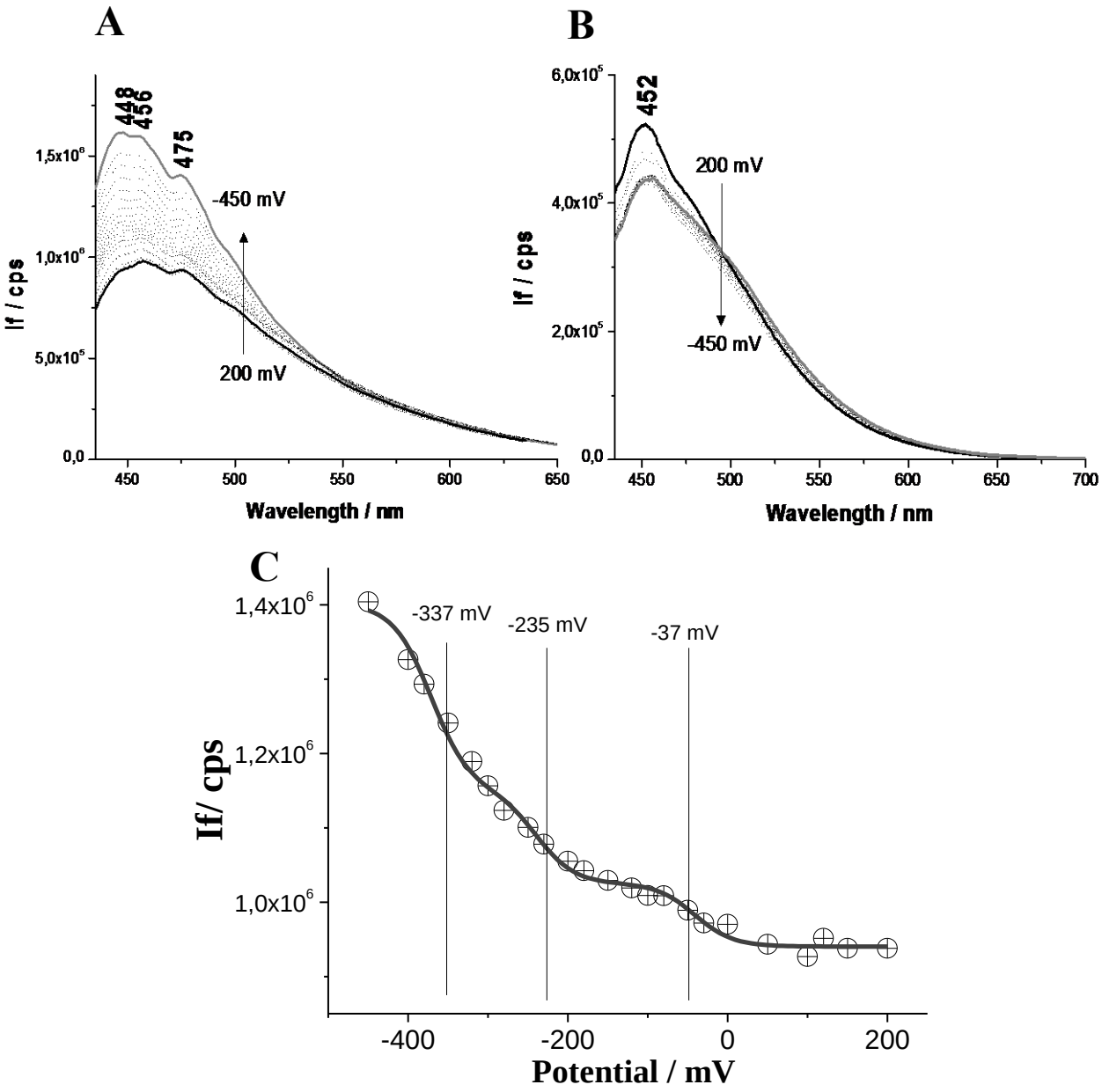

Figure 4.3-40. Electrochemically controlled fluorescence emission spectra of A. complex I and B. NDF for the potential step from -450 to 200 mV (vs. SHE) with ; λ_{ex} = 420 nm (C). Redox dependent changes monitored in the intensity of complex I spectrum at 475 nm.

As previously reported[220], complex I contains a NADH-reducible redox group with a midpoint potential above –100 mV (vs. SHE). Since the signals of the chromophores detected

in this study show an absorbance in the same spectral range to what is expected for quinones[228, 456], it can be proposed then that the redox transition previously reported is an average of the transition of the two transitions depicted in this study. Similar results were presented by the studies of Bauscher *et al*[457].

As model compound, UQ-10 was studied with the aim to confirm the attribution of the signals observed in the complex I spectra. Monitoring the reduction of UQ-10 in an environment with an aprotic solvent, CH_3CN, two individual electron-transfer reactions can be detected under these conditions, including the formation of the protonated radical[457].

.

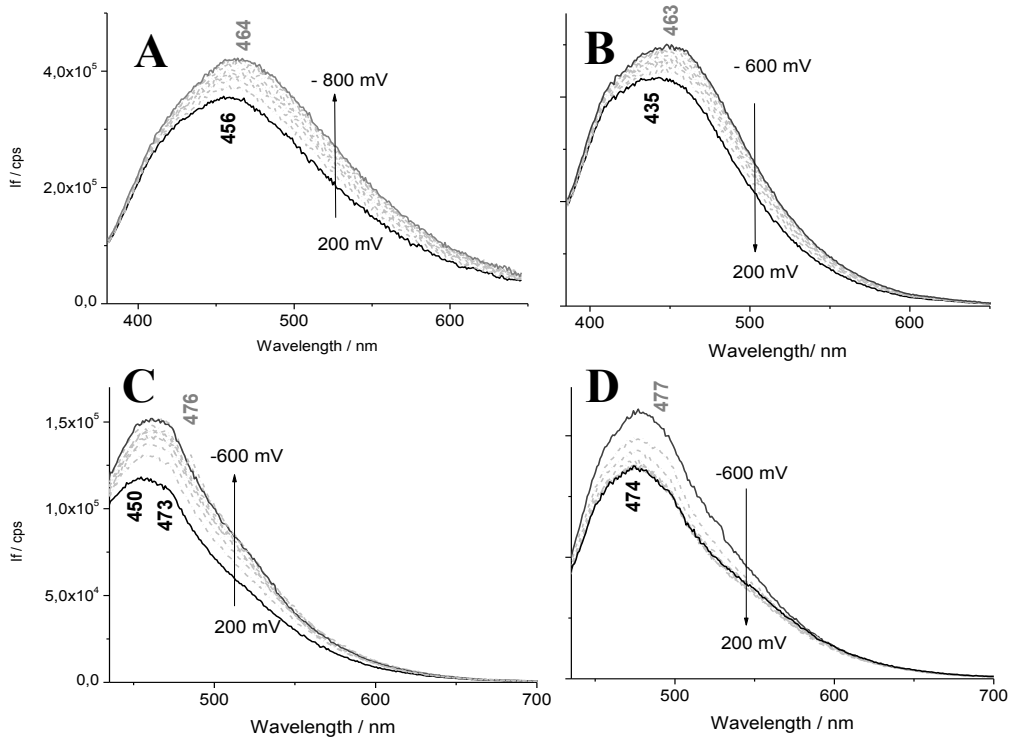

Figure 4.3-41. Electrochemically controlled fluorescence emission spectra of ubiquinone-10 in CH_3CN for the potential step from -450 to 200 mV (vs. SHE) The fluorescence emission obtained for A. λex: 365 nm at B. 456 nm and for C. λex : 420 nm at D.476 nm

In general, quinoid compound and their homologs had been widely studies by fluorescence. The characterization of their redox function in many cellular processes as electron shuttles and pigments had been described in many studies[458-460]. The transitions associated with fluorescence, they are characterized by an intense absorption at 250-300 nm and an emission 400-500 nm. Their reduction is generally accompanied by an increase of intensity that reflects the π - π* transitions[461]

The fluorescence emission obtained for λ_{ex}: 365 nm at 456 nm and for λ_{ex} : 420 nm at 476 nm (Figure 4.3-41.A-D) clearly correspond to the signals seen in complex I, and have the same behavior upon reduction, the increased of the intensity may thus correspond to the π - π^* transitions due to the reduction process [462].

4.3.6.1 Conclusion

In summary, it can be suggested that the signals seen in the fluorescence spectra of complex I, arise from quinoid cofactors, typically the presence of this kind of cofactors derives from post translational modifications of amino acids [463]. However, mass spectrometric analysis of bovine heart complex I subunits revealed no evidence for such post-translational modifications [464]. Nevertheless, with the observation that ubiquinone in an aprotic solvent shows comparable signals to the one detected in complex I, it can be conclude that the redox transitions described here derive from intermediates of the electron transfer involving two protonated ubiquinone radical species.

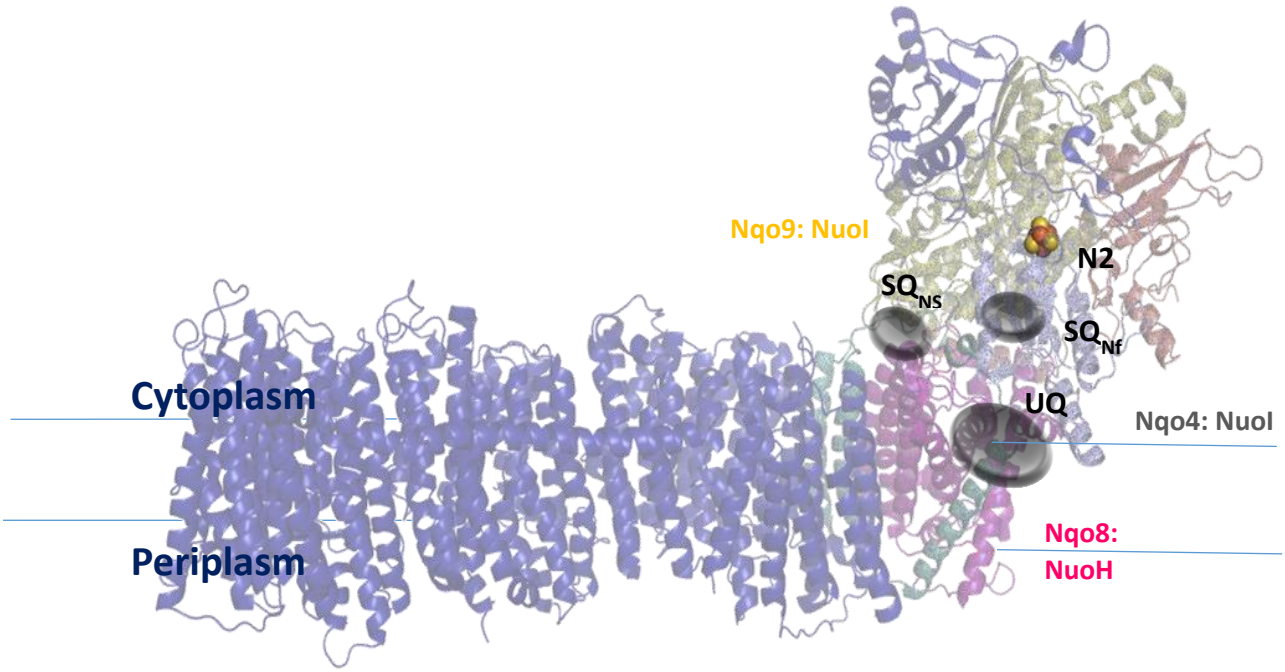

Figure 4.3-42. Schematic representation of the quinone reductase fragment of Complex I of *T. thermophilus*. (PDB:4HEA)

Based on structural data the presence of one ubiquinone binding-site was reported for complex I[183]. On the other hand, two quinone radicals were described by EPR spectroscopy, named as SQ_{Nf} and SQ_{Ns}, for **f**aster and **s**lower relaxing semiquinone (**SQ**) in the **N**ADH-Q

oxidoreductase segment of the respiratory chain, their main difference is their spin relaxation properties that reflects their different strengths of spin coupling with the N2 cluster[295, 450, 451, 465]. It can be suggested that the signals described in this work correspond to these semiquinones; as the stability of SQ_{Nf} strongly depends of the presence of a proton motive force [170] which is not established in the current experimental parameters, it can be deduced that the signals are coming from SQ_{Ns} that is insensitive to the proton motive force [212]

The distance between these SQs and N2 is a key parameter in the electron transfer process, the SQs should be located in within the electron tunneling distance from N2 cluster (<15 Å, edge-to-edge distance), providing in this way a reasonable electron transfer rate.

Without the semiquinone radicals, to ensure the electron transfer between N2 and the UQ, the ring of the UQ should move out from the membrane domain at least 10 A, leaving one of the isoprenoid tale segments exposed to the hydrophilic part of the protein, this movement would present an energetic barrier. Many theories had exposed how the mechanism can be energetically favorable[193, 219, 444], but even with the crystal structure the interaction remains unclear.

In the studies of Ohnishi *et al* [170] it was described that the distance between N2 and the SQ_{Nf} is close to 12 Å, placing the ubiquinone at 5 Å within the lipid bilayer [465], this was confirmed by the recently published structure of the complex[183]; while the binding site for the slower relaxing SQ, is estimated to be located further away, towards the cytosolic side of the membrane. As can be seen in Figure 4.3-42, the most probable position for the SQs to be located is in a cleft of the hydrophilic domain facing the membrane surface but with a certain distance from it. According to Verkhovsky *et al*[219] and Narayanan *et al*[295], one of them should be tightly bound at the N2 proximal site and the other near the membrane quinone pool, close enough to the tail of the exchangeable UQ, like this the UQ remains in the membrane part.

The redox potentials of the transitions observed are in line with the properties presented in previous studies, implying an involvement of SQ_{Nf} in the electron transfer reaction to the ubiquinone pool during the catalytic cycle [220]. Taking this into account, it can be suggested that SQ_{Nf} is sensitive to the presence of a membrane potential been the direct electron acceptor from the cluster N2, while SQ_{NS} being insensitive to the presence of a membrane potential might work as a converter to transform two one electron transitions to

one two electron transition, a similar mechanism was previously reported for the Q_A/Q_B couple in photosystem II [466-468].

As a final conclusion, fluorescence emission spectra obtained with a coupled electrochemistry technique allowed to follow the redox titration of a possible quinone cofactor of complex I that is not present in the fragment, additionally the mid-point potential was determined and its properties described.

4.3.7 Conclusion

RR spectroscopy, in the low frequency region, allows describing the properties of all the oxidized clusters of complex I through the analysis of the metal-ligand vibrations. The differences between the NuoEF, NDF and the complex I give the facility in the attribution of the vibrational modes corresponding to each cluster. It is important to comment, that this is the first time that the RR spectra of a protein with so many Fe-S cluster have been recorded.

From the protein analysis in their oxidized state, the first characteristic that calls the attention is that N1a and N1b does not have the same spectral properties, which is the reflection of the difference of their cluster motif (See Figure 4.3-2). For the [4Fe-4S] it is clear that the N2 and N5 clusters display several differences, where for the first, a particular bridging and terminal mode was assigned, while for the second a peculiar Fe-S-C dihedral angle can be assumed.

In the RR spectra, the contribution from the amino acid side chains showed that the Tyr residues have a key role in the environment of the cluster, where in the case of N6a, N6b and N2 the ratio between the "exposed" and "buried" residues is different from the other subunits in the protein. Also, in the environment of this cluster strongly-hydrogen bonded Trp residues have a significant role. Besides, in the *E. coli* proteins, Ala, Met, His and Lys residues are characteristic of the clusters environment whereas in the subcomplex from *A. aeolicus* the characteristic residues are Ile, Leu, Iso, His and Phe.

From the spectroelectrochemistry, the oxidized and reduced differential spectra were achieved for all the proteins, the subcomplex (NuoEF) and the fragment (NDF) facilitated the attribution and the description of the Fe-S clusters properties. By RR spectroscopy more information about the cofactor and its vicinity due to enhancement of the $\nu(\text{Fe-S})^b$, while FIR

gave a more complete picture of what happens beyond the cluster motif, due to the resolution of the ν(Fe-S)^t modes.

The reduced state of the cluster gives an idea of their differences and how this can be important to the mechanism. The clusters, N1a, N5 and N2, expand more upon reduction, according to the observed redox properties; they are clusters that need to stabilize a high-energy electron and/or an electron that will not travel to the next electron acceptor very fast.

Thus these clusters play a crucial role in the timing of the electron flow and hence the coupling of the electron and proton transfer reaction or be the rate-limiting step in the kinetics of the electron transfer reactions. On the other hand, the cluster that does not need to expand to stabilize an additional electron is a cluster that does not hold the electron for a long time. Thus its role is only to deliver the electron at a fast rate.

From the substrate binding it is evident that the reduction with NADPH has a similar effect on the Fe-S cluster as the ones described in the electrochemistry. However, N1a in the *A. aeolicus* subcomplex is only partially reduced by NADH, whereas in the NDF and complex I from *E. coli* is fully reduced, suggesting a different mechanism in both organisms. According to the residues obtained around the cluster, the properties of this cluster are directed correlated to the hydrogen bonding, where the amino acid of the loop 1 play a key role in stabilizing the cluster and the amino acid in the CT-β loop can be described as a support mechanism in the hydrogen bonding dynamics.

From the measurements, with NAD^+ and NADPH, the Fe-S-C dihedral angle and the Fe-S^t modes were perturbed in a different manner as it was observed for NADH, where bending motions were accompanied by narrower Fe-S-C dihedral angles and shorter Fe-S^t bonds. In the case of the NAD^+ binding, the changes observed related to a different the cysteinyl coordination, no bending motions are observed for the clusters in the NuoG, I and B subunit, while for the cluster N1a in NuoE and N3 in NuoF it seems that the clusters are being "decompress" in a more relaxed geometry, where the Fe-S^t are longer and the Fe-S^b shorter. This shift in geometry can be linked to the re-oxidation mechanism of the clusters. This means that while the NAD^+ is binding to the protein, certain conformational changes are triggered in order to assure that the cluster comes back to its oxidized state.

Previous studies demonstrated that the bovine and *P. denitrificans* enzyme has a higher affinity for NAD^+ than NADH[471, 472], this suggested that redox-dependent changes in

the nucleotide binding site of complex I might be related to the binding affinity, which was also proposed by the inhibition studies with NADH-OH of Kotlyar *et al.*[473], raising the fact that the difference observed in the cluster geometry might be a rate-limiting step for the forward reaction, preventing in this way the fast formation of ROS. This hypothesis had been proposed before by the studies in the mammalian enzyme by Grivennikova *et al.*[474] and more recently by Verkhovskaya and Bloch[194].

With NADPH, almost all the clusters exhibit particular characteristics, than the Fe-S-C dihedral angle get wider in relation to their symmetry in the oxidized state, while the internal coordination of the cluster are the same as the one observed upon the binding of NADH. It can be suggested, that the clusters are reduced but on a slower rate. A similar result had been observed in studies with mammalian enzyme, where the oxidation of NADPH is also pH-dependent[419, 475].

The only clusters that do not show this particularity are N6a, N6b and N2, where N6a and N6b are not perturbed at all, but N2 is still being reduced. Many had proposed that NADPH may second binding site, our results suggest that the FMN is similar affected by the binding Of NADH as for the binding of NADPH. Albracht[420] disclosed that a second binding site for the nucleotide is at the opposite end of the chain of redox groups near Q10, which is proposed to react deep inside the hydrophilic domain. The reduction of N2, while N6a and N6b seem to remain in oxidized state might support this idea. However if this is not the case a new mechanism where the electron transfer from N5 jumps to N2 must be proposed.

From EPR the midpoint potential and many of the properties and the location of the Fe-S clusters in complex I have been widely described. Nevertheless, this is the first time that the molecular transition from the oxidized to the reduced state of these cofactors in the complete complex I had been experimentally analyzed.

5 CONCLUSION

In this thesis three main protein complexes had been studied. Each system showed how protein activity can be regulated by different effectors through the differences in their conformation. The first protein of interest was PDZ1 from MAGI-1, involved in cellular signaling. This scaffold domain, known to interact with the E6 protein from HPV16, showed that the different conformational states and their affinity with the C-terminus of the viral protein is regulated by the dynamics of the hydrogen bonding network formed by the connection of specific amino acids in three regions of the protein (see Figure 4.1-14).

The difference in the relative contribution of β-sheets and the β-turns elements in presence of the 16E6 L_0/V peptide in comparison with the 16E6, suggested that a different hydrogen bonding pattern is occurring in the binding process with the mutant, where as a result the peptide have a more pleated structure[77, 317]. The higher the affinity, the more pleated the structure of the peptides, as the hydrogen bonding network is stronger between the peptide and the protein. These results suggest that the differences in the affinity is directly correlated to the hydrogen bonding, indicating that the pathogenicity and prevalence of the HPV16 virus is in its ability to have a strong hydrogen bonding network in comparison to the natural binder.

From the study with the PDZ1 GGG (see Figure 4.1-14) mutant, it was demonstrated that the C-terminal is crucial for the assembly of the hydrogen bonding network to stabilize the binding. The same could be said for mutant of the Lys44 residue, where the mutation K44/A (see Figure 4.1-23) inhibited the H-bond formation seen in the wild type, while in the case of K44/E (see Figure 4.1-24/4.1-27), the mutation generates a new coordination of the H-bonds network that it is completely different from the characteristics previously described in PDZ1-HPV16 E6 interactions.

The allosteric “shift population” model, correlates that, upon binding conformational changes distal to binding carboxylate site might be the key to understanding the binding dynamics between the PDZ domains and the viral proteins. Ligand-dependent dynamics of this allosteric behavior and the inter-molecular signaling was show to be directly correlated to the methyl side chains. The β-augmentation upon binding triggers the C-H groups of specific amino acids make the hydrogen bond network stronger, as it was observed in our results from the amino acids side chains perturbed and the mutations studied.

From the study of this protein and its interaction with a viral peptide as ligand, it can be said that the affinity depends more on the conformation of the tertiary structure than on changes in the secondary structure. This suggests that the binding of the ligand has an effect on the behavior of the protein where the signal triggered by changes in the binding pocket is able to modify the protein function though the changes in the network of the hydrogen bonding.

The second protein of interest was a model that constitutes a small scale prototype of the conformational changes observed in more complex proteins;it is a short peptide in presence of Copper (Cu) ions, the amyloid beta, which is a model peptide of the naturally occurring amyloid beta 39-42, known to be involved in the Alzheimer's disease. The objective with this model was to describe the role of histidine ligands in the metal center and how their changes can be translated in the mechanism of the protein.

For this, the difference FTIR spectra of two small peptides (DAHK and GHK) recorded in presence of Cu, showed that the coordination of the metal ion is very similar, represented of a mixture of both models (see Figure 4.2-4). In summary, the results showed a difference sphere of coordination between the Cu(II) and Cu(I), where the major changes in the structure will be dominated by the contribution of the imidazole ring of the different His highlighted residues (His6, His13 and His14), Asp1 and Tyr10. Changes in coordination geometry due to pH dependence of the aggregation observed in the presence of Cu(I) may be the trigger to the formation of the aggregates that will lead to fibrils formation

It is believed that amyloid formation in AD and other amyloidogenic diseases such as prion disease are the result of protein or peptide misfolding[125, 348]. The Aβ peptide has a structural transition associated with amyloid formation, with conversion from random coil to an extended β sheet-like conformation in aqueous medium[142]. According to recent studies in presence of Cu, both monomeric and dimeric species have been proposed[349].

This indicates that the formation of the fibrils observed in AD patients is not only trigger by the presence of Cu and its redox process. It can be proposed then the effect of metal ions in AD pathology is a two steps process as it was described by Faller[145, 350] and by Hardy and Selkoe [351]. First, the development of the fibrils is pH dependent and the contribution of the protonation of other amino acids is suggested. The second step will be production of reactive oxygen species (ROS) induced by Aβ.

From the study of this metal-peptide complex it can be concluded the effect of metal ions as ligands depend on the sphere of coordination. Changes in the geometry of the metal coordination lead to disruption of cellular mechanism and the protein or peptide involved may become an agent of disease.

The last system of interest in this thesis was a metalloprotein, the NADH: ubiquinone oxidoreductase (complex I), which plays a key role in the bioenergetics cell. This protein bears several Fe-S clusters and one flavin and its activity is regulated by the energy produced by a bound substrate and the electron transfer of its cofactors.

From the protein analysis in their oxidized state, the first characteristic that calls the attention is that the [2Fe-2S] clusters, N1a and N1b, do not have the same spectral properties, which is the reflection of the difference of their cluster motif (See Figure 4.3-2). For the [4Fe-4S] it is evident that the N2 and N5 clusters display several differences, where for the first a particular bridging and terminal mode was assigned, while the second a peculiar Fe-S-C dihedral angle can be assumed.

The studies in the reduced state by substrate binding and electrochemistry allowed to described in more detail the redox properties of the Fe-S clusters. From the spectroelectrochemistry, the oxidized and reduced differential spectra were achieved for all the proteins. The study of the subcomplex (NuoEF) and the fragment (NDF) facilitated the attribution and the description of the Fe-S clusters properties. By RR spectroscopy more information about the cofactor and its vicinity due to enhancement of the $\nu(Fe\text{-}S)^{b}$, while FIR gave more complete picture of what happens beyond the cluster motif, due to the resolution of the $\nu(Fe\text{-}S)^{t}$ modes.

In general, according to the difference in the $Fe\text{-}S^{t}$ and $Fe\text{-}S^{b}$ bonds, the clusters N1a, N5 and N2, showed an expansion of their geometry upon reduction. According to the redox properties described for similar clusters[352, 364, 406], these are metal centers where function is related to the need to stabilize a high-energy electron and/or an electron that will not be transferred to the next electron acceptor very fast. It is noted that these clusters play a crucial role in the timing of the electron flow and hence the coupling of the electron and proton transfer reaction as well as the rate-limiting step in the kinetics of the electron transfer reactions.

From the RR results obtained in the reduced state with NADH and the effect of other nucleotides, NAD^+ and NADPH, it can be suggested that the reduction of the [2Fe-2S] clusters induce the distancing of the Fe orbitals, whereas in the presence of NAD^+ changes in the geometry of the cluster are more associated with narrower dihedral angles and with NADPH, wider ones. As it was shown, N1a in the NuoEF subcomplex was partially reduced or not reduced at all, suggesting that N1a in *A. aeolicus* and the N1a in *E. coli* do not have the same reduction mechanism.

For the [4Fe-4S] clusters, N3, N4, N6a and N6b, in presence of all the nucleotides the coordination of the $Fe\text{-}S^b$ was found to change to a more "relaxed" state, while N6a, N6b and N2 are likely to have "rigid" $Fe\text{-}S^b$ bonds. The "relaxed" centers are likely have a faster electron transfer than the "rigid" centers, where in the second the reversibility to a oxidized state is slower due to the change in the energy of the Fe-S bridging bonds[166]

In summary, the binding of NADH induces long range global conformational changes that are possibly linked to the mechanism of the enzyme, implying that the addition of NADH and NADPH to complex I has two different effects: first, it leads to local conformational changes caused, by the reduction of the iron-sulfur clusters, and second, it leads to global conformational changes possibly linked to quinone binding. Nevertheless, is important to recall that the conformation changes seems to be the prime pivot to the function of the protein, regulating the environment of the Fe-S cluster, and thus the redox properties.

In a further part of this study, mutations of specific amino acids around N1a and N2, helped to analyze their special properties and crucial roles in complex I mechanism; and furthermore to define which factors are important to define the redox properties of these clusters. From the variations around N1a cluster (see Figure 4.3-21) was that changes in the redox midpoint potential can be correlated to changes in the intramolecular hydrogen bonding network in the protein (see Figure 4.3-24). These changes exert an effect on the terminal modes of the cluster, as the band corresponding to the vibrations presented a displacement to higher frequency in NuoEF-V90P and NuoEF-V90P/V136M; this indicates a decrease in the bond strength between the Cys residues and the metal center. In summary, changes in residues in Loop 1 and the CT-β region form part the extended hydrogen bonding that maintain the stability of N1a. As observed in RR results, changes in this hydrogen bonding have as a consequence an overlapping of the Fe orbitals and displacement of the dihedral angles of the

cysteines residues, coordinating the metal center. By homology with previous studies on other thioredoxin like proteins[361], it seem that the vicinity of the loops and [2Fe-2S] clusters, together with the demonstrated versatility of the polypeptide chain in that region[6] may suggest the possibility of a redox switch regulation[446-448].

Mutations around the N2 cluster (see Figure 4.3-34), pointed to a role of Glu67 that is most likely protonated by the oxidation of N2. It might be involved in the proton translocation. The analysis of the RR spectra in their oxidized state revealed that the mutations are able to affect the terminal ν(Fe-S) modes. Changes in dihedral angle between the Fe-S-C on the Cys residues belonging to the cluster motif were proven and, furthermore perturbation in the hydrogen bonding of several Tyr residues, which is Tyr154 and Tyr139.

On other hand, the spectroelectrochemistry measurements perform by fluorescence spectroscopy showed the redox titration of a possible quinone cofactor of complex I that is not present in the fragment. Additionally the mid-point potential was determined and its properties described. The values obtained represent two transitions of one cofactor, which in comparison with previous results by EPR spectroscopy may correspond to a semiquinone, named SQ_{Nf}, for its spin relaxation properties [295, 450, 451, 465].

As a general conclusion from the study of Complex I, it can be said that the properties of its cofactors are dominated by the environment around them. Changes in the conformation of the protein have a higher impact on their redox properties and thus on the proper function of the protein.

In summary, FIR is shown to be an area of interest where the reflection of allosteric and the effect of the cofactors in protein function can be monitored. From the three protein complexes studied it was evident that each system is regulated by their own factors and where the effector usually target specific amino acids that trigger a cascade reaction through other regions or domains of the protein.

6 REFERENCES

1. Flemming, D., Hellwig, P., Lepper, S., Kloer, D. P., and Friedrich, T. (2006) Catalytic importance of acidic amino acids on subunit NuoB of the Escherichia coli NADH:ubiquinone oxidoreductase (complex I), *The Journal of biological chemistry 281*, 24781-24789.
2. Kriegel, S. (2013) Transformation of a membrane protein from the respiratory chain into a sensor for the analysis of its interaction with substrates, inhibitors and lipids, In *Chemistry*, p 226, Universite de Strasbourg, Strasbourg.
3. El Khoury, Y., Dorlet, P., Faller, P., and Hellwig, P. (2011) New insights into the coordination of Cu(II) by the amyloid-B 16 peptide from Fourier transform IR spectroscopy and isotopic labeling, *The journal of physical chemistry. B 115*, 14812-14821.
4. Hureau, C., Eury, H., Guillot, R., Bijani, C., Sayen, S., Solari, P. L., Guillon, E., Faller, P., and Dorlet, P. (2011) X-ray and solution structures of Cu(II) GHK and Cu(II) DAHK complexes: influence on their redox properties, *Chemistry 17*, 10151-10160.
5. Trapaidze, A., Hureau, C., Bal, W., Winterhalter, M., and Faller, P. (2012) Thermodynamic study of Cu2+ binding to the DAHK and GHK peptides by isothermal titration calorimetry (ITC) with the weaker competitor glycine, *Journal of biological inorganic chemistry : JBIC : a publication of the Society of Biological Inorganic Chemistry 17*, 37-47.
6. Birrell, J. A., Morina, K., Bridges, H. R., Friedrich, T., and Hirst, J. (2013) Investigating the function of [2Fe-2S] cluster N1a, the off-pathway cluster in complex I, by manipulating its reduction potential, *The Biochemical journal 456*, 139-146.
7. (2001) UV Raman Spectroscopy, http://www.semrock.com/uv-raman-spectroscopy.aspx.
8. G., H. G. (2006) *Spectroscopy for the Biological Sciences*, John Wiley & Sons, Inc, United State of America.
9. Siegfried, W. (2003) *IR and Raman Spectroscopy*, Wiley-VCH Verlag GmbH and Co, Germany.
10. Larkin, P. (2011) *IR and Raman Spectroscopy : principles and spectral interpretation*, 1st Edition ed., Elsevier Inc., Oxford, UK.
11. Lakowicz, J. (2006) *Principles of Fluorescence Spectroscopy*, Springer, Singapore.
12. Han, S., Czernuszewicz, R. S., and Spiro, T. G. (1989) Vibrational spectra and normal mode analysis for [2Fe-2S] protein analogues using 34S, 54Fe, and 2H substitution: Coupling of Fe-S stretching and S-C-C bending modes, *Journal of the American Chemical Society 111*, 3496-3504.
13. Ianoul, A., Boyden, M. N., and Asher, S. A. (2001) Dependence of the peptide amide III vibration on the phi dihedral angle, *J Am Chem Soc 123*, 7433-7434.
14. Moss, D., Nabedryk, E., Breton, J., and Mantele, W. (1990) Redox-Linked Conformational-Changes in Proteins Detected by a Combination of Infrared-Spectroscopy and Protein Electrochemistry - Evaluation of the Technique with Cytochrome-C, *European Journal of Biochemistry 187*, 565-572.
15. Ivarsson, Y. (2012) Plasticity of PDZ domains in ligand recognition and signaling, *FEBS letters 586*, 2638-2647.
16. Efremov, R. G., and Sazanov, L. A. (2011) Respiratory complex I: 'steam engine' of the cell?, *Current opinion in structural biology 21*, 532-540.
17. Hirst, J. (2013) Mitochondrial complex I, *Annual review of biochemistry 82*, 551-575.
18. Hirst, J. (2010) Towards the molecular mechanism of respiratory complex I, *The Biochemical journal 425*, 327-339.
19. GM, C. (2000) *The Cell: A Molecular Approach*, 2nd edition ed., Sunderland (MA).
20. Jagannathan, B., and Marqusee, S. (2013) Protein folding and unfolding under force, *Biopolymers 99*, 860-869.
21. Trudy, M. (2009) *Biochemistry the molecular basis of life*, Oxford UP, New York.

22. Jucker, M., and Walker, L. C. (2013) Self-propagation of pathogenic protein aggregates in neurodegenerative diseases, *Nature 501*, 45-51.
23. Pandya, C., Brown, S., Pieper, U., Sali, A., Dunaway-Mariano, D., Babbitt, P. C., Xia, Y., and Allen, K. N. (2013) Consequences of domain insertion on sequence-structure divergence in a superfold, *Proceedings of the National Academy of Sciences of the United States of America 110*, E3381-E3387.
24. Rademacher, N., Kunde, S. A., Kalscheuer, V. M., and Shoichet, S. A. (2013) Synaptic MAGUK Multimer Formation Is Mediated by PDZ Domains and Promoted by Ligand Binding, *Chemistry & biology 20*, 1044-1054.
25. Seifert, C., and Gräter, F. (2013) Protein mechanics: How force regulates molecular function, *Biochimica et Biophysica Acta - General Subjects 1830*, 4762-4768.
26. Cuanalo-Contreras, K., Mukherjee, A., and Soto, C. (2013) Role of protein misfolding and proteostasis deficiency in protein misfolding diseases and aging, *International Journal of Cell Biology*.
27. Fischer, M., and Riemer, J. (2013) The mitochondrial disulfide relay system: Roles in oxidative protein folding and beyond, *International Journal of Cell Biology*.
28. Brodsky, J. L. (2014) The threads that tie protein-folding diseases, *DMM Disease Models and Mechanisms 7*, 3-4.
29. Levchenko, I., Smith, C. K., Walsh, N. P., Sauer, R. T., and Baker, T. A. (1997) PDZ-like domains mediate binding specificity in the Clp/Hsp100 family of chaperones and protease regulatory subunits, *Cell 91*, 939-947.
30. Gloge, F., Becker, A. H., Kramer, G., and Bukau, B. (2014) Co-translational mechanisms of protein maturation, *Current opinion in structural biology 24*, 24-33.
31. Hingorani, K. S., and Gierasch, L. M. (2014) Comparing protein folding in vitro and in vivo: Foldability meets the fitness challenge, *Current opinion in structural biology 24*, 81-90.
32. Khoury, G. A., Smadbeck, J., Kieslich, C. A., and Floudas, C. A. (2014) Protein folding and de novo protein design for biotechnological applications, *Trends in Biotechnology 32*, 99-109.
33. Bray, D. (2013) The propagation of allosteric states in large multiprotein complexes, *Journal of Molecular Biology 425*, 1410-1414.
34. Voorhees, R. M., and Ramakrishnan, V. (2013) Structural basis of the translational elongation cycle, pp 203-236.
35. McGettrick, A. F., and O'Neill, L. A. J. (2013) How metabolism generates signals during innate immunity and inflammation, *Journal of Biological Chemistry 288*, 22893-22898.
36. Yamashita, M. M., Wesson, L., Eisenman, G., and Eisenberg, D. (1990) Where metal ions bind in proteins, *Proceedings of the National Academy of Sciences 87*, 5648-5652.
37. Beinert, H. (1990) Recent developments in the field of iron-sulfur proteins, *Faseb J 4*, 2483-2491.
38. Beinert, H., and Kiley, P. J. (1999) Fe-S proteins in sensing and regulatory functions, *Current opinion in chemical biology 3*, 152-157.
39. Beinert, H. (2000) Iron-sulfur proteins: ancient structures, still full of surprises, *Journal of biological inorganic chemistry : JBIC : a publication of the Society of Biological Inorganic Chemistry 5*, 2-15.
40. Ghisla, S., Massey, V., Lhoste, J. M., and Mayhew, S. G. (1974) Fluorescence and optical characteristics of reduced flavines and flavoproteins, *Biochemistry 13*, 589-597.
41. Li, J., and Buchner, J. (2013) Structure, function and regulation of the Hsp90 machinery, *Biomedical Journal 36*, 106-117.
42. Kubrycht, J., Sigler, K., Souček, P., and Hudeček, J. (2013) Structures composing protein domains, *Biochimie 95*, 1511-1524.
43. Changeux, J. P. (2013) The origins of allostery: From personal memories to material for the future, *Journal of Molecular Biology 425*, 1396-1406.

44. Swain, J. F., and Gierasch, L. M. (2006) The changing landscape of protein allostery, *Current opinion in structural biology 16*, 102-108.
45. Hilser, V. J. (2010) Biochemistry. An ensemble view of allostery, *Science 327*, 653-654.
46. Gonzalez-Mariscal, L., Betanzos, A., and Avila-Flores, A. (2000) MAGUK proteins: structure and role in the tight junction, *Seminars in cell & developmental biology 11*, 315-324.
47. McCann, J. J., Zheng, L., Rohrbeck, D., Felekyan, S., Kuhnemuth, R., Sutton, R. B., Seidel, C. A., and Bowen, M. E. (2012) Supertertiary structure of the synaptic MAGuK scaffold proteins is conserved, *Proc Natl Acad Sci U S A 109*, 15775-15780.
48. Kim, E., DeMarco, S. J., Marfatia, S. M., Chishti, A. H., Sheng, M., and Strehler, E. E. (1998) Plasma membrane Ca2+ ATPase isoform 4B binds to membrane-associated guanylate kinase (MAGUK) proteins via their PDZ (PSD-95/Dlg/ZO-1) domains, *Journal of Biological Chemistry 273*, 1591-1595.
49. Elias, G. M., Funke, L., Stein, V., Grant, S. G., Bredt, D. S., and Nicoll, R. A. (2006) Synapse-specific and developmentally regulated targeting of AMPA receptors by a family of MAGUK scaffolding proteins, *Neuron 52*, 307-320.
50. Bachmann, A., Draga, M., Grawe, F., and Knust, E. (2008) On the role of the MAGUK proteins encoded by Drosophila varicose during embryonic and postembryonic development, *BMC developmental biology 8*, 55.
51. Zhu, J., Shang, Y., Xia, C., Wang, W., Wen, W., and Zhang, M. (2011) Guanylate kinase domains of the MAGUK family scaffold proteins as specific phospho-protein-binding modules, *The EMBO journal 30*, 4986-4997.
52. Dobrosotskaya, I., Guy, R. K., and James, G. L. (1997) MAGI-1, a membrane-associated guanylate kinase with a unique arrangement of protein-protein interaction domains, *The Journal of biological chemistry 272*, 31589-31597.
53. Dobrosotskaya, I. Y., and James, G. L. (2000) MAGI-1 interacts with β-catenin and is associated with cell-cell adhesion structures, *Biochemical and Biophysical Research Communications 270*, 903-909.
54. Patrie, K. M., Drescher, A. J., Goyal, M., Wiggins, R. C., and Margolis, B. (2001) The membrane-associated guanylate kinase protein MAGI-1 binds megalin and is present in glomerular podocytes, *Journal of the American Society of Nephrology 12*, 667-677.
55. Charbonnier, S., Stier, G., Orfanoudakis, G., Kieffer, B., Atkinson, R. A., and Travé, G. (2008) Defining the minimal interacting regions of the tight junction protein MAGI-1 and HPV16 E6 oncoprotein for solution structure studies, *Protein Expression and Purification 60*, 64-73.
56. Kennedy, M. B. (1995) Origin of PDZ (DHR, GLGF) domains, *Trends Biochem Sci 20*, 350.
57. Lue, R. A., Brandin, E., Chan, E. P., and Branton, D. (1996) Two independent domains of hDlg are sufficient for subcellular targeting: The PDZ1-2 conformational unit and an alternatively spliced domain, *Journal of Cell Biology 135*, 1125-1137.
58. Marfatia, S. M., Cabral, J. H. M., Lin, L., Hough, C., Bryant, P. J., Stolz, L., and Chishti, A. H. (1996) Modular organization of the PDZ domains in the human discs-large protein suggests a mechanism for coupling PDZ domain-binding proteins to ATP and the membrane cytoskeleton, *Journal of Cell Biology 135*, 753-766.
59. Harrison, S. C. (1996) Peptide-surface association: the case of PDZ and PTB domains, *Cell 86*, 341-343.
60. Ponting, C. P. (1997) Evidence for PDZ domains in bacteria, yeast, and plants, *Protein science : a publication of the Protein Society 6*, 464-468.
61. Pallen, M. J., and Ponting, C. P. (1997) PDZ domains in bacterial proteins, *Molecular microbiology 26*, 411-413.
62. Ponting, C. P., Phillips, C., Davies, K. E., and Blake, D. J. (1997) PDZ domains: targeting signalling molecules to sub-membranous sites, *BioEssays : news and reviews in molecular, cellular and developmental biology 19*, 469-479.

63. Lee, H. J., and Zheng, J. J. (2010) PDZ domains and their binding partners: structure, specificity, and modification, *Cell communication and signaling : CCS 8*, 8.
64. Dobrosotskaya, I., Guy, R. K., and James, G. L. (1997) MAGI-1, a membrane-associated guanylate kinase with a unique arrangement of protein-protein interaction domains, *Journal of Biological Chemistry 272*, 31589-31597.
65. Chi, C. N., Engstrom, A., Gianni, S., Larsson, M., and Jemth, P. (2006) Two conserved residues govern the salt and pH dependencies of the binding reaction of a PDZ domain, *The Journal of biological chemistry 281*, 36811-36818.
66. Harris, B. Z., Lau, F. W., Fujii, N., Guy, R. K., and Lim, W. A. (2003) Role of electrostatic interactions in PDZ domain ligand recognition, *Biochemistry 42*, 2797-2805.
67. Smock, R. G., and Gierasch, L. M. (2009) Sending signals dynamically, *Science 324*, 198-203.
68. Akiva, E., Friedlander, G., Itzhaki, Z., and Margalit, H. (2012) A dynamic view of domain-motif interactions, *PLoS computational biology 8*, e1002341.
69. Birrane, G., Mulvaney, E. P., Pal, R., Kinsella, B. T., and Kocher, O. (2013) Molecular Analysis of the Prostacyclin Receptor's Interaction with the PDZ1 Domain of Its Adaptor Protein PDZK1, *PloS one 8*.
70. Zhang, Z., Li, H., Chen, L., Lu, X., Zhang, J., Xu, P., Lin, K., and Wu, G. (2011) Molecular basis for the recognition of adenomatous polyposis coli by the discs large 1 protein, *PloS one 6*.
71. Charbonnier, S., Nominé, Y., Ramírez, J., Luck, K., Chapelle, A., Stote, R. H., Travé, G., Kieffer, B., and Atkinson, R. A. (2011) The structural and dynamic response of MAGI-1 PDZ1 with noncanonical domain boundaries to the binding of human papillomavirus E6, *Journal of Molecular Biology 406*, 745-763.
72. Zhang, Q., Fan, J. S., and Zhang, M. (2001) Interdomain chaperoning between PSD-95, Dlg, and Zo-1 (PDZ) domains of glutamate receptor-interacting proteins, *The Journal of biological chemistry 276*, 43216-43220.
73. Smith, C. A., and Kortemme, T. (2010) Structure-based prediction of the peptide sequence space recognized by natural and synthetic PDZ domains, *J Mol Biol 402*, 460-474.
74. Schneider, S., Buchert, M., Georgiev, O., Catimel, B., Halford, M., Stacker, S. A., Baechi, T., Moelling, K., and Hovens, C. M. (1999) Mutagenesis and selection of PDZ domains that bind new protein targets, *Nature biotechnology 17*, 170-175.
75. Ye, F., and Zhang, M. (2013) Structures and target recognition modes of PDZ domains: recurring themes and emerging pictures, *The Biochemical journal 455*, 1-14.
76. Doyle, D. A., Lee, A., Lewis, J., Kim, E., Sheng, M., and MacKinnon, R. (1996) Crystal structures of a complexed and peptide-free membrane protein-binding domain: molecular basis of peptide recognition by PDZ, *Cell 85*, 1067-1076.
77. Harris, B. Z., Hillier, B. J., and Lim, W. A. (2001) Energetic determinants of internal motif recognition by PDZ domains, *Biochemistry 40*, 5921-5930.
78. Bezprozvanny, I., and Maximov, A. (2001) PDZ domains: More than just a glue, *Proc Natl Acad Sci U S A 98*, 787-789.
79. Bhattacharya, S., Ju, J. H., Orlova, N., Khajeh, J. A., Cowburn, D., and Bu, Z. (2013) Ligand-induced dynamic changes in extended PDZ domains from NHERF1, *J Mol Biol 425*, 2509-2528.
80. Songyang, Z., Fanning, A. S., Fu, C., Xu, J., Marfatia, S. M., Chishti, A. H., Crompton, A., Chan, A. C., Anderson, J. M., and Cantley, L. C. (1997) Recognition of unique carboxyl-terminal motifs by distinct PDZ domains, *Science 275*, 73-77.
81. Sheng, M., and Sala, C. (2001) PDZ domains and the organization of supramolecular complexes, *Annual review of neuroscience 24*, 1-29.
82. Kornau, H. C., and Seeburg, P. H. (1997) Partner selection by PDZ domains, *Nature biotechnology 15*, 319.

83. Kim, E., and Sheng, M. (1996) Differential K+ channel clustering activity of PSD-95 and SAP97, two related membrane-associated putative guanylate kinases, *Neuropharmacology 35*, 993-1000.
84. Hallam, S. J., Goncharov, A., McEwen, J., Baran, R., and Jin, Y. (2002) SYD-1, a presynaptic protein with PDZ, C2 and rhoGAP-like domains, specifies axon identity in C. elegans, *Nature neuroscience 5*, 1137-1146.
85. Valiente, M., Andres-Pons, A., Gomar, B., Torres, J., Gil, A., Tapparel, C., Antonarakis, S. E., and Pulido, R. (2005) Binding of PTEN to specific PDZ domains contributes to PTEN protein stability and phosphorylation by microtubule-associated serine/threonine kinases, *The Journal of biological chemistry 280*, 28936-28943.
86. Zhang, Y., Yeh, S., Appleton, B. A., Held, H. A., Kausalya, P. J., Phua, D. C., Wong, W. L., Lasky, L. A., Wiesmann, C., Hunziker, W., and Sidhu, S. S. (2006) Convergent and divergent ligand specificity among PDZ domains of the LAP and zonula occludens (ZO) families, *The Journal of biological chemistry 281*, 22299-22311.
87. Tonikian, R., Zhang, Y., Sazinsky, S. L., Currell, B., Yeh, J. H., Reva, B., Held, H. A., Appleton, B. A., Evangelista, M., Wu, Y., Xin, X., Chan, A. C., Seshagiri, S., Lasky, L. A., Sander, C., Boone, C., Bader, G. D., and Sidhu, S. S. (2008) A specificity map for the PDZ domain family, *PLoS biology 6*, e239.
88. Lee, S. S., Weiss, R. S., and Javier, R. T. (1997) Binding of human virus oncoproteins to hDlg/SAP97, a mammalian homolog of the Drosophila discs large tumor suppressor protein, *Proc Natl Acad Sci U S A 94*, 6670-6675.
89. Rousset, R., Fabre, S., Desbois, C., Bantignies, F., and Jalinot, P. (1998) The C-terminus of the HTLV-1 Tax oncoprotein mediates interaction with the PDZ domain of cellular proteins, *Oncogene 16*, 643-654.
90. Kiyono, T., Hiraiwa, A., Fujita, M., Hayashi, Y., Akiyama, T., and Ishibashi, M. (1997) Binding of high-risk human papillomavirus E6 oncoproteins to the human homologue of the Drosophila discs large tumor suppressor protein, *Proceedings of the National Academy of Sciences of the United States of America 94*, 11612-11616.
91. Hiraiwa, A., and Ishibashi, M. (1998) [Binding of viral oncogenic proteins and PDZ domains of cellular proteins], *Tanpakushitsu kakusan koso. Protein, nucleic acid, enzyme 43*, 237-243.
92. Dev, K. K. (2004) Making protein interactions druggable: targeting PDZ domains, *Nature reviews. Drug discovery 3*, 1047-1056.
93. Thomas, M., Narayan, N., Pim, D., Tomaic, V., Massimi, P., Nagasaka, K., Kranjec, C., Gammoh, N., and Banks, L. (2008) Human papillomaviruses, cervical cancer and cell polarity, *Oncogene 27*, 7018-7030.
94. Laimins, L. A. (1993) The biology of human papillomaviruses: from warts to cancer, *Infectious agents and disease 2*, 74-86.
95. Ganguly, N., and Parihar, S. P. (2009) Human papillomavirus E6 and E7 oncoproteins as risk factors for tumorigenesis, *Journal of Biosciences 34*, 113-123.
96. Subbaiah, V. K., Kranjec, C., Thomas, M., and Banks, L. (2011) PDZ domains: the building blocks regulating tumorigenesis, *The Biochemical journal 439*, 195-205.
97. Kiyono, T., Hiraiwa, A., Fujita, M., Hayashi, Y., Akiyama, T., and Ishibashi, M. (1997) Binding of high-risk human papillomavirus E6 oncoproteins to the human homologue of the Drosophila discs large tumor suppressor protein, *Proc Natl Acad Sci U S A 94*, 11612-11616.
98. Zhang, Y., Dasgupta, J., Ma, R. Z., Banks, L., Thomas, M., and Chen, X. S. (2007) Structures of a human papillomavirus (HPV) E6 polypeptide bound to MAGUK proteins: Mechanisms of targeting tumor suppressors by a high-risk HPV oncoprotein, *Journal of Virology 81*, 3618-3626.

99. Nagasaka, K., Kawana, K., Osuga, Y., and Fujii, T. (2013) PDZ Domains and Viral Infection: Versatile Potentials of HPV-PDZ Interactions in relation to Malignancy, *BioMed research international 2013*, 369712.
100. Pim, D., Tomaić, V., and Banks, L. (2009) The human papillomavirus (HPV) E6* proteins from high-risk, mucosal HPVs can direct degradation of cellular proteins in the absence of full-length E6 protein, *Journal of Virology 83*, 9863-9874.
101. Narisawa-Saito, M., and Kiyono, T. (2007) Basic mechanisms of high-risk human papillomavirus-induced carcinogenesis: Roles of E6 and E7 proteins, *Cancer Science 98*, 1505-1511.
102. Milewski, M. (2003) [Structure and function in PDZ domains], *Postepy biochemii 49*, 257-267.
103. Beuming, T., Skrabanek, L., Niv, M. Y., Mukherjee, P., and Weinstein, H. (2005) PDZBase: a protein-protein interaction database for PDZ-domains, *Bioinformatics 21*, 827-828.
104. Pim, D., Bergant, M., Boon, S. S., Ganti, K., Kranjec, C., Massimi, P., Subbaiah, V. K., Thomas, M., Tomaić, V., and Banks, L. (2012) Human papillomaviruses and the specificity of PDZ domain targeting, *FEBS Journal 279*, 3530-3537.
105. Rebeaud, F., Hailfinger, S., and Thome, M. (2007) Dlgh1 and Carma1 MAGUK proteins contribute to signal specificity downstream of TCR activation, *Trends in immunology 28*, 196-200.
106. Cardenas, M. L. (2013) Michaelis and Menten and the long road to the discovery of cooperativity, *FEBS letters 587*, 2767-2771.
107. Monod, J., Wyman, J., and Changeux, J.-P. (1965) On the nature of allosteric transitions: A plausible model, *Journal of Molecular Biology 12*, 88-118.
108. Koshland, D. E., Némethy, G., and Filmer, D. (1966) Comparison of Experimental Binding Data and Theoretical Models in Proteins Containing Subunits*, *Biochemistry 5*, 365-385.
109. Kern, D., and Zuiderweg, E. R. P. (2003) The role of dynamics in allosteric regulation, *Current opinion in structural biology 13*, 748-757.
110. Petit, C. M., Zhang, J., Sapienza, P. J., Fuentes, E. J., and Lee, A. L. (2009) Hidden dynamic allostery in a PDZ domain, *Proceedings of the National Academy of Sciences of the United States of America 106*, 18249-18254.
111. Gerek, Z. N., and Ozkan, S. B. (2011) Change in allosteric network affects binding affinities of PDZ domains: analysis through perturbation response scanning, *PLoS computational biology 7*, e1002154.
112. Lechtenberg, B. C., Freund, S. M., and Huntington, J. A. (2012) An ensemble view of thrombin allostery, *Biological chemistry 393*, 889-898.
113. Moritsugu, K., Miyashita, O., and Kidera, A. (2000) Vibrational energy transfer in a protein molecule, *Physical review letters 85*, 3970-3973.
114. De Los Rios, P., Cecconi, F., Pretre, A., Dietler, G., Michielin, O., Piazza, F., and Juanico, B. (2005) Functional dynamics of PDZ binding domains: a normal-mode analysis, *Biophysical journal 89*, 14-21.
115. Badarau, A., Firbank, S. J., McCarthy, A. A., Banfield, M. J., and Dennison, C. (2010) Visualizing the metal-binding versatility of copper trafficking sites, *Biochemistry 49*, 7798-7810.
116. Ferré-D'Amaré, A. R., and Winkler, W. C. (2011) The roles of metal ions in regulation by riboswitches, *Metal ions in life sciences 9*, 141-173.
117. Maret, W. (2012) New perspectives of zinc coordination environments in proteins, *J Inorg Biochem 111*, 110-116.
118. Lu, C. H., Lin, Y. F., Lin, J. J., and Yu, C. S. (2012) Prediction of metal ion-binding sites in proteins using the fragment transformation method, *PloS one 7*, e39252.
119. Kozlowski, H., Potocki, S., Remelli, M., Rowinska-Zyrek, M., and Valensin, D. (2013) Specific metal ion binding sites in unstructured regions of proteins, *Coordination Chemistry Reviews 257*, 2625-2638.

120. Okamoto, M., Nakajima, Y., Matsuyama, T., and Sugita, M. (2001) Amyloid precursor protein associates independently and collaboratively with PTB and PDZ domains of mint on vesicles and at cell membrane, *Neuroscience 104*, 653-665.
121. Faller, P., Hureau, C., and Berthoumieu, O. (2013) Role of metal ions in the self-assembly of the Alzheimer's amyloid-β peptide, *Inorganic chemistry 52*, 12193-12206.
122. Wärmländer, S., Tiiman, A., Abelein, A., Luo, J., Jarvet, J., Söderberg, K. L., Danielsson, J., and Gräslund, A. (2013) Biophysical studies of the amyloid β-peptide: Interactions with metal ions and small molecules, *Chembiochem : a European journal of chemical biology 14*, 1692-1704.
123. Crescenzi, O., Tomaselli, S., Guerrini, R., Salvadori, S., D'Ursi, A. M., Temussi, P. A., and Picone, D. (2002) Solution structure of the Alzheimer amyloid β-peptide (1–42) in an apolar microenvironment, *European Journal of Biochemistry 269*, 5642-5648.
124. Kirkitadze, M. D., and Kowalska, A. (2005) Molecular mechanisms initiating amyloid β-fibril formation in Alzheimer's disease, *Acta Biochimica Polonica 52*, 417-423.
125. Veerhuis, R., Boshuizen, R. S., and Familian, A. (2005) Amyloid associated proteins in Alzheimer's and prion disease, *Current Drug Targets: CNS and Neurological Disorders 4*, 235-248.
126. Takahashi, T., and Mihara, H. (2008) Peptide and protein mimetics inhibiting amyloid β-peptide aggregation, *Accounts of Chemical Research 41*, 1309-1318.
127. Zhang, W., Du, Y., Bai, M., Xi, Y., Li, Z., and Miao, J. (2013) S14G-humanin inhibits Aβ1-42 fibril formation, disaggregates preformed fibrils, and protects against Aβ-induced cytotoxicity in vitro, *Journal of Peptide Science 19*, 159-165.
128. Aly, W. W., Elsaid, S. M. S., and Wahba, H. M. (2013) Copper, zinc and iron serum levels in patients with Alzheimer's disease, *Life Science Journal 10*, 2628-2632.
129. Tiiman, A., Palumaa, P., and Tõugu, V. (2013) The missing link in the amyloid cascade of Alzheimer's disease-Metal ions, *Neurochemistry International 62*, 367-378.
130. Savelieff, M. G., Lee, S., Liu, Y., and Lim, M. H. (2013) Untangling amyloid-β, tau, and metals in Alzheimer's disease, *ACS Chemical Biology 8*, 856-865.
131. Cassagnes, L. E., Hervé, V., Nepveu, F., Hureau, C., Faller, P., and Collin, F. (2013) The catalytically active copper-amyloid-beta state: Coordination site responsible for reactive oxygen species production, *Angewandte Chemie - International Edition 52*, 11110-11113.
132. Chassaing, S., Collin, F., Dorlet, P., Gout, J., Hureau, C., and Faller, P. (2012) Copper and heme-mediated abeta toxicity: Redox chemistry, abeta oxidations and anti-ROS compounds, *Current Topics in Medicinal Chemistry 12*, 2573-2595.
133. Furlan, S., Hureau, C., Faller, P., and La Penna, G. (2012) Modeling copper binding to the amyloid-β peptide at different pH: Toward a molecular mechanism for Cu reduction, *Journal of Physical Chemistry B 116*, 11899-11910.
134. Maly, T., Zwicker, K., Cernescu, A., Brandt, U., and Prisner, T. F. (2009) New pulsed EPR methods and their application to characterize mitochondrial complex I, *Biochimica et biophysica acta 1787*, 584-592.
135. Miura, T., Suzuki, K., Kohata, N., and Takeuchi, H. (2000) Metal binding modes of Alzheimer's amyloid beta-peptide in insoluble aggregates and soluble complexes, *Biochemistry 39*, 7024-7031.
136. Hureau, C., Balland, V., Coppel, Y., Solari, P. L., Fonda, E., and Faller, P. (2009) Importance of dynamical processes in the coordination chemistry and redox conversion of copper amyloid-β complexes, *Journal of Biological Inorganic Chemistry 14*, 995-1000.
137. Guilloreau, L., Combalbert, S., Sournia-Saquet, M., Mazarguil, H., and Faller, P. (2007) Redox chemistry of copper-amyloid-β: The generation of hydroxyl radical in the presence of ascorbate is linked to redox-potentials and aggregation state, *Chembiochem : a European journal of chemical biology 8*, 1317-1325.

138. Hureau, C., Sasaki, I., Gras, E., and Faller, P. (2010) Two functions, one molecule: A metal-binding and a targeting moiety to combat Alzheimer's disease, *Chembiochem : a European journal of chemical biology 11*, 950-953+838.
139. Peralvarez-Marin, A., Barth, A., and Graslund, A. (2008) Time-resolved infrared spectroscopy of pH-induced aggregation of the Alzheimer A beta(1-28) peptide, *Journal of Molecular Biology 379*, 589-596.
140. Alies, B., Bijani, C., Sayen, S., Guillon, E., Faller, P., and Hureau, C. (2012) Copper coordination to native N-terminally modified versus full-length amyloid-β: Second-sphere effects determine the species present at physiological pH, *Inorganic chemistry 51*, 12988-13000.
141. Hong, L., Carducci, T. M., Bush, W. D., Dudzik, C. G., Millhauser, G. L., and Simon, J. D. (2010) Quantification of the Binding Properties of Cu2+ to the Amyloid Beta Peptide: Coordination Spheres for Human and Rat Peptides and Implication on Cu2+-Induced Aggregation†, *The Journal of Physical Chemistry B 114*, 11261-11271.
142. Syme, C. D., Nadal, R. C., Rigby, S. E. J., and Viles, J. H. (2004) Copper Binding to the Amyloid-β (Aβ) Peptide Associated with Alzheimer's Disease: FOLDING, COORDINATION GEOMETRY, pH DEPENDENCE, STOICHIOMETRY, AND AFFINITY OF Aβ-(1–28): INSIGHTS FROM A RANGE OF COMPLEMENTARY SPECTROSCOPIC TECHNIQUES, *Journal of Biological Chemistry 279*, 18169-18177.
143. Drew, S. C., Noble, C. J., Masters, C. L., Hanson, G. R., and Barnham, K. J. (2009) Pleomorphic Copper Coordination by Alzheimer's Disease Amyloid-β Peptide, *Journal of the American Chemical Society 131*, 1195-1207.
144. Kowalik-Jankowska, T., Ruta, M., Wiśniewska, K., and Łankiewicz, L. (2003) Coordination abilities of the 1–16 and 1–28 fragments of β-amyloid peptide towards copper(II) ions: a combined potentiometric and spectroscopic study, *J Inorg Biochem 95*, 270-282.
145. Faller, P. (2012) Copper in Alzheimer disease: Too much, too little, or misplaced?, *Free Radical Bio Med 52*, 747-748.
146. Alies, B., Sasaki, I., Proux, O., Sayen, S., Guillon, E., Faller, P., and Hureau, C. (2013) Zn impacts Cu coordination to amyloid-β, the Alzheimer's peptide, but not the ROS production and the associated cell toxicity, *Chem Commun 49*, 1214-1216.
147. Faller, P., and Hureau, C. (2012) Metal ions in neurodegenerative diseases, *Coordination Chemistry Reviews 256*, 2127-2128.
148. Laussac, J. P., and Sarkar, B. (1984) Characterization of the Copper(Ii)-Transport and Nickel(Ii)-Transport Site of Human-Serum Albumin - Studies of Copper(Ii) and Nickel(Ii) Binding to Peptide 1-24 of Human-Serum Albumin by C-13 and H-1-Nmr Spectroscopy, *Biochemistry 23*, 2832-2838.
149. Harford, C., and Sarkar, B. (1997) Amino terminal Cu(II)- and Ni(II)-binding (ATCUN) motif of proteins and peptides: Metal binding, DNA cleavage, and other properties, *Accounts of Chemical Research 30*, 123-130.
150. Pickart, L. (2008) The human tri-peptide GHK and tissue remodeling, *J Biomat Sci-Polym E 19*, 969-988.
151. Reiber, H. (2001) Dynamics of brain-derived proteins in cerebrospinal fluid, *Clin Chim Acta 310*, 173-186.
152. Rozga, M., and Bal, W. (2010) The Cu(II)/A beta/Human Serum Albumin Model of Control Mechanism for Copper-Related Amyloid Neurotoxicity, *Chem Res Toxicol 23*, 298-308.
153. Perrone, L., Mothes, E., Vignes, M., Mockel, A., Figueroa, C., Miquel, M. C., Maddelein, M. L., and Faller, P. (2010) Copper Transfer from Cu-A beta to Human Serum Albumin Inhibits Aggregation, Radical Production and Reduces A beta Toxicity, *Chembiochem : a European journal of chemical biology 11*, 110-118.

154. Conato, C., Gavioli, R., Guerrini, R., Kozlowski, H., Mlynarz, P., Pasti, C., Pulidori, F., and Remelli, M. (2001) Copper complexes of glycyl-histidyl-lysine and two of its synthetic analogues: chemical behaviour and biological activity, *Bba-Gen Subjects 1526*, 199-210.
155. Gum, E. T., Swanson, R. A., Alano, C., Liu, J., Hong, S., Weinstein, P. R., and Panter, S. S. (2004) Human Serum Albumin and its N-Terminal Tetrapeptide (DAHK) Block Oxidant-Induced Neuronal Death, *Stroke 35*, 590-595.
156. Guilloreau, L., Combalbert, S., Sournia-Saquet, A., Mazarguil, H., and Faller, P. (2007) Redox chemistry of copper-amyloid-beta: the generation of hydroxyl radical in the presence of ascorbate is linked to redox-potentials and aggregation state, *Chembiochem : a European journal of chemical biology 8*, 1317-1325.
157. Fontecilla-Camps, J. C., Volbeda, A., Cavazza, C., and Nicolet, Y. (2007) Structure/function relationships of [NiFe]- and [FeFe]-hydrogenases, *Chemical Reviews 107*, 4273-4303.
158. Iwai, K., and Ueta, R. (2007) Mechanism underlying iron metabolism: Involvement of mitochondria in cellular iron sensing, *Seikagaku 79*, 1021-1031.
159. Evstatiev, R., and Gasche, C. (2012) Iron sensing and signalling, *Gut 61*, 933-952.
160. Saini, V., Farhana, A., Glasgow, J. N., and Steyn, A. J. C. (2012) Iron sulfur cluster proteins and microbial regulation: Implications for understanding tuberculosis, *Current opinion in chemical biology 16*, 45-53.
161. Ortiz De Orué Lucana, D. (2012) Redox sensing: Novel avenues and paradigms, *Antioxidants and Redox Signaling 16*, 636-638.
162. Ayala-Castro, C., Saini, A., and Outten, F. W. (2008) Fe-S cluster assembly pathways in bacteria, *Microbiology and Molecular Biology Reviews 72*, 110-125.
163. Niu, S. Q., and Ichiye, T. (2009) Probing Ligand Effects on the Redox Energies of [4Fe-4S] Clusters Using Broken-Symmetry Density Functional Theory, *J Phys Chem A 113*, 5671-5676.
164. Spiro, T. G., and Czernuszewicz, R. S. (1995) Resonance Raman spectroscopy of metalloproteins, *Methods in enzymology 246*, 416-460.
165. Marquet, A., Tse Sum Bui, B., Smith, A. G., and Warren, M. J. (2007) Iron-sulfur proteins as initiators of radical chemistry, *Natural Product Reports 24*, 1027-1040.
166. Beratan, D. N., Betts, J. N., and Onuchic, J. N. (1992) Tunneling Pathway and Redox-State-Dependent Electronic Couplings at Nearly Fixed Distance in Electron-Transfer Proteins, *J Phys Chem-Us 96*, 2852-2855.
167. Sazanov, L. A., Baradaran, R., Efremov, R. G., Berrisford, J. M., and Minhas, G. (2013) A long road towards the structure of respiratory complex I, a giant molecular proton pump, *Biochemical Society transactions 41*, 1265-1271.
168. Brandt, U. (2011) A two-state stabilization-change mechanism for proton-pumping complex i, *Biochimica et Biophysica Acta - Bioenergetics 1807*, 1364-1369.
169. Friedrich, T. (1998) The NADH:ubiquinone oxidoreductase (complex I) from Escherichia coli, *Biochimica et biophysica acta 1364*, 134-146.
170. Dutton, P. L., Moser, C. C., Sled, V. D., Daldal, F., and Ohnishi, T. (1998) A reductant-induced oxidation mechanism for Complex I, *Bba-Bioenergetics 1364*, 245-257.
171. Bottcher, B., Scheide, D., Hesterberg, M., Nagel-Steger, L., and Friedrich, T. (2002) A novel, enzymatically active conformation of the Escherichia coli NADH:ubiquinone oxidoreductase (complex I), *The Journal of biological chemistry 277*, 17970-17977.
172. Liu, Y., Fiskum, G., and Schubert, D. (2002) Generation of reactive oxygen species by the mitochondrial electron transport chain, *Journal of neurochemistry 80*, 780-787.
173. McLennan, H. R., and Degli Esposti, M. (2000) The contribution of mitochondrial respiratory complexes to the production of reactive oxygen species, *Journal of bioenergetics and biomembranes 32*, 153-162.

174. Kussmaul, L., and Hirst, J. (2006) The mechanism of superoxide production by NADH:ubiquinone oxidoreductase (complex I) from bovine heart mitochondria, *Proc Natl Acad Sci U S A 103*, 7607-7612.
175. Efremov, R. G., and Sazanov, L. A. (2011) Structure of the membrane domain of respiratory complex I, *Nature 476*, 414-420.
176. Cheresh, P., Kim, S. J., Tulasiram, S., and Kamp, D. W. (2013) Oxidative stress and pulmonary fibrosis, *Biochimica et Biophysica Acta - Molecular Basis of Disease 1832*, 1028-1040.
177. Han, Y., and Chen, J. Z. (2013) Oxidative stress induces mitochondrial DNA damage and cytotoxicity through independent mechanisms in human cancer cells, *BioMed research international 2013*.
178. Fedotcheva, T. A., Kruglov, A. G., Teplova, V. V., Fedotcheva, N. I., Rzheznikov, V. M., and Shimanovskii, N. L. (2012) Effect of steroid hormones on production of reactive oxygen species in mitochondria, *Biophysics (Russian Federation) 57*, 792-795.
179. Blake, R., and Trounce, I. A. (2013) Mitochondrial dysfunction and complications associated with diabetes, *Biochimica et Biophysica Acta - General Subjects*.
180. Yu, Z., Poppe, J. L., and Wang, X. (2013) Mitochondrial mechanisms of neuroglobin's neuroprotection, *Oxidative medicine and cellular longevity 2013*, 756989.
181. James Surmeier, D., Guzman, J. N., Sanchez, J., and Schumacker, P. T. (2012) Physiological phenotype and vulnerability in Parkinson's disease, *Cold Spring Harbor Perspectives in Medicine 2*.
182. Brennan, L. A., and Kantorow, M. (2009) Mitochondrial function and redox control in the aging eye: Role of MsrA and other repair systems in cataract and macular degenerations, *Experimental Eye Research 88*, 195-203.
183. Baradaran, R., Berrisford, J. M., Minhas, G. S., and Sazanov, L. A. (2013) Crystal structure of the entire respiratory complex I, *Nature 494*, 443-448.
184. Friedrich, T., Hofhaus, G., Ise, W., Nehls, U., Schmitz, B., and Weiss, H. (1989) A small isoform of NADH:ubiquinone oxidoreductase (complex I) without mitochondrially encoded subunits is made in chloramphenicol-treated Neurospora crassa, *European journal of biochemistry / FEBS 180*, 173-180.
185. Gershoni, M., Fuchs, A., Shani, N., Fridman, Y., Corral-Debrinski, M., Aharoni, A., Frishman, D., and Mishmar, D. (2010) Coevolution predicts direct interactions between mtDNA-encoded and nDNA-encoded subunits of oxidative phosphorylation complex I, *Journal of Molecular Biology 404*, 158-171.
186. Efremov, R. G., and Sazanov, L. A. (2012) The coupling mechanism of respiratory complex i - A structural and evolutionary perspective, *Biochimica et Biophysica Acta - Bioenergetics 1817*, 1785-1795.
187. Hunte, C., Zickermann, V., and Brandt, U. (2010) Functional modules and structural basis of conformational coupling in mitochondrial complex I, *Science 329*, 448-451.
188. Ohnishi, T. (1998) Iron-sulfur clusters semiquinones in Complex I, *Bba-Bioenergetics 1364*, 186-206.
189. Guenebaut, V., Schlitt, A., Weiss, H., Leonard, K., and Friedrich, T. (1998) Consistent structure between bacterial and mitochondrial NADH:ubiquinone oxidoreductase (complex I), *J Mol Biol 276*, 105-112.
190. Baranova, E. A., Holt, P. J., and Sazanov, L. A. (2007) Projection structure of the membrane domain of Escherichia coli respiratory complex I at 8 A resolution, *J Mol Biol 366*, 140-154.
191. Birrell, J. A., and Hirst, J. (2013) Investigation of NADH binding, hydride transfer, and NAD(+) dissociation during NADH oxidation by mitochondrial complex I using modified nicotinamide nucleotides, *Biochemistry 52*, 4048-4055.

192. Kleinschroth, T., Anderka, O., Ritter, M., Stocker, A., Link, T. A., Ludwig, B., and Hellwig, P. (2008) Characterization of mutations in crucial residues around the Q(o) binding site of the cytochrome bc complex from Paracoccus denitrificans, *The FEBS journal 275*, 4773-4785.
193. Tocilescu, M. A., Zickermann, V., Zwicker, K., and Brandt, U. (2010) Quinone binding and reduction by respiratory complex I, *Biochimica et biophysica acta 1797*, 1883-1890.
194. Verkhovskaya, M., and Bloch, D. A. (2013) Energy-converting respiratory Complex I: on the way to the molecular mechanism of the proton pump, *The international journal of biochemistry & cell biology 45*, 491-511.
195. Friedrich, T., Abelmann, A., Brors, B., Guenebaut, V., Kintscher, L., Leonard, K., Rasmussen, T., Scheide, D., Schlitt, A., Schulte, U., and Weiss, H. (1998) Redox components and structure of the respiratory NADH:ubiquinone oxidoreductase (complex I), *Biochimica et biophysica acta 1365*, 215-219.
196. Clason, T., Ruiz, T., Schagger, H., Peng, G., Zickermann, V., Brandt, U., Michel, H., and Radermacher, M. (2010) The structure of eukaryotic and prokaryotic complex I, *Journal of structural biology 169*, 81-88.
197. Pohl, T., Spatzal, T., Aksoyoglu, M., Schleicher, E., Rostas, A. M., Lay, H., Glessner, U., Boudon, C., Hellwig, P., Weber, S., and Friedrich, T. (2010) Spin labeling of the Escherichia coli NADH ubiquinone oxidoreductase (complex I), *Biochimica et biophysica acta 1797*, 1894-1900.
198. Gabaldón, T., Rainey, D., and Huynen, M. A. (2005) Tracing the evolution of a large protein complex in the eukaryotes, NADH:ubiquinone oxidoreductase (Complex I), *Journal of Molecular Biology 348*, 857-870.
199. Cardol, P. (2011) Mitochondrial NADH:Ubiquinone oxidoreductase (complex I) in eukaryotes: A highly conserved subunit composition highlighted by mining of protein databases, *Biochimica et Biophysica Acta - Bioenergetics 1807*, 1390-1397.
200. Screpanti, E., and Hunte, C. (2007) Discontinuous membrane helices in transport proteins and their correlation with function, *Journal of structural biology 159*, 261-267.
201. Martha, V. (2013) Heterologous production, purification and characterization of respiratory proteins from *Aquifex aeolicus* in *Escherichia coli* strains, In *Faculty of Chemistry and Pharmacy*, Albert-Ludwigs-Universität Freiburg, Freiburg, Germany.
202. Schuler, F., and Casida, J. E. (2001) Functional coupling of PSST and ND1 subunits in NADH:ubiquinone oxidoreductase established by photoaffinity labeling, *Biochimica et Biophysica Acta - Bioenergetics 1506*, 79-87.
203. Lambert, A. J., and Brand, M. D. (2004) Inhibitors of the quinone-binding site allow rapid superoxide production from mitochondrial NADH:ubiquinone oxidoreductase (complex I), *Journal of Biological Chemistry 279*, 39414-39420.
204. Fato, R., Bergamini, C., Bortolus, M., Maniero, A. L., Leoni, S., Ohnishi, T., and Lenaz, G. (2009) Differential effects of mitochondrial Complex I inhibitors on production of reactive oxygen species, *Biochimica et Biophysica Acta - Bioenergetics 1787*, 384-392.
205. Verkhovskaya, M. L., Belevich, N., Euro, L., Wikstrom, M., and Verkhovsky, M. I. (2008) Real-time electron transfer in respiratory complex I, *Proc Natl Acad Sci U S A 105*, 3763-3767.
206. Friedrich, T., and Böttcher, B. (2004) The gross structure of the respiratory complex I: A Lego System, *Biochimica et Biophysica Acta - Bioenergetics 1608*, 1-9.
207. Braun, M., Bungert, S., and Friedrich, T. (1998) Characterization of the overproduced NADH dehydrogenase fragment of the NADH:ubiquinone oxidoreductase (complex I) from Escherichia coli, *Biochemistry 37*, 1861-1867.
208. Tocilescu, M. A., Fendel, U., Zwicker, K., Drose, S., Kerscher, S., and Brandt, U. (2010) The role of a conserved tyrosine in the 49-kDa subunit of complex I for ubiquinone binding and reduction, *Biochimica et biophysica acta 1797*, 625-632.
209. Hellwig, P., Scheide, D., Bungert, S., Mantele, W., and Friedrich, T. (2000) FT-IR spectroscopic characterization of NADH:ubiquinone oxidoreductase (complex I) from Escherichia coli:

oxidation of FeS cluster N2 is coupled with the protonation of an aspartate or glutamate side chain, *Biochemistry 39*, 10884-10891.

210. Flemming, D., Stolpe, S., Schneider, D., Hellwig, P., and Friedrich, T. (2005) A possible role for iron-sulfur cluster N2 in proton translocation by the NADH: ubiquinone oxidoreductase (complex I), *Journal of molecular microbiology and biotechnology 10*, 208-222.
211. Page, C. C., Moser, C. C., Chen, X., and Dutton, P. L. (1999) Natural engineering principles of electron tunnelling in biological oxidation-reduction, *Nature 402*, 47-52.
212. Ohnishi, T., Ohnishi, S. T., Shinzawa-Itoh, K., Yoshikawa, S., and Weber, R. T. (2012) EPR detection of two protein-associated ubiquinone components (SQ(Nf) and SQ(Ns)) in the membrane in situ and in proteoliposomes of isolated bovine heart complex I, *Biochimica et biophysica acta 1817*, 1803-1809.
213. Jeuken, L. J. C., Jones, A. K., Chapman, S. K., Cecchini, G., and Armstrong, F. A. (2002) Electron-transfer mechanisms through biological redox chains in multicenter enzymes, *Journal of the American Chemical Society 124*, 5702-5713.
214. Hayashi, T., and Stuchebrukhov, A. A. (2010) Electron tunneling in respiratory complex I, *Proc Natl Acad Sci U S A 107*, 19157-19162.
215. Euro, L., Bloch, D. A., Wikstrom, M., Verkhovsky, M. I., and Verkhovskaya, M. (2008) Electrostatic interactions between FeS clusters in NADH:ubiquinone oxidoreductase (Complex I) from Escherichia coli, *Biochemistry 47*, 3185-3193.
216. Roessler, M. M., King, M. S., Robinson, A. J., Armstrong, F. A., Harmer, J., and Hirst, J. (2010) Direct assignment of EPR spectra to structurally defined iron-sulfur clusters in complex I by double electron-electron resonance, *Proc Natl Acad Sci U S A 107*, 1930-1935.
217. Bridges, H. R., Bill, E., and Hirst, J. (2012) Mössbauer spectroscopy on respiratory complex I: The iron-sulfur cluster ensemble in the NADH-reduced enzyme is partially oxidized, *Biochemistry 51*, 149-158.
218. Pohl, T., Bauer, T., Dorner, K., Stolpe, S., Sell, P., Zocher, G., and Friedrich, T. (2007) Iron-sulfur cluster N7 of the NADH:ubiquinone oxidoreductase (complex I) is essential for stability but not involved in electron transfer, *Biochemistry 46*, 6588-6596.
219. Verkhovsky, M., Bloch, D. A., and Verkhovskaya, M. (2012) Tightly-bound ubiquinone in the Escherichia coli respiratory complex I, *Biochimica et biophysica acta 1817*, 1550-1556.
220. Friedrich, T., Brors, B., Hellwig, P., Kintscher, L., Rasmussen, T., Scheide, D., Schulte, U., Mantele, W., and Weiss, H. (2000) Characterization of two novel redox groups in the respiratory NADH:ubiquinone oxidoreductase (complex I), *Biochimica et biophysica acta 1459*, 305-309.
221. Batista, A. P., Marreiros, B. C., and Pereira, M. M. (2012) The role of proton and sodium ions in energy transduction by respiratory complex i, *IUBMB Life 64*, 492-498.
222. Dieteren, C. E. J., Koopman, W. J. H., Swarts, H. G., Peters, J. G. P., Maczuga, P., Van Gemst, J. J., Masereeuw, R., Smeitink, J. A. M., Nijtmans, L. G. J., and Willems, P. H. G. M. (2012) Subunit-specific incorporation efficiency and kinetics in mitochondrial complex i homeostasis, *Journal of Biological Chemistry 287*, 41851-41860.
223. Staples, C. R., Ameyibor, E., Fu, W., Gardet-Salvi, L., Stritt-Etter, A. L., Schurmann, P., Knaff, D. B., and Johnson, M. K. (1996) The function and properties of the iron-sulfur center in spinach ferredoxin: thioredoxin reductase: a new biological role for iron-sulfur clusters, *Biochemistry 35*, 11425-11434.
224. Efremov, R. G., Baradaran, R., and Sazanov, L. A. (2010) The architecture of respiratory complex I, *Nature 465*, 441-445.
225. Andreyev, A. Y., Kushnareva, Y. E., and Starkov, A. A. (2005) Mitochondrial metabolism of reactive oxygen species, *Biochemistry. Biokhimiia 70*, 200-214.
226. Kohlstadt, M., Dorner, K., Labatzke, R., Koc, C., Hielscher, R., Schiltz, E., Einsle, O., Hellwig, P., and Friedrich, T. (2008) Heterologous Production, Isolation, Characterization and

Crystallization of a Soluble Fragment of the NADH:Ubiquinone Oxidoreductase (Complex I) from Aquifex aeolicus, *Biochemistry*.

227. Sled, V. D., Friedrich, T., Leif, H., Weiss, H., Meinhardt, S. W., Fukumori, Y., Calhoun, M. W., Gennis, R. B., and Ohnishi, T. (1993) Bacterial NADH-quinone oxidoreductases: iron-sulfur clusters and related problems, *Journal of bioenergetics and biomembranes 25*, 347-356.
228. Fernandes, A. S., Pereira, M. M., and Teixeira, M. (2002) Purification and characterization of the complex I from the respiratory chain of Rhodothermus marinus, *Journal of bioenergetics and biomembranes 34*, 413-421.
229. Flemming, D., Hellwig, P., and Friedrich, T. (2003) Involvement of tyrosines 114 and 139 of subunit NuoB in the proton pathway around cluster N2 in Escherichia coli NADH:ubiquinone oxidoreductase, *The Journal of biological chemistry 278*, 3055-3062.
230. Friedrich, T., and Hellwig, P. (2010) Redox-induced conformational changes within the Escherichia coli NADH ubiquinone oxidoreductase (complex I): an analysis by mutagenesis and FT-IR spectroscopy, *Biochimica et biophysica acta 1797*, 659-663.
231. Zwicker, K., Galkin, A., Drose, S., Grgic, L., Kerscher, S., and Brandt, U. (2006) The Redox-Bohr group associated with iron-sulfur cluster N2 of complex I, *The Journal of biological chemistry 281*, 23013-23017.
232. Hielscher, R. (2009) The role of lipids and nucleotides in the catalytic mechanism of proteins from the respiratory chain, In *Faculty of Chemistry*, p 156, Universitè de Strasbourg, Strasbourg.
233. Haris, P. I., Robillard, G. T., Vandijk, A. A., and Chapman, D. (1992) Potential of C-13 and N-15 Labeling for Studying Protein-Protein Interactions Using Fourier-Transform Infrared-Spectroscopy, *Biochemistry 31*, 6279-6284.
234. Hollas, N. M. (2004) *Modern Spectroscopy*, 4th ed., Wiley, West Sussex, England.
235. Dorr, S., Schade, U., Hellwig, P., and Ortolani, M. (2007) Characterization of temperature-dependent iron-imidazole vibrational modes in far infrared, *The journal of physical chemistry. B 111*, 14418-14422.
236. Bengt, N. (2006) *Methods in Modern Biophysics*, 2nd ed., Springer, Germany.
237. Smith, E. a. D., Geoffrey (2005) *Modern Raman spectroscopy - A Practical Approach*, John Wiley and Sons, Ltd, England.
238. Babaei, A., Connor, P. A., McQuillan, A. J., and Umapathy, S. (1997) UV-Visible Spectrooelectrochemistry of the Reduction Products of Anthraquinone in Dimethylformamide Solutions: An Advanced Undergraduate Experiment, *Journal of Chemical Education 74*, 1200.
239. Voicescu, M., Angelescu, D. G., Ionescu, S., and Teodorescu, V. S. (2013) Spectroscopic analysis of the riboflavin-serum albumins interaction on silver nanoparticles, *J Nanopart Res 15*.
240. Gremlich, H. G. a. H.-U. (2003) *Handbook of Spectroscopy*, Wiley-VCH GmBH and Co. KGaA, Weinheim.
241. Voicescu, M., Rother, D., Bardischewsky, F., Friedrich, C. G., and Hellwig, P. (2011) A combined fluorescence spectroscopic and electrochemical approach for the study of thioredoxins, *Biochemistry 50*, 17-24.
242. Neehaul, Y., Chen, Y., Werner, C., Fee, J. A., Ludwig, B., and Hellwig, P. (2012) Electrochemical and infrared spectroscopic analysis of the interaction of the Cu-A domain and cytochrome c(552) from Thermus thermophilus, *Bba-Bioenergetics 1817*, 1950-1954.
243. Schulte, U., Abelmann, A., Amling, N., Brors, B., Friedrich, T., Kintscher, L., Rasmussen, T., and Weiss, H. (1998) Search for novel redox groups in mitochondrial NADH:ubiquinone oxidoreductase (complex I) by diode array UV/VIS spectroscopy, *Biofactors 8*, 177-186.
244. Kong, J., and Yu, S. (2007) Fourier transform infrared spectroscopic analysis of protein secondary structures, *Acta biochimica et biophysica Sinica 39*, 549-559.

245. Goldberg, M. E., and Chaffotte, A. F. (2005) Undistorted structural analysis of soluble proteins by attenuated total reflectance infrared spectroscopy, *Protein Sci 14*, 2781-2792.
246. Mikhonin, A. V., Ahmed, Z., Ianoul, A., and Asher, S. A. (2004) Assignments and conformational dependencies of the amide III peptide backbone UV resonance Raman bands, *Journal of Physical Chemistry B 108*, 19020-19028.
247. Barth, A. (2007) Infrared spectroscopy of proteins, *Bba-Bioenergetics 1767*, 1073-1101.
248. Haris, P. I., and Chapman, D. (1992) Does Fourier-Transform Infrared-Spectroscopy Provide Useful Information on Protein Structures, *Trends Biochem Sci 17*, 328-333.
249. Cai, S. W., and Singh, B. R. (2004) A distinct utility of the amide III infrared band for secondary structure estimation of aqueous protein solutions using partial least squares methods, *Biochemistry 43*, 2541-2549.
250. Barth, A. (2000) The infrared absorption of amino acid side chains, *Prog Biophys Mol Bio 74*, 141-173.
251. Hasegawa, K., Ono, T.-a., and Noguchi, T. (2000) Vibrational Spectra and Ab Initio DFT Calculations of 4-Methylimidazole and Its Different Protonation Forms: Infrared and Raman Markers of the Protonation State of a Histidine Side Chain, *The Journal of Physical Chemistry B 104*, 4253-4265.
252. Oladepo, S. A., Xiong, K., Hong, Z., and Asher, S. A. (2011) Elucidating Peptide and Protein Structure and Dynamics: UV Resonance Raman Spectroscopy, *The journal of physical chemistry letters 2*, 334-344.
253. Kumar, S., and Barth, A. (2011) The Allosteric Effect of Fructose Bisphosphate on Muscle Pyruvate Kinase Studied by Infrared Spectroscopy, *Journal of Physical Chemistry B 115*, 11501-11505.
254. Kumar, S., and Barth, A. (2010) Following Enzyme Activity with Infrared Spectroscopy, *Sensors-Basel 10*, 2626-2637.
255. Valdivia, A. A., Barth, A., Batista, Y. R., and Kumar, S. (2013) Characterization of recombinant antibodies for cancer therapy by infrared spectroscopy, *Biologicals 41*, 104-110.
256. Barth, A. (1999) Phosphoenzyme conversion of the sarcoplasmic reticulum Ca2+-ATPase - Molecular interpretation of infrared difference spectra, *Journal of Biological Chemistry 274*, 22170-22175.
257. Xie, A., van der Meer, L., and Austin, R. H. (2002) Excited-state lifetimes of far-infrared collective modes in proteins, *J Biol Phys 28*, 147-154.
258. Miyazawa, T., Shimanouchi, T., and Muzushima, S. I. (1958) Normal vibrations of N-methylacetamide, *The Journal of Chemical Physics 29*, 611-616.
259. El Khoury, Y., Hielscher, R., Voicescu, M., Gross, J., and Hellwig, P. (2011) On the specificity of the amide VI band for the secondary structure of proteins, *Vib Spectrosc 55*, 258-266.
260. L I Maklakov, S. V. A. (1997) Low-frequency vibrational spectroscopy of amides and urethanes *Russian Chemical Reviews 66*, 375-388.
261. El Khoury, Y., and Hellwig, P. (2009) Infrared spectroscopic characterization of copper-polyhistidine from 1,800 to 50 cm(-1): model systems for copper coordination, *Journal of biological inorganic chemistry : JBIC : a publication of the Society of Biological Inorganic Chemistry 14*, 23-34.
262. Marboutin, L., Desbois, A., and Berthomieu, C. (2009) Low-frequency heme, iron-ligand, and ligand modes of imidazole and imidazolate complexes of iron protoporphyrin and microperoxidase in aqueous solution. An analysis by far-infrared difference spectroscopy, *The journal of physical chemistry. B 113*, 4492-4499.
263. Tremey, E., Bonnot, F., Moreau, Y., Berthomieu, C., Desbois, A., Favaudon, V., Blondin, G., Houee-Levin, C., and Niviere, V. (2013) Hydrogen bonding to the cysteine ligand of superoxide reductase: acid-base control of the reaction intermediates, *Journal of biological*

inorganic chemistry : JBIC : a publication of the Society of Biological Inorganic Chemistry 18, 815-830.

264. Ryan, M. D., Li, L., and Matyniak, N. (2003) Far infrared and resonance Raman spectroelectrochemistry of Mo/Fe/S clusters, *J Inorg Biochem 96*, 222-222.
265. Vita, N., Brubach, J. B., Hienerwadel, R., Bremond, N., Berthomieu, D., Roy, P., and Berthomieu, C. (2013) Electrochemically induced far-infrared difference spectroscopy on metalloproteins using advanced synchrotron technology, *Anal Chem 85*, 2891-2898.
266. El Khoury, Y., and Hellwig, P. (2011) A combined far-infrared spectroscopic and electrochemical approach for the study of iron-sulfur proteins, *Chemphyschem : a European journal of chemical physics and physical chemistry 12*, 2669-2674.
267. Xerri, B., Flament, J. P., Petitjean, H., Berthomieu, C., and Berthomieu, D. (2009) Vibrational modeling of copper-histamine complexes: metal-ligand IR modes investigation, *The journal of physical chemistry. B 113*, 15119-15127.
268. Spiro, T. G., and Strekas, T. C. (1974) Resonance Raman spectra of heme proteins. Effects of oxidation and spin state, *J Am Chem Soc 96*, 338-345.
269. Tang, S. P., Spiro, T. G., Mukai, K., and Kimura, T. (1973) Resonance Raman scattering and optical absorption of adrenodoxin and selena-adrenodoxin, *Biochem Biophys Res Commun 53*, 869-874.
270. Moulis, J. M., Meyer, J., and Lutz, M. (1984) Characterization of [4Fe-4S]2+, [4Fe-4Se]2+ and hybrid (S, Se) clusters in Clostridium pasteurianum ferredoxin. A resonance Raman study, *The Biochemical journal 219*, 829-832.
271. Johnson, M. K., Hare, J. W., Spiro, T. G., Moura, J. J., Xavier, A. V., and LeGall, J. (1981) Resonance Raman spectra of three-iron centers in ferredoxins from Desulfovibrio gigas, *J Biol Chem 256*, 9806-9808.
272. El Khoury, Y., Trivella, A., Gross, J., and Hellwig, P. (2010) Probing the hydrogen bonding structure in the Rieske protein, *Chemphyschem : a European journal of chemical physics and physical chemistry 11*, 3313-3319.
273. MacMillan, F., Kacprzak, S., Hellwig, P., Grimaldi, S., Michel, H., and Kaupp, M. (2011) Elucidating mechanisms in haem copper oxidases: the high-affinity QH binding site in quinol oxidase as studied by DONUT-HYSCORE spectroscopy and density functional theory, *Faraday discussions 148*, 315-344; discussion 421-341.
274. Pohl, T., Uhlmann, M., Kaufenstein, M., and Friedrich, T. (2007) Lambda Red-mediated mutagenesis and efficient large scale affinity purification of the Escherichia coli NADH:ubiquinone oxidoreductase (complex I), *Biochemistry 46*, 10694-10702.
275. Wallace, B. J., and Young, I. G. (1977) Role of quinones in electron transport to oxygen and nitrate in Escherichia coli. Studies with a ubiA− menA− double quinone mutant, *Biochimica et Biophysica Acta (BBA) - Bioenergetics 461*, 84-100.
276. Bungert, S., Krafft, B., Schlesinger, R., and Friedrich, T. (1999) One-step purification of the NADH dehydrogenase fragment of the Escherichia coli complex I by means of Strep-tag affinity chromatography, *FEBS letters 460*, 207-211.
277. Studier, F. W., and Moffatt, B. A. (1986) Use of bacteriophage T7 RNA polymerase to direct selective high-level expression of cloned genes, *Journal of Molecular Biology 189*, 113-130.
278. Miller, J. H. (1972) *Experiments in molecular genetics*, [Cold Spring Harbor, N. Y.] Cold Spring Harbor Laboratory, United States.
279. Grull, J. M., Hennecke, H., Frohler, J., Thomale, J., Nass, G., and Bock, A. (1979) Escherichia-Coli Mutants over-Producing Phenylalanyl-Synthetase and Threonyl-Transfer Rna-Synthetase, *Journal of bacteriology 137*, 480-489.
280. Kohlstädt, M., Dörner, K., Labatzke, R., Koç, C., Hielscher, R., Schiltz, E., Einsle, O., Hellwig, P., and Friedrich, T. (2008) Heterologous production, isolation, characterization and

crystallization of a soluble fragment of the NADH:ubiquinone oxidoreductase (Complex I) from Aquifex aeolicus, *Biochemistry 47*, 13036-13045.

281. Fournane, S., Charbonnier, S., Chapelle, A., Kieffer, B., Orfanoudakis, G., Travé, G., Masson, M., and Nominé, Y. (2011) Surface plasmon resonance analysis of the binding of high-risk mucosal HPV E6 oncoproteins to the PDZ1 domain of the tight junction protein MAGI-1, *Journal of Molecular Recognition 24*, 511-523.
282. Andrushchenko, V. V., Vogel, H. J., and Prenner, E. J. (2007) Optimization of the hydrochloric acid concentration used for trifluoroacetate removal from synthetic peptides, *Journal of Peptide Science 13*, 37-43.
283. Roux, S., Zékri, E., Rousseau, B., Cintrat, J. C., and Fay, N. (2008) Elimination and exchange of trifluoroacetate counter-ion from cationic peptides: A critical evaluation of different approaches, *Journal of Peptide Science 14*, 354-359.
284. Hellwig, P., Rost, B., Kaiser, U., Ostermeier, C., Michel, H., and Mantele, W. (1996) Carboxyl group protonation upon reduction of the Paracoccus denitrificans cytochrome c oxidase: direct evidence by FTIR spectroscopy, *FEBS letters 385*, 53-57.
285. Neehaul, Y., Juárez, O., Barquera, B., and Hellwig, P. (2012) Thermodynamic Contribution to the Regulation of Electron Transfer in the Na+-Pumping NADH:Quinone Oxidoreductase from Vibrio cholerae, *Biochemistry 51*, 4072-4077.
286. Baymann, F., Moss, D. A., and Mantele, W. (1991) An Electrochemical Assay for the Characterization of Redox Proteins from Biological Electron-Transfer Chains, *Anal Biochem 199*, 269-274.
287. Bauscher, M., and Mantele, W. (1992) Electrochemical and Infrared-Spectroscopic Characterization of Redox Reactions of P-Quinones, *J Phys Chem-Us 96*, 11101-11108.
288. Thoenges, D., and Barth, A. (2002) Direct measurement of enzyme activity with infrared spectroscopy, *J Biomol Screen 7*, 353-357.
289. Fabian, H., and Anzenbacher, P. (1993) New developments in Raman spectroscopy of biological systems, *Vib Spectrosc 4*, 125-148.
290. Barth, A., and Zscherp, C. (2000) Substrate binding and enzyme function investigated by infrared spectroscopy, *FEBS letters 477*, 151-156.
291. Venyaminov, S., and Kalnin, N. N. (1990) Quantitative IR spectrophotometry of peptide compounds in water (H2O) solutions. II. Amide absorption bands of polypeptides and fibrous proteins in alpha-, beta-, and random coil conformations, *Biopolymers 30*, 1259-1271.
292. Kalnin, N. N., Baikalov, I. A., and Venyaminov, S. (1990) Quantitative IR spectrophotometry of peptide compounds in water (H2O) solutions. III. Estimation of the protein secondary structure, *Biopolymers 30*, 1273-1280.
293. Byler, D. M., and Susi, H. (1986) Examination of the secondary structure of proteins by deconvolved FTIR spectra, *Biopolymers 25*, 469-487.
294. Goormaghtigh, E., Cabiaux, V., and Ruysschaert, J. M. (1994) Determination of soluble and membrane protein structure by Fourier transform infrared spectroscopy. III. Secondary structures, *Sub-cellular biochemistry 23*, 405-450.
295. Narayanan, M., Gabrieli, D. J., Leung, S. A., Elguindy, M. M., Glaser, C. A., Saju, N., Sinha, S. C., and Nakamaru-Ogiso, E. (2013) Semiquinone and Cluster N6 Signals in His-tagged Proton-translocating NADH:Ubiquinone Oxidoreductase (Complex I) from Escherichia coli, *J Biol Chem 288*, 14310-14319.
296. Nomine, Y., Charbonnier, S., Miguet, L., Potier, N., Van Dorsselaer, A., Atkinson, R. A., Trave, G., and Kieffer, B. (2005) 1H and 15N resonance assignment, secondary structure and dynamic behaviour of the C-terminal domain of human papillomavirus oncoprotein E6, *J Biomol NMR 31*, 129-141.
297. Nomine, Y., Masson, M., Charbonnier, S., Zanier, K., Ristriani, T., Deryckere, F., Sibler, A. P., Desplancq, D., Atkinson, R. A., Weiss, E., Orfanoudakis, G., Kieffer, B., and Trave, G. (2006)

Structural and functional analysis of E6 oncoprotein: insights in the molecular pathways of human papillomavirus-mediated pathogenesis, *Molecular cell 21*, 665-678.

298. Fournane, S., Charbonnier, S., Chapelle, A., Kieffer, B., Orfanoudakis, G., Trave, G., Masson, M., and Nomine, Y. (2011) Surface plasmon resonance analysis of the binding of high-risk mucosal HPV E6 oncoproteins to the PDZ1 domain of the tight junction protein MAGI-1, *J Mol Recognit 24*, 511-523.
299. Wong, P. T. T., Wong, R. K., Caputo, T. A., Godwin, T. A., and Rigas, B. (1991) Infrared spectroscopy of exfoliated human cervical cells: Evidence of extensive structural changes during carcinogenesis, *Proceedings of the National Academy of Sciences of the United States of America 88*, 10988-10992.
300. Rigas, B., Morgello, S., Goldman, I. S., and Wong, P. T. (1990) Human colorectal cancers display abnormal Fourier-transform infrared spectra, *Proceedings of the National Academy of Sciences 87*, 8140-8144.
301. Krafft, C., and Popp, J. (2012) Diagnosis and screening of cancer tissues by vibrational spectroscopy, pp 212-237.
302. Wolpert, M., and Hellwig, P. (2006) Infrared spectra and molar absorption coefficients of the 20 alpha amino acids in aqueous solutions in the spectral range from 1800 to 500 cm(-1), *Spectrochimica acta. Part A, Molecular and biomolecular spectroscopy 64*, 987-1001.
303. Trivella, A., Gaillard, T., Stote, R. H., and Hellwig, P. (2010) Far infrared spectra of solid state aliphatic amino acids in different protonation states, *J Chem Phys 132*, 115105.
304. Matei, A., Drichko, N., Gompf, B., and Dressel, M. (2005) Far-infrared spectra of amino acids, *Chem Phys 316*, 61-71.
305. Brubach, J. B., Mermet, A., Filabozzi, A., Gerschel, A., and Roy, P. (2005) Signatures of the hydrogen bonding in the infrared bands of water, *J Chem Phys 122*.
306. Ding, T., Middelberg, A. P. J., Huber, T., and Falconer, R. J. (2012) Far-infrared spectroscopy analysis of linear and cyclic peptides, and lysozyme, *Vib Spectrosc 61*, 144-150.
307. Choi, J. H., and Cho, M. (2013) Computational IR spectroscopy of water: OH stretch frequencies, transition dipoles, and intermolecular vibrational coupling constants, *J Chem Phys 138*.
308. Overman, S. A., and Thomas, G. J., Jr. (1998) Amide modes of the alpha-helix: Raman spectroscopy of filamentous virus fd containing peptide 13C and 2H labels in coat protein subunits, *Biochemistry 37*, 5654-5665.
309. Jenkins, A. L., Larsen, R. A., and Williams, T. B. (2005) Characterization of amino acids using Raman spectroscopy, *Spectrochim Acta A 61*, 1585-1594.
310. Zhu, G., Zhu, X., Fan, Q., and Wan, X. (2011) Raman spectra of amino acids and their aqueous solutions, *Spectrochimica Acta Part A: Molecular and Biomolecular Spectroscopy 78*, 1187-1195.
311. Howell, N. K., Arteaga, G., Nakai, S., and Li-Chan, E. C. Y. (1999) Raman Spectral Analysis in the C–H Stretching Region of Proteins and Amino Acids for Investigation of Hydrophobic Interactions, *Journal of Agricultural and Food Chemistry 47*, 924-933.
312. Charbonnier, S., Nomine, Y., Ramirez, J., Luck, K., Chapelle, A., Stote, R. H., Trave, G., Kieffer, B., and Atkinson, R. A. (2011) The structural and dynamic response of MAGI-1 PDZ1 with noncanonical domain boundaries to the binding of human papillomavirus E6, *J Mol Biol 406*, 745-763.
313. Culka, A., Jehlička, J., and Edwards, H. G. M. (2010) Acquisition of Raman spectra of amino acids using portable instruments: Outdoor measurements and comparison, *Spectrochimica Acta Part A: Molecular and Biomolecular Spectroscopy 77*, 978-983.
314. Saras, J., and Heldin, C. H. (1996) PDZ domains bind carboxy-terminal sequences of target proteins, *Trends Biochem Sci 21*, 455-458.

315. Nomine, Y., Charbonnier, S., Ristriani, T., Stier, G., Masson, M., Cavusoglu, N., Van Dorsselaer, A., Weiss, E., Kieffer, B., and Trave, G. (2003) Domain substructure of HPV E6 oncoprotein: biophysical characterization of the E6 C-terminal DNA-binding domain, *Biochemistry 42*, 4909-4917.
316. Remaut, H., and Waksman, G. (2006) Protein-protein interaction through beta-strand addition, *Trends Biochem Sci 31*, 436-444.
317. Goormaghtigh, E., Cabiaux, V., and Ruysschaert, J. M. (1994) Determination of soluble and membrane protein structure by Fourier transform infrared spectroscopy. III. Secondary structures, *Sub-cellular biochemistry 23*, 405-450.
318. Arrondo, J. L. R., Young, N. M., and Mantsch, H. H. (1988) The solution structure of concanavalin A probed by FT-IR spectroscopy, *Biochimica et Biophysica Acta (BBA)/Protein Structure and Molecular 952*, 261-268.
319. Cowburn, D. (1997) Peptide recognition by PTB and PDZ domains, *Current opinion in structural biology 7*, 835-838.
320. Papp, R., Ekiel, I., and English, A. M. (2003) ESI-MS and FTIR studies of the interaction between the second PDZ domain of hPTP1E and target peptides, *Biochemistry and cell biology = Biochimie et biologie cellulaire 81*, 71-80.
321. Tsuboi, M., Suzuki, M., Overman, S. A., and Thomas, G. J., Jr. (2000) Intensity of the polarized Raman band at 1340-1345 cm-1 as an indicator of protein alpha-helix orientation: application to Pf1 filamentous virus, *Biochemistry 39*, 2677-2684.
322. Choulier, L., Nomine, Y., Zeder-Lutz, G., Charbonnier, S., Didier, B., Jung, M. L., and Altschuh, D. (2013) Chemical Library Screening Using a SPR-Based Inhibition in Solution Assay: Simulations and Experimental Validation, *Anal Chem 85*, 8787-8795.
323. Chi, C. N., Bach, A., Stromgaard, K., Gianni, S., and Jemth, P. (2012) Ligand binding by PDZ domains, *Biofactors 38*, 338-348.
324. Luck, K., Charbonnier, S., and Trave, G. (2012) The emerging contribution of sequence context to the specificity of protein interactions mediated by PDZ domains, *FEBS letters 586*, 2648-2661.
325. Liu, Y., and Baleja, J. D. (2008) Structure and function of the papillomavirus E6 protein and its interacting proteins, *Frontiers in Bioscience 13*, 121-134.
326. Zanier, K., Ruhlmann, C., Melin, F., Masson, M., Ould M'hamed Ould Sidi, A., Bernard, X., Fischer, B., Brino, L., Ristriani, T., Rybin, V., Baltzinger, M., Vande Pol, S., Hellwig, P., Schultz, P., and Trave, G. (2010) E6 proteins from diverse papillomaviruses self-associate both in vitro and in vivo, *J Mol Biol 396*, 90-104.
327. Cecconi, F., De Los Rios, P., and Piazza, F. (2007) Diffusion-limited unbinding of small peptides from PDZ domains, *The journal of physical chemistry. B 111*, 11057-11063.
328. Kozlov, G., Gehring, K., and Ekiel, I. (2000) Solution structure of the PDZ2 domain from human phosphatase hPTP1E and its interactions with C-terminal peptides from the Fas receptor, *Biochemistry 39*, 2572-2580.
329. Armas, A., Sonois, V., Mothes, E., Mazarguil, H., and Faller, P. (2006) Zinc(II) binds to the neuroprotective peptide humanin, *Journal of inorganic biochemistry 100*, 1672-1678.
330. Bush, A. I. (2013) The metal theory of Alzheimer's disease, *Journal of Alzheimer's disease : JAD 33 Suppl 1*, S277-281.
331. Watt, A. D., Villemagne, V. L., and Barnham, K. J. (2013) Metals, membranes, and amyloid-beta oligomers: key pieces in the Alzheimer's disease puzzle?, *Journal of Alzheimer's disease : JAD 33 Suppl 1*, S283-293.
332. Alies, B., Bijani, C., Sayen, S., Guillon, E., Faller, P., and Hureau, C. (2012) Copper coordination to native N-terminally modified versus full-length amyloid-beta: second-sphere effects determine the species present at physiological pH, *Inorganic chemistry 51*, 12988-13000.

333. Nakamura, M., Shishido, N., Nunomura, A., Smith, M. A., Perry, G., Hayashi, Y., Nakayama, K., and Hayashi, T. (2007) Three histidine residues of amyloid-beta peptide control the redox activity of copper and iron, *Biochemistry 46*, 12737-12743.
334. Hureau, C., Coppel, Y., Dorlet, P., Solari, P. L., Sayen, S., Guillon, E., Sabater, L., and Faller, P. (2009) Deprotonation of the Asp1-Ala2 peptide bond induces modification of the dynamic copper(II) environment in the amyloid-beta peptide near physiological pH, *Angew Chem Int Ed Engl 48*, 9522-9525.
335. Thies, W., and Bleiler, L. (2013) 2013 Alzheimer's disease facts and figures, *Alzheimer's & dementia : the journal of the Alzheimer's Association 9*, 208-245.
336. Talmard, C., Guilloreau, L., Coppel, Y., Mazarguil, H., and Faller, P. (2007) Amyloid-beta peptide forms monomeric complexes with Cu(II) and Zn(II) prior to aggregation, *Chembiochem : a European journal of chemical biology 8*, 163-165.
337. Furlan, S., Hureau, C., Faller, P., and La Penna, G. (2012) Modeling copper binding to the amyloid-beta peptide at different pH: toward a molecular mechanism for Cu reduction, *The journal of physical chemistry. B 116*, 11899-11910.
338. Bin, Y., Chen, S., and Xiang, J. (2013) pH-dependent kinetics of copper ions binding to amyloid-beta peptide, *Journal of inorganic biochemistry 119*, 21-27.
339. Faller, P., Hureau, C., Dorlet, P., Hellwig, P., Coppel, Y., Collin, F., and Alies, B. (2012) Methods and techniques to study the bioinorganic chemistry of metal-peptide complexes linked to neurodegenerative diseases, *Coordination Chemistry Reviews 256*, 2381-2396.
340. Conato, C., Gavioli, R., Guerrini, R., Kozlowski, H., Mlynarz, P., Pasti, C., Pulidori, F., and Remelli, M. (2001) Copper complexes of glycyl-histidyl-lysine and two of its synthetic analogues: chemical behaviour and biological activity, *Biochimica et biophysica acta 1526*, 199-210.
341. Moss, D., Nabedryk, E., Breton, J., and Mantele, W. (1990) Redox-linked conformational changes in proteins detected by a combination of infrared spectroscopy and protein electrochemistry. Evaluation of the technique with cytochrome c, *European journal of biochemistry / FEBS 187*, 565-572.
342. Hasegawa, K., Ono, T. A., and Noguchi, T. (2000) Vibrational Spectra and Ab Initio DFT Calculations of 4-Methylimidazole and Its Different Protonation Forms: Infrared and Raman Markers of the Protonation State of a Histidine Side Chain, *Journal of Physical Chemistry B 104*, 4253-4265.
343. Miyamoto, T., Kamino, S., Odani, A., Hiromura, M., and Enomoto, S. (2013) Basicity of N-Terminal amine in ATCUN peptide regulates stability constant of albumin-like Cu2+ complex, *Chemistry Letters 42*, 1099-1101.
344. Barth, A., and Zscherp, C. (2002) What vibrations tell us about proteins, *Quarterly reviews of biophysics 35*, 369-430.
345. Barth, A. (2000) The infrared absorption of amino acid side chains, *Progress in biophysics and molecular biology 74*, 141-173.
346. Hienerwadel, R., Diner, B. A., and Berthomieu, C. (2008) Molecular origin of the pH dependence of tyrosine D oxidation kinetics and radical stability in photosystem II, *Biochimica et biophysica acta 1777*, 525-531.
347. Loksztejn, A., Dzwolak, W., and Krysinski, P. (2008) Tyrosine side chains as an electrochemical probe of stacked beta-sheet protein conformations, *Bioelectrochemistry 72*, 34-40.
348. Roberts, B. R., Ryan, T. M., Bush, A. I., Masters, C. L., and Duce, J. A. (2012) The role of metallobiology and amyloid-β peptides in Alzheimer's disease, *Journal of neurochemistry 120*, 149-166.
349. Garzon-Rodriguez, W., Yatsimirsky, A. K., and Glabe, C. G. (1999) Binding of Zn(II), Cu(II), and Fe(II) ions to alzheimer's Aß peptide studied by fluorescence, *Bioorganic & medicinal chemistry letters 9*, 2243-2248.

350. Faller, P. (2009) Copper and Zinc Binding to Amyloid-β: Coordination, Dynamics, Aggregation, Reactivity and Metal-Ion Transfer, *Chembiochem : a European journal of chemical biology 10*, 2837-2845.
351. Hardy, J., and Selkoe, D. J. (2002) The amyloid hypothesis of Alzheimer's disease: progress and problems on the road to therapeutics, *Science 297*, 353-356.
352. Johnson, M. K., Staples, C. R., Duin, E. C., Lafferty, M. E., and Duderstadt, R. E. (1998) Novel roles for Fe-S clusters in stabilizing or generating radical intermediates, *Pure and Applied Chemistry 70*, 939-946.
353. Kuila, D., Schoonover, J. R., Dyer, R. B., Batie, C. J., Ballou, D. P., Fee, J. A., and Woodruff, W. H. (1992) Resonance Raman studies of Rieske-type proteins, *Biochimica et biophysica acta 1140*, 175-183.
354. Vidakovic, M., Fraczkiewicz, G., Dave, B. C., Czernuszewicz, R. S., and Germanas, J. P. (1995) The environment of [2Fe-2S] clusters in ferredoxins: the role of residue 45 probed by site-directed mutagenesis, *Biochemistry 34*, 13906-13913.
355. Czernuszewicz, R. S., Macor, K. A., Johnson, M. K., Gewirth, A., and Spiro, T. G. (1987) Vibrational mode structure and symmetry in proteins and analogues containing Fe4S4 clusters: Resonance Raman evidence For different degrees of distortion in HiPIP and ferredoxin, *Journal of the American Chemical Society 109*, 7178-7187.
356. Mitra, D., Pelmenschikov, V., Guo, Y., Case, D. A., Wang, H., Dong, W., Tan, M. L., Ichiye, T., Jenney, F. E., Adams, M. W., Yoda, Y., Zhao, J., and Cramer, S. P. (2011) Dynamics of the [4Fe-4S] cluster in Pyrococcus furiosus D14C ferredoxin via nuclear resonance vibrational and resonance Raman spectroscopies, force field simulations, and density functional theory calculations, *Biochemistry 50*, 5220-5235.
357. Yachandra, V. K., Hare, J., Gewirth, A., Czernuszewicz, R. S., Kimura, T., Holm, R. H., and Spiro, T. G. (1983) Resonance Raman spectra of spinach ferredoxin and adrenodoxin and of analogue complexes, *Journal of the American Chemical Society 105*, 6462-6468.
358. Madden, J. F., Han, S. H., Siegel, L. M., and Spiro, T. G. (1989) Resonance Raman studies of Escherichia coli sulfite reductase hemoprotein. 2. Fe4S4 cluster vibrational modes, *Biochemistry 28*, 5471-5477.
359. Han, S., Czernuszewicz, R. S., Kimura, T., Adams, M. W. W., and Spiro, T. G. (1989) Fe2S2 protein resonance Raman spectra revisited: Structural variations among adrenodoxin, ferredoxin, and red paramagnetic protein, *Journal of the American Chemical Society 111*, 3505-3511.
360. Rasmussen, T., Scheide, D., Brors, B., Kintscher, L., Weiss, H., and Friedrich, T. (2001) Identification of two tetranuclear FeS clusters on the ferredoxin-type subunit of NADH:ubiquinone oxidoreductase (complex I), *Biochemistry 40*, 6124-6131.
361. Yeh, A. P., Chatelet, C., Soltis, S. M., Kuhn, P., Meyer, J., and Rees, D. C. (2000) Structure of a thioredoxin-like [2Fe-2S] ferredoxin from Aquifex aeolicus, *Journal of Molecular Biology 300*, 587-595.
362. Crouse, B. R., Yano, T., Finnegan, M. G., Yagi, T., and Johnson, M. K. (1994) Properties of the iron-sulfur center in the 25-kilodalton subunit of the proton-translocating NADH-quinone oxidoreductase of Paracoccus denitrificans, *J Biol Chem 269*, 21030-21036.
363. Meyer, J., Moulis, J. M., and Lutz, M. (1984) Structural differences between [2Fe-2S] clusters in spinach ferredoxin and in the "red paramagnetic protein" from Clostridium pasteurianum. A resonance Raman study, *Biochem Biophys Res Commun 119*, 828-835.
364. Tirrell, T. F., Paddock, M. L., Conlan, A. R., Smoll Jr, E. J., Nechushtai, R., Jennings, P. A., and Kim, J. E. (2009) Resonance Raman studies of the (His)(Cys)3 2Fe-2S cluster of mitoNEET: Comparison to the (Cys)4 mutant and implications of the effects of pH on the labile metal center, *Biochemistry 48*, 4747-4752.

365. Evangeliou, A., Lionis, C., Michailidou, H., Spilioti, M., Kanitsakis, A., Nikitakis, P., Drakonakis, N., Giannakopoulou, C., Sbyrakis, S., Sewell, A. C., Boehles, H. J., Smeitink, J., and Wevers, R. A. (2001) Selective screening for inborn errors of metabolism: the primary care-based model in rural Crete, *Journal of inherited metabolic disease 24*, 877-880.
366. Niers, L. E., Smeitink, J. A., Trijbels, J. M., Sengers, R. C., Janssen, A. J., and van den Heuvel, L. P. (2001) Prenatal diagnosis of NADH:ubiquinone oxidoreductase deficiency, *Prenatal diagnosis 21*, 871-880.
367. Nestor, L., Reinhammar, B., and Spiro, T. G. (1986) 63/65Cu and 1/2H2O isotope shifts in the low-temperature resonance Raman spectrum of fungal laccase, *Biochim Biophys Acta 869*, 286-292.
368. Dave, B. C., Czernuszewicz, R. S., Prickril, B. C., and Kurtz, D. M. (1994) Resonance Raman-Spectroscopic Evidence for the Fes4 and Fe-O-Fe Sites in Rubrerythrin from Desulfovibrio-Vulgaris, *Biochemistry 33*, 3572-3576.
369. Wen, Y. D., Liao, C. T., Liou, K. M., Wang, W. H., Huang, W. C., and Chang, B. Y. (2000) Adrenodoxin: Structure, stability, and electron transfer properties, *Proteins: Structure, Function and Genetics 40*, 590-612.
370. Staples, C. R., Gaymard, E., Stritt-Etter, A. L., Telser, J., Hoffman, B. M., Schürmann, P., Knaff, D. B., and Johnson, M. K. (1998) Role of the [Fe4S4] cluster in mediating disulfide reduction in spinach ferredoxin:thioredoxin reductase, *Biochemistry 37*, 4612-4620.
371. Lyubenova, S., Maly, T., Zwicker, K., Brandt, U., Ludwig, B., and Prisner, T. (2009) Multifrequency Pulsed Electron Paramagnetic Resonance on Metalloproteins, *Accounts of Chemical Research 43*, 181-189.
372. Brereton, P. S., Duderstadt, R. E., Staples, C. R., Johnson, M. K., and Adams, M. W. (1999) Effect of serinate ligation at each of the iron sites of the [Fe4S4] cluster of Pyrococcus furiosus ferredoxin on the redox, spectroscopic, and biological properties, *Biochemistry 38*, 10594-10605.
373. Fu, W., O'Handley, S., Cunningham, R. P., and Johnson, M. K. (1992) The role of the iron-sulfur cluster in Escherichia coli endonuclease III. A resonance Raman study, *J Biol Chem 267*, 16135-16137.
374. Fu, W. G., Morgan, T. V., Mortenson, L. E., and Johnson, M. K. (1991) Resonance Raman studies of the [4Fe-4S] to [2Fe-2S] cluster conversion in the iron protein of nitrogenase, *FEBS Lett 284*, 165-168.
375. Loscher, S., Gebler, A., Stein, M., Sanganas, O., Buhrke, T., Zebger, I., Dau, H., Friedrich, B., Lenz, O., and Haumann, M. (2010) Protein-protein complex formation affects the Ni-Fe and Fe-S centers in the H2-sensing regulatory hydrogenase from Ralstonia eutropha H16, *Chemphyschem : a European journal of chemical physics and physical chemistry 11*, 1297-1306.
376. Moulis, J. M., Lutz, M., Gaillard, J., and Noodleman, L. (1988) Characterization of [4Fe-4Se]2+/3+ high-potential iron-sulfur protein from Chromatium vinosum, *Biochemistry 27*, 8712-8719.
377. Czernuszewicz, R. S., Kilpatrick, L. K., Koch, S. A., and Spiro, T. G. (1994) Resonance Raman-Spectroscopy of Iron(Iii) Tetrathiolate Complexes - Implications for the Conformation and Force-Field of Rubredoxin, *Journal of the American Chemical Society 116*, 7134-7141.
378. Kilpatrick, L. K., Kennedy, M. C., Beinert, H., Czernuszewicz, R. S., Qiu, D., and Spiro, T. G. (1994) Cluster Structure and H-Bonding in Native, Substrate-Bound, and 3fe Forms of Aconitase as Determined by Resonance Raman-Spectroscopy, *Journal of the American Chemical Society 116*, 4053-4061.
379. Benecky, M., Li, T. Y., Schmidt, J., Frerman, F., Watters, K. L., and McFarland, J. (1979) Resonance Raman study of flavins and the flavoprotein fatty acyl coenzyme A dehydrogenase, *Biochemistry 18*, 3471-3476.

380. Copeland, R. A., and Spiro, T. G. (1986) Ultraviolet resonance Raman spectroscopy of flavin mononucleotide and flavin adenine dinucleotide, *J Phys Chem-Us 90*, 6648-6654.
381. Nishina, Y., Kitagawa, T., Shiga, K., Horiike, K., Matsumura, Y., Watari, H., and Yamano, T. (1978) Resonance Raman spectra of riboflavin and its derivatives in the bound state with egg riboflavin binding proteins, *J Biochem 84*, 925-932.
382. Kitagawa, T., Nishina, Y., Kyogoku, Y., Yamano, T., Ohishi, N., Takai-Suzuki, A., and Yagi, K. (1979) Resonance Raman spectra of carbon-13- and nitrogen-15-labeled riboflavin bound to egg-white flavoprotein, *Biochemistry 18*, 1804-1808.
383. Sugiyama, T., Nisimoto, Y., Mason, H. S., and Loehr, T. M. (1985) Flavins of NADPH-cytochrome P-450 reductase: Evidence for structural alteration of flavins in their one-electron-reduced semiquinone states from resonance Raman spectroscopy, *Biochemistry 24*, 3012-3019.
384. Eisenberg, A. S., and Schelvis, J. P. M. (2008) Contributions of the 8-methyl group to the vibrational normal modes of flavin mononucleotide and its 5-methyl semiquinone radical, *J Phys Chem A 112*, 6179-6189.
385. Sakai, M., and Takahashi, H. (1996) One-electron photoreduction of flavin mononucleotide: Time-resolved resonance Raman and absorption study, *J Mol Struct 379*, 9-18.
386. Bowman, W. D., and Spiro, T. G. (1981) Normal mode analysis of lumiflavin and interpretation of resonance Raman spectra of flavoproteins, *Biochemistry 20*, 3313-3318.
387. Nishina, Y., Shiga, K., Horiike, K., Tojo, H., Kasai, S., Matsui, K., Watari, H., and Yamano, T. (1980) Resonance Raman spectra of semiquinone forms of flavins bound to riboflavin binding protein, *J Biochem 88*, 411-416.
388. Sugiyama, H., Nakatsubo, R., Yamaguchi, S., Ogura, T., Shinzawa-Itoh, K., and Yoshikawa, S. (2007) Resonance Raman spectra of the FMN of the bovine heart NADH: Ubiquinone oxidoreductase, the largest membrane protein in the mitochondrial respiratory system, *Journal of bioenergetics and biomembranes 39*, 145-148.
389. Smeitink, J., van den Heuvel, L., and DiMauro, S. (2001) The genetics and pathology of oxidative phosphorylation, *Nature reviews. Genetics 2*, 342-352.
390. Fabian, J. R., Daar, I. O., and Morrison, D. K. (1993) Critical tyrosine residues regulate the enzymatic and biological activity of Raf-1 kinase, *Molecular and cellular biology 13*, 7170-7179.
391. Powers, L., Schagger, H., von Jagow, G., Smith, J., Chance, B., and Ohnishi, T. (1989) EXAFS studies of the isolated bovine heart Rieske [2Fe-2S]1+(1+,2+) cluster, *Biochim Biophys Acta 975*, 293-298.
392. Chen, J., Bender, S. L., Keough, J. M., and Barry, B. A. (2009) Tryptophan as a probe of photosystem I electron transfer reactions: a UV resonance Raman study, *J Phys Chem B 113*, 11367-11370.
393. Morgan, D. J., and Sazanov, L. A. (2008) Three-dimensional structure of respiratory complex I from Escherichia coli in ice in the presence of nucleotides, *Biochim Biophys Acta 1777*, 711-718.
394. Miura, T., Takeuchi, H., and Harada, I. (1988) Characterization of individual tryptophan side chains in proteins using Raman spectroscopy and hydrogen-deuterium exchange kinetics, *Biochemistry-Us 27*, 88-94.
395. Sweeney, J. A., and Asher, S. A. (1990) Tryptophan UV resonance Raman excitation profiles, *The Journal of Physical Chemistry 94*, 4784-4791.
396. Petersen, M. T. N., Jonson, P. H., and Petersen, S. B. (1999) Amino acid neighbours and detailed conformational analysis of cysteines in proteins, *Protein engineering 12*, 535-548.
397. Chi, Z., Chen, X. G., Holtz, J. S., and Asher, S. A. (1998) UV resonance Raman-selective amide vibrational enhancement: quantitative methodology for determining protein secondary structure, *Biochemistry 37*, 2854-2864.

398. Xiao, Z., Gardner, A. R., Cross, M., Maes, E. M., Czernuszewicz, R. S., Sola, M., and Wedd, A. G. (2001) Redox thermodynamics of mutant forms of the rubredoxin from Clostridiumpasteurianum: identification of a stable Fe(III)(S-Cys)3(OH) centre in the C6S mutant, *Journal of biological inorganic chemistry : JBIC : a publication of the Society of Biological Inorganic Chemistry 6*, 638-649.
399. Xiao, Y., Wang, H., George, S. J., Smith, M. C., Adams, M. W. W., Jenney Jr, F. E., Sturhahn, W., Alp, E. E., Zhao, J., Yoda, Y., Dey, A., Solomon, E. I., and Cramer, S. P. (2005) Normal mode analysis of Pyrococcus furiosus rubredoxin via nuclear resonance vibrational spectroscopy (NRVS) and resonance Raman spectroscopy, *Journal of the American Chemical Society 127*, 14596-14606.
400. Guo, Y., Brecht, E., Aznavour, K., Nix, J. C., Xiao, Y., Wang, H., George, S. J., Bau, R., Keable, S., Peters, J. W., Adams, M. W. W., Jenney Jr, F. E., Sturhahn, W., Alp, E. E., Zhao, J., Yoda, Y., and Cramer, S. P. (2013) Nuclear resonance vibrational spectroscopy (NRVS) of rubredoxin and MoFe protein crystals, *Hyperfine Interactions 222*, 77-90.
401. Antonkine, M. L., Maes, E. M., Czernuszewicz, R. S., Breitenstein, C., Bill, E., Falzone, C. J., Balasubramanian, R., Lubner, C., Bryant, D. A., and Golbeck, J. H. (2007) Chemical rescue of a site-modified ligand to a [4Fe-4S] cluster in PsaC, a bacterial-like dicluster ferredoxin bound to Photosystem I, *Biochimica et biophysica acta 1767*, 712-724.
402. Kennedy, M. C., Werst, M., Telser, J., Emptage, M. H., Beinert, H., and Hoffman, B. M. (1987) Mode of substrate carboxyl binding to the [4Fe-4S]+ cluster of reduced aconitase as studied by 17O and 13C electron-nuclear double resonance spectroscopy, *Proc Natl Acad Sci U S A 84*, 8854-8858.
403. Werst, M. M., Kennedy, M. C., Houseman, A. L., Beinert, H., and Hoffman, B. M. (1990) Characterization of the [4Fe-4S]+ cluster at the active site of aconitase by 57Fe, 33S, and 14N electron nuclear double resonance spectroscopy, *Biochemistry 29*, 10533-10540.
404. Backes, G., Mino, Y., Loehr, T. M., Meyer, T. E., Cusanovich, M. A., Sweeney, W. V., Adman, E. T., and Sanders-Loehr, J. (1991) The Environment of Fe4S4 Clusters in Ferredoxins and High-Potential Iron Proteins. New Information from X-ray Crystallography and Resonance Raman Spectroscopy, *Journal of the American Chemical Society 113*, 2055-2064.
405. Mansy, S. S., Xiong, Y., Hemann, C., Hille, R., Sundaralingam, M., and Cowan, J. A. (2002) Crystal structure and stability studies of C77S HiPIP: A serine ligated [4Fe-4S] cluster, *Biochemistry 41*, 1195-1201.
406. Duderstadt, R. E., Brereton, P. S., Adams, M. W., and Johnson, M. K. (1999) A pure S = 3/2 [Fe4S4]+ cluster in the A33Y variant of Pyrococcus furiosus ferredoxin, *FEBS letters 454*, 21-26.
407. Hayashi, T., and Stuchebrukhov, A. A. (2011) Quantum electron tunneling in respiratory complex i, *Journal of Physical Chemistry B 115*, 5354-5364.
408. Siiman, O., and Callaghan, R. (1981) Resonance Raman Studies of Ferric Nadh Transients, *Journal of the American Chemical Society 103*, 5526-5529.
409. Austin, J. C., Wharton, C. W., and Hester, R. E. (1989) An Ultraviolet Resonance Raman-Study of Dehydrogenase Enzymes and Their Interactions with Coenzymes and Substrates, *Biochemistry 28*, 1533-1538.
410. Yue, K. T., Martin, C. L., Yang, J. P., Lee, S. K., Sloan, D. L., and Callender, R. H. (1985) A Raman-Study of Reduced Nicotinamide Adenine-Dinucleotide Bound to Liver Alcohol-Dehydrogenase, *Biophysical journal 47*, A412-A412.
411. Deng, H., Zheng, J., Sloan, D., Burgner, J., and Callender, R. (1989) Classical Raman-Spectroscopic Studies of Nadh and Nad+ Bound to Lactate-Dehydrogenase by Difference Techniques, *Biochemistry 28*, 1525-1533.

412. Stevenson, R. C., Dunham, W. R., Sands, R. H., Singer, T. P., and Beinert, H. (1986) Studies on the spin-spin interaction between flavin and iron-sulfur cluster in an iron-sulfur flavoprotein, *Biochimica et biophysica acta 869*, 81-88.
413. Dooijewaard, G., and Slater, E. C. (1976) Steady-state kinetics of high molecular weight (type-I) NADH dehydrogenase, *Biochimica et biophysica acta 440*, 1-15.
414. Vinogradov, A. D. (1993) Kinetics, control, and mechanism of ubiquinone reduction by the mammalian respiratory chain-linked NADH-ubiquinone reductase, *Journal of bioenergetics and biomembranes 25*, 367-375.
415. Sled, V. D., and Vinogradov, A. D. (1993) Kinetics of the mitochondrial NADH-ubiquinone oxidoreductase interaction with hexammineruthenium(III), *Biochimica et biophysica acta 1141*, 262-268.
416. Albracht, S. P. (2010) The reaction of NADPH with bovine mitochondrial NADH:ubiquinone oxidoreductase revisited: II. Comparison of the proposed working hypothesis with literature data, *Journal of bioenergetics and biomembranes 42*, 279-292.
417. Albracht, S. P. (2010) The reaction of NADPH with bovine mitochondrial NADH:ubiquinone oxidoreductase revisited: I. Proposed consequences for electron transfer in the enzyme, *Journal of bioenergetics and biomembranes 42*, 261-278.
418. Li, Y. N., Xi, M. M., Guo, Y., Hai, C. X., Yang, W. L., and Qin, X. J. (2014) NADPH oxidase-mitochondria axis-derived ROS mediate arsenite-induced HIF-1α stabilization by inhibiting prolyl hydroxylases activity, *Toxicology Letters 224*, 165-174.
419. Čermáková, P., Verner, Z., Man, P., Lukeš, J., and Horváth, A. (2007) Characterization of the NADH:ubiquinone oxidoreductase (complex I) in the trypanosomatid Phytomonas serpens (Kinetoplastida), *FEBS Journal 274*, 3150-3158.
420. Galkin, A., and Moncada, S. (2007) S-nitrosation of mitochondrial complex I depends on its structural conformation, *Journal of Biological Chemistry 282*, 37448-37453.
421. Grivennikova, V. G., Kotlyar, A. B., Karliner, J. S., Cecchini, G., and Vinogradov, A. D. (2007) Redox-dependent change of nucleotide affinity to the active site of the mammalian complex I, *Biochemistry 46*, 10971-10978.
422. Pohl, T., Schneider, D., Hielscher, R., Stolpe, S., Dorner, K., Kohlstadt, M., Bottcher, B., Hellwig, P., and Friedrich, T. (2008) Nucleotide-induced conformational changes in the Escherichia coli NADH:ubiquinone oxidoreductase (complex I), *Biochemical Society transactions 36*, 971-975.
423. Abdrakhmanova, A., Zwicker, K., Kerscher, S., Zickermann, V., and Brandt, U. (2006) Tight binding of NADPH to the 39-kDa subunit of complex I is not required for catalytic activity but stabilizes the multiprotein complex, *Biochimica et Biophysica Acta - Bioenergetics 1757*, 1676-1682.
424. Niu, S., and Ichiye, T. (2011) Density functional theory calculations of redox properties of iron-sulphur protein analogues, *Molecular Simulation 37*, 572-590.
425. Khoroshilova, N., Popescu, C., Munck, E., Beinert, H., and Kiley, P. J. (1997) Iron-sulfur cluster disassembly in the FNR protein of Escherichia coli by O2: [4Fe-4S] to [2Fe-2S] conversion with loss of biological activity, *Proc Natl Acad Sci U S A 94*, 6087-6092.
426. Werst, M. M., Kennedy, M. C., Beinert, H., and Hoffman, B. M. (1990) 17O, 1H, and 2H electron nuclear double resonance characterization of solvent, substrate, and inhibitor binding to the [4Fe-4S]+ cluster of aconitase, *Biochemistry 29*, 10526-10532.
427. Hayashi, T., and Stuchebrukhov, A. A. (2011) First principles studies of electron tunneling in proteins, *Computational and Theoretical Chemistry 975*, 61-68.
428. Moulis, J. M., Scherrer, N., Gagnon, J., Forest, E., Petillot, Y., and Garcia, D. (1993) Primary structure of Chromatium tepidum high-potential iron-sulfur protein in relation to thermal denaturation, *Archives of biochemistry and biophysics 305*, 186-192.

429. Qian, W. L., and Krimm, S. (1992) Conformation Dependence of the Sh and Cs Stretch Frequencies of the Cysteine Residue, *Biopolymers 32*, 1503-1518.
430. Krimm, S., and Reisdorf, W. C. (1994) Understanding Normal-Modes of Proteins, *Faraday discussions 99*, 181-197.
431. Macor, K. A., Czernuszewicz, R. S., Adams, M. W., and Spiro, T. G. (1987) An investigation of hydrogenase I and hydrogenase II from Clostridium pasteurianum by resonance Raman spectroscopy. Evidence for a [2Fe-2S] cluster in hydrogenase I, *The Journal of biological chemistry 262*, 9945-9947.
432. Benecky, M., Yu, T. J., Watters, K. L., and McFarland, J. T. (1980) Metal-flavin complexation. A resonance Raman investigation, *BBA - Protein Structure 626*, 197-207.
433. Benecky, M. J., Copeland, R. A., and Spiro, T. G. (1983) Resonance raman spectra of flavin semiquinones stabilized by N5 methylation, *BBA - General Subjects 760*, 163-168.
434. Nishina, Y., Sato, K., Miura, R., Matsui, K., and Shiga, K. (1998) Resonance Raman study on reduced flavin in purple intermediate of flavoenzyme: Use of [4-Carbonyl-18O]-Enriched flavin, *Journal of Biochemistry 124*, 200-208.
435. Desbois, A., Tegoni, M., Gervais, M., and Lutz, M. (1989) Flavin and heme structures in lactate:Cytochrome c oxidoreductase: A resonance raman study, *Biochemistry 28*, 8011-8022.
436. Schmidt, J., Coudron, P., Thompson, A. W., Watters, K. L., and Mcfarland, J. T. (1983) Hydrogen-Bonding between Flavin and Protein - a Resonance Raman-Study, *Biochemistry 22*, 76-84.
437. Hikita, M., Shinzawa-Itoh, K., Moriyama, M., Ogura, T., Kihira, K., and Yoshikawa, S. (2013) Resonance Raman Spectral Properties of FMN of Bovine Heart NADH:ubiquinone Oxidoreductase Suggesting a Mechanism for the Prevention of Spontaneous Production of Reactive Oxygen Species, *Biochemistry 52*, 98-104.
438. Zheng, Y., Dong, J., Palfey, B. A., and Carey, P. R. (1999) Using raman spectroscopy to monitor the solvent-exposed and 'buried' forms of flavin in p-hydroxybenzoate hydroxylase, *Biochemistry 38*, 16727-16732.
439. Talati, M., and Jha, P. K. (2006) Acoustic phonon quantization and low-frequency Raman spectra of spherical viruses, *Physical review. E, Statistical, nonlinear, and soft matter physics 73*, 011901.
440. Dykeman, E. C., Sankey, O. F., and Tsen, K. T. (2007) Raman intensity and spectra predictions for cylindrical viruses, *Physical review. E, Statistical, nonlinear, and soft matter physics 76*, 011906.
441. Chi, Z., and Asher, S. A. (1998) UV resonance Raman determination of protein acid denaturation: selective unfolding of helical segments of horse myoglobin, *Biochemistry 37*, 2865-2872.
442. Yakovlev, G., and Hirst, J. (2007) Transhydrogenation reactions catalyzed by mitochondrial NADH-ubiquinone oxidoreductase (complex I), *Biochemistry 46*, 14250-14258.
443. Birrell, J. A., Yakovlev, G., and Hirst, J. (2009) Reactions of the flavin mononucleotide in complex I: a combined mechanism describes NADH oxidation coupled to the reduction of APAD+, ferricyanide, or molecular oxygen, *Biochemistry 48*, 12005-12013.
444. Sazanov, L. A., and Hinchliffe, P. (2006) Structure of the hydrophilic domain of respiratory complex I from Thermus thermophilus, *Science 311*, 1430-1436.
445. Berrisford, J. M., Thompson, C. J., and Sazanov, L. A. (2008) Chemical and NADH-induced, ROS-dependent, cross-linking between subunits of complex I from Escherichia coli and Thermus thermophilus, *Biochemistry 47*, 10262-10270.
446. Higa, A., and Chevet, E. (2012) Redox signaling loops in the unfolded protein response, *Cellular Signalling 24*, 1548-1555.
447. Bindoli, A., and Rigobello, M. P. (2013) Principles in redox signaling: From chemistry to functional significance, *Antioxidants and Redox Signaling 18*, 1557-1593.

448. Hemmis, C. W., and Schildbach, J. F. (2013) Thioredoxin-like proteins in F and other plasmid systems, *Plasmid 70*, 168-189.
449. Conover, R. C., Kowal, A. T., Fu, W. G., Park, J. B., Aono, S., Adams, M. W., and Johnson, M. K. (1990) Spectroscopic characterization of the novel iron-sulfur cluster in Pyrococcus furiosus ferredoxin, *The Journal of biological chemistry 265*, 8533-8541.
450. Ohnishi, T. (1998) Iron-sulfur clusters/semiquinones in complex I, *Biochim Biophys Acta 1364*, 186-206.
451. Ohnishi, S. T., Salerno, J. C., and Ohnishi, T. (2010) Possible roles of two quinone molecules in direct and indirect proton pumps of bovine heart NADH-quinone oxidoreductase (complex I), *Biochim Biophys Acta 1797*, 1891-1893.
452. Mukherjee, A., Walker, J., Weyant, K. B., and Schroeder, C. M. (2013) Characterization of Flavin-Based Fluorescent Proteins: An Emerging Class of Fluorescent Reporters, *PloS one 8*.
453. Vetrova, E. V., Kudryasheva, N. S., and Cheng, K. H. (2009) Effect of quinone on the fluorescence decay dynamics of endogenous flavin bound to bacterial luciferase, *Biophysical Chemistry 141*, 59-65.
454. Kao, Y. T., Saxena, C., He, T. F., Guo, L., Wang, L., Sancar, A., and Zhong, D. (2008) Ultrafast dynamics of flavins in five redox states, *J Am Chem Soc 130*, 13132-13139.
455. Sled, V. D., Rudnitzky, N. I., Hatefi, Y., and Ohnishi, T. (1994) Thermodynamic analysis of flavin in mitochondrial NADH:ubiquinone oxidoreductase (complex I), *Biochemistry 33*, 10069-10075.
456. Cory, R. M., and McKnight, D. M. (2005) Fluorescence Spectroscopy Reveals Ubiquitous Presence of Oxidized and Reduced Quinones in Dissolved Organic Matter, *Environmental Science & Technology 39*, 8142-8149.
457. Bauscher, M. a. W. M. (1992) Electrochemical and infrared-spectroscopic characterization of redox reactions of p-quinones, *The Journal of Physical Chemistry 96*, 11101-11108.
458. Stites, T. E., Mitchell, A. E., and Rucker, R. B. (2000) Physiological importance of quinoenzymes and the O-quinone family of cofactors, *J Nutr 130*, 719-727.
459. Stites, T. E., and Rucker, R. B. (2000) The uptake and subcellular distribution of pyrroloquinoline quinone (PQQ) in human fibroblasts, *Faseb J 14*, A231-A231.
460. Rucker, R., Stites, T., Steinberg, F., and Mitchell, A. (2000) Physiological importance of pyrroloquinoline quinone, *Biochemistry and Molecular Biology of Vitamin B6 and Pqq-Dependent Proteins*, 61-66.
461. Babaei, A., Connor, P. A., McQuillan, A. J., and Umapathy, S. (1997) UV-visible spectroelectrochemistry of reduction products of anthraquinone in dimethylformamide solutions - An advanced undergraduate experiment, *Journal of Chemical Education 74*, 1200-1204.
462. Babaei, A. C., P.; McQuillan,A.and Umapathy, S. (1997) UV Visible spectroelectrochemistry of reduction products of anthraquinone in dymethylformamide, *J Chem Educ 74*, 1200-1204.
463. Reddy, S. Y., and Bruice, T. C. (2004) Determination of enzyme mechanisms by molecular dynamics: Studies on quinoproteins, methanol dehydrogenase, and soluble glucose dehydrogenase, *Protein Science 13*, 1965-1978.
464. Carroll, J., Fearnley, I. M., Wang, Q., and Walker, J. E. (2009) Measurement of the molecular masses of hydrophilic and hydrophobic subunits of ATP synthase and complex I in a single experiment, *Analytical biochemistry 395*, 249-255.
465. Ohnishi, T., and Salerno, J. C. (2005) Conformation-driven and semiquinone-gated proton-pump mechanism in the NADH-ubiquinone oxidoreductase (complex I), *FEBS letters 579*, 4555-4561.
466. Minagawa, J., Narusaka, Y., Inoue, Y., and Satoh, K. (1998) Electron Transfer between QA and QB in Photosystem II Is Thermodynamically Perturbed in Phototolerant Mutants of Synechocystis sp. PCC 6803, *Biochemistry 38*, 770-775.

467. Boussac, A., Sugiura, M., and Rappaport, F. (2011) Probing the quinone binding site of Photosystem II from Thermosynechococcus elongatus containing either PsbA1 or PsbA3 as the D1 protein through the binding characteristics of herbicides, *Bba-Bioenergetics 1807*, 119-129.
468. de Wijn, R., and van Gorkom, H. J. (2001) Kinetics of Electron Transfer from QA to QB in Photosystem II†, *Biochemistry 40*, 11912-11922.
469. Kotlyar, A. B., and Borovok, N. (2002) NADH oxidation and NAD+ reduction catalysed by tightly coupled inside-out vesicles from Paracoccus denitrificans, *European journal of biochemistry / FEBS 269*, 4020-4024.
470. Grivennikova, V. G., Roth, R., Zakharova, N. V., Hägerhäll, C., and Vinogradov, A. D. (2003) The mitochondrial and prokaryotic proton-translocating NADH:ubiquinone oxidoreductases: Similarities and dissimilarities of the quinone-junction sites, *Biochimica et Biophysica Acta - Bioenergetics 1607*, 79-90.
471. Kotlyar, A. B., Karliner, J. S., and Cecchini, G. (2005) A novel strong competitive inhibitor of complex I, *FEBS letters 579*, 4861-4866.
472. Grivennikova, V. G., Kotlyar, A. B., Karliner, J. S., Cecchini, G., and Vinogradov, A. D. (2007) Redox-dependent change of nucleotide affinity to the active site of the mammalian complex I, *Biochemistry 46*, 10971-10978.
473. Yamaguchi, M., Belogrudov, G. I., Matsuno-Yagi, A., and Hatefi, Y. (2000) The multiple nicotinamide nucleotide-binding subunits of bovine heart mitochondrial NADH:ubiquinone oxidoreductase (complex I), *European journal of biochemistry / FEBS 267*, 329-336.

7 APPENDIX

7.1 Materials and methods

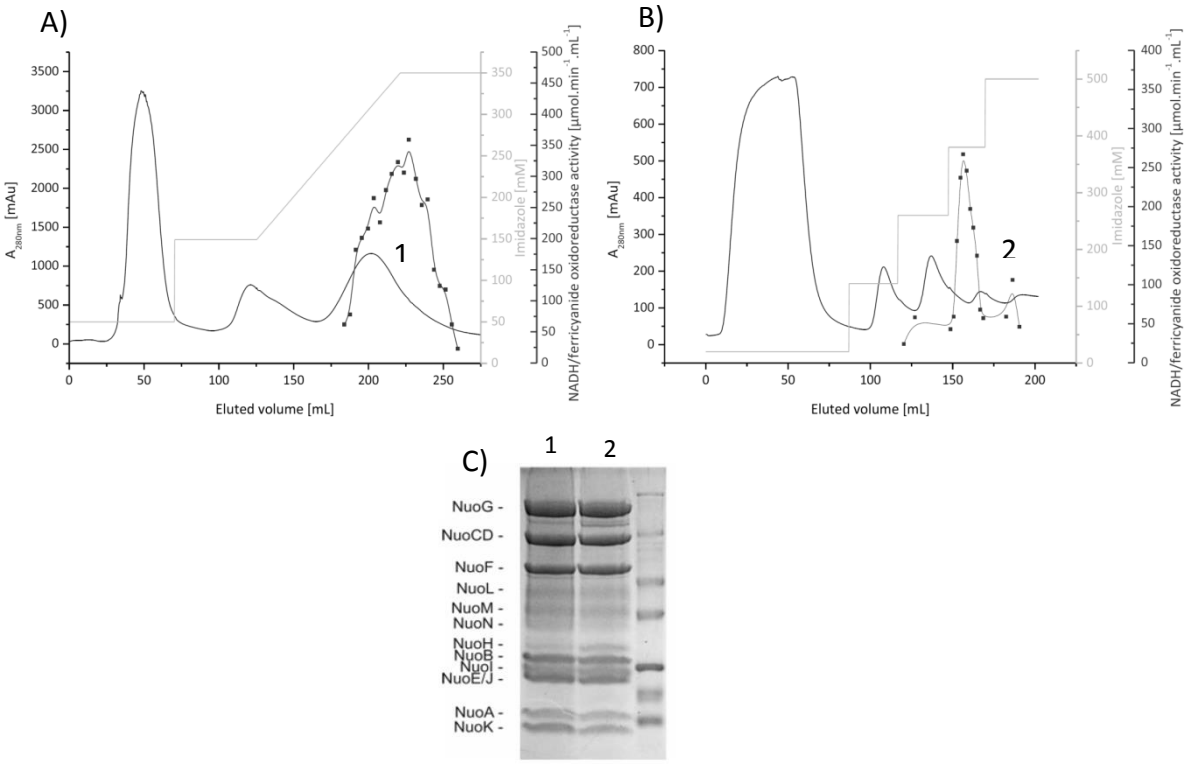

Figure 7.1-1. Elution profiles of the Fractogel EMD anion exchange (A), the Ni^{+2} IDA affinity column (B) and the SDS-PAGEof the purified *nuoEF-*$_{His}$-complex I

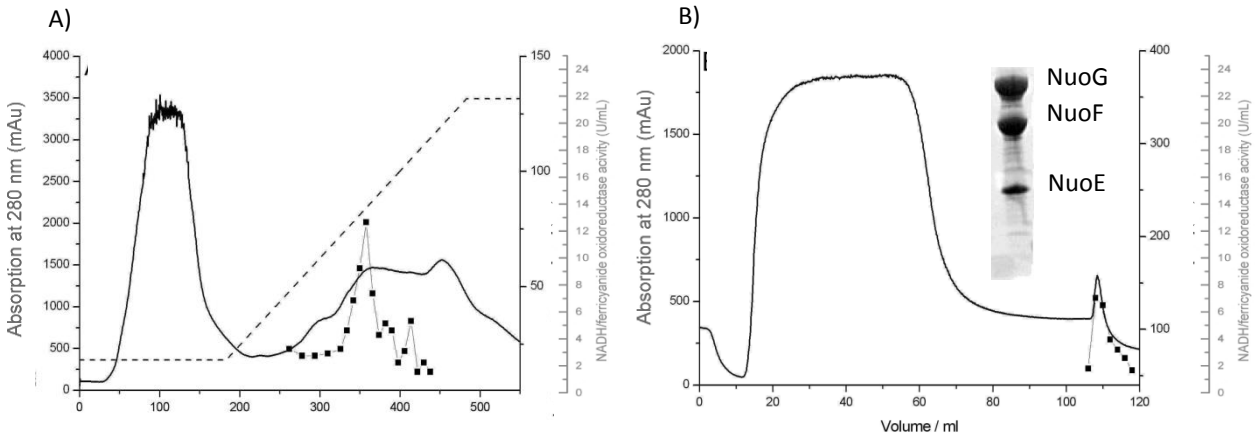

Figure 7.1-2. Elution profiles of Fractogel EMD (A) and the chromatography of the StrepTactin-Sepharose (B) of the NADH dehydrogenase fragment from *E. coli.*

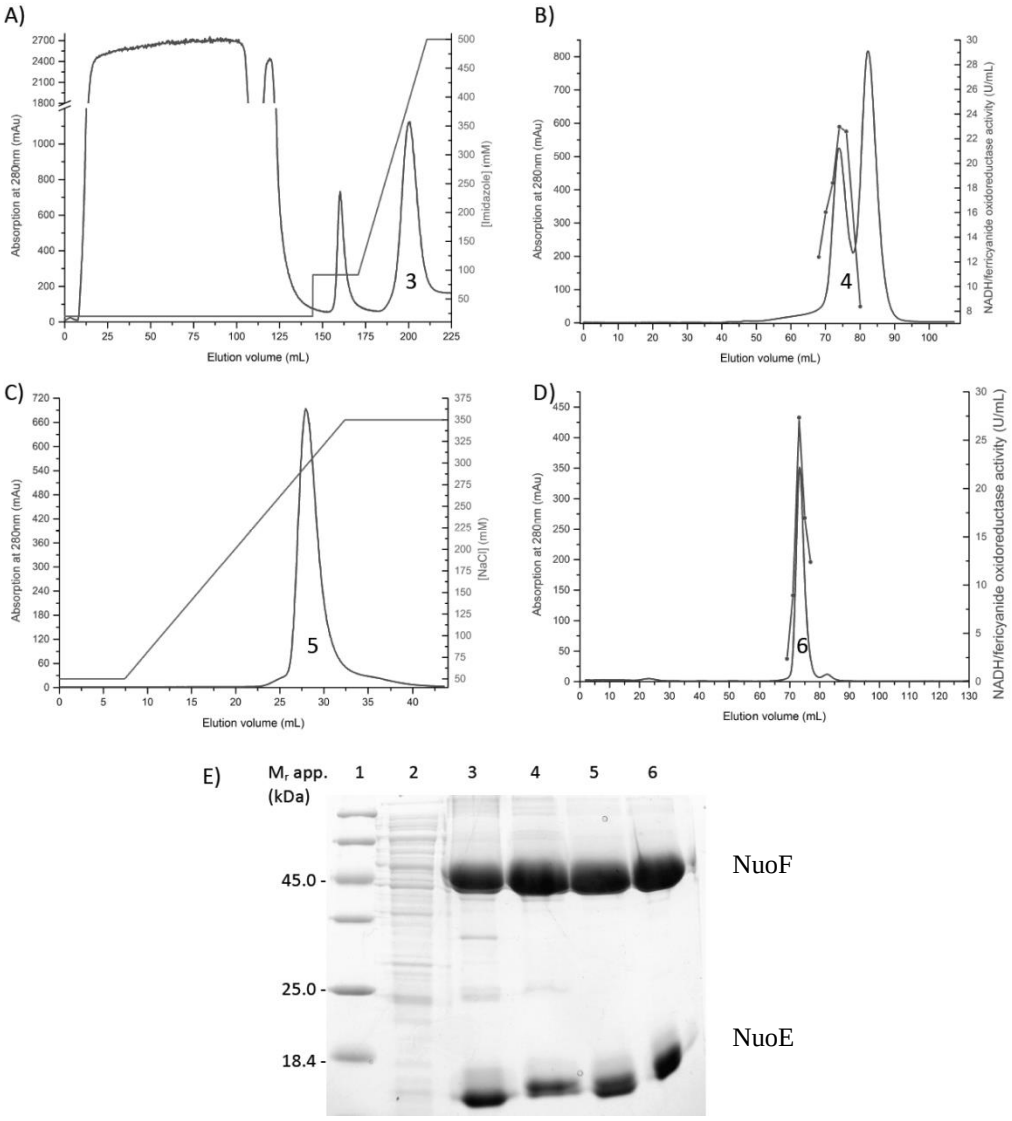

Figure 7.1-3. Emution profile of the ProBond material (A), Superdex 200 16/60 (B), Source 15Q (C), second superdex 20016/60 (D) and SDS-PAGE (E) of NuoEF subcomplex from *A. aeolicus*

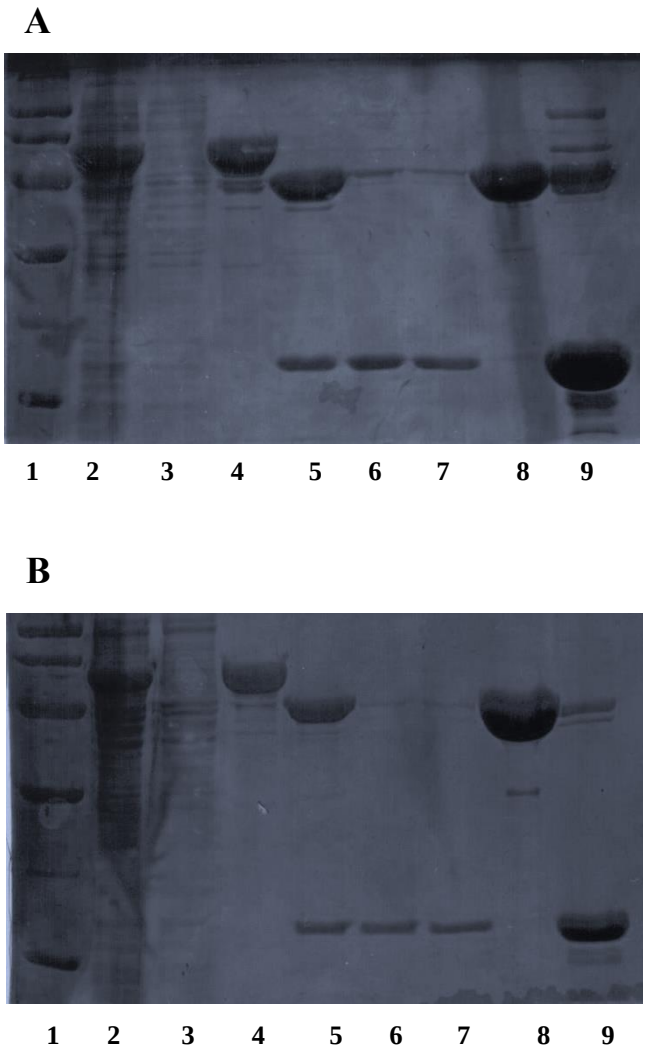

1. Molecular weight marker
2. Supernatant
3. Washing - amylose agarose resin
4. Elution – amylose agarose resin
5. Proteolitic cleavage
6. Ni-NTA resin nro.1
7. Ni-NTA resin nro.2
8. Size exclusion chromatography – PDZ1
9. Size exclusion chromatography - MBP

Figure 7.1-4. SDS-PAGE of the purification steps of A. PDZ1 WT and B. PDZ1-GGG

7.2 Results

7.2.1 PDZ domains

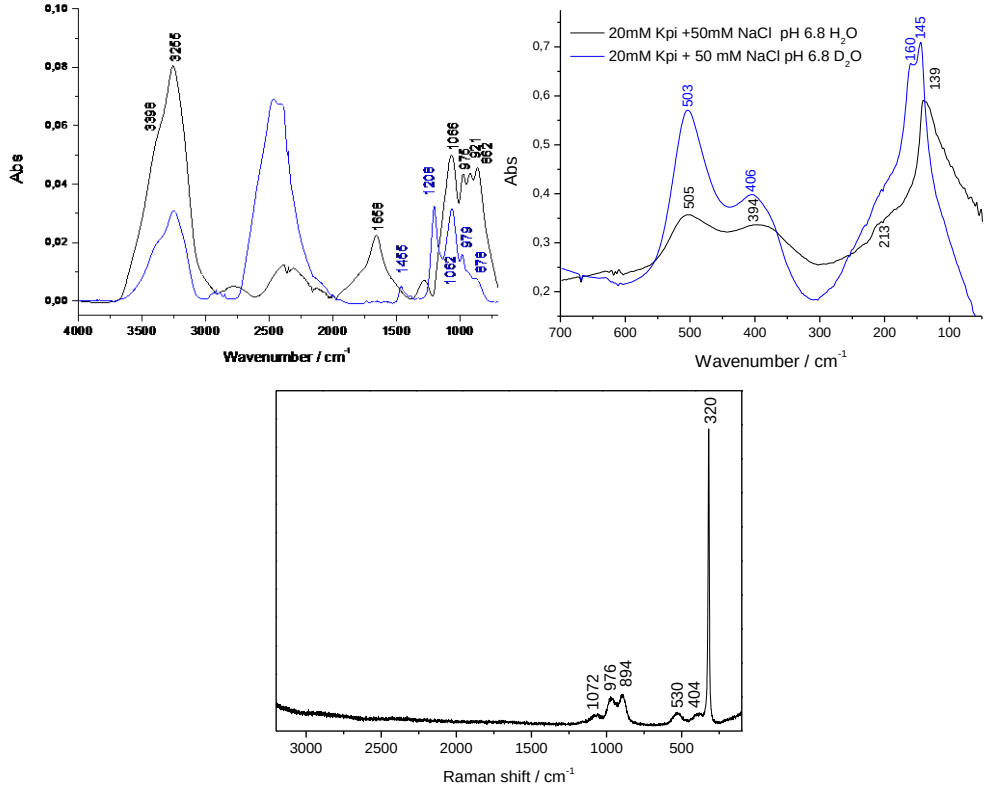

Figure 7.2-1. Mid (A) and far (B) infrared and Raman (C) spectra of the sodium phosphate buffer. Composition: 20mM Na-Phopshate+ 50mM NaCl pH 6.8

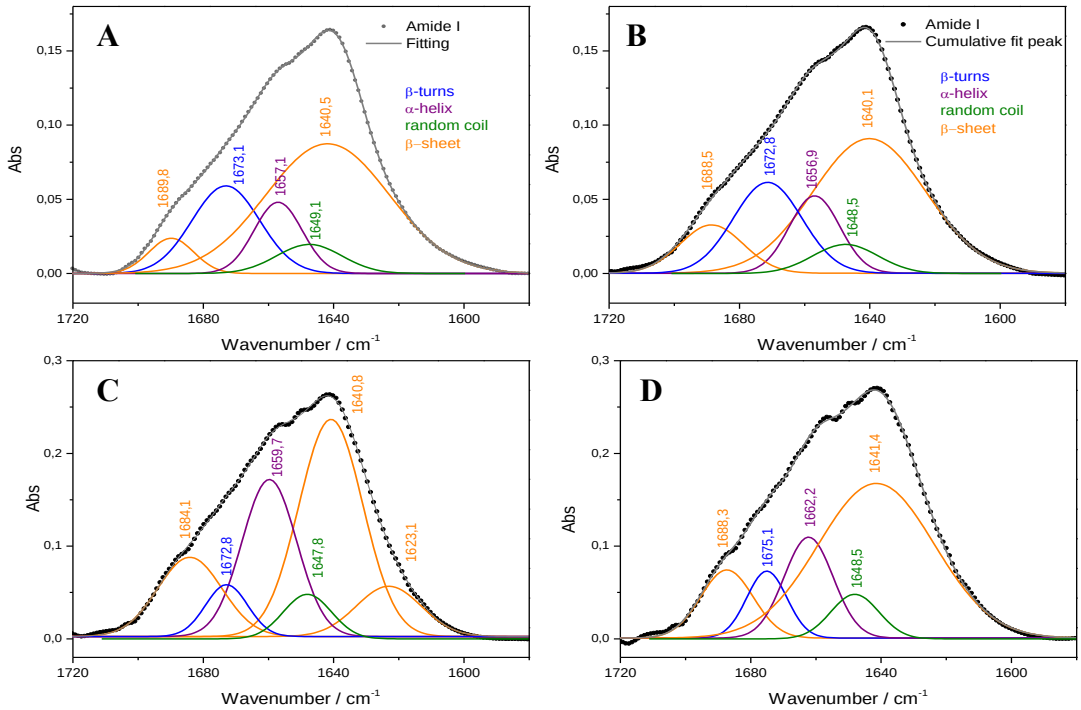

Figure 7.2-2. Amide I deconvolution of PDZ1 WT in presence of 16E6 (A), 16E6 R_{-5}/A (B), 16E6 5_{ct} L_0/A (C) and 16E6 6_{ct} L_0/A

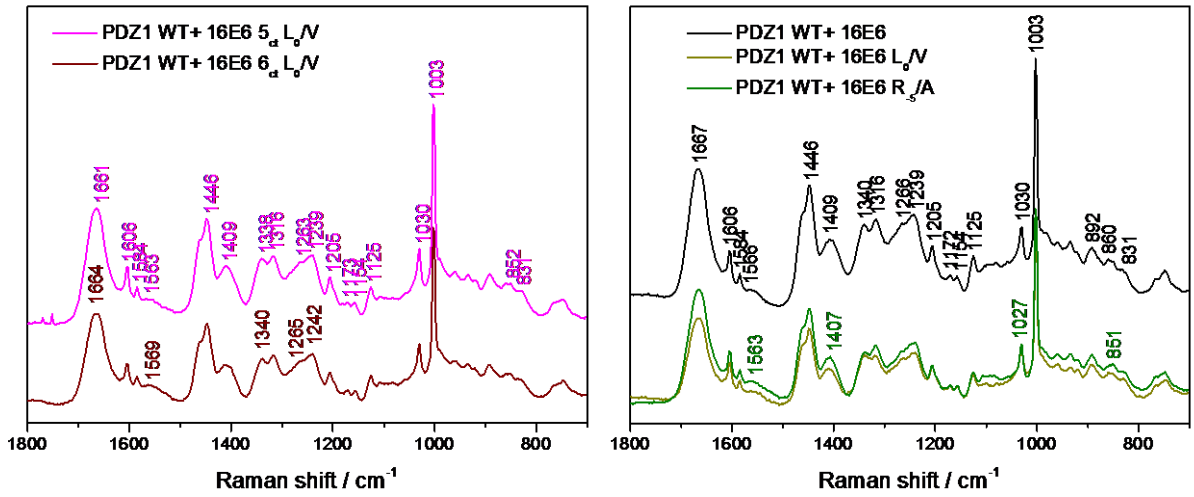

Figure 7.2-3. Mid frequency region of the Raman spectra of the different bound forms of PDZ1 WT

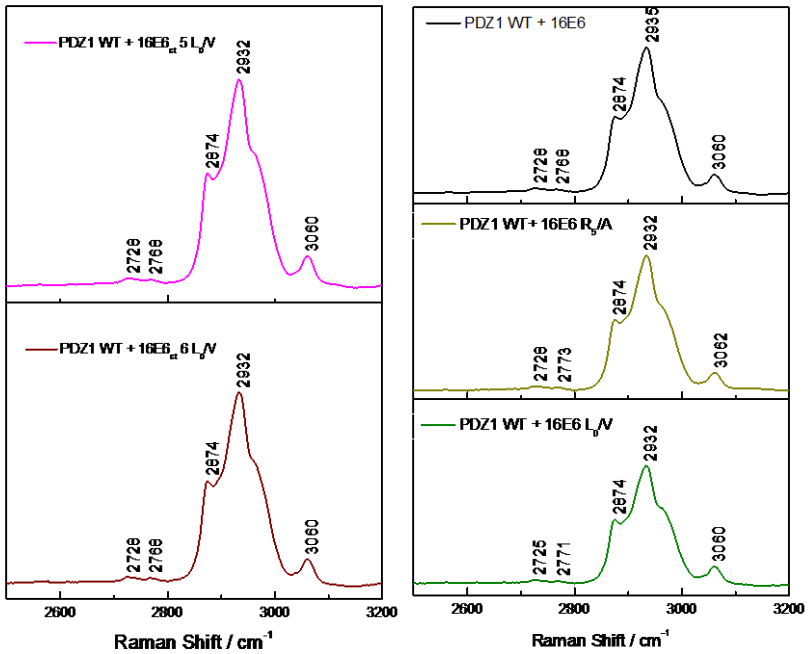

Figure 7.2-4. ν(C-H) region of PDZ1 WT in its free and bound form by Raman spectroscopy

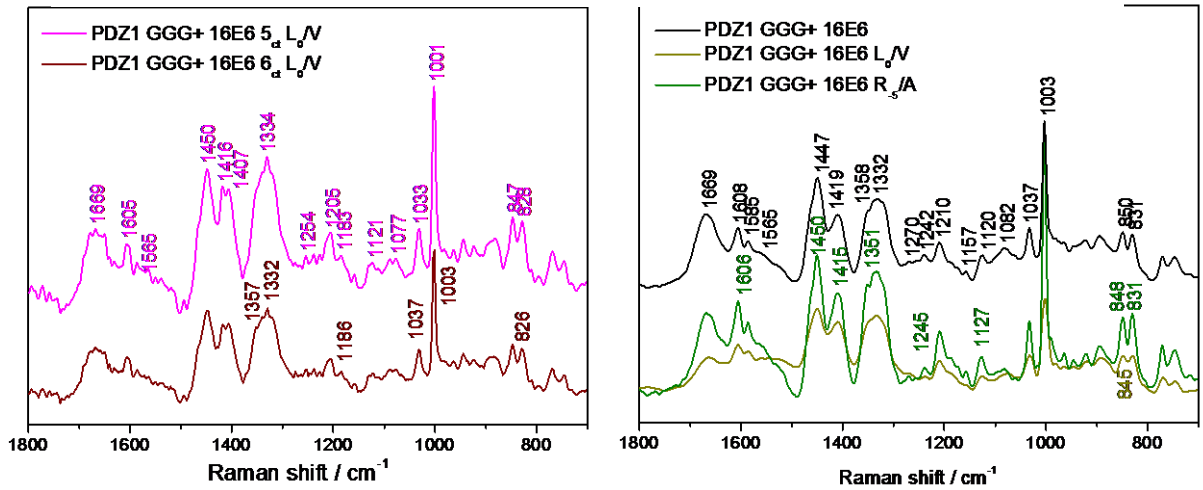

Figure 7.2-5. Mid frequency region of the Raman spectra of the different bound forms of PDZ1 GGG

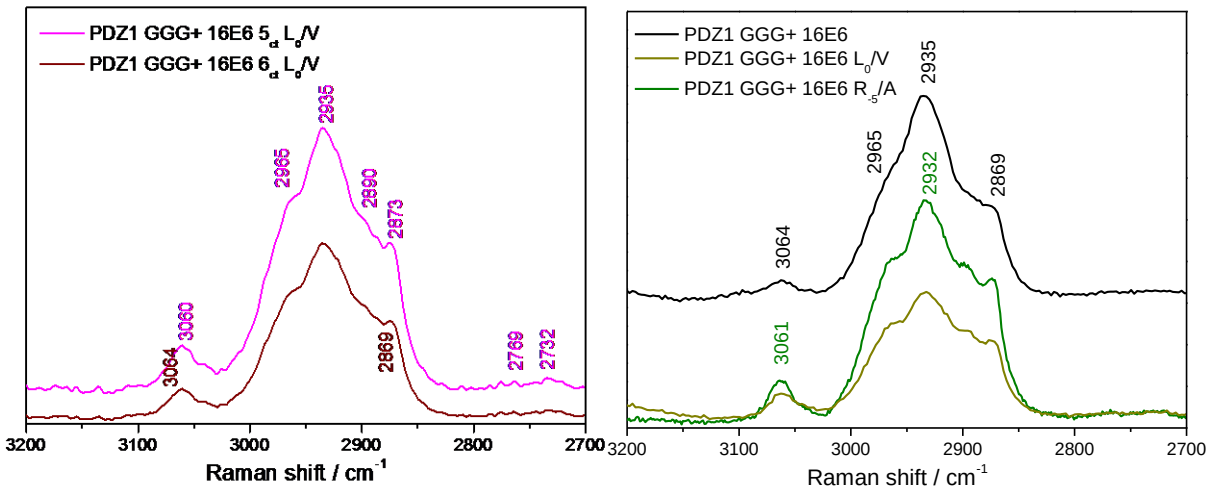

Figure 7.2-6. ν(C-H) region of PDZ1 GGG in its bound forms by Raman spectroscopy

7.2.2 CuAβ16

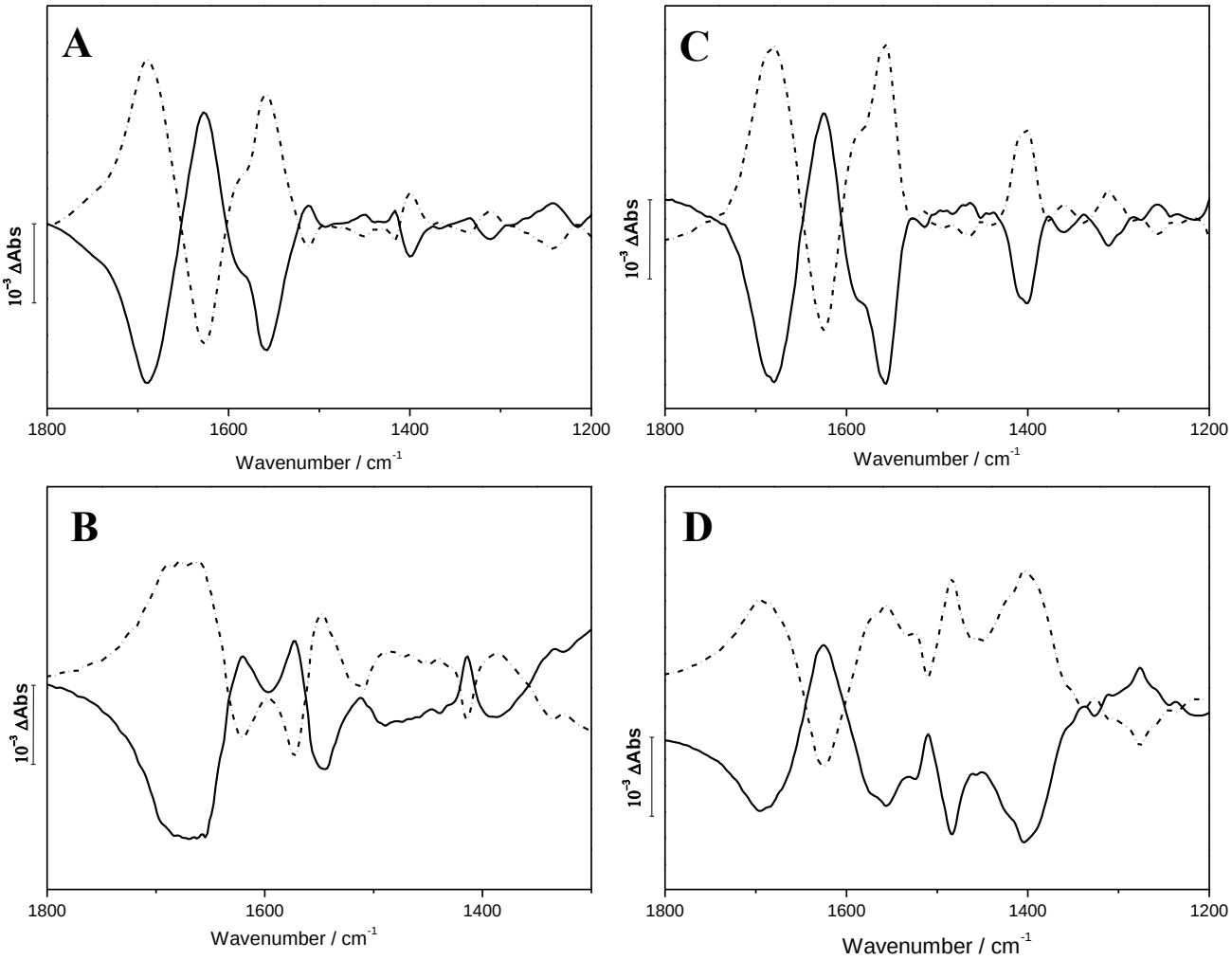

Figure 7.2-7. Ox-red (solid line) and red-ox (dotted line) of the electrochemistry of CuGHK at pH 6.8 (A) pH and 8.9(B) and CuDAHK at pH 6.8 (C) and at pH 8.9 (D)

Table 7.2-1. Tentative assignments of vibrational modes of the oxidized and reduced state of CuGHK, CuDAHK and CuAβ16 at pH 6.8 and pH 8.9 (the positive signal are an indication of the oxidized state and the negative the reduced)

		pH 6.8			pH 8.9		
Contribution	Modes	CuDAHK	CuGHK	Aβ16	CuDAHK	CuGHK	Aβ16
Amide I	υ(C=O) backbone	-1688 -1680	-1691	-1661	-1695 -1684	-1684	-1665
His	$\upsilon(C_4{=}C_5)$	+1626	+1628	+1620	+1624	+1620	+1599
His	$\upsilon(C_4{=}C_5)$ $N^{\pi}H$	-1589	-1592		--	-1596	
His	$\upsilon(C_4{=}C_5)$ $N^{\tau}H$	+1579	+1579		+1574	+1574	
Amide II	NH/CN	-1556	-1559	-1560	-1558	-1545	-1555
Asp	$\upsilon^{13}(COO^-)^{as}$	+1527			+1537 -1522		
Tyr	υ(CC) δ(CH)			-1517			-1500
His	$\upsilon^{9}(N\tau\text{-}C_2)$	-1514	+1513		+1511	+1511	
His	$\upsilon^{8}(C_2\text{-}N_{\pi})$	+1492 -1482	-1492		-1485	- 1489	
Glu	$\upsilon(COO^-)^{as}$			+1480			+1488
His	$\upsilon^{10}(N\tau\text{-}C_2)$	-1464	-1472		+1462 -1460	-1473	+1466 -1478
His	N^{π}	+1452	+1448	-1453	+1447	+1446	+1456
Deprotonated amide group	υ(C=O) + υ(C–N$^-$)	+1439	-1439	+1431	-1430	-1439	+1434
His	Def N^1H		+1416			+1414	
His	υ(CN) δ(CH)	-1400	-1400	-1403	-1403 -1388	-1387	-1404
Asp	$\upsilon(COO^-)^{s}$	-1360			+1359		
His	υ(CN)	+1338	+1346		+1342	+1346	
		+1336	+1334	+1335	-1327	+1336	+1335
Lys	$\omega(CH_2)$	-1311	-1311	-1316	+1311	+1311	-1316
Tyr				+1299			+1299
Lys	$T(CH_2)$	+1284	-1282		-1287	-1294	
His	υ(CN)	-1273	+1276	+1277	+1277	+1272	+1277
Gly	$\gamma(CH_2)$		-1269	-1265		-1263	-1265
Lys	$\delta(CH_2)$	+1257	+1256		+1257	+1256	
His	υ(CN) δ(CH)	-1243	+1243	-1250	+1238	+1243	-1250

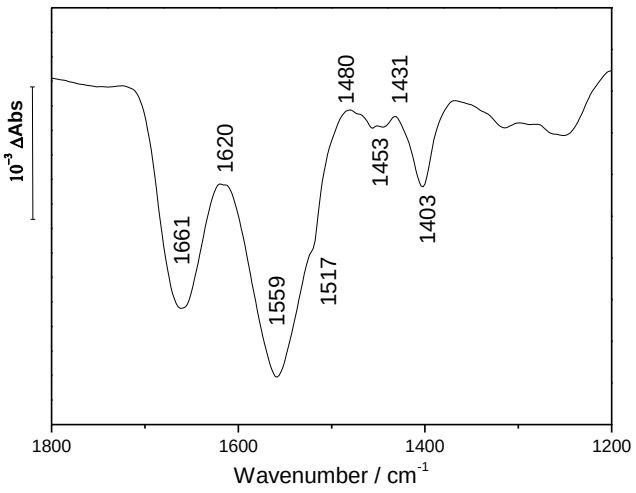

Figure 7.2-8. FTIR difference spectra (ox – red) of the CuA*β*16 complex at pH 6.8

7.2.3 Complex I

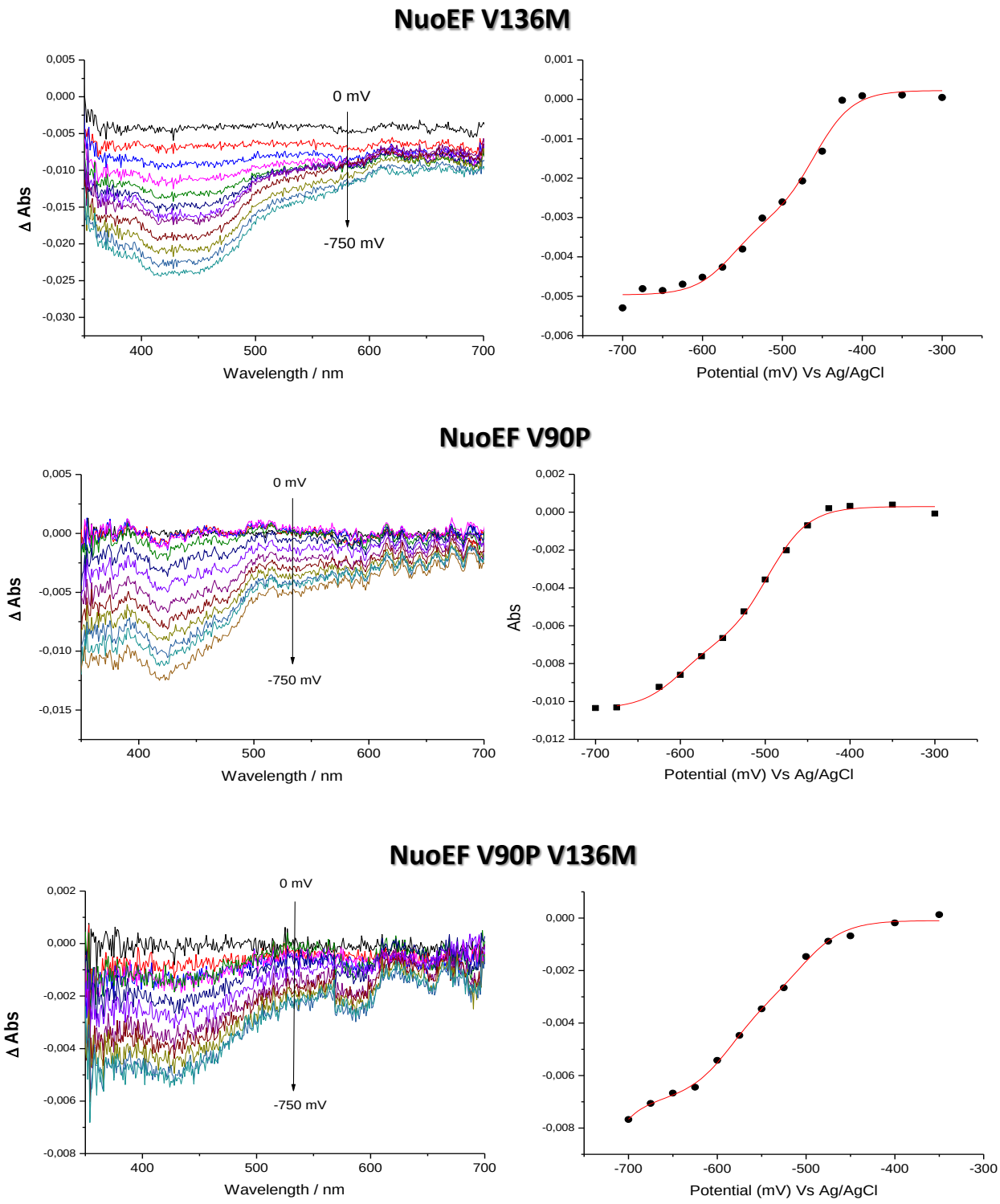

Figure 7.2-9. Uv/Visible titrations of the NuoEF variants of *A. aeolicus*

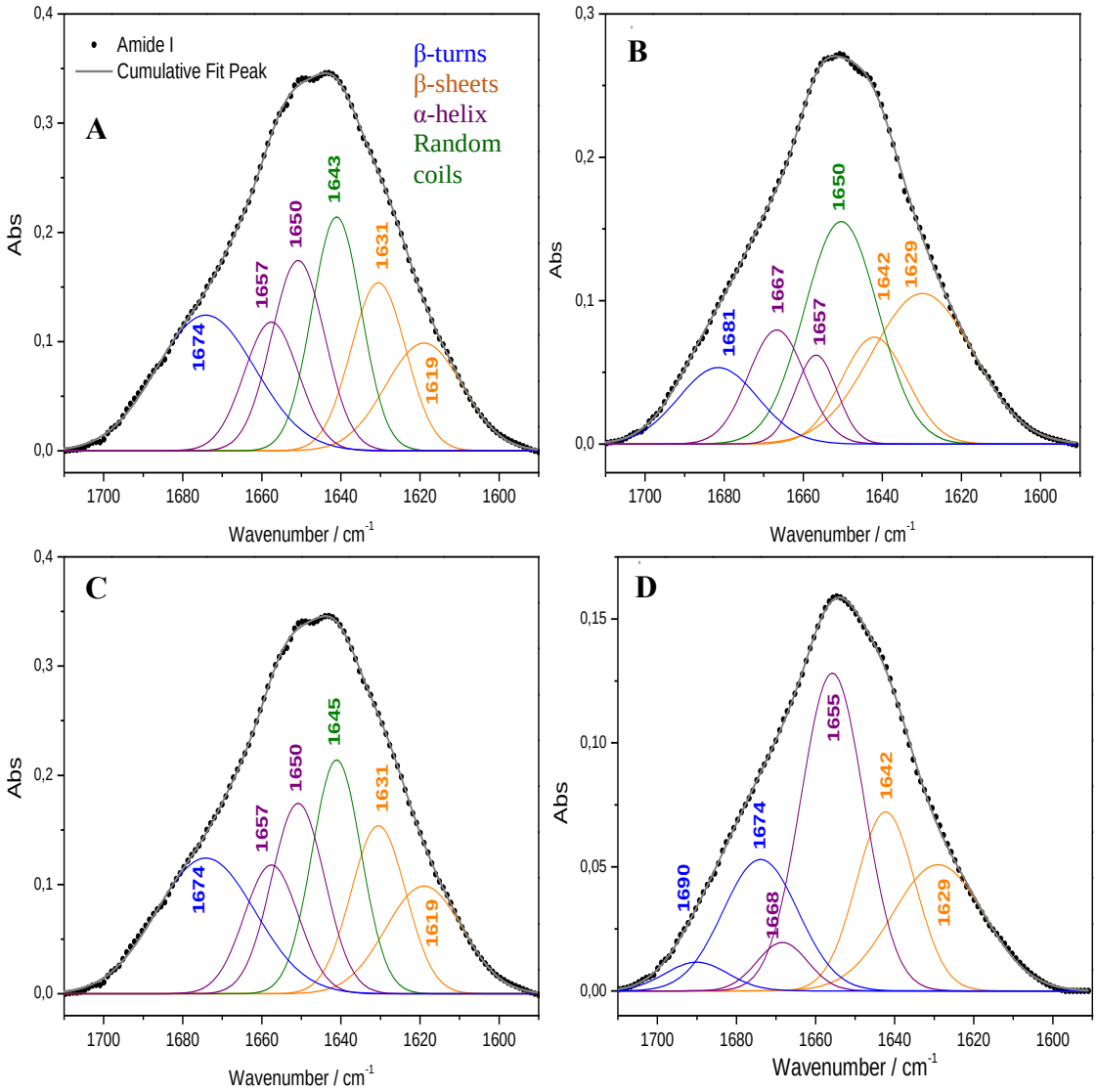

Figure 7.2-10. Amide I deconvolution of NuoEF-WT (A), NuoEF-V90P (B), NuoEF-V136M (C) and NuoEF-V90P/V136M (D)

Table 7.2-2. N1a and N3 metal ligand vibrations by RR spectroscopy of the NuoEF subcomplex WT and its variants from *A. aeolicus* (laser: 514.5nm)

Modes		Type of cluster	Cluster contribution	WT	V136M	V90P	V90P/ V136M
Fe-S stretching	A_g Fe-Fe	2Fe-2S	N1a	211	212	222	216
	Bridging (T_2: B_2/E)	2Fe-2S 4Fe-4S	N1a N3	--	243 261	245 259	--
	Terminal(B_{3u}) Bridging (T_1:A_2/E)	4Fe-4S 2Fe-2S	N3 N1a	287	288	288	288
	Bridging (B_{1g})	2Fe-2S	N1a	319	320	322	320
	Bridging ($A_{1\ breathing}$)	2Fe-2S 4Fe-4S	N1a N3	335	334	334	338
	Terminal Fe-S (Cys)	4Fe-4S	N3	347	349	355	354
	Bridging(A_g)	2Fe-2S	N1a	388	387	387	388
	Bridging(B_{2u})			404	404	414	413
Bending motions	C_α-C_β-N	4Fe-4S	N3	466	465	466	463
	Fe-S-C + A_1 overtone	2Fe-2S 4Fe-4S	N1a N3	484	485	488	488
Fe-S Overtones	2x B_2	2Fe-2S	N1a	527	528	535	534
	2X B_{3u}	4Fe-4S	N3	551	551	551	551
	A1 x υ(Fe-S-Fe)	4Fe-4S	N3	591	592	592	591
C-S Stretching		2Fe-2S	N1a	621	622	629	611
		4Fe-4S	N3	--	642	641	641